Si-Fe-O-based Anodes for Lithium-ion Batteries

by

Yijia Liu

Submitted in partial fulfilment of the requirements
for the degree of Doctor of Philosophy

at

Dalhousie University
Halifax, Nova Scotia
July 2021

TABLE OF CONTENTS

LIST OF TABLES

LIST OF FIGURES

ABSTRACT

Conventional lithium-ion batteries with graphite anodes are approaching their capacity limit. Silicon-based anode materials are expected to be incorporated into the next generation lithium ion batteries because of the high theoretical capacity of Si. However, issues regarding the huge volume expansion/contraction of Si upon lithiation/delithiation need to be alleviated. Nanostructured Si-M (M = transition metal) alloy negative electrode materials have received lots of attention since they show good cycling performance and suppressed volume expansion. However, Si-M alloys still suffer from side reactions with electrolyte during cycling. SiO_x (Silicon oxide) is another focus for Li-ion anode research. SiO_x has relatively low volume expansion, less side reactions with electrolyte, and high capacity retention during cycling. However, the first coulombic efficiency of SiO_x is low because of the irreversible formation of lithium silicates. For practical application of Si-based alloys, anode material design and optimization efforts are required.

In this thesis, the synthesis, microstructure and electrochemical properties of ball milled $Si_{85}Fe_{15}O_x$ and $SiFe_xO_y$ alloys are investigated. Specifically, Si and Fe alloys are ball milled in air for different amounts of time to make Si-Fe-O alloys. The effects of oxygen and iron content on structure and electrochemistry were studied. These alloys also have high thermal stability, which makes them compatible with the chemical vapor deposition process, enabling the formation of composite materials with further enhanced performance. It was demonstrated that the $SiFe_{0.20}O_{0.39}$ alloys can be embedded into spherical natural graphite and CVD-coated to create high performance composite anode particles. The resulting carbon-coated graphite composite particles can cycle well even without the use of advanced binders or electrolyte additives.

LIST OF ABBREVIATIONS AND SYMBOLS USED

a-Si	Amorphous Silicon
at. %	Atomic Percent
BSE	Backscattered Electrons
C	C as in C-rate
CCCV	Constant Current, Constant Voltage
CE	Coulombic Efficiency
CMC	Carboxymethyl Cellulose
CP	Cross Section Polisher
CVD	Chemical Vapor Deposition
d	Atomic Plane Spacing
DEC	Diethyl Carbonate
DMC	Dimethyl Carbonate
EC	Ethylene Carbonate
EDS	Energy Dispersive Spectrometry
EV	Electric Vehicle
FEC	Fluoroethylene Carbonate
FG	Flake Graphite
ICE	Initial Coulombic Efficiency
LECO	Laboratory Equipment Corporation
LiPAA	Lithium Polyacrylate Acid
MA	Mechanical Alloying
MF	Mechanofusion

NCA	$LiNi_{0.8}Co_{0.15}Al_{0.05}O_2$
NDIR	Non-dispersive Infrared
NMC	$LiNi_xMn_yCo_{1-x-y}O_2$
NMP	N-methyl Pyrrolidinone
PR	Phenolic Resin
PVC	Polyvinyl Chloride
PVDF	Polyvinylidene Fluoride
SBR	Styrene Butadiene Rubber
SE	Secondary Electrons
SEI	Solid Electrolyte Interface
SEM	Scanning Electron Microscopy
SG	Spherical Graphite
SiO_x	Silicon Oxide
SLMP	Stabilized Lithium Metal Powder
TEM	Transmission Electron Microscopy
V	Potential
VC	Vinylene Carbonate
wt.%	Weight Percent
XRD	X-Ray Diffraction
ZEV	Zero Emission Vehicle
λ	Wavelength of Radiation
θ	Scattering Angle in XRD

ACKNOWLEDGEMENTS

I would first like to acknowledge my supervisor Dr. Mark Obrovac for the opportunity to study here. I am grateful for the guidance, patience, and inspiration he provided. His valuable and constructive suggestions during the planning and development of this thesis project have been very much appreciated.

I would like to thank Dr. Tim Hatchard for his countless help with instruments. All the members of the Obrovac lab, past and present, are also acknowledged.

Finally, I would like to thank my parents for their endless support.

CHAPTER 1 INTRODUCTION

Lithium-ion batteries are important secondary batteries for today's world. By 2025, Li ion batteries are expected to reach a market share of 94.4 billion US dollars, growing from 44.2 billion in 2020 [1]. Lithium batteries are extensively used for portable electronic devices (such as laptops, cell phones and digital cameras) and are increasingly used in electric tools, electric vehicles (EVs), and grid energy storage in recent years. Although dominant demands in the current market for Li-ion batteries are from electronic devices, it is predicted that EVs will overtake the rechargeable battery market in the near future. In Canada, transportation has become the second largest source of carbon emissions which can take up to 24% of the overall emissions [2]. Federal, provincial, territorial governments and other stakeholders in Canada are working together to develop a zero-emission vehicle (ZEV) strategy to accelerate the adoption of ZEVs and alternative fuel vehicles. Policies such as cash rebates for purchases, millions of dollars of investment on charging stations, tax credits for businesses buying electric cars and encouraging automakers to make sales quotas have been made by the federal government. There are about 168,000 electric vehicles on road now, however, Transport Canada aims to have 825,000 electric cars registered in 2025, and 2.7 million in 2030 [3]. Much effort has been made to pursue better lithium ion batteries with a higher energy density and excellent performance to deal with the fast-growing demands of lithium ion batteries for EVs.

Conventional Li–ion batteries have graphite as the anode material. Graphite has a theoretical capacity of 372 mAh/g (719 Ah/L). Si-based anode materials are promising candidates for the next generation of Li-ion batteries because of their higher theoretical capacity (3579 mAh/g and 2194 Ah/L) and high earth abundance. However, Si-based alloys suffer from huge volume changes during the lithiation/delithiation process, which can result in capacity fade. This thesis is focused on understanding and improving Si-based anode materials for Li-ion batteries. Recent advances in lithium-ion batteries with a particular focus on anode materials will be discussed. A main goal of this thesis is to prepare nanostructured Si-based alloys with suppressed volume expansion, good thermal stability, and good cycling performance. It is hoped that such materials could enable the practical use of Si-based anode materials in Li-ion cells. The preparation, characterization, and use of Si-Fe-O negative electrodes in Li-ion batteries will be described. As an outline of this thesis, Chapter 1 gives a brief introduction to lithium-ion batteries, mainly focusing on negative electrode materials. Chapter 2 outlines the experimental techniques used in this work, including material preparation and characterization. Chapter 3 describes the electrochemical performance and thermal stability of the ball-milled $Si_{85}Fe_{15}O_x$ alloys in detail. Chapter 4 focuses on the electrochemical performance of $SiFe_xO_y$ alloys with different iron content. Following studies on the optimized composition of $Si_{85}Fe_{15}O_x$ were discussed on Chapter 5 while Chapter 6 discloses the preparation of mechanofusion-derived Si-Fe-O alloy/graphite composite electrode material, it shows that advanced binder and electrolyte additive is not required for the composite materials. Chapter 7 summarizes the thesis and provides suggestions for the future work.

1.1 Lithium-Ion Batteries

Lithium-ion batteries have several advantages over other battery types, such as high energy density (~700 Wh/L), long cycle life (>1000 cycles), rapid charge capability, low self-discharge rate and high coulombic efficiency [4–7]. They are commonly comprised of a cathode and an anode separated by an electrolyte containing separator, as shown in Figure 1.1. Lithium transition metal oxides, such as $LiCoO_2$, $LiNi_xMn_yCo_zO_2$ (NMC), and $LiNi_{0.8}Co_{0.15}Al_{0.05}O_2$ (NCA), are typical cathode materials, while graphite is the most common anode material [8–10]. A porous membrane separator is typically used to separate the positive and negative electrodes. The use of a separator prevents electric short circuits, minimizes the electrolyte usage, and increases the structural integrity of the batteries. Non-aqueous liquid electrolytes are commonly used in lithium-ion cells [11]. These are solutions of a lithium salt in organic solvents. Lithium hexafluorophosphate ($LiPF_6$) is commonly used as the lithium salt and the organic electrolyte solvents normally consist of ethylene carbonate (EC) and a linear carbonate, such as diethyl carbonate (DEC) or dimethyl carbonate (DMC). The electrolyte works as a medium to transport lithium ions back and forth between the positive electrode and the negative electrode.

In Figure 1.1 graphite and $LiMO_2$ are active materials. $LiMO_2$ represents a metal oxide positive material, where M is typically Co or combinations of Co, Ni, and Mn. In these active materials, lithium ions can be reversibly incorporated in an intercalation/deintercalation process. When a Li-ion battery is charged, the active positive electrode is oxidized, Li-ions are removed from the cathode, and together with electrons, flow into the anode through different routes. The active anode material gets reduced due to the flow of electrons. In this process, Li ions are extracted from $LiMO_2$ and insert into graphite. Upon discharge, Li-ions travel from a higher energy state in the graphite anode to a lower energy state in the cathode through the electrolyte, while transition metal ions in the cathode are reduced. The electrons released from the anode transfer through the external circuit to the cathode to balance the charge. The resulting current flow in the external circuit can be used to supply power. In the intercalation/deintercalation process, no significant structural change occurs in the $LiMO_2$ or graphite hosts because graphite negative electrode materials have a layered structure and $LiMO_2$ positive electrode materials have either a tunneled or a layered structure that can incorporate lithium ions without significant structural distortion.

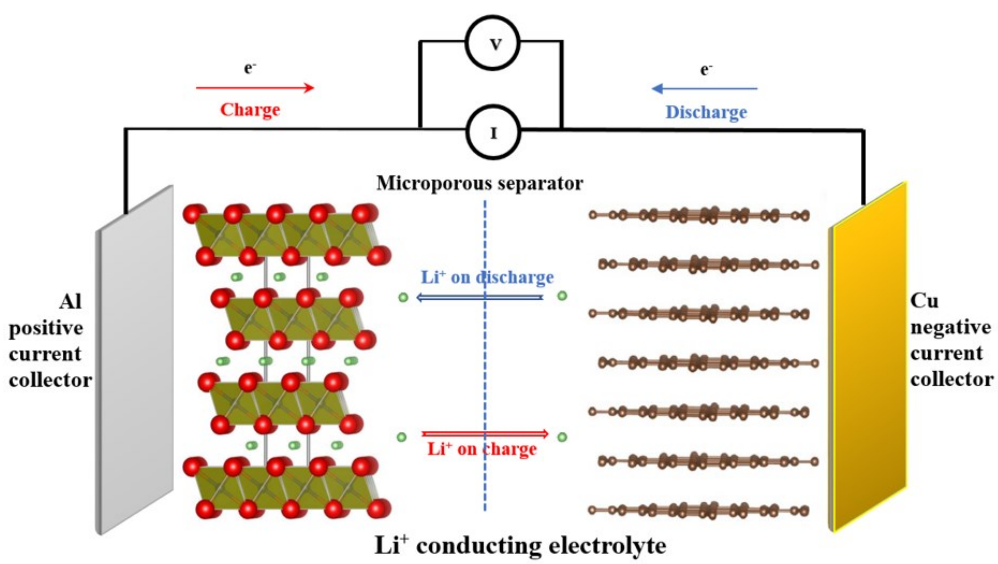

Figure 1.1 Schematic of electrochemical process in a lithium-ion cell, with a $LiMO_2$ (metal oxide material) positive electrode and a graphite negative electrode. Red, blue, green, and brown spheres represent oxygen, transitional metal, lithium, and carbon atoms, respectively.

These spontaneous reactions are driven by a chemical potential difference between the negative and positive electrodes. The resulting working potential, V, can be expressed as:

$$V = -\frac{(\mu_{cathode} - \mu_{anode})}{ne}$$

where e is the charge of an electron, n is the number of electrons taking part in the reaction, and $\mu_{cathode}$ and μ_{anode} are the chemical potentials of the positive and the negative electrodes with respect to lithium, respectively, in electron volts (eV).

Developments in lithium-ion batteries have been focused on improvements in performance (cycle life, rate capability, coulombic efficiency (CE), safety properties, etc.) and increased energy density, mainly via improvements in electrodes and electrolytes. Properties, such as high capacity, a stable structure where lithium could reversibly insert/exit, low production cost, high electronic conductivity, high lithium ion diffusivity, and compatibility with other components, are desired when developing new electrode materials.

1.2 Cathode Materials

$LiCoO_2$ was the cathode material in the first successful commercial LIB launched by Sony in 1991 [12]. Up to today, $LiCoO_2$ is still used in many portable devices due to its high capacity and stability. However, the high cost of cobalt encourages the search of alternative materials. For example, $LiFePO_4$ is a very low-cost material with excellent cycling performance, however, its low specific capacity limits its application to ground transport such as bus transportation. Cathode materials for LIBs, especially for EV applications, require high specific and volumetric capacities, high potentials versus Li/Li^+, high safety property, high tap density (the ratio of powder mass to the volume occupied by the powder after the vessel containing the powder has been repeatedly tapped according to ASTM B527-20), fast kinetics and good capacity retention [13]. $LiMO_2$-type layered oxide cathodes, where M represents transition metals (M) such as nickel, cobalt and manganese (NMC) or nickel, cobalt and aluminum (NCA), are currently most widely used as positive active materials for automotive batteries [13]. Ni-rich layered oxides and Li-rich layered oxides have received lots of attention as potential next-generation cathodes for LIBs due to their low cost and higher discharge capacities compared to $LiCoO_2$. However, there are some challenges for Ni-rich layered oxides as cathode materials for LIBs, such as difficulty in making a well-ordered material with all Ni^{3+} ions, poor cyclability, moisture sensitivity, safety properties, and side reactions with electrolyte [10].

1.3 Anode Materials

Lithium metal was used as an anode material in the 1980s because of its high capacity. However, safety issues have essentially limited the use of lithium metal as a rechargeable battery electrode. In addition, changes in the morphology of lithium during cycling increases its surface area, leading to poor columbic efficiency [8]. On the other hand, graphite offers stable surface morphology, high volumetric capacity, low average potential, low potential hysteresis, good rate capability, low volume expansion, good cycle life, high coulombic efficiency, good electronic conductivity, high abundance, and affordable cost. These properties make it an almost unbeatable anode material [12]. For these reasons, graphite still plays a major role in today's lithium-ion battery industry.

Although graphite has so many advantages, materials with higher volumetric capacity exist that could theoretically increase cell energy density beyond what is possible with conventional Li-ion batteries using graphite anodes. For this reason, metals and alloys have been studied as anode materials since the 1970s [14]. Figure 1.2 shows the specific and volumetric capacities of various Li-metal alloys compared to graphite. This figure illustrates why alloy-based negative electrode materials are promising and lists some good candidate elements to be studied. Concerning the specific capacity, Si is far ahead of other metals and abundant in the Earth's crust, giving it a significant advantage over others. However, the difference amongst the elements is less with respect to volumetric capacity. Ge is slightly higher in volumetric capacity than Si, however, the high cost of Ge metal (1000 USD/kg) has prohibited its applications in most cases [15]. Si is the next highest, with a volumetric capacity around 2194 Ah/L, Sn and Sb are not far behind the volumetric capacity of Si. Table 1.1 compares the cost of some of the interested elements and the corresponding capacity normalized cost. It is clear that Si is by far the cheapest material per unit capacity, making Si to be the main element to focus on. Besides the desired high-capacity and low-cost earth abundance, potential window and low toxicity are also of great importance when selecting the right elements to study [16].

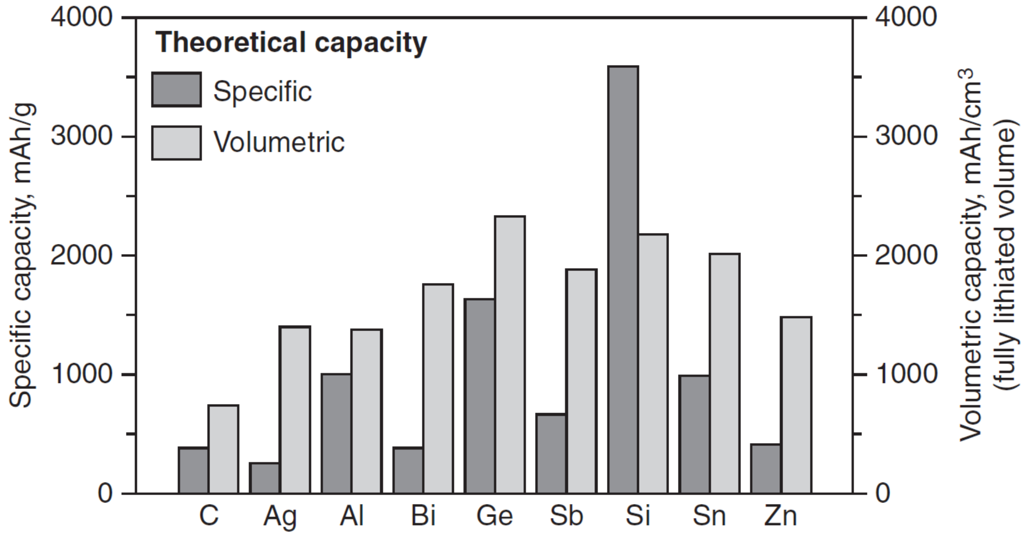

Figure 1.2 Specific and volumetric capacities of Li alloys compared to LiC_6. The volumetric capacities were calculated based on the fully lithiated volume. Reproduced with permission from Reference [8], Copyright 2011 McGraw-Hill.

Table 1.1 Candidate elements for high-capacity Li-ion battery anode material applications. The commodity cost of metals in USD/kg, specific capacity of each element in mAh/g and capacity normalized cost in USD/kAh are listed.

Element	**Price USD/kg**	**Capacity mAh/g**	**Capacity normalized cost USD/kAh**
Ge	1000 [15]	1384	722
Graphite	9-20 [17]	372	13-54
Sn	17.2 [18]	960	18
Si	2.7 [19]	3579	0.75

It is worth noting that because all alloys undergo large volume expansion (up to 280%) during lithiation, it is essential to consider the trade-off between the benefit of having increased energy density vs. alloy volume expansion in a full cell. Figure 1.3 shows the energy density at 100% volume expansion for selected elements calculated in a full cell. The energy density for each element in this figure is about the same at the given volume expansion [20]. The maximum improvement in the energy density of full cells with alloy anodes compared to graphite is about 20% [12]. This energy increase is deemed a significant enough incentive to encourage researchers to solve the problems associated with alloy volume expansion.

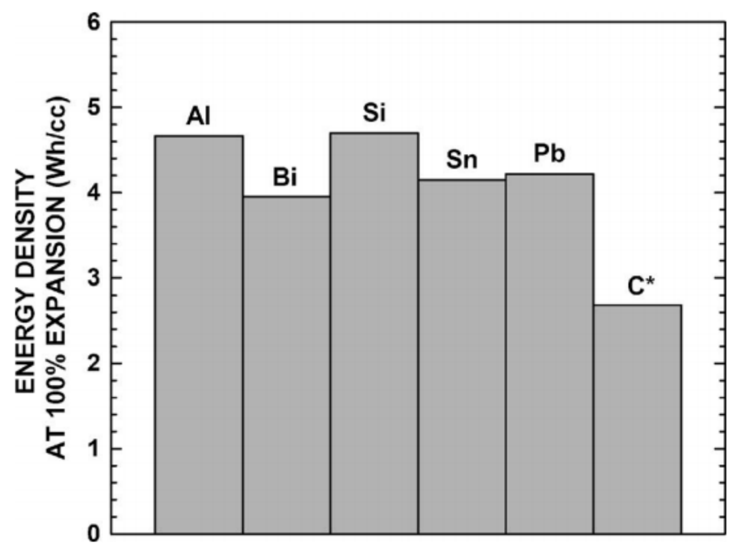

Figure 1.3 The volumetric energy density (vs a 3.75 V cathode) of Li alloys at a 100% volume expansion. *Carbon expands by 10% during lithiation, it is included for comparison. Reproduced with permission from Reference [20], Copyright 2007 The Electrochemical Society.

1.4 Si-based Anode Materials

Si, with high theoretical capacity and high earth abundance, has received lots of attention for application in Li ion batteries. This section will introduce electrochemistry of Si and methods that are used to optimize Si-based anode materials.

1.4.1 Electrochemical Properties of Pure Si

Unlike the intercalation/deintercalation process between graphite and Li, the reaction between Li and Si follows an alloying mechanism, Li forms alloys with Si, involving bond breaking between host atoms and drastic structural changes [21]. This results in large volume expansion/contraction during lithiation/delithiation. As a result, large amounts of capacity fade can occur in just a few cycles. The electrochemistry of bulk Si has been studied by Obrovac *et al.* [22,23]. In 2004, Obrovac and Christensen performed a detailed *ex situ* X-ray diffraction (XRD) study on the electrochemical reaction of lithium with silicon [23]. They confirmed the transition from crystalline Si to an amorphous structure upon lithiation and discovered the formation of crystalline $Li_{15}Si_4$ below 50 mV. This was an important finding because $Li_{15}Si_4$ is a metastable phase that is not present in the Li-Si phase diagram and only appears during electrochemical cycling. In a later study, Li and Dahn performed an *in-situ* XRD study on crystalline Si negative electrodes to study the electrochemical alloying mechanism of crystalline and amorphous Si with lithium and provided a detailed phase diagram during lithiation and delithiation [24]. Li *et al.* utilized ^{119}Sn Mössbauer spectroscopy to further understand the electrochemical reaction between a-Si and Li using Sn as probe atom [25]. It was found that the two sloping plateaus in the discharge profile correspond to two arrangements of Li atoms in the host structure. The higher potential plateau is a result of Li-ions being inserted into environments where each Li has Si neighbours primarily. While at lower potentials, the Li atoms have Li neighbours primarily, meaning that their insertion potential will be closer to that of Li-plating (occurring at 0 V vs. Li).

The current understandings of Li-Si electrochemistry are summarized in the Si potential profile in Figure 1.4. As crystalline silicon is lithiated, it turns into amorphous Li_xSi (a-Li_xSi, I in Figure 1.4) in a two-phase region with a potential of about 70 mV, if the potential proceeds below 50 mV, the a-Li_xSi will crystallize to form $Li_{15}Si_4$ (II in Figure 1.4). During the first delithiation, $Li_{15}Si_4$ is delithiated to form amorphous Li_xSi, a plateau at about 0.43 V is observed because of this two-phase region. At higher potentials, the amorphous Li_xSi is completely delithiated to form a-Si. In the following discharge, if the cut-off potential is above 50 mV, silicon will remain amorphous, and a single phase region is observed (IV in Figure 1.4), the reversible process is observed as V in Figure 1.4, showing the delithiation process of amorphous lithiated silicon [23][24]. VII and VII in Figure 1.4 are the two sloping plateaus during the lithiation of amorphous Si, as carefully studied by Mössbauer spectroscopy in Reference [25], the first sloping plateau at higher potential represents the Li-Si neighbours filling while the second corresponds to Li-Li neighbours filling. Again, if the lithiation potential goes below 50 mV, crystalline $Li_{15}Si_4$ forms and a plateau will appear during the next delithiation potential profile.

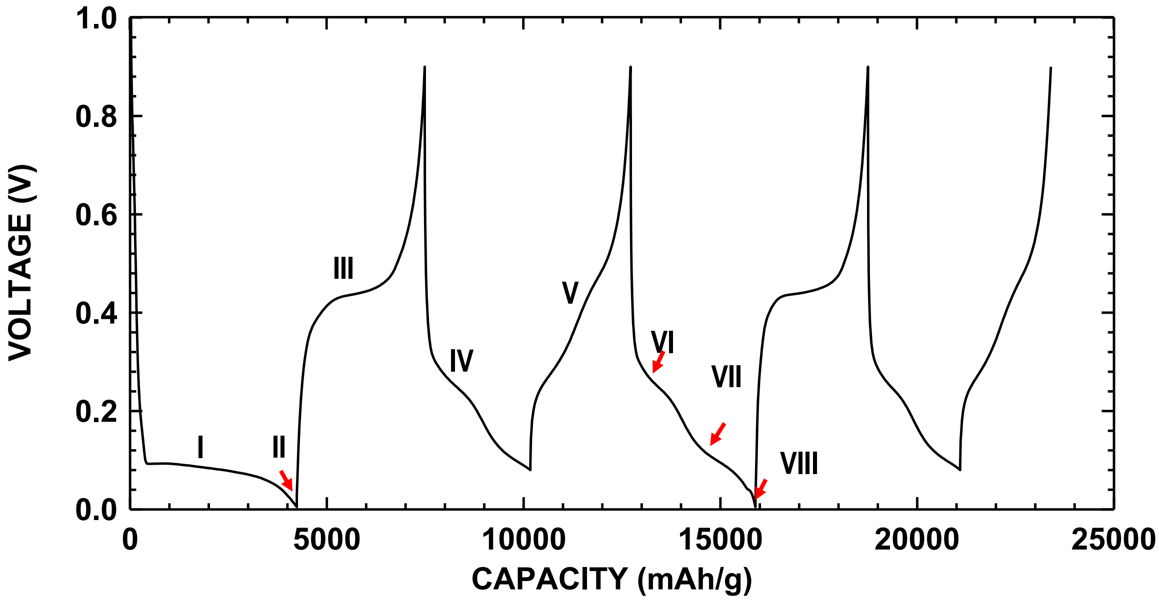

Figure 1.4 Potential profile of a crystalline silicon electrode cycled in a way to illustrate the electrochemical conversion of crystalline silicon to amorphous silicon, amorphous silicon to crystalline $Li_{15}Si_4$, and $Li_{15}Si_4$ back to amorphous silicon. Reproduced with permission from Reference [22]. Copyright 2013 The Electrochemical Society.

The significant volume expansion (fully lithiated Si expands by 280%) of alloy negative electrodes upon lithiation makes it difficult to implement them in commercial cells. Active alloys undergo mechanical stress during lithiation with huge and repeated volume changes during subsequent cycling. As a result, alloy particles can become pulverized with repeated cycling, leading to cell fade [22]. Reference [26] proposes three possible mechanisms to explain the cell failure initiating from volume expansion, including pulverization, delamination and an unstable solid electrolyte interface (SEI) layer. A schematic diagram of the cell failure mechanism is shown in Figure 1.5. Large stress generated from the huge volume change during lithiation/delithiation could cause pulverization, which results in loss of electrical contact and eventual capacity fade. This fade mechanism is mainly observed in early studies of bulk Si or Si films [27][28]. In addition, loss of contact can happen between the active materials and current collector upon cycling, which means the entire electrode integrity can suffer from volume changes during cycling. Besides the mechanical failure of cells, the irreversible consumption of Li ions is a major cause of fade. During cell operation, an SEI layer is formed on the electrode surfaces. This passivating SEI layer mainly consists of Li_2CO_3, various lithium alkyl carbonates ($ROCO_2Li$), LiF, Li_2O, and nonconductive polymers [29][30]. The SEI conducts ions and insulates electrons, therefore protecting active materials from further side chemical reactions [29]. However, for a Si-based anode, its large volume changes may affect the stability of the SEI. The SEI is likely to be disturbed by the volume changes of the active material, and fresh alloy surfaces will be exposed to the electrolyte during cycling. This may lead to continuous consumption of the electrolyte and the formation of a thick heterogeneous SEI layer with high resistance. The properties of the SEI layer directly determines an electrode's coulombic efficiency and electrochemical impedance. A stable and dense SEI layer is a vital factor for better cycle life of silicon anodes.

In addition, a two-phase region might be observed in some cases during alloy lithiation/delithiation. This will cause a potential plateau. Phase boundaries encountered during two-phase regions can result in additional particle damage due to inhomogeneous volume changes, while lithiation in a single-phase region results in more homogeneous volume change [12][21][24][31][32]. In the case of Si, the formation of crystalline $Li_{15}Si_4$ will result in a two-phase region during delithiation. Since fade and two-phase regions are often coincident, it is thought that two-phase regions should be avoided during cycling [12].

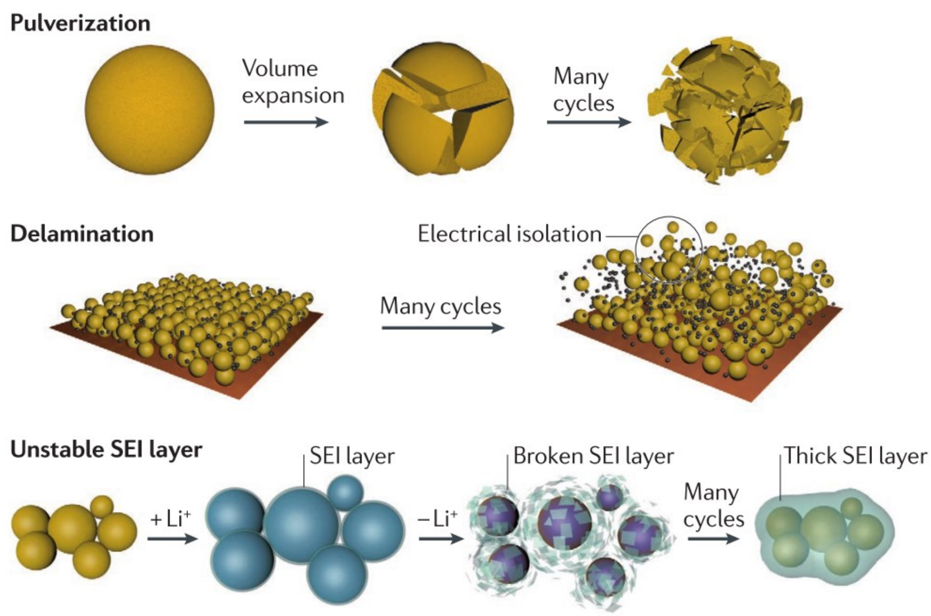

Figure 1.5 Cell failure mechanism of silicon. Reproduced with permission from Reference [26], Copyright 2016 Springer Nature.

1.4.2 Si-containing Anodes

In view of the above issues of pure Si electrodes, it has been demonstrated that such drawbacks could be partly overcome through electrode material design, including (1) nanostructure designing; (2) making active/inactive phase Si-M(metal) alloys; (3) SiO_x materials; (4) making Si-C alloys and composites.

1.4.2.1 Nanostructure Designing

Unlike bulk silicon, nano-Si can reduce fracture and improve cycling by decreasing the mechanical stress generated during lithiation and delithiation [22][33]. Several nano-Si materials, including 1D Si nanowires [34] and 2D Si nanosheets and nanowalls [35,36] have been studied. It has been demonstrated that there is a strong dependence between the size of nano-Si and its pulverization (a threshold size of 150 nm) [37]. The movement of the two-phase boundary between the inner core of pristine Si and the outer shell of a-Li_xSi during lithiation causes the propagation of cracking in large-sized Si nanoparticles [37]. Although the cracking issue can be partially alleviated by using nano-Si below the threshold size, current bare Si anodes still suffer from capacity fade due to the high internal stresses associated with the formation of crystalline $Li_{15}Si_4$ phase upon full lithiation [38,39]. In addition, nanometer-sized Si negative electrode materials suffer from the high specific surface area and thus cause large irreversible capacity and related safety issues. The high surface area of nanosized Si materials increases the possibility of chemical reactions with electrolytes. For example, after the decomposition of a commonly used electrolyte $LiPF_6$, the resulting HF can react with Si, making the active Si network become electrochemically inactive, which is undesired in a good anode material [40][41].

1.4.2.2 Making Active/inactive Phase Si-M(metal) Alloys

Active-inactive alloys represent another method to deal with volume expansion, the inactive phases can act as a matrix to hold the active phase upon the lithiation/delithiation process [33]. Si-based alloys are designed to be made of active Si surrounded by inactive phases. This design strategy can not only buffer the volume expansion but also give high volumetric energy density and show lower average potential than that of pure Si for a given volume expansion [20]. It was also demonstrated that confining nano-sized silicon in an alloy matrix can suppress particle pulverization and reduces the surface area of Si exposed to the electrolyte [42]. Si active/inactive alloys can offer high specific capacity, high reversible capacity, good capacity retention and good $Li_{15}Si_4$ suppression, and therefore are good candidates for commercial applications of Si-based electrode materials. For example, 3M V6 alloy (as shown in Figure 1.6) is a formerly commercially viable Si active/inactive alloy that has been shown to have good cycling performance. In addition, composite electrodes that are made of 3M V6 alloy particles and graphite are shown to have improved cycling performance even at a high loading of 4.5 mg/cm^2. The graphite-blended electrodes show superior electrochemical properties compared to neat V6 electrodes [43].

Some other nanostructured Si-M alloys, such as Si-V [44], Si-Cr, Si-Mn [45], Si-Fe [46], Si-Co [47], Si-Ni [48], Si-Ti [49] have been extensively studied as negative electrode material in LIB. According to studies on Si-Ni thin films by Du *et al.*, Ni was found to depress the lithiation potential, resulting in a reduction in capacity. This potential depression was attributed to internal stress in the thin film during lithiation from the presence of Ni [50]. In the study of the Si-Ti system, inactive $TiSi_2$ phase was found to effectively suppress the formation of $Li_{15}Si_4$ during cycling with no noticeable change in the average potential (in contrast to Si-Ni alloys), resulting in relatively low polarization cycling. It is claimed that the $Li_{15}Si_4$ phase suppression was coincident with good cycling performance and good electrode structure maintenance upon lithiation/delithiation [49]. Si-Fe alloy is one of the most studied Si-M alloy materials as anode materials [45,46,51–57]. Fe has some favourable properties such as high abundance, low-cost, environmental compatibility, and high electronic conductivity [54]. In addition, iron and iron silicides are electrochemically inactive towards Li, but with high electronic conductivity, thus, they can serve as conductive Li-inert matrices to buffer the volume changes of Si-based electrodes during cycling [46,51,54]. A capacity of 1010 mAh/g and a capacity retention of 94% after 200 cycles were achieved for ball milled $FeSi_2$/Si@C alloy, however, A capacity of 1010 mAh/g and a capacity retention of 94% after 200 cycles were achieved for ball milled FeSi2/Si@C alloy, however, the volumetric capacity of this material was not reported [53].

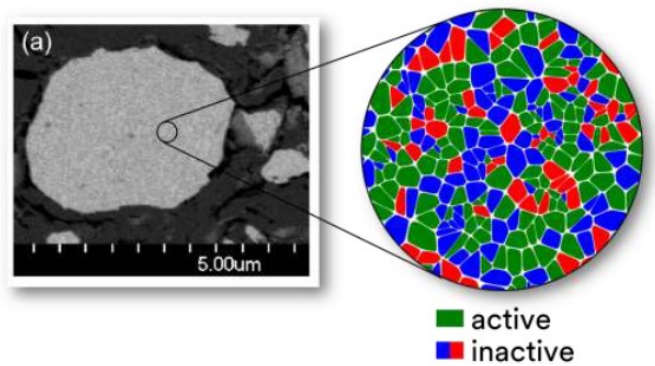

Figure 1.6 FESEM image at 10 kX magnification of an ion polished cross section of a 3M V6 Si alloy particle showing compositional uniformity. Surrounding darker regions are graphite. Reproduced with permission from Reference [42][58], Copyright 2014 The Electrochemical Society.

1.4.2.3 SiO_x Materials

Nanostructured materials, such as SiO_x, which comprises micron-size particles made up of nanometer-size grains of electrochemically active Si and inactive matrix (SiO_2), have been found to be very useful anode materials [59]. SiO_x has relatively low volume expansion, less side reactions with electrolyte than nanosized Si, and high capacity retention during cycling. Moreover, the phases formed during the first lithiation, such as Li oxide (Li_2O) and Li silicates (Li_4SiO_4) also work as a buffer matrix for Si expansion in the following lithiation/delithiation. Drawbacks of SiO_x include its high cost and its high irreversible capacity loss which is due to the irreversible formation of lithium silicates during its initial lithiation [60]. Amorphous SiO is commonly manufactured from the vapor deposition of silicon and silicon dioxide ($Si(s) + SiO_2(s) \rightarrow 2SiO(g)$) in vacuum at high temperatures [59,61,62]. Solid SiO is thermodynamically unstable at all temperatures, it will disproportionate into Si and SiO_2 during heat treatments.

Disproportionated SiO (d-SiO) are nano-crystallite Si embedded in amorphous silicon oxide matrix [63]. In the disproportionated SiO_x, increased Si^0 and Si^{4+} valence states were identified and Si^{1+}, Si^{2+}, and Si^{3+} states decreased, resulting in different electrochemical performance than that of amorphous SiO_x. The potential profile of the first lithiation of disproportionated SiO_x is similar to Si anodes due to the formation of nanocrystalline Si in the reaction [64]. Park et al. found that superior cycling and reversibility were achieved in disproportionated SiO_x at 1000 ºC compared to pristine SiO_x and d-SiO_x (800 ºC). They explained as the formation of well-distributed Si nanocrystallites of 5 nm and amorphous SiO_x matrix [61]. However further increase of heat treatment temperature to 1200 ºC caused poor performance which possibly due to the increased formation of Si^{4+}-based amorphous suboxide which were inert toward Li electrochemically. The disproportionated SiO_x at 1200 ºC showed almost no capacity because Si nano-crystallites and amorphous SiO_2 were surround by inactive Si suboxides and could not react with Li [62]. However, it was found that after ball milling, disproportionated SiO_x particles broke into smaller sizes and Si nano-crystallites and amorphous SiO_2 were exposed, giving rise to excellent electrochemical performance [62]. The oxygen content in SiO_x also plays an important role in their electrochemical performance [60][65]. It was suggested that an increase in oxygen content of SiO_x ($0.4 \leq x \leq 1.3$) can decrease electrolyte reduction but oxides are subject to degradation by acidetching [65]. Increased x also causes low initial coulombic efficiency (ICE), due to the formation of Li_2O and Li_4SiO_4. Cycling performance, however, is improved with the increase of the x values, indicating that stress and volume change during lithiation/delithiation were accommodated by the oxide buffer around Si. Therefore, the optimized electrochemical performance of SiO_x needs to be carefully considered either by synthesis process or the control of oxygen content. Cao et al. have reported a reactive gas milling method to prepare SiO_x with tunable oxygen content [66]. The amorphous $SiO_{0.37}$ anode showed a very comparable cycling performance compared to a commercial SiO, but with a higher volumetric capacity (1800 Ah L^{-1} vs. 1400 Ah L^{-1}) and ICE (70% vs. 55%) as well as better rate capability (1648 mAh g^{-1} vs. 600 mAh g^{-1} at 2 C) [66].

To take advantage of the high capacity and excellent performance of SiO_x materials, a very common method is to add small amounts of SiO_x to graphite, for example, a reversible specific capacity of 397 mAh/g with 76 % capacity retention after 200 cycles in a full-cell system was reported when blending 3 wt% of $SiO_{1.06}$ with graphite [67]. The blending of small amounts of SiO_x content was thought to be a short-term solution for the quick adoption of SiO_x materials to minimize modifications of other cell components (such as electrolyte and binder). BTR China has released a commercial SiO_x/graphite composite product with capacity of 600-650 mAh/g [68]. It is also suggested that SiO_x are already being used in batteries for Tesla electric vehicles [69]. However, it should be noted that higher SiO_x contents lead to a large increase of irreversible capacity losses in Li-restricted full-cell systems [43,70]. Lots of studies from all aspects are still required in order to fulfill the implement of SiO_x electrodes either by itself or in graphite composites [71].

1.4.2.4 Si-C Composites

Si-C materials are an important type of Si-containing anode material that have been widely studied. Carbon can dilute volume expansion, contribute to cell capacity, and increase electronic conductivity. Mechanical mixing, ball milling and pyrolysis are some common methods to prepare Si-C materials, where silicon particles are distributed in the carbon matrix. Carbon coated Si particles have been intensively studied as an important type of Si-C composites. Considerable efforts had been made on different sources and approaches for carbon coating. Carbon precursors such as pitch [72], citric acid [73], polyvinylidene fluoride [74] and glucose [75]were investigated for pyrolysis process. Chemical vapor deposition (CVD) has been demonstrated as a promising approach to improve the electrochemical performance of Si-based electrodes [75–84]. Yu et al. reported a CVD carbon coated (about 12 nm thick) Si material can deliver a specific capacity of about 1600 mAh/g at 0.3 A /g for 70 cycles, with a good rate performance at 5 A/ g(a 750 mAh /g capacity was retained), compared to 240 mAh/g for pristine Si [76]. They also found that different thickness of carbon layer will results in different performance in the specific capacity, cycle stability, and rate capability [76]. A thick carbon layer was initially preferred to withstand the interface tension. However, a dense and thick carbon layer will add additional weight to the electrode, dilute the overall specific capacity, and slow down the movement of Li ions from electrolyte to silicon, causing poor rate capability [80]. Therefore, a suitable thickness of the carbon layer should be carefully engineered to achieve good balance between capacity and particle design. The desirable carbon coatings should not only homogeneously coat the silicon particles with reduced side reaction, allow fast transport of Li ions, improve the stability of SEI layer, but also deal with the internal stress induced by the volume changes during lithiation and delithiation process to improve the structural integrity of the electrode.

Some novel nanomaterial design strategies of Si-C materials have been demonstrated, such as making Si–C yolk–shell and pomegranate structures [85–87] or graphene-encapsulated Si particles [88,89] with an impressive cycle life. For example, Liu et al. proposed a Si@C yolk-shell structure by employing the SiO_2 sacrificial layer for void spaces and using polydopamine as a carbon precursor. As a result, silicon nanoparticles were sealed by the 5–10 nm thick carbon shells with void space inside (≈40 ‑ 50 nm). The void space allowed the silicon cores to expand without disturbing the outer carbon shell, therefore maintaining the high specific capacity of 2800 mA h g−1 at a rate of C/10, long cycle life with 74% capacity retention over 1000 cycles, and coulombic efficiency of 99.84% [87] Such novel nanomaterial structure designs seem very promising in terms of improving cycling performance. However, their large-scale production cost tends to be high because of the need to use HF, expensive catalysts and templates, and relatively low yields. In addition, reduced volumetric energy density from such hollow structures should also be considered for their commercial applications. Ko et al. have proposed an architecture using silicon-nanolayer-embedded graphite/carbon (as shown in Figure 1.7) [84]. Both the silicon nanolayer and the surface carbon coating were produced via CVD, which was likely scalable as claimed by the authors. The void space inside the particle can accommodate Si volume expansion during lithiation. The carbon coating on the surface can dilute the volume expansion of the electrode, but also reduces side reactions of Si with electrolyte, and increase conductivity and mechanical stability. This anode material shows a high first cycle CE of 92% with a capacity retention of 96% after 100 cycles. A full cell with this material vs. a $LiCoO_2$ cathode demonstrated a high energy density of 1043Wh/L [84].

The idea of Si/graphite or Si-alloy/graphite composite materials is to form a nanocomposite that is made of electrochemically active species surrounded by graphite phases. The nanostructure of such negative electrode material is considered to comprise nanometer-size active grains dispersed in a graphite matrix. Jo et al. produced a Si/graphite composite by ball milling natural flake graphite and Si particles. The resulting material has reversible specific capacities of 568 mAh/g with a first cycle CE of 86% [70]. However, this Si-graphite composite only has a capacity retention of 73% after 30 cycles due to the incompatibility between the irregular particle sizes of Si and graphite. Cao et al. [90] prepared Si-alloy/graphite composite electrode materials via mechanofusion (as shown in Figure 1.8). The resulting microstructure was described as Si-alloy particles well dispersed between graphite layers. This material demonstrated a reversible capacity of 950 mAh/g with almost no obvious capacity fade up to 50 cycles. The authors proposed that the graphite matrix acts a buffer for Si-alloy expansion and may protect the surface of the alloy from reacting with the electrolyte, resulting the superior cyclability and rate capability [90].

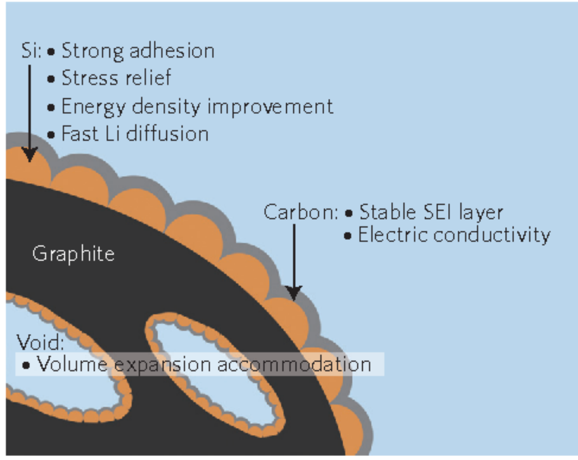

Figure 1.7 Cross-sectional schematic view showing the detailed structural characteristics of an SGC hybrid particle. Reproduced with permission from Reference [84], Copyright 2016 Springer Nature.

Du et al. demonstrated that blending graphite with Si alloy in electrode coatings allows calendering processing without particle fracture of the Si alloy. Such calendered electrodes achieve increased energy density in full cells as compared to cells with graphite [43]. Commercial coatings are often calendered under high pressures to achieve appropriate porosity (10−40%), with improved electrode density, cycling stability, coating adhesion, and electrical conductivity [12]. Therefore, it would be very promising if electrodes comprising Si /graphite or Si-alloy /graphite composite could be calendered with no particle fracture without the need to incorporate additional graphite in the coating formulation. Silicon-based/C composites, such as SiO_x/carbon/graphite and Si/carbon/graphite, are the most practical high energy density anode materials, because these materials show the balanced advantages of graphite and silicon or silicon oxide. However, commercial silicon-based materials such as SiO_x/C/Graphite and Si/C/Graphite have many inevitable parasitic reactions with electrolytes and exhibit large volume expansion towards graphite. In addition, the selection of binders and electrolyte additives for such Si/graphite composites should be carefully considered. For example, the high or low content of Si may favour different binder chemistry or follow different interphase chemistry when interacting with electrolytes. A homogeneous distribution of active particles with graphite and an optimized ratio between active and graphite materials still need to be explored to achieve a higher first cycle CE, less side reactions with electrolyte, suppressed volume expansion, and good post-calendering properties [84].

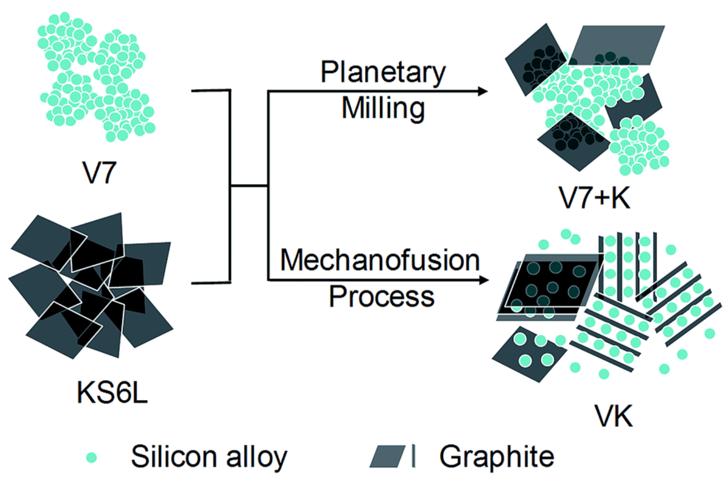

Figure 1.8 Schematic illustration of planetary milled and mechanofusion dry processed Si-alloy/graphite composites. Reproduced with permission from Reference [90], Copyright 2019 The Royal Society of Chemistry.

1.5 Other Key Components of Si-based Anodes

Besides engineering better anode materials, other non-electrode components in lithium ion batteries, such as binders, electrolyte and electrolyte additives are also of great importance.

1.5.1 Binders

Binders are materials such as polymers to bind active materials and current collector together to maintain mechanical and electronic integrity of electrodes [91]. Good binders should have good adhesion to active material and current collector; able to coat the surface of active particles to prevent excessive SEI formation while maintaining fast Li ion conduction; withstand dimensional changes by stretching or self-healing; and maintain good electrical conduction [12]. In Si-based anodes, binders with high mechanical strength are required to accommodate the large volume changes during lithiation/delithiation, while maintaining the integrity of the electrode. Some polymeric binders used for Si-alloy anodes, such as polyacrylic acid (PAA) and carboxymethyl cellulose (CMC), can uniformly cover and chemically bond to the surfaces of active materials [12], good cycling performance is therefore expected. Figure 1.9 compares the cycling performance of Si electrodes made with different binders. Severe capacity fade was observed on the conventional polyvinylidene fluoride (PVDF) binder while PAA binder shows good capacity retention. Figure 1.10 shows the proposed mechanism of PAA and PVDF binders [92]. In the PVDF electrode, the PVDF forms a thin net of fine (<30 nm) polymer threads, alloy surface is exposed to electrolyte and severe SEI growth occurred during cycling (as evidenced by 2.5 times higher resistance across the PVDF electrode thickness). PVDF does not chemically bond to the alloy particles or current collector and experiences severe swelling when exposed to electrolyte. Worse still, the electrolyte decomposition products increase electrode impedance and cause some alloy particles to become isolated. During cycling the mechanical integrity of the electrode is further disrupted by alloy expansion, alloy particles can easily become disconnected [93]. However, when PAA-based binders are in contact with electrolyte, they do not swell and maintain strong adhesion to Si surfaces [92]. PAA binders can also maintain good adhesion on Si surfaces via hydrogen bonding [94]. It is also reported that during cycling, PAA binders can be electrochemically reduced, converting carboxylic groups to lithium carboxylates and forming a protective layer (so-called artificial SEI), this binder covered Si surface can then impedes further SEI growth [93]. Through the comparison between PAA and PVDF binders, the importance of binders in Si-based electrode is clearly demonstrated. Studies on advanced binders that can improve the stability and integrity of the Si-based electrode during lithiation/delithiation process are of great necessity for the future application of Si-based anode materials.

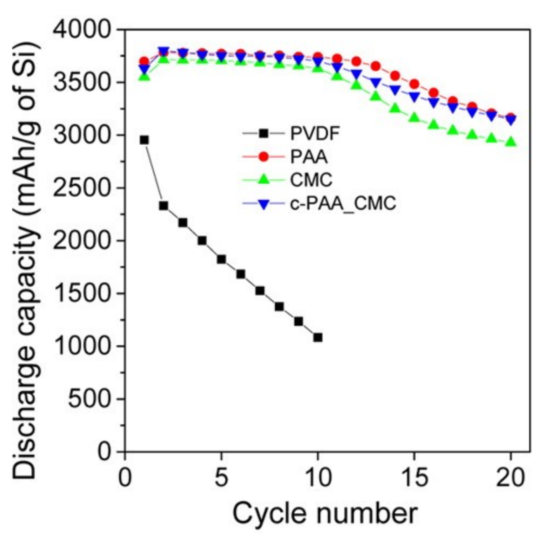

Figure 1.9 A comparison of the cycling performance of Si nanoparticle electrodes using PVDF, PAA, CMC and cross-linked PAA−CMC binders. Reprinted with permission from Ref [93]. Copyright 2016 American Chemical Society

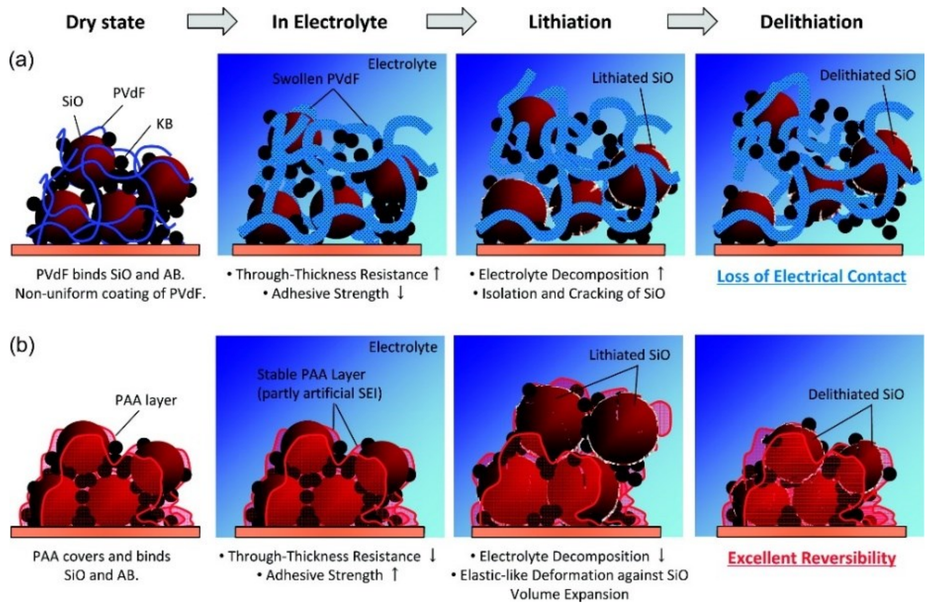

Figure 1.10 Comparison of binding mechanisms between PVDF and PAA binders. (a) SiO coating with PVDF binder showing PVDF swelling upon exposure to electrolyte and poor adhesion. (b) SiO coating with PAA binder, showing no swelling, the formation of an artificial SEI layer, and strong binder adhesion Reprinted with permission from Ref [92]Copyright 2011 American Chemical Society

1.5.2 Electrolytes and Electrolyte Additives

Both graphitic and Si-based anodes have low working potentials (0.05−0.5 V vs Li/Li^+), which are outside the thermodynamic stability window of most of electrolyte components (solvents, Li salts, and additives) [95]. Hence, decomposition of these components is inevitable during cell operation. The precipitation of the reduction products passivates the anode surfaces, which dictates the interphasial chemistry. In the pristine state, both materials are in the unlithiated state, and SEI layer is formed in steps. This is where electrolyte additives can step in to do some useful work over the operating voltage window. Unlike graphitic anodes, the native surface of Si-based anodes containing redox-active passivating species, such as SiO_2 and Si−OH [96], and these can irreversibly react with lithium, organic solvents, and lithium salts, some of them being detrimental to the subsequent cycling performance [61,97–99]. In addition, the repeated volume change of Si electrodes upon lithiation/delithiation will result in continuous SEI growth, which may cause poor cycling. In response to such differences among graphite and Si anodes, care must be paid while designing functional electrolyte and electrolyte additives for Si-based anode materials, additives that work well with graphitic anodes may not necessarily be suitable for Si anode-based electrode materials [100].

Fluoroethylene carbonate (FEC) is the most common additive in carbonate-based electrolytes for Si electrodes [101–103]. Si-based electrodes in FEC-containing electrolytes were found to show excellent performance in both capacity retention and coulombic efficiency as shown in Figure 1.11 [104]. It is widely accepted that FEC-derived interphases seem to be denser and thinner, whereas FEC-free interphases tend to be more porous and permeable by electrolytes [101,105]. Ex-situ surface analysis of the cycled electrodes shows that the additives are reduced to form a stable SEI composed of polycarbonate, lithium alkyl carbonates, Li_2CO_3 and LiF [102,103]. Nguyen et al. have found that electrolyte containing 10% FEC has a good combination of reasonable cost, low impedance and high capacity retention [102]. However, it was reported that high concentration of FEC can cause significant gas evolution (After 500 hours cycling, cells with 6% FEC will produce about 10 times more gas than cells with 2% FEC) in Si-graphite/$LiCoO_2$ full cells compared to electrolytes containing VC [106,107]. In addition, the presence of LiF in the interphase is controversial and its advantage to electrochemical performance is under discussion. For instance, some studies have argued that HF can cause SEI degradation and transition metal ion dissolution from the cathode [108].

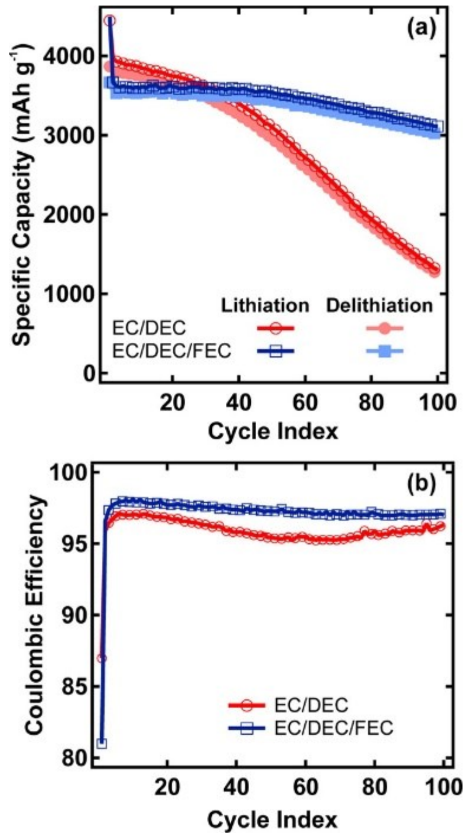

Figure 1.11 (a)Specific capacity and (b) Coulombic efficiency versus cycle at ~C/2 rate as a function of cycle for a-Si thin film electrodes cycled in EC/DEC (red circles) and EC/DEC/FEC (navy squares). Reprinted with permission from Ref [104] Copyright 2015 American Chemical Society

1.6 Motivation and Goals of this Thesis

In addition to improved cell performance, some practical considerations are necessary for the development of useful anode materials, such as compatibility with large-scale production, compatibility with cathode materials and the sustainability and cost of raw materials. In this thesis, Si-Fe-O anode materials were prepared by reactive ball milling with the hope of combining the advantages of SiO_x and Si-M alloys. Reactive gas ball milling was selected as a very simple and low-cost method to prepare the Si-Fe-O anode materials. The Si-Fe-O alloys were incorporated into alloy/graphite composites to enable cell manufacturers to utilize them as a drop-in replacement for graphite. The goal of these efforts being to enable large-scale production and practical utilization of Si-Fe-O alloy anodes. In addition, these methods can also be extended for making other alloy anode materials. This thesis describes the synthesis and structural characterization of these materials and their evaluation for use as active anode materials in Li-ion cells.

CHAPTER 2 EXPERIMENTAL METHODS

2.1 Material Preparation Methods

2.1.1 Ball Milled Alloy Preparation

Mechanical alloying (MA) is a powder processing method to prepare amorphous alloys, nanostructures, supersaturated solid solutions, metastable crystalline and quasicrystalline phases from mixtures of elemental powders [109]. Elemental powders are milled mechanically in high impact ball mills, resulting intermetallic phases with reduced grain size [110]. MA was developed in 1970s with the purpose to disperse nanosized oxide into nickel-based alloy powders [111,112]. It was also found that amorphous alloys can form in this ball-milling method. Since then, MA has attracted lots of attention for the preparation of supersaturated solid solutions, amorphous alloys, nanostructured composites, quasicrystals, intermetallic, and crystalline phases [113].

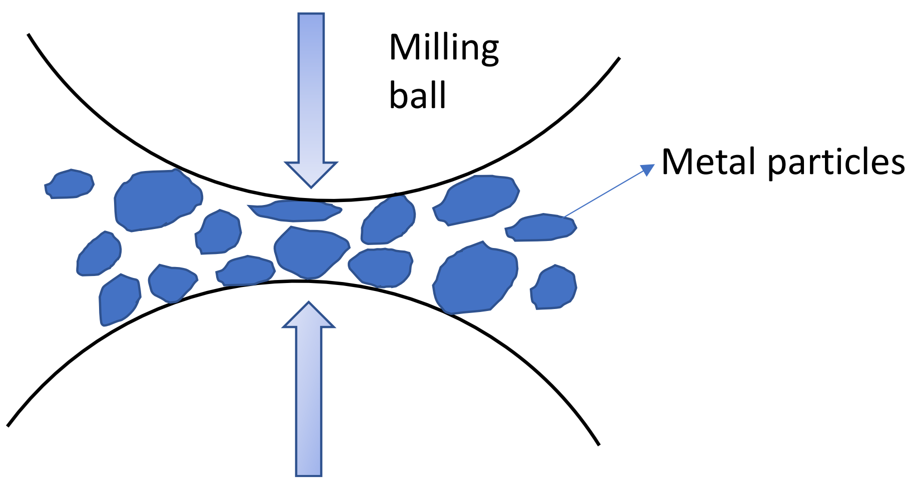

Figure 2.1 Schematic drawing of ball-powder-ball collision.

In the mechanical alloying process, ball-powder-ball collisions are the most frequent events (shown in Figure 2.1). During such collisions, powder particles are trapped between colliding balls and undergo deformation and/or fracture processes. It is commonly agreed that the crystallite size of alloys decreases with milling time. The final grain size is achieved when there is a balance between dislocation accumulation and dynamic recovery or recrystallization [110,114]. The mechanical properties of the processed powders, such as their phase equilibria, and the stress state during milling, determines different behaviors of MA processes [110]. Thermodynamics can be the driving force for phase formation during high energy ball milling if the resulting phase is an equilibrium phase. When the resulting phase is a non-equilibrium, or metastable phase, the driving force may come from accumulated energy stored by the processed powder mixtures during repeated collisions [115]. After repeated deformation from ball-powder-ball collisions, pure elements can form nanocrystalline structures and energy can be stored in grain boundaries and defects, where the atoms that reside in grain boundaries or other defects are in a higher energy state than atoms in the bulk of crystalline grains. In this way, the severe deformation that occurs during milling increases the free energy of the pure metals. In addition, the interfacial energy arising from lattice defects and new grain boundaries also raises the free energy of solid solutions [116]. The gained energy could be the driving force for reactions that occur during mechanical alloying [117]. MA as an affordable, efficient, and flexible powder processing method that has become popular for battery material synthesis [48,49,118–127,51,128–133,53–57,77,117].

In this thesis, silicon (325 mesh, 99%, Aldrich) and iron (325 mesh, 99.9%, Aldrich) powders in several stoichiometric ratios ($Si_{100-x}Fe_x$, x = 5, 10, 15, 20) were ball milled in a SPEX 8000-D mill (SPEX Certiprep, Metuchen, N.J.) using the optimized conditions for high energy ball milling described in Reference [134]: 180g of 1.6mm 440C stainless steel balls, 65mL hardened steel container, 0.5 mL total volume of sample powders, based on the powder bulk density. Total milling time was fixed at 16 hours but with different milling periods in argon atmosphere or in air, in order to control the oxygen content. Milling in an Ar atmosphere was accomplished by sealing the milling vessel in an Ar-filled glovebox prior to milling. Milling in air was accomplished by "sealing" the milling vessel in air with the o-ring seal removed prior to milling. This allowed the free passage of gasses into or out of the milling vessel while retaining the powder charge. Ethanol (99.89%, containing 0.10% H_2O, Commercial Alcohols) was used for sample recovery. Sample vials were half filled with ethanol and milled for five more minutes. The resulting ethanol slurry was then collected in a pan and then dried in a solvent oven at 120°C in air. Some samples were subsequently heated in a tube furnace at 600°C and 800°C for 3 hours under an argon flow.

2.1.2 Mechanofusion

Mechanofusion (MF) is a dry powder processing method, which was developed in Japan in the 1980s [135]. Figure 2.2 schematically illustrates the main components of a mechanofusion machine. It consists of a fixed press-head, a scraper, and a rotating chamber. During operation, the loaded powder is forced outward towards the chamber wall, and when the chamber rotates, powder also rotates along the chamber wall by centrifugal action [90,136]. When particles are passing through the gap between the press-head and the rotating chamber wall, a high shear field is generated. After particles exit the diverging space of the press-head region, they adhere to each other and travel towards the chamber wall. The scraper is used to remove any powder attached to the chamber wall. The sheared powder mixture then moves towards the press-head region again, and repeatedly undergoes the process of compression, frictional shearing, and deagglomeration during machine operation [90]. MF can spheronize particles. As an example, it is used to spheronize natural graphite to prepare negative electrodes [137,138]. This dry powder processing method can also be used to coat soft/small particles onto large particle [136]. When particles pass through the narrow gap between the press-head and the rotating chamber wall, they may strongly collide with each other, generating heat that fuses them together [40]. Such fused particles can then be coated onto the core particles by the rotary motion of the nucleus particles and the strong compressive forces, while the rotary motion of the nucleus particles is generated by friction between the particles [40]. The MF method can also be used to embed small particles into large particles [136], which is its main function for this thesis.

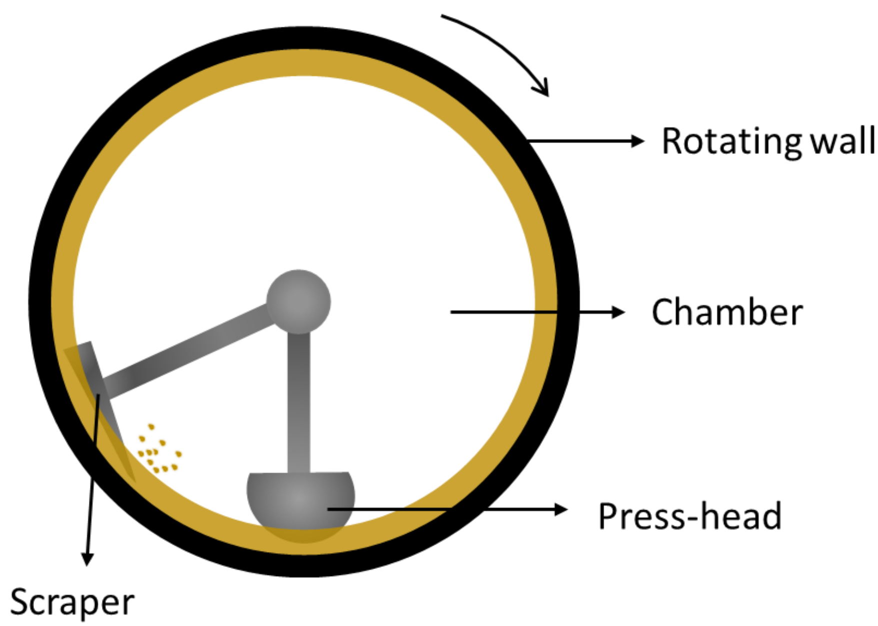

Figure 2.2 Schematic diagram of a Mechanofusion machine.

In this thesis, a 30 g mixture of Si-Fe-O alloy and A3901 graphite (Asbury Carbons) (weight ratio: 1:6) was processed using an AM-15F Mechanofusion System (Hosokawa Micron Corporation, Osaka, Japan). This equipment was modified by replacing the standard stainless-steel chamber, scraper, and press-head with identical hardened steel parts (provided by DPM Solutions, Hebville NS Canada) to reduce wear [90]. Mechanofusion was operated at 2500 rpm with a 0.5 mm scraper/wall gap, and a 1.4 mm press-head/wall gap.

2.2 Characterization Techniques

2.2.1 X-Ray Diffraction

X-ray diffraction (XRD) is one of the most useful methods to study materials' crystal structure. X-rays are electromagnetic radiation of a wavelength ~ 1 Å, which is about the same scale as the distance between lattice planes in a crystal [139]. Both structural and compositional information about crystalline materials can be obtained by XRD. For laboratory XRD measurements, X-rays are typically produced in a vacuum tube by the interaction of high energy electrons with a heavy metal target. Copper K_{α} radiation is a common type of X-radiation used for XRD, which is generated by applying a high potential (~45 kV) between a tungsten filament cathode and a copper anode in a vacuum X-ray tube. Electrons from the heated filament cathode are accelerated towards the anode and strike atoms in the copper anode. The core electrons of copper can be knocked out. Electrons from higher energy levels will drop down to fill the resulting vacancies, resulting in a photon emission with characteristic X-radiation wavelengths. The energy of the characteristic X-radiation equals the energy difference between the initial and final energy states of the electron. K_{α} radiation is emitted when electrons from an 2p orbital drop to fill an empty 1s orbital. Due to the spin-orbit interaction, two energy levels exist within the Cu 2p orbital: the $2p_{1/2}$ and $2p_{3/2}$ orbitals. Therefore, K_{α} radiation consists of $K_{\alpha1}$ and $K_{\alpha2}$ radiations. The $K_{\alpha1}$ transition is generated from the L_3 ($2p_{3/2}$) to the K (1s) orbital and corresponds to a photon with a wavelength of 1.5405 Å. The $K_{\alpha 2}$ transition is from the L_2 ($2p_{1/2}$) to the K (1s) energy level, resulting in the emission of a photon with a wavelength of 1.5443 Å [139]. The relative intensity ratio between $K_{\alpha 1}$ and $K_{\alpha 2}$ radiation is 2:1, because there are four $2p_{3/2}$ orbitals and two $2p_{1/2}$ orbitals, giving rise to a higher $K_{\alpha 1}$ transition probability. Other radiations with lower intensity such as K_{β} radiation can be filtered out with a monochromator. It is difficult to separate $K_{\alpha 1}$ and $K_{\alpha 2}$ with a monochromator because their wavelengths are too similar. However, nanocrystalline or amorphous samples have broad peaks and the presence of $K_{\alpha 2}$ radiation has little effect on their XRD pattern. Peaks arising $K_{\alpha 2}$ radiation in crystalline materials can be subtracted by numerical methods.

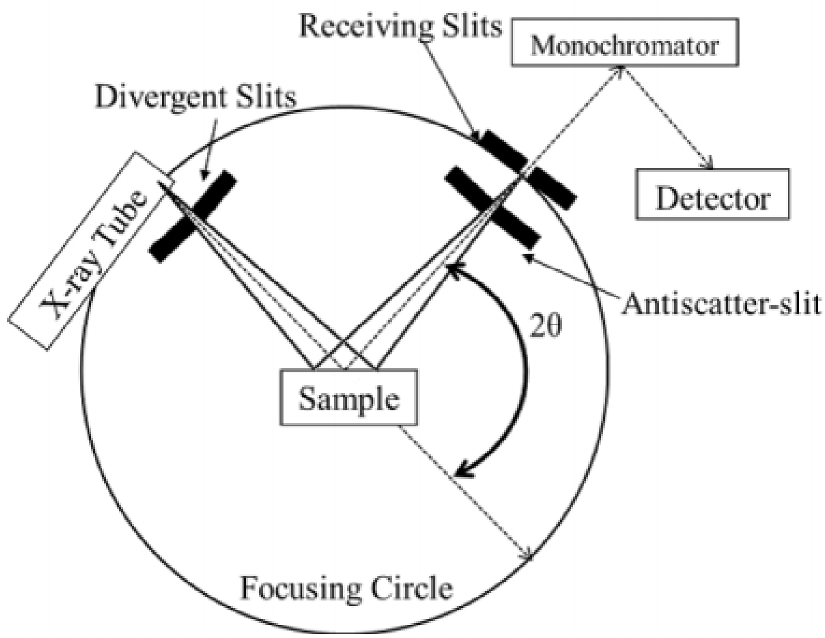

Figure 2.3 Schematic diagram of the Bragg-Brentano diffractometer, shown with divergent slits, antiscatter slits and receiving slits. Reproduced with permission from Reference [140], Copyright 2015 Camardese, J.

Figure 2.3 shows a schematic of a Bragg-Brentano diffractometer. Once X-rays leave the X-ray tube, they pass a divergence slit, which defines the size of the X-ray beam. The X-rays then interact with the powder sample and get scattered from the electrons in the sample [140]. When the scattered X-rays are in phase, constructive interference occurs. The angles at which constructive interference may occur are given by:

$$2d \sin\theta = n\lambda \tag{2.1}$$

This equation is known as Bragg's law, where n is an integer, λ is the wavelength of the incident radiation (1.54 Å for CuKα), and θ is the angle of the incident radiation to the sample. This relationship can be derived from trigonometry, as shown in Figure 2.4.

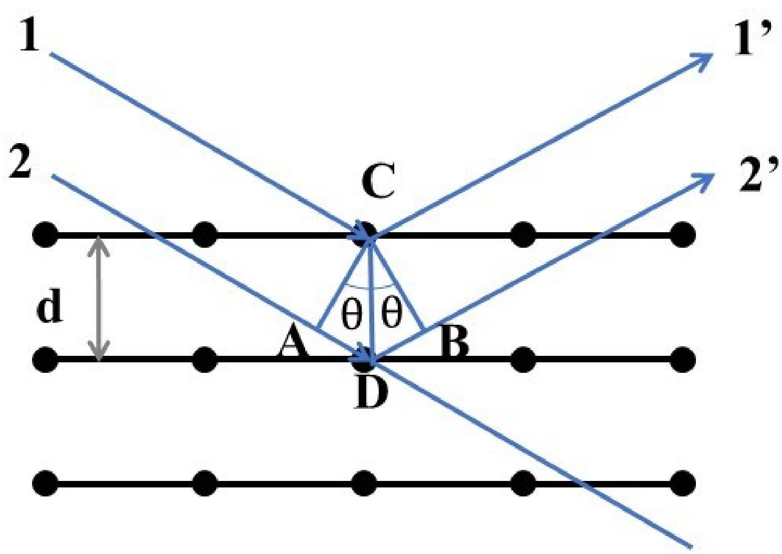

Figure 2.4 Schematic diagram of Bragg diffraction from crystalline planes in a solid.

Beam 1 and 2 are two parallel incident beams and beam 1' and 2' are the corresponding diffracted beams. When the difference in the distance travelled by beam 1 and beam 2 (AD + BD in Figure 2.4) is equal to an integer multiple of its wavelength, the photons will be in phase, and the amplitudes of their waves will add (constructive interference), resulting in radiation with increased intensity. In a Bragg-Brentano diffractometer, the diffracted beam then passes through anti-scatter slits followed by a receiving slit and then a diffracted beam monochromator to filter out any radiation other than Cu-K_α radiation (e.g., Cu-K_β radiation and radiation from sample fluorescence). Finally, the filtered radiation is converted to an electronic signal by a detector. XRD patterns are often plotted as the intensity of the scattered radiation vs. the scattering angle, 2θ. At values of 2θ which give constructive interference, peaks in the scattered X-ray intensity will be observed. The peak intensity is associated with a few factors, which can be represented as:

$$I(2\theta) = P(2\theta)\, L\,(2\theta)\, [F\,(h\,k\,l)]^2 m(h\,k\,l)\, DW(2\,\theta) \tag{2.2}$$

where I is the measured intensity, P is the polarization factor, L is the Lorentz polarization factor, F is the structure factor, m is the multiplicity, and DW is the Debye-Waller factor. The Miller indices ($h\ k\ l$) are used to define the reciprocal of the intercepts of a plane of atoms with the unit cell. For a set of lattice planes with Miller indices of h, k, l, the structure factor is defined as:

$$F(h\,k\,l) = \sum_n f_n e^{2\pi i\,(hx+ky+lz)} \tag{2.3}$$

The structure factor F ($h\ k\ l$) sums scattering from all atoms in the unit cell to form a diffraction peak (n atoms in total). x, y, and z are the positional coordinates of each atom, and f_n is the atomic form factor of the atom. The atomic form factor is the scattering amplitude of X-rays by the atom. Atoms with different atomic number will scatter X-rays differently. Generally, the atomic form factor increases with the atomic number of an atom (more electrons). Atomic form factors have been computed as a function of sin θ/λ and are available in the International Tables for X-Ray Crystallography Volume 3 [139].

The polarization factor represents intensity reduction due to the polarization of a diffracted X-ray in the plane of diffraction, while the Lorentz polarization factor considers the dependence of scattering intensity on scattering angles. Multiplicity considers the scattering of a set of planes having the same interplanar spacings. The multiplicity is the number of such lattice planes with a different Miller index but the d-spacings are the same. For instance, a cubic unit cell has a multiplicity of 48, for the set of $\{h\ k\ l\}$ $(h \neq k \neq l \neq 0)$ planes The Debye-Waller factor $DW(2\theta)$ reflects thermal effect on the electron intensity as a function of incident angle. Atoms are constantly vibrating about their mean lattice position, and vibrational amplitude and frequency will be affected by temperature. Using the above parameters, structural information, such as lattice constants, site occupations, and atom positions, can be obtained by fitting an experimental XRD pattern and calculating an optimized pattern based on trial crystal structures by Rietveld refinement.

In this thesis, XRD patterns were collected with a Rigaku Ultima IV diffractometer equipped with a CuKα radiation X-ray tube, a dual position diffracted graphite monochromator and a scintillation counter detector. A filament current of 40 mA and an accelerating potential of 45 kV were used to generate X-rays. Powder samples were loaded into a stainless-steel sample well with dimensions of 25 mm × 20 mm × 3 mm on a stainless-steel plate and pressed flat with a glass slide to ensure a flat upper surface that was coplanar with the top of the sample holder before measurement. Measurements were taken in 0.05° steps with a count time of 3 seconds per step, in the range of 10° to 80° 2θ. The collected XRD patterns were compared with the ICDD PDF2 database for phase identification [141].

2.2.2 Scanning Electron Microscopy

Scanning electron microscopy (SEM) is a useful technique for investigating the surface morphology of materials and conducting elemental analysis, if equipped with an energy dispersive X-ray spectrometer. SEM images are produced from interactions between the incident electron beam and the specimen. Two major interactions can occur when a high energy electron beam interacts with the specimen: elastic scattering and inelastic scattering. Backscattered electrons (BSE) arise when incident electrons are elastically deflected (i.e. negligible energy loss) from the specimen surface. BSEs can have an energy range from 50 eV to nearly the incident beam energy [142]. More electrons can be back scattered from elements with higher atomic number, which are accordingly brighter in images. Therefore, SEM images produced from BSEs can show atomic contrast, allowing chemical composition information to be obtained [142,143]. When inelastic scattering occurs, the incident electrons lose energy by transferring some of their initial energy to the specimen. This can result in an ejection of an electron from the specimen, generating secondary electrons (SE) with energies that are normally less than 50 eV [142,143]. Secondary electrons are used principally for topographic contrast in SEM images, such as surface texture and roughness imaging [142,143]. SEs are mostly generated from regions near the surface of a specimen and BSEs are generated from regions that are generally deeper within the specimen [142].

Besides the SEs and BSEs signals that are used to generate SEM images, other signals are also produced when the incident beam strikes a sample, including the emission of characteristic X-rays, Auger electrons, and cathodoluminescence (as shown in Figure 2.5. For example, characteristic X-rays are generated during the interaction between the primary electron beam and the specimen, if a vacancy due to the ejection of a SE is filled by an outer shell electron [142,144]. Since each element has unique atomic structure, the resulting X-rays generated are characteristic of each element. This characteristic X-ray emission spectrum enables both quantitative and quantitative elemental analysis by the energy dispersive spectroscopy (EDS) technique [142,144]. In this thesis, SEM images were obtained using a TESCAN MIRA 3 field-emission electron microscope. This instrument is equipped with a secondary electron detector, a backscattered electron detector, and an energy dispersive spectroscopy (EDS) system.

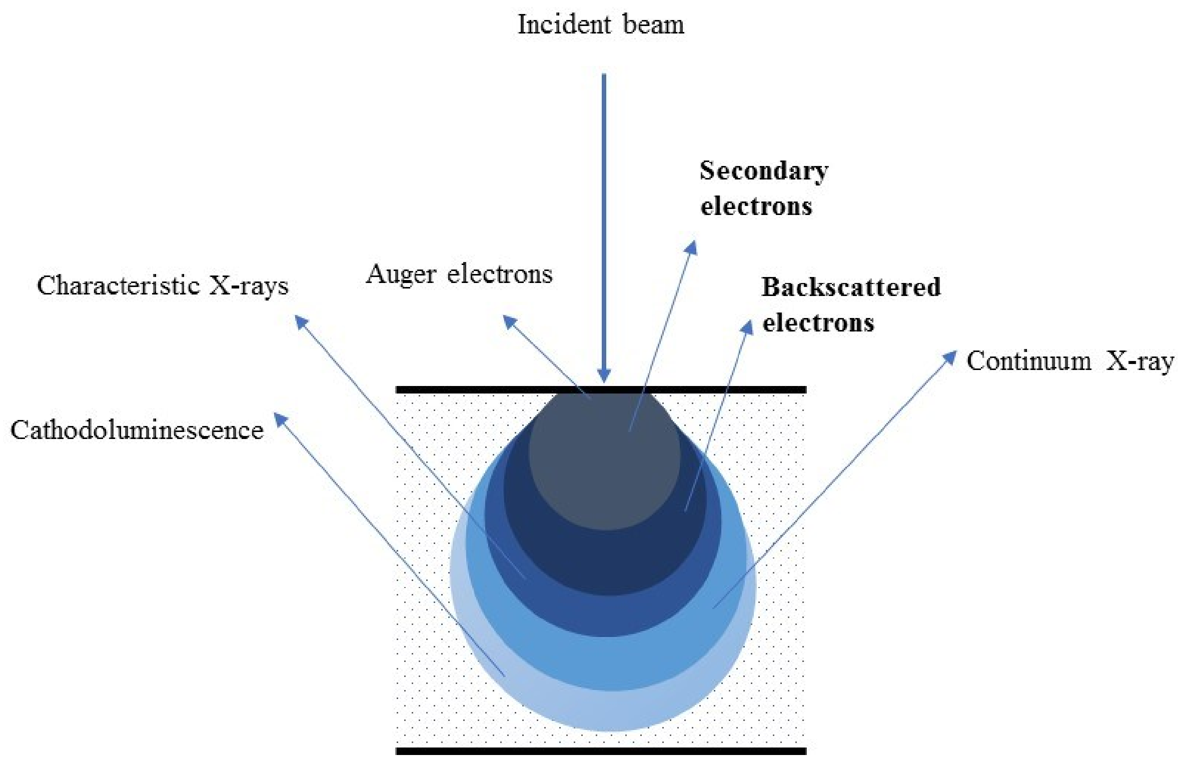

Figure 2.5 Schematic diagram of several signals generated by the electron-specimen interaction in the SEM and the regions from which the signals can be detected.

2.2.3 Transmission Electrochemical Microscopy

In contrast to SEM and EDS, the transmission electron microscope (TEM) detects transmitted electrons and radiation. TEM allows the acquisition of diffraction patterns and magnified images from the same sample area [139]. TEM diffraction patterns can provide unit cell, space group and grain size information, while TEM images offer morphological information. Grain size and orientation can also be visualized in images via lattice fringe patterns. Thin specimens and high accelerating potentials (200 – 300 kV) are used in TEM. TEM samples are normally thinner than 200 nm because electrons interact strongly with matter and are completely absorbed by thick particles [145]. High spatial resolution images are therefore achieved from transmission signals of thin samples, allowing better observations of atomic configuration within the nanostructure [139].

Contrast in the TEM image is produced by the scattering of electrons due to their interaction with atoms in the sample. Bright and dark areas refer to the density of electrons striking the detector. Brighter areas correspond to where more electrons are transmitted, while darker areas correspond to where electrons are scattered. Image contrast can be explained by several mechanisms: mass contrast, because heavier atoms deflect more electrons; thickness contrast, due to differences in sample thickness; diffraction contrast, resulting from the scattering of the electron beams by structural defects; and phase contrast [145]. The TEM images in this thesis were taken from a Philips CM30 TEM. TEM samples were prepared by suspending sample powders in methanol, sonicating for about 5 minutes then putting a drop onto a lacey carbon coated TEM grid.

2.2.4 Mössbauer Spectroscopy

The Mössbauer effect was first discovered by Rudolf Mössbauer in 1958. The Mössbauer spectroscopy employs recoil-free absorption and emission of γ-rays in solids to study the energy levels of nuclei in atoms. ^{57}Fe can be used in Mössbauer spectroscopy to study the structure of Fe-containing materials, because it has a natural abundance of ~2% in bulk Fe. In addition, Mössbauer spectroscopy is a useful tool for probing nanostructured material, which can provide complementary information to XRD techniques.

^{57}Co is used as the radioactive source in ^{57}Fe Mössbauer spectroscopy. A range of γ-rays matching the energy range of the nuclear transitions of the sample are generated from a ^{57}Co source by moving the source at a controlled velocity and utilizing the Doppler effect. A typical Mössbauer spectrum is plotted as the transmission counts vs. the relative source velocity (in mm/s). When the Doppler-shifted γ-ray energy matches the energy of a nuclear transition in the sample, the γ-rays are resonantly absorbed, resulting in an adsorption peak in the Mössbauer spectrum.

The isomer shift, quadrupole splitting, and Zeeman effect are three types of hyperfine interactions in Mössbauer spectroscopy. These interactions can be used to probe different Fe environments in the sample. The isomer shift (δ) is a measure of differences in s-electron densities of the source and sample. If the source and sample are in identical chemical environments, the centre shift will be zero. Any difference in the s-electron environment between the source and the sample will result in a non-zero resonant peak shift. The isomer shift is usually measured relative to a known standard, α-Fe was used (isomer shift defined as 0 mm/s) in this thesis.

Nuclei with a spin quantum number greater than 1/2 have a non-spherical charge distribution. The non-spherical charge distribution produces an asymmetrical electric field and a quadrupole moment. The quadrupole moment can interact with the electric field gradient and splits the nuclear energy level. The splitting is called quadrupole splitting, which produces two lines of equal intensity in the Mössbauer spectrum. The centre of the quadrupole splitting is the centre shift.

A nucleus with a spin quantum number $I > 0$ will interact with the magnetic field by its magnetic dipole moment: this is known as the Nuclear Zeeman effect. The magnetic dipole interaction can result from either an internal magnetic field (as in the case of metallic ^{57}Fe) and/or, an applied magnetic field. This interaction splits the degeneracy of the nuclear state into $2I + 1$ states. In the case of ^{57}Fe, the ground state spin quantum number is $I = 1/2$, this state is then split into two non-degenerate states: mI = ±1/2. The excited state with a spin quantum number of I = 3/2 is split into four non-degenerate states: mI = ±3/2, ±1/2. This gives rise to six allowed transitions according to the selection rules (ΔmI = 0 or ±1) and accordingly, a six-line spectrum.

In this thesis, room temperature ^{57}Fe Mössbauer spectroscopy was conducted using a SEE Co. spectrometer operating in the constant acceleration mode with a ^{57}Co(Rh) source. The velocity scale was calibrated according to room temperature α-Fe foil. Alloy sample powders were loaded in a 4 cm^2 PET sample holder.

2.2.5 Density Measurements (Gas Pycnometer)

Gas pycnometry is a non-destructive technique used to determine sample volume by gas (an inert gas, such as nitrogen, argon, or helium) displacement, allowing measurements of true sample densities. In this thesis, densities of samples were measured with a helium pycnometer (AccuPyc II 1340, Micrometritics) under isothermal conditions. Figure 2.6 shows a schematic diagram of the pycnometer. The major components are two chambers: a measurement chamber of a known volume V_{cell} with a lid for sample loading and a reference chamber of volume V_{ref}. The two chambers are connected via a valve.

During the measurement, a dry solid sample of known mass is placed in a measurement chamber and sealed in air with the valve between two chambers closed. Then the following operations are performed automatically by the instrument. The measurement chamber is purged with He 10 times to remove possible moisture. The measurement chamber is then filled with He gas up to pressure P_1. Then the valve connecting the two chambers is opened, allowing He gas to flow from the measurement chamber to the reference chamber. When equilibrium is reached again, the pressure is recorded as P_2. The volume of a sample V_{samp} is calculated by applying ideal gas law:

$$V_{samp} = V_{cell} - \frac{P_2}{P_1 - P_2} V_{ref}$$

Where V_{cell} and V_{ref} were determined by calibration procedures as 2.8844 cm^3 and 9.1458 cm^3. Pressures P_1 and P_2 are measured by the pressure gauge. Five measurements were done on each sample and the average density of the sample is then calculated with the acquired V_{samp} and known sample mass.

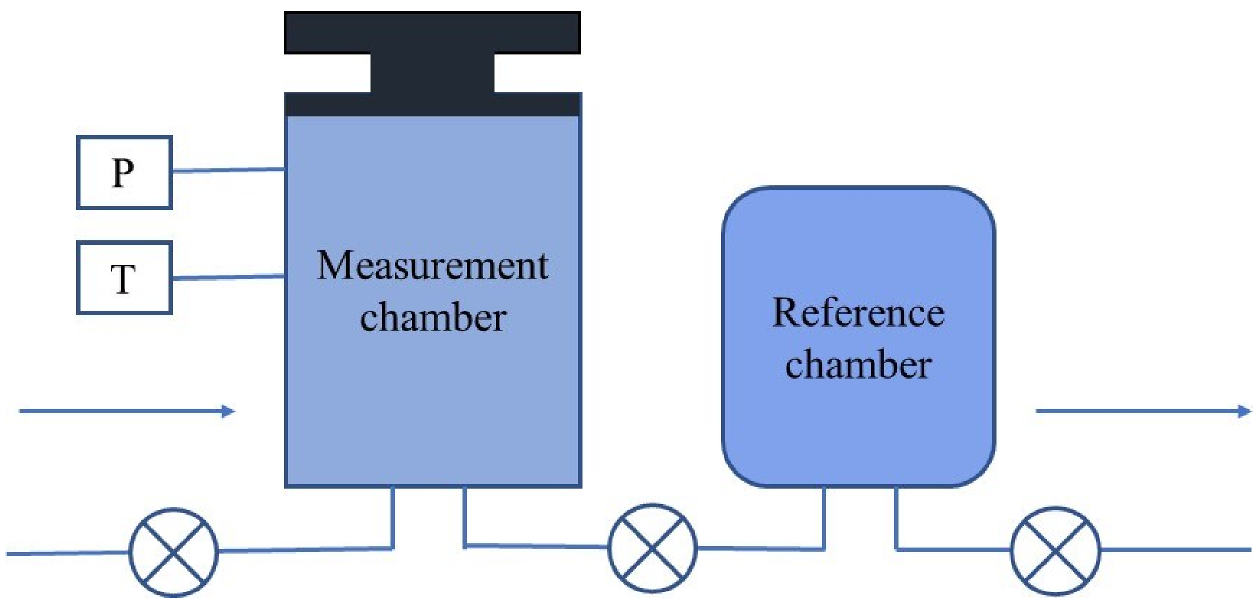

Figure 2.6 Schematic diagram of a gas pycnometer.

2.2.6 Oxygen Content Determination (LECO test)

Oxygen contents of alloy samples were determined by LECO (Laboratory Equipment Corporation) analysis by NSL Analytical of Cleveland, OH. The LECO analysis measures the oxygen content in the form of CO and CO_2 using a non-dispersive infrared cell (NDIR) [146]. A pre-weighed sample (~0.05 g) is placed in a graphite crucible and heated in a furnace to 2800 °C. At this high temperature, oxygen and nitrogen are released from the sample. The released oxygen reacts with the graphite crucible to form CO and CO_2. Gases are carried out by an inert gas (such as helium) with controlled flow rate. CO and CO_2 in the liberated analyte gases are detected using NDIR cells. The gases then flow through a heated reagent, where the CO is oxidized to form CO_2. Another set of NDIR cells are used to measure the amount of CO_2. In NDIR cells, when gases pass through the IR absorption cells, analyte gas molecules will absorb infrared energy at specific wavelengths of the incident IR beam. Multiple CO and CO_2 NDIR cells are utilized to provide more accurate oxygen results for a wider range of sample types and concentrations. The concentration of an unknown sample is then determined using calibration standards and reference measurements of pure carrier gas [147].

2.2.7 Cross Section Polisher

A Cross Section Polisher (CP) is an instrument using a high-energy argon ion beam to remove materials from a sample surface to prepare a cross section for subsequent observation, such as SEM. Figure 2.7 shows a schematic diagram of a cross section polisher (CP). The major components of the CP are the ion gun, shielding plate and specimen. During operation, an argon ion beam is emitted from ion gun, perpendicular to the sample. The sample is partially covered with a shielding plate and the ion beam cuts the sample along the edge of the shielding plate. The shielding plate is made of a material which has a slow milling rate, and the edge of the shielding plate is placed at the desired cross section position of the sample. The sample region protruding from the edge of the shielding plate gets milled and the cross section at the edge of the shielding plate is exposed after the milling process. For samples that containing both hard and soft components, the processing rate of the Ar^+ ion beam will be different for materials of different properties. This may cause a streaked roughness. Stage swing can efficiently reduce this roughness and this method is utilized when preparing cross section samples in this thesis. Working potential (0-8 kV), argon gas flow rate, and milling time are three important parameters during the operation of the CP. The potential can affect the cut width and removal rate. A higher potential gives a wider cut and a faster removal rate. The argon flow can affect the argon ion beam current. Both insufficient and excess gas flow can make the cutting beam unstable. For a given potential, there is a stable argon gas region (70-80% of the maximum). Extended milling time can increase the depth of the cut for the same sample. However, the long milling time may cause heat damage for heat-sensitive samples. Extra care, such as intermittent milling and sample thinning should be taken for such materials. Ablated sample redeposition occurs when some of the atoms removed by the ion beam reattach on the surface. This redeposition mostly builds up on already sectioned particles on their side nearest to the part of the sample currently being ablated. Redeposition results in ablated materials covering over the bulk material that is intended to be exposed for observation by SEM and can result in making cross-section images difficult/impossible to interpret or can lead to mistakes in their interpretation. It can be minimized by using smaller sample protrusions (less material to be removed) and using a fine milling (low current) mode to clean the cross-sectioned surface. In this thesis, a JEOL IB-19530CP Cross Section Polisher was used to prepare smooth cross-sections of specimens. Samples were cross-sectioned at 6 kV with an argon gas flow of 5.5 (a unitless machine setting) for 50 min then a fine mode (4 kV) for 5 min.

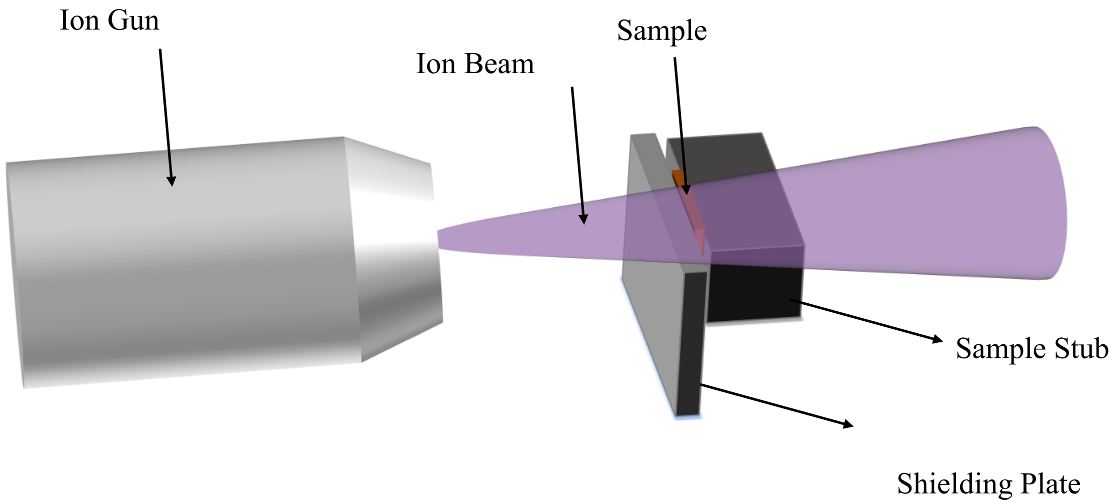

Figure 2.7 Schematic diagram of a cross-section polisher

2.2.8 Electrochemical Methods

2.2.8.1 Cell Construction

Coin cells were used to evaluate the electrochemistry Si-Fe-O alloys synthesized in this thesis. To prepare electrodes incorporating the Si-Fe-O alloys developed in this thesis, powders of Si-Fe-O alloys were mixed with carbon black (Super C65, Imerys Graphite and Carbon) and a 10 wt.% aqueous solution of lithium polyacrylate (LiPAA) at a volumetric ratio of 70/5/25 in distilled water using a planetary ball mill (Retsch PM 200) with two 11 mm WC balls at 100 rpm for 1 hour. A thin layer of slurry was coated on Cu foil (Furukawa Electric, Japan) using a 0.1 mm coating bar. The coating was then dried in air at 120°C for 1 hour. The alloy electrodes were incorporated into 2325 type coin cells with Li metal as the counter/reference electrode and 1M $LiPF_6$ (BASF) in a solution of FEC: EC: DEC (1:3:6 by volume, BASF) electrolyte. The electrodes were separated by two layers of Celgard 2300 separators.

Figure 2.8 shows a general schematic of a 2325-type lithium coin cell made in this thesis. Cells were made in an argon atmosphere glovebox. First the electrodes and separator were wet with excess electrolyte in a stainless steel can. Spacers were added to apply an appropriate pressure on the electrodes, to maintain good electrical contact. The bottom and top casings were separated by a plastic gasket, to prevent electrical contact. Cells were crimped twice to ensure a good seal.

Half-cells are easy to make and easy to understand as a first evaluation step. All materials prepared in this thesis were tested in half-cells. Lithium foil was used as the counter electrode so that the amount of lithium is not limited. Assuming impedance of the counter electrode is small, changes in the measured potential in a half-cell may be attributed to changes from the working electrode. The capacity of a single electrode is therefore measured. Combined with excess electrolyte, the improved or worsened performance of tested half cells can be directly related to the alloy material. However, it is noted that when using half cells, a good cycling can still be obtained even if a material has poor coulombic efficiency (CE). In a full cell, CE is defined as the ratio of the cell discharge capacity and its previous charge capacity. The CE of a negative electrode material evaluated in a in a half cell is the discharge capacity over the charge capacity of the previous half-cycle. Variations in CE values can be caused by the property of active material, electrode compositions, cycling protocols (temperature, current rate, cutoff voltage), electrolyte formulations, and the precision of charger. Higher coulombic efficiency leads to better cycling performance, especially in a full cell, as the amount of available Li ions and electrolyte is limited. However, in half cells Li metal is used as the counter electrode and a huge excess of electrolyte is present, resulting in a practically unlimited supply of Li and electrolyte. Therefore, good cycling performance in a half cell is not necessarily associated with good CE performance.

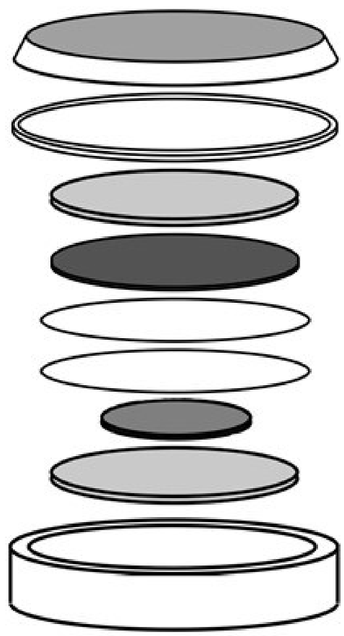

Figure 2.8 Schematic diagram of 2325-type coin cell assembly.

2.2.8.2 Electrochemical Tests

Electrochemical techniques were used to test the performance of electrode materials. Electrochemical tests were performed using a Neware Test System. The cycling protocol is listed in Table 2.1. Coin cells were cycled at 30°C, between 5 mV and 0.9 V at a rate of C/20 and signature discharged (lower currents in steps with a relaxation time between each current change, step 1-5 in Table 2.1) to C/40 for the first cycle; and at a C/10 and signature discharged to C/20 (step 8-12 in Table 2.1) for following cycles. Cells were charged and discharged with a constant current until the upper cut-off potential (0.9 V) or the lower cut-off potential limit was reached. 'C-rate' is used to describe the constant current used during cycling. It is defined as the theoretical capacity of a cell (in mAh) over the desired charge/discharge (in h). For instance, C/10 means the charge/discharge current required for a cell to be fully charged or discharged to reach its theoretical capacity in 10 hours. In this thesis, a signature discharge, which simulates the cycling conditions of commercial lithium-ion cells, were performed on all candidate anode materials to mimic the constant current, constant potential charging protocol that is typically used in full cells [12].

Electrochemical measurements can provide important information, such as the working potential window, capacity, energy density, rate capability and cycle life. Phase changes and diffusion behavior can also be interpreted from appropriate electrochemical measurements. Those properties are essential parameters when evaluating the commercial potential of electrode materials. Potential curves are one of the most important electrochemical measurements. The measured potential is plotted versus the gravimetric capacity. The potential curve shows changes in the chemical potential as the discharge/charge proceeds. According to the Gibbs phase rule, the degrees of freedom in a closed system at equilibrium is defined as $f = C - P + N$, where C is the number of independent components, P is the number of phases existing in the system, and N is the number of any additional system variables [148]. For the Li-Si binary system at constant temperature and pressure, plateaus occur in the potential curves when there is a two-phase region. This is because $C = 2$, $P = 2$, and $N = 0$ corresponds to zero degrees of freedom. In such a region, the potential does not change with the Li concentration. In contrast, a sloping region in the potential curve indicates the existence of a single-phase region. In this case, only one phase exists. Therefore the number of degrees of freedom is one and thus the potential can change with Li concentration [149].

Table 2.1 Cycling protocol used in electrochemical tests

STEP	OPERATION
1	Discharge C/20 to 5 mV
2	Rest 10 minutes
3	Discharge C/30 to 5 mV
4	Rest 10 minutes
5	Discharge C/40 to 5 mV
6	Charge C/20 to 0.9 V
7	Rest 15 min
8	Discharge C/10 to 5 mV
9	Rest 10 minutes
10	Discharge C/15 to 5 mV
11	Rest 10 minutes
12	Discharge C/20 to 5 mV
13	Charge C/10 to 0.9 V
14	Repeat step 7-13 for rest cycles

Differential capacity curves (dQ/dV vs. V, where Q = capacity and V = cell potential) allow small changes in potential curves to be observed more easily. For example, plateaus in a potential profile (presence of two-phase regions) correspond to sharp peaks in a differential capacity curve, while sloping regions in a potential curve (single phase region) result in broad peaks in the differential capacity. These characteristics are very useful. For example, the formation of two-phase regions during the cycling of alloys is undesirable, as two-phase regions cause inhomogeneous volume expansion and high internal stresses, which can result in rapid capacity fade. During the alloying process between Si and Li, a sharp peak at 0.43 V during delithiation will be observed if $Li_{15}Si_4$ is formed during cycling. However, the differential capacity plot of amorphous Si without formation of $Li_{15}Si_4$ during cycling shows two broad peaks during delithiation [150]. In the present study, suppression of $Li_{15}Si_4$ formation is expected for the as-prepared Si-Fe-O alloy, where dQ/dV plots could be applied to verify this expectation.

Additionally, cycling performance plots, which show the capacity versus cycle number, are very useful as well. Information including charge/discharge capacity at each cycle, irreversible capacity, coulombic efficiency (CE), and cycling stability can be directly obtained. After cycling tests, cells were dissembled in an Argon-filled glovebox, alloy electrodes were rinsed with DMC thoroughly to remove remaining electrolyte. Ion beam polished cross sections were obtained with the cross section polisher. Cross-sectional SEM images was then taken as described in section 2.2.2. By observing electrodes after cycling, information such as alloy degradation and structural changes can be obtained.

This chapter has introduced experimental techniques that are utilized in this present study. The following chapters will discuss results that are obtained from those studies as well as some supplemental experiment details.

CHAPTER 3 $Si_{85}Fe_{15}O_x$ ALLOYS

3.1 Introduction

It was introduced in Chapter 1 that cell fade associated with Si volume changes can be reduced if nanostructured or amorphous Si-based alloys are used, which have reduced volume expansion and in which the a-Li_xSi - $Li_{15}Si_4$ phase transition is suppressed. Iron is an excellent candidate as an inactive component for Si alloys due to its high earth abundance, low cost, and good conductivity. For these reasons, the Fe-Si system has been intensively studied and prepared by various methods (such as magnetron sputtering, ball milling, reduction, and spark plasma) in recent years [45,46,152–159,51–57,126].

However, Si-based alloys still suffer from side reactions with electrolyte during cycling, although the rate of these reactions is greatly reduced [160]. SiO_x has also been extensively studied as an anode material because of reduced volume expansion, less side reactions with electrolyte, and high capacity retention during cycling [59]. However, the first coulombic efficiency of SiO_x is low because of the irreversible formation of lithium silicates [60]. In addition, the preparation method of SiO_x can be expensive. However, it was recently reported that SiO_x can be made by ball milling Si in air [66]. SiO_x has an additional advantage in that it can maintain its amorphous microstructure, even when heated to high temperatures (e.g. 800 °C). Indeed, such thermal treatment has been reported to improve its capacity retention [161]. Also, this high temperature stability makes it compatible with carbon coating by chemical vapor deposition, which has been shown to improve its capacity retention further.

Furthermore, it has been shown that Si-alloy particles made by ball milling can be embedded within graphite particles by mechanofusion processing [90]. Ball milled particles are ideal for this purpose, since they typically have primary particle sizes of ~0.5

μm, which can be embedded into ~10 μm graphite particles without changing their morphology. However, electrolyte can still permeate into such particles and react with the embedded alloys, causing cell fade. Applying a carbon coating to the composite particles by CVD can eliminate electrolyte infiltration. The main goal of this thesis is to create alloy particles that can be embedded within graphite particles by mechanofusion to create composite particles that can be subsequently carbon-coated to eliminate electrolyte/alloy interactions, while maintaining good cycling properties and low irreversible capacity. In order to achieve this, the Si-alloy should have the following properties:

- ~0.5 μm primary particle size
- low irreversible capacity
- retains nanostructured Si phase when heated to CVD processing temperatures (~800 °C)

This chapter will show that such alloy particles can be obtained by utilizing $Si_{85}Fe_{15}O_x$ alloys, which combine the low irreversible capacity of Si-M alloys with the high thermal stability of SiO_x. By making the $Si_{85}Fe_{15}O_x$ alloys by reactive ball milling in air, the target 0.5 μm primary particle size can be achieved, while additionally making this alloy economical to produce. This synthesis would be very attractive from a commercial point of view since SiO_x-containing materials with enhanced cell performance can be easily processed. The milling process introduces air as a convenient source of oxygen by simply removing the O-ring of a milling vial. Figure 3.1 shows the parts of a milling vial. During air milling period, air can flow in the vial though a hole in the cap when the O-ring is not utilized. Different milling procedures were used to study the effect of air exposure time, which are shown in Figure 3.2.

Figure 3.1 The different parts of a SPEX milling vial.

Figure 3.2 Scheme of ball milling procedures for different $Si_{85}Fe_{15}O_x$ alloys.

The resulting ball milled materials were studied as anode materials for lithium-ion cells. The microstructure and the electrochemical performance of the prepared $Si_{85}Fe_{15}O_x$ alloys are discussed in detail. The introduced oxygen content was quantitatively followed during milling, allowing the understanding of its effect on cell performance. It was also hoped that $Si_{85}Fe_{15}O_x$ alloys could show good thermal stability to enable high-temperature thermal processing. Therefore, air milled $Si_{85}Fe_{15}O_x$ alloys were subsequently heated in a tube furnace at 600°C and 800°C for 3 hours under an argon flow and their microstructure and electrochemistry were investigated accordingly.

3.2 Material Characterization

3.2.1 Material Compositions

Figure 3.3 shows the oxygen content of the $Si_{85}Fe_{15}O_x$ alloys as a function of time milled in air. At zero milling time, the oxygen content is about 7 at.%. A previous LECO test identified that the Si precursor contains 8 at.% of oxygen impurity [49]. Therefore, alloys prepared with this Si precursor may contain at least 8 atomic % oxygen with respect to their Si content, which is consistent with the oxygen content reported here for the 0h $Si_{85}Fe_{15}O_x$ alloy. From 0 h to 6 h air milling time, the oxygen contents linearly increase with the time milled in air until an oxygen composition of about 20 at.% is reached. After 6 h, there is no significant change (> 2 at.%) in the oxygen content even when the air milling time was increased to 10 h. The same trend has been observed for reactive ball milling of Si in air to make SiO_x in which the maximum oxygen content that could be achieved by reactive ball milling was $SiO_{0.37}$. As the alloy particles become fractured, new surfaces react with the air, until the particles become too small to fracture, at which point no further reaction occurs [161]. Therefore, the samples range in composition from $[Si_{0.85}Fe_{0.15}]_{93}O_7$ (0h air milled sample) to $[Si_{0.85}Fe_{0.15}]_{80}O_{20}$ (6-10h air milled samples). This corresponds to a maximum O:Si ratio of 0.29. However, if it is assumed that the iron has reacted with the Si to make $FeSi_2$, as suggested by XRD results shown in section 3.2.2, then the O:(unreacted Si) ratio is 0.45, which is somewhat higher than the maximum O:Si ratio of 0.37 achieved for reactive ball milled SiO_x [161]. The iron content was 14.8 ± 0.6 at.% (metals basis) for all samples according to EDS elemental analysis, and had no dependence on the air milling time. This indicates that the Fe contamination from milling was insignificant compared to the overall Fe content (i.e. < 2 % of the total Fe composition).

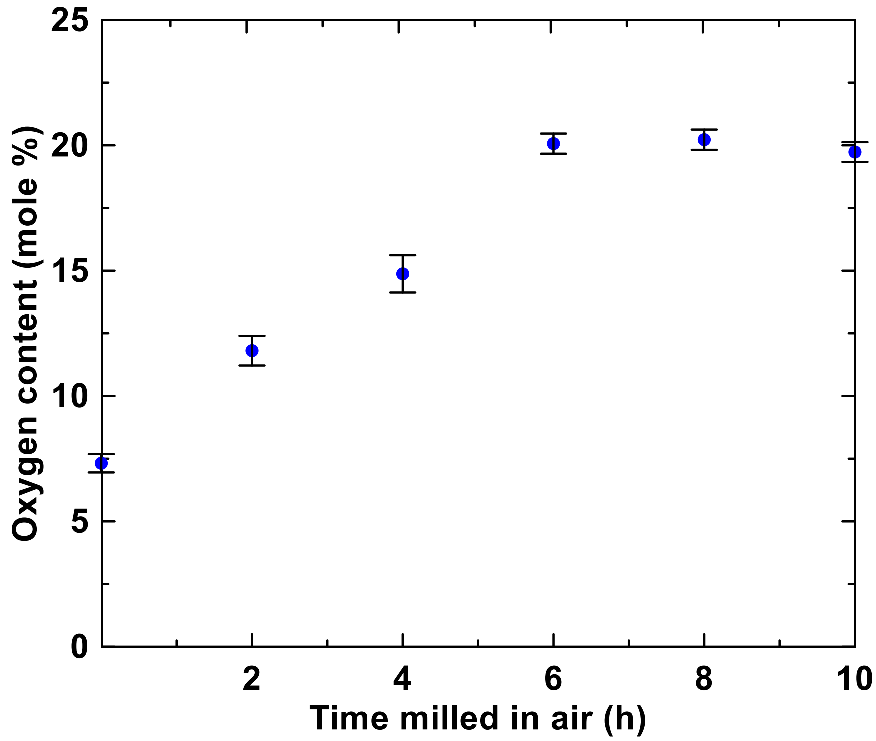

Figure 3.3 Oxygen content of $Si_{85}Fe_{15}O_x$ alloys versus air milling time. The accuracy of the LECO method is ±2% of the measured value for oxygen contents in the range of 10-25% and ±5 % of the measured value for oxygen contents in the range of 3-10% (provided by NSL Analytical).

3.2.2 Microstructure studies

X-ray diffraction was used to study the structure of each material. Figure 3.4 shows powder XRD patterns of ball milled $Si_{85}Fe_{15}O_x$ alloys at different air milling times. Peaks of known phases are indicated. The as-milled $Si_{85}Fe_{15}O_x$ alloys are composed of α-$FeSi_2$ (PDF: 00-089-2024), β-$FeSi_2$ (PDF: 00-071-0642) and an amorphous phase consistent with broad intensities consistent with Si or SiO_x. Here α-$FeSi_2$ is the high temperature (>937 °C) stable phase of $FeSi_2$ and β-$FeSi_2$ is the low-temperature stable phase (<937 °C), which can be found on Figure 3.5. The high temperature α-$FeSi_2$ phase has a tetragonal crystal structure, with Fe and Si atoms arranged in planes of square lattices in a Fe-Si-Si layer stacking sequence, and each Fe coordinated to eight Si atoms in a cube [55]. The crystal structure of the β-FeSi2 phase is orthorhombic. The β-FeSi2 phase has a more disordered structure, with many partially occupied lattice positions. The coordination number of Fe atoms is still eight, but the Si and Fe atoms are arranged in a highly distorted cube. The preferential formation of metastable α-$FeSi_2$ during ball milling Fe and Si has been reported previously [51,162]. Samples prepared with different air milling times have very similar XRD patterns, despite having significant differences (> 5 at.% for 0-6 h samples) in oxygen content, as discussed above.

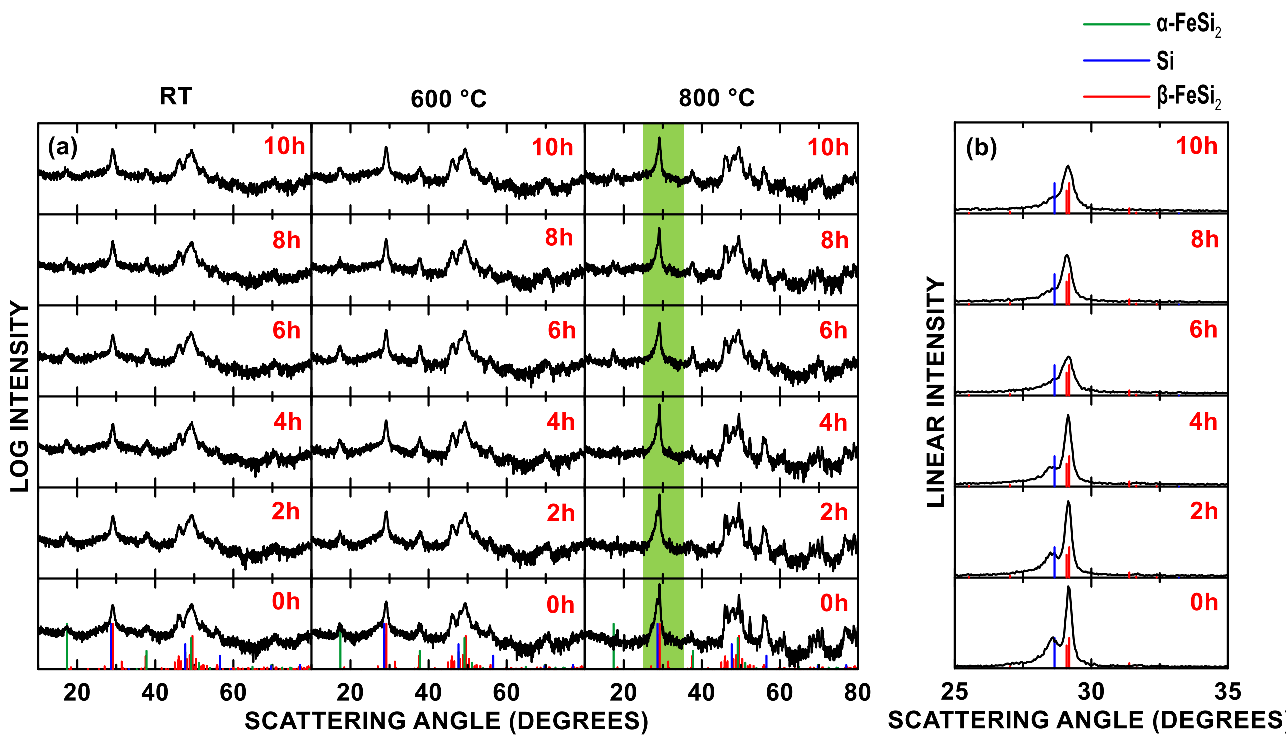

Figure 3.4 (a) XRD patterns of $Si_{85}Fe_{15}O_x$ alloys as milled and after thermal annealing at 600°C and 800°C. Known phase peak positions and intensities are indicated by vertical lines. (b) Expanded XRD patterns of highlighted regions in (a).

The diffraction patterns of ball milled $Si_{85}Fe_{15}O_x$ alloys before and after annealing at 600°C and 800°C are shown in Figure 3.4. The XRD patterns of 600°C annealed $Si_{85}Fe_{15}O_x$ alloys are almost identical to the unheated $Si_{85}Fe_{15}O_x$ alloys, indicating that no phase transitions or crystal growth detectible by XRD occurs at 600°C. At 800°C, the heat treatment causes crystallization of the β-$FeSi_2$ phase. The β-$FeSi_2$ phase exhibits increased intensity and becomes the dominant phase in the XRD patterns for all the 800°C annealed alloys, while the α-$FeSi_2$ peaks almost disappear. For alloys prepared with shorter air milling times (0 h, 2 h and 4h), a small shoulder appears at 28° (Figure 3.4 (b)), on the left of the main β-$FeSi_2$ peak ($2\theta = 29.19°$), corresponding to crystallized Si (111). However, the 28° and 30° peaks are not resolved for samples made at longer air milling hours (6 h, 8 h and 10 h air milled samples), which may indicate that the Si in those samples are still amorphous/nanocrystalline. This excellent thermal stability is highly desired for post-treatment methods such as carbon coating, where pyrolysis and CVD normally requires high temperatures.

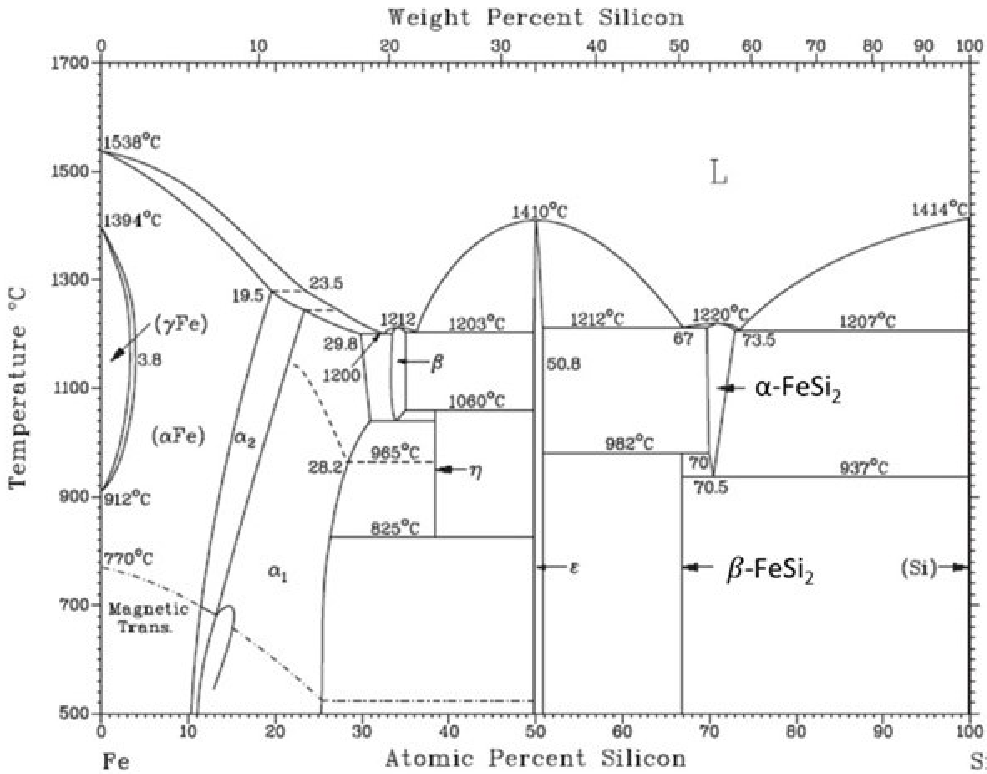

Figure 3.5 Fe-Si binary phase diagram, Reproduced with permission from Reference [163]. Copyright 1993 ASM International.

Figure 3.6 shows SEM images of as-milled $Si_{85}Fe_{15}O_x$ alloys. It was found that $Si_{85}Fe_{15}O_x$ alloys made with different air milling times have very similar morphologies. The samples are all composed of submicron to micron-sized particles as significant size reduction (> 10 % change in observed mean particle size) occurred during the mechanical milling process. Increasing air milling time does not significantly change the morphology of the $Si_{85}Fe_{15}O_x$ alloy particles as could be detected by observation of the SEM images.

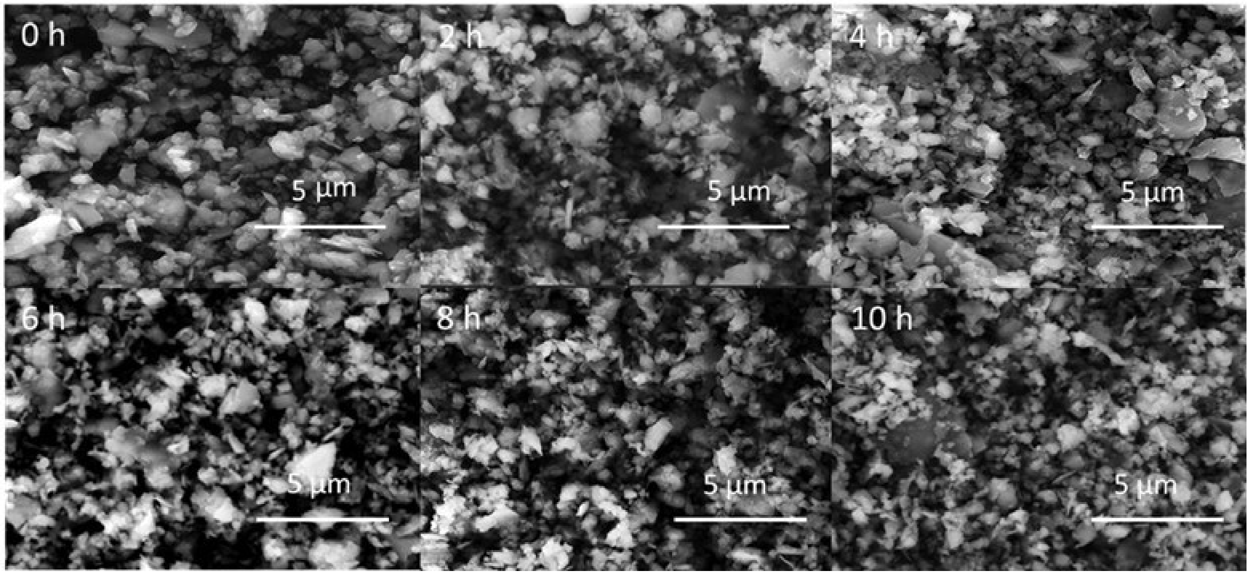

Figure 3.6 SEM images of $Si_{85}Fe_{15}O_x$ alloys with different air milling times

TEM images of 0 h and 8 h air milled $Si_{85}Fe_{15}O_x$ alloys are shown in Figure 3.7(a) and Figure 3.7(b). The images show dark regions that are about 10-20 nm in size surrounded by a lighter matrix. Dark areas correspond to those that are electron-rich, while light regions correspond to those that are electron poor. In this case, this suggests that the dark regions are those that include Fe and the light regions do not include Fe. Combining with XRD results suggests that the dark regions are $FeSi_2$ phases, while the light regions consist of Si or SiO_x.

Additionally, ^{57}Fe Mössbauer spectra were obtained for 0 h air milled $Si_{85}Fe_{15}O_x$ and 10 h air milled $Si_{85}Fe_{15}O_x$ and are shown in Figure 3.8(a) and (b), respectively. Both spectra can be fitted with a doublet, which is consistent with the presence of $FeSi_2$ phases [163]. However, the spectra show some asymmetry, which possibly corresponding to paramagnetic nanograined Fe (a singlet) introduced from milling media. No significant changes (i.e. changes in isomer shift and quadrupole shift of the $FeSi_2$ peak are within 4%) can be found in the Mössbauer spectrum after the introduction of oxygen. In particular, the characteristic sextet pattern associated with Fe_2O_3 was not observed in all three alloy samples [164]. This result also indicates that in the $Si_{85}Fe_{15}O_x$ alloys made here, oxygen is present in the form of silicon suboxides, while all elemental Fe reacted with Si to form iron silicides.

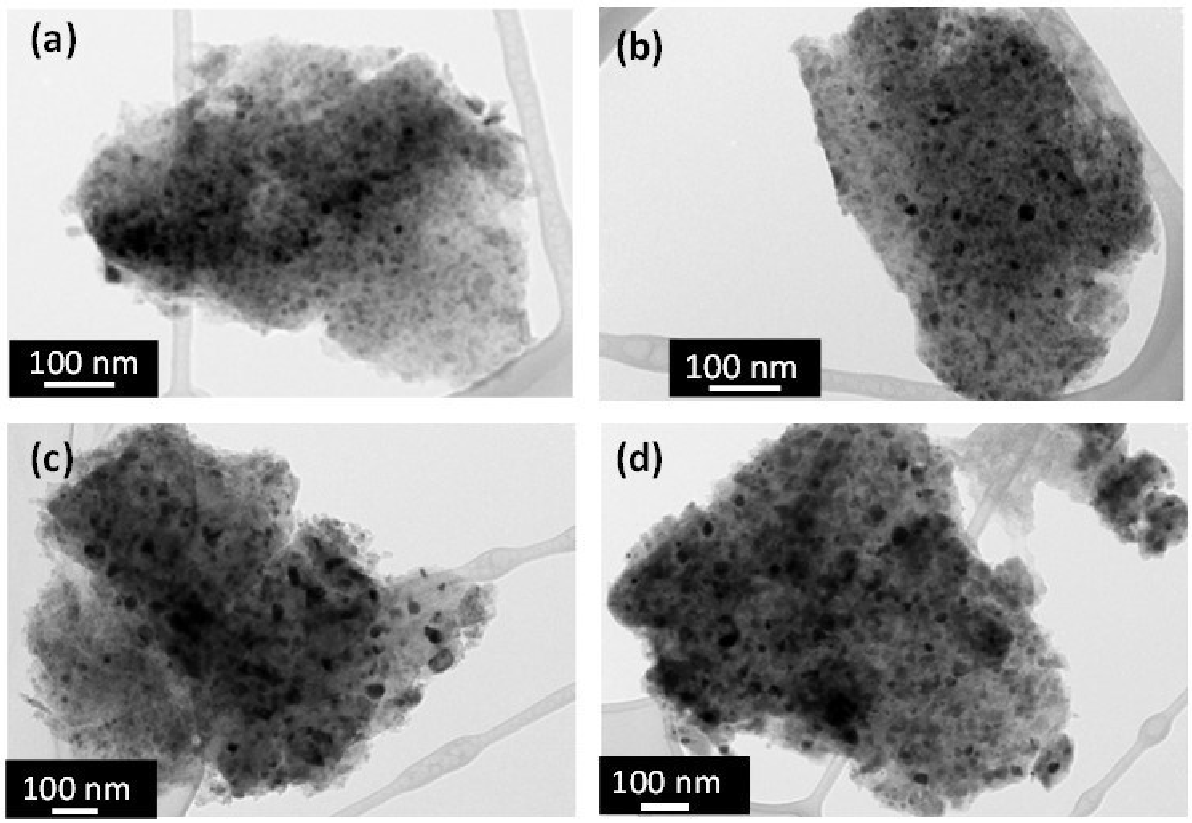

Figure 3.7 TEM images of (a) $Si_{85}Fe_{15}O_x$(0h), (b) $Si_{85}Fe_{15}O_x$(8h), (c) 600°C annealed $Si_{85}Fe_{15}O_x$(8h), and (d) 800°C annealed $Si_{85}Fe_{15}O_x$(8h) alloys.

In summary, significant differences in the $Si_{85}Fe_{15}O_x$ alloys could not be detected by SEM, XRD, TEM or ^{57}Fe Mössbauer measurements, despite significant differences in the oxygen contents in these samples. However, differences between the alloys became apparent after the samples were heated. The diffraction patterns of ball milled $Si_{85}Fe_{15}O_x$ alloys before and after annealing at 600°C and 800°C are shown in Figure 3.4. The XRD patterns of 600°C annealed $Si_{85}Fe_{15}O_x$ alloys are almost identical to the unheated

$Si_{85}Fe_{15}O_x$ alloys, indicating that no phase transitions or crystal growth detectible by XRD occurs at 600°C. At 800°C, the β-$FeSi_2$ phase, which is the thermodynamically stable phase at 800°C, crystallizes and becomes the dominant silicide phase in the XRD patterns for all the 800°C annealed alloys, while the α-$FeSi_2$ peaks almost disappear. After heating to 800°C a distinct peak also appears at about 28° for samples ball milled in air for 4h or less. This peak corresponds to the Si (111) peak, indicating that crystallization of elemental Si occurs in these samples during heating. The intensity of this peak is highly correlated to the air milling time, with the peak becoming smaller as the air milling time is increased. This is understandable, since with longer milling time in air, the amount of elemental Si should reduce, as Si reacts to form SiO_x. In contrast to the samples with low oxygen content, the samples with greater than 4h air milling time show no evidence of crystalline Si formation after heating to 800°C, indicating excellent thermal stability.

TEM images were also obtained for the heated $Si_{85}Fe_{15}O_x$ alloys, as shown in Figure 3.7(c)-(d) for the case of the $Si_{85}Fe_{15}O_x$(8h) alloy. In general, the overall microstructure is well-maintained even after heating to 800°C. Cao et al. have found that the isolated Si nanocrystallites in ball milled SiO_x materials (prepared in a similar way as the study conducted here) maintain their size (< 10 nm) even after heating to 800°C [66]. This may be similar to the observed behavior of the Si phase in the $Si_{85}Fe_{15}O_x$(8h) alloy. However, the $FeSi_2$ phases in the $Si_{85}Fe_{15}O_x$ alloys create interference in TEM images, making it hard to observe changes in the Si nanocrystallites during the annealing process. From the TEM and XRD results, it appears that the 800°C annealed samples with > 4h air milling time comprise small (~10 nm) Si nanocrystallites and $FeSi_2$ nanocrystallites with larger crystallite sizes. Figure 3.9 provides a simple drawing of the possible microstructure the air milled $Si_{85}Fe_{15}O_x$ alloys. Further confirmation of this proposed microstructure is provided by the electrochemical studies below.

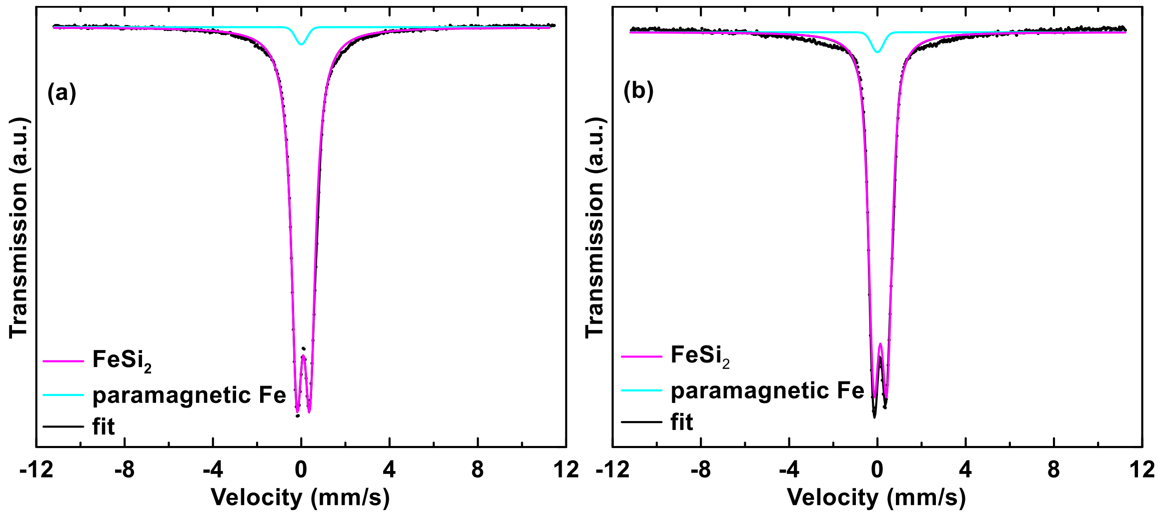

Figure 3.8 ^{57}Fe Mössbauer spectra of (a) 0 h and (b) 10 h air milled $Si_{85}Fe_{15}O_x$ alloy.

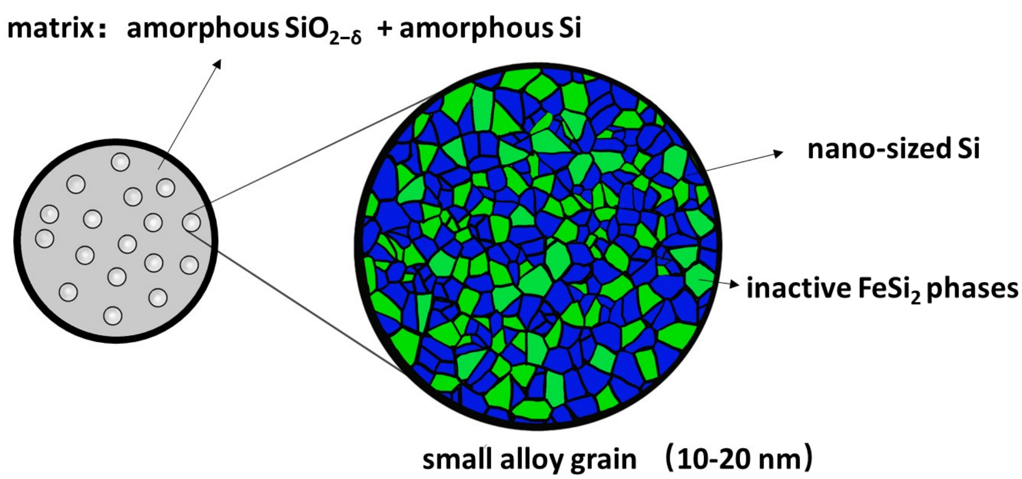

.

Figure 3.9 Proposed microstructure of $Si_{85}Fe_{15}O_x$(8h) alloys.

3.3 Electrochemical Performance of $Si_{85}Fe_{15}O_x$ Alloys

Figure 3.10 and Figure 3.11 show the potential profiles and corresponding differential capacity curves (first three cycles) of the $Si_{85}Fe_{15}O_x$(0-10h) alloys. The observed first reversible capacity decreases as air milling time increases, changing from about 1600 mAh/g to 1200 mAh/g, due to the reaction between Si and oxygen, resulting in the loss of active Si.

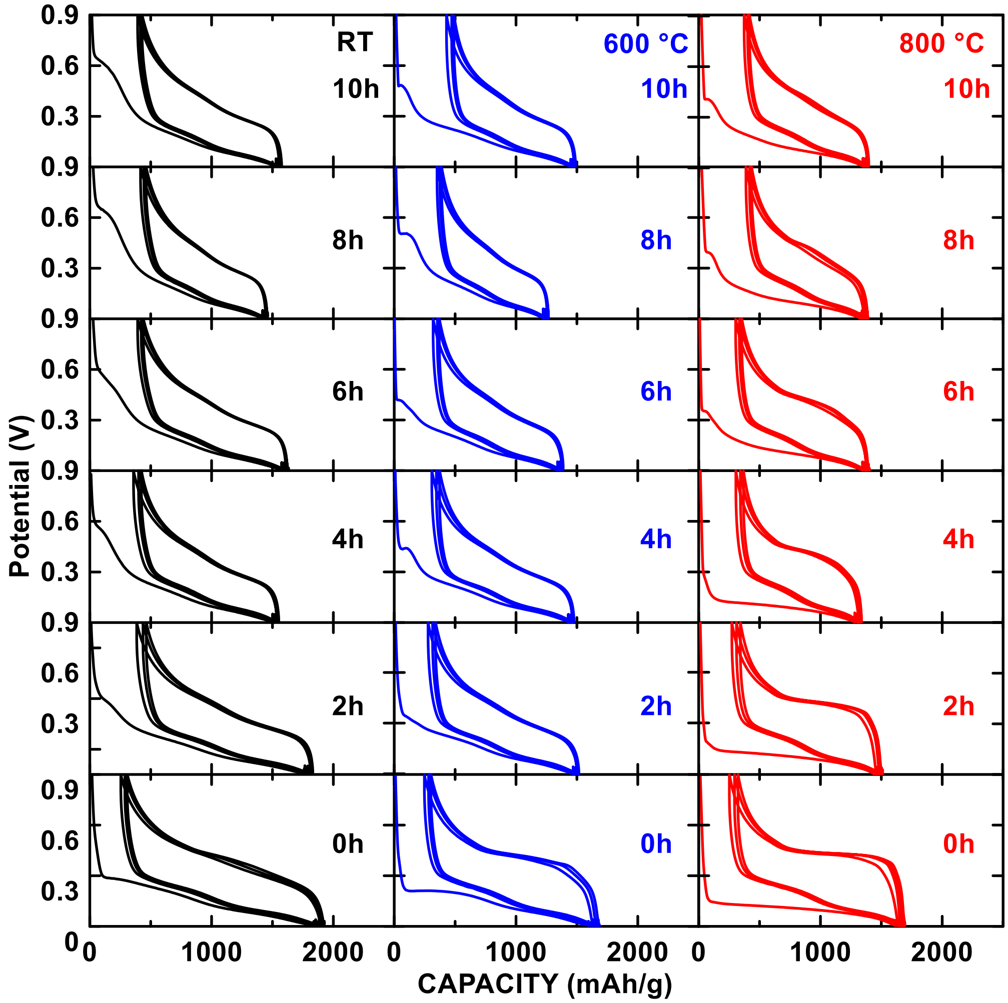

Figure 3.10 Potential profiles of $Si_{85}Fe_{15}O_x$ alloys (at different air milling time) as milled and after thermal annealing at 600°C and 800°C.

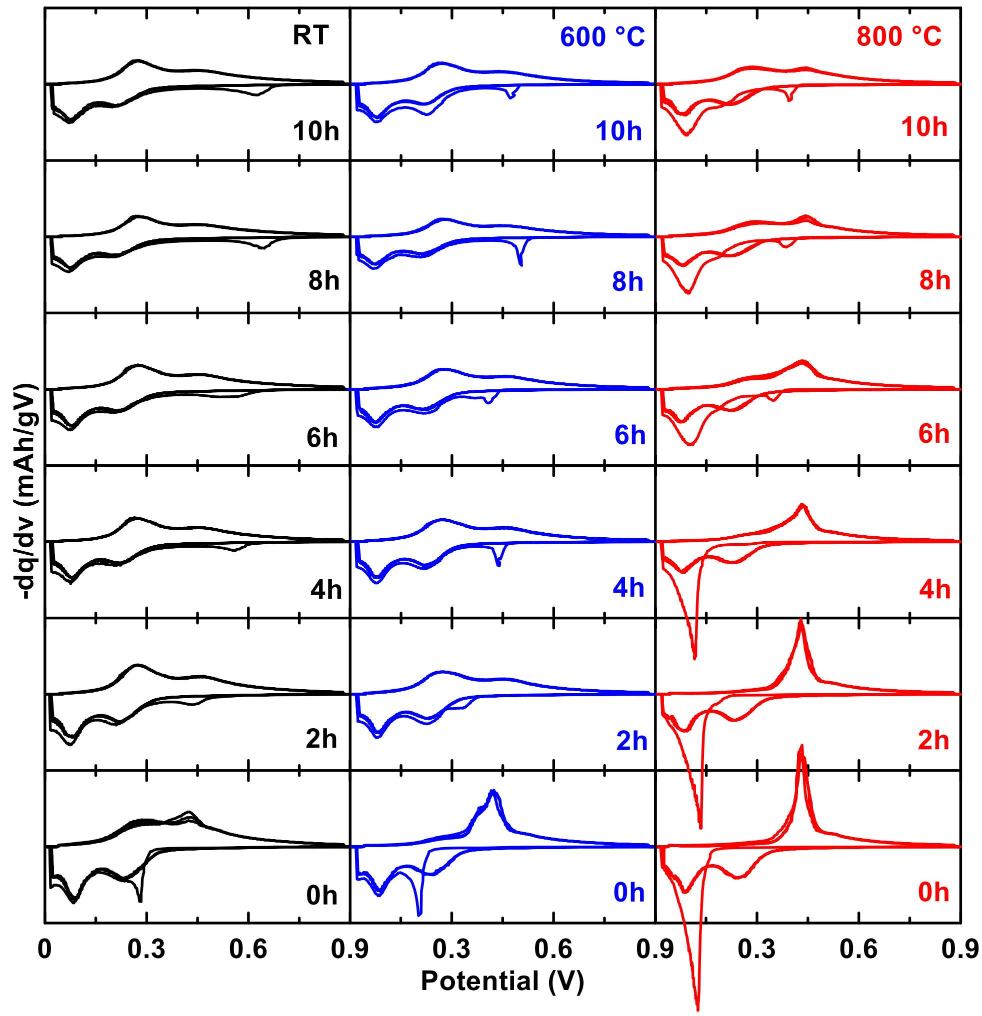

Figure 3.11 Differential capacity as a function of potential for the alloys shown in Figure 3.10

Figure 3.12 shows the predicted and experimental capacities of the electrodes during first lithiation and delithiation. The lithiation capacity was calculated assuming that any oxygen present in the alloys will form inactive Li_4SiO_4 during the first lithiation, any $FeSi_2$ phases are inactive and the remaining active Si can reversibly react with 3.75 Li to form $Li_{15}Si_4$. This model has been shown to work well for ball milled $FeSi_2$ and SiO_x alloys [51,161] and sputtered Si-Fe-O alloys [56]. Here, the model also works well for the $Si_{85}Fe_{15}O_x$(0h) sample. For this sample, the theoretical lithiation capacity is larger than predicted (as expected from SEI formation), while the delithiation capacity is nearly exactly as predicted. For higher oxygen contents, the measured lithiation and delithiation capacities become reduced with increasing oxygen content at a rate that is faster than predicted by the model. It is difficult to understand the reason for this. As will be shown below, capacities become even further reduced after thermal treatment. It is speculated that some active Si in these samples may become completely surrounded and isolated by inactive phases, as the inactive phase fraction increases and therefore becomes inaccessible towards lithiation. This behavior has also been observed in SiO, where isolated Si species also exist and the fraction of isolated Si increases with thermal treatment, resulting in reduced capacity [61]. Further details about the thermal treatment of these samples will be discussed later.

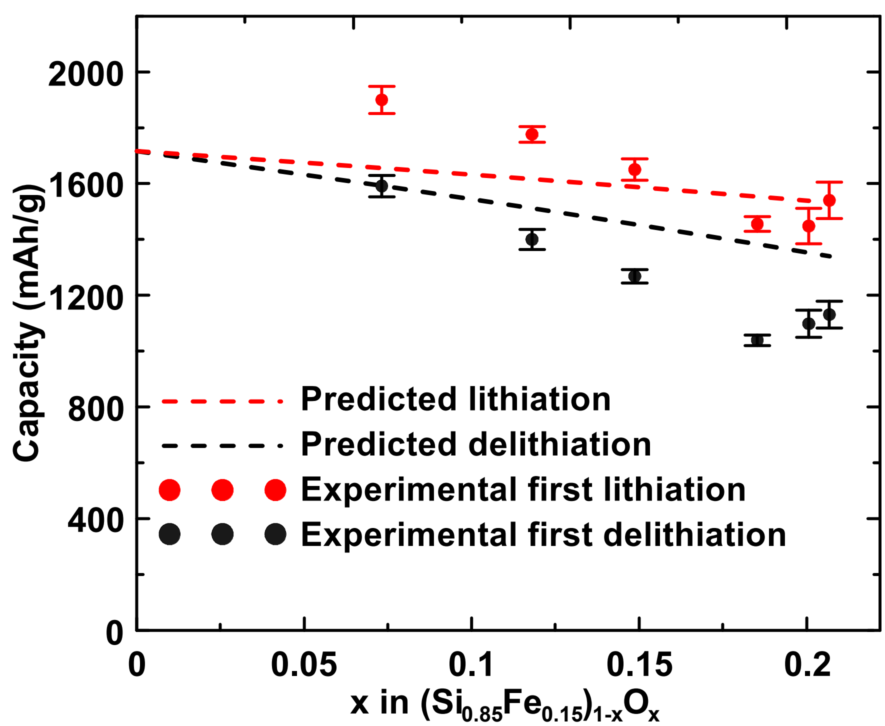

Figure 3.12 The first lithiation and delithiation capacities of ball milled $Si_{85}Fe_{15}O_x$ alloys as a function of oxygen content (error bars based on the standard error of 3 - 6 replicates).

A small plateau at 0.45-0.65 V in the potential profiles (Figure 3.10) and a corresponding peak in the differential capacity curves (Figure 3.11) during the first lithiation is observed for all the air milled alloys and disappears in the following cycles. In SiO_x made by reactive air milling, this first lithiation high potential plateau is believed to be associated with the irreversible formation of Li_4SiO_4 at oxygen defect sites [56,161]. The potential and capacity of this plateau have been found to increase with increasing oxygen content [56,161]. This was also found to be the case here. Figure 3.13 shows an overlay of the first lithiation differential capacity curves of all the alloys, in which it can clearly be seen that both the potential and the area under this peak increase with increasing air milling time/oxygen content. This is quantified in Figure 3.14 in which the amount of Li inserted per mole of $(Si_{0.85}Fe_{0.15})_{1-x}O_x$ during the initial 0.45-0.65 V lithiation potential plateau is plotted as a function of the oxygen content. Also plotted in this figure is the amount of Li extracted during delithiation between 0.9 V and 2 V for each alloy (differential capacity curves of the alloys cycled above 0.9 V are shown in Figure 3.15). The amount of Li extracted above 0.9 V has been shown to be directly correlated to the amount of oxygen in ball milled and sputtered SiO_x [60,161]. As the oxygen content increases, the amount of Li associated with the high potential initial lithiation plateau and the capacity above 0.9 V both increase linearly. In addition, the slope of both plots is close to 1, which is consistent with the formation of Li_4SiO_4 (Li:O=1:1) during the first lithiation. This is also consistent with earlier studies of SiO_x [60,161]. This result shows that all of the oxygen in the sample can be converted to the Li_4SiO_4 phase, as in the case of ball milled and sputtered SiO_x. It furthermore verifies the accuracy of the measured oxygen contents in these samples.

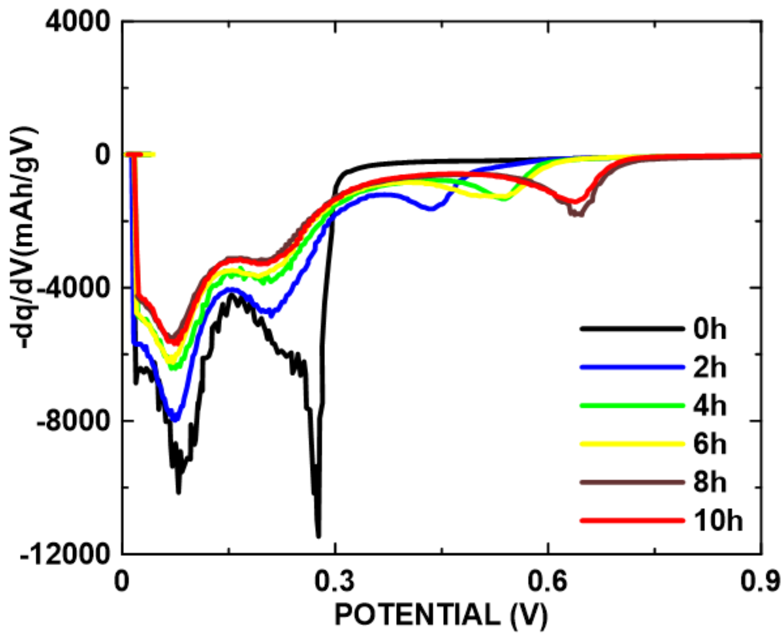

Figure 3.13 The first lithiation differential capacity curves of ball milled $Si_{85}Fe_{15}O_x$ alloys at different air milling times.

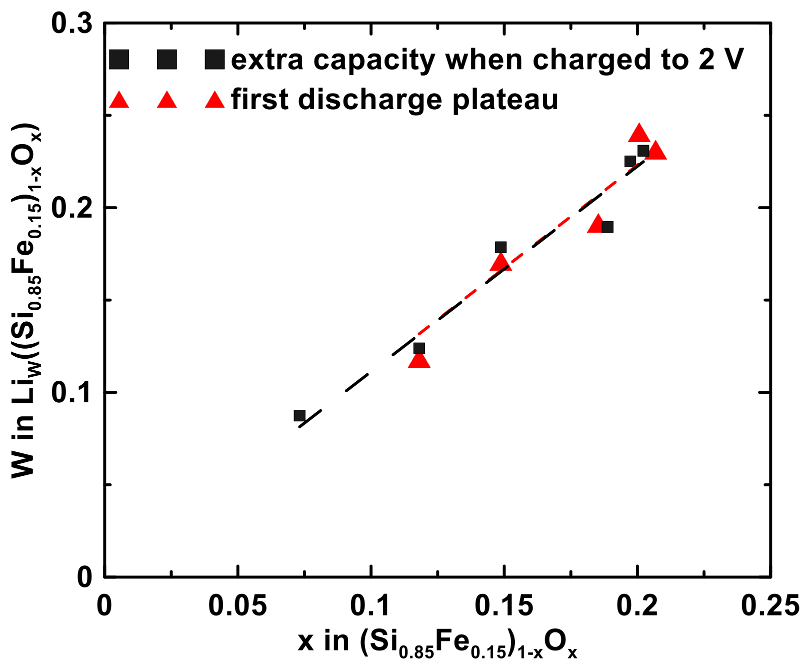

Figure 3.14 The amount of Li inserted per mole of $(Si_{0.85}Fe_{0.15})_{1-x}O_x$ during the initial ~0.5 V oxygen-related potential plateau and the amount of Li extracted between 0.9 V and 2 V versus the oxygen content, x.

During the initial lithiation, subsequent to the high potential plateau, a sharp peak at about 0.28 V in some of the $Si_{85}Fe_{15}O_x$ alloys was also observed. This peak has been associated with a nucleation and growth process for the initial lithiation step of Si [39]. As lithiation progresses, two broad peaks are then observed, corresponding to two single-phase lithiation processes that occur for amorphous Si. During delithiation, two corresponding broad peaks are observed which correspond to the delithiation of amorphous Si [22]. No pronounced peak at around 0.43 V, associated with $Li_{15}Si_4$ delithiation, were observed for any sample, indicating $Li_{15}Si_4$ formation is fully suppressed during the lithiation of these alloys. The suppression of $Li_{15}Si_4$ formation is thought to be due to stress-potential coupling between the active Si and the inactive phases in Si-M alloys [46,50,165] and is thought to enhance cycling performance, since the two-phase $Li_{15}Si_4$ delithiation reaction is avoided.

Figure 3.16 shows the specific capacity vs. cycle number of ball-milled $Si_{85}Fe_{15}O_x$ alloys. $Si_{85}Fe_{15}O_x$(0h) suffers from capacity fade. With increasing air milling time, the initial reversible capacity decreases as the amount of active Si is reduced, as discussed above. However, improved cycling performance was obtained with increasing air milling time, likely as the result of increased inactive phase and reduced volume expansion. The inactive Li-O species formed during the first lithiation not only can reduce the overall volume expansion of $Si_{85}Fe_{15}O_x$ alloys, but also improve the ion conductivity [71,78,166,167]. The 10 h air milled alloys have the highest capacity retention of about 1100 mAh/g after 50 cycles.

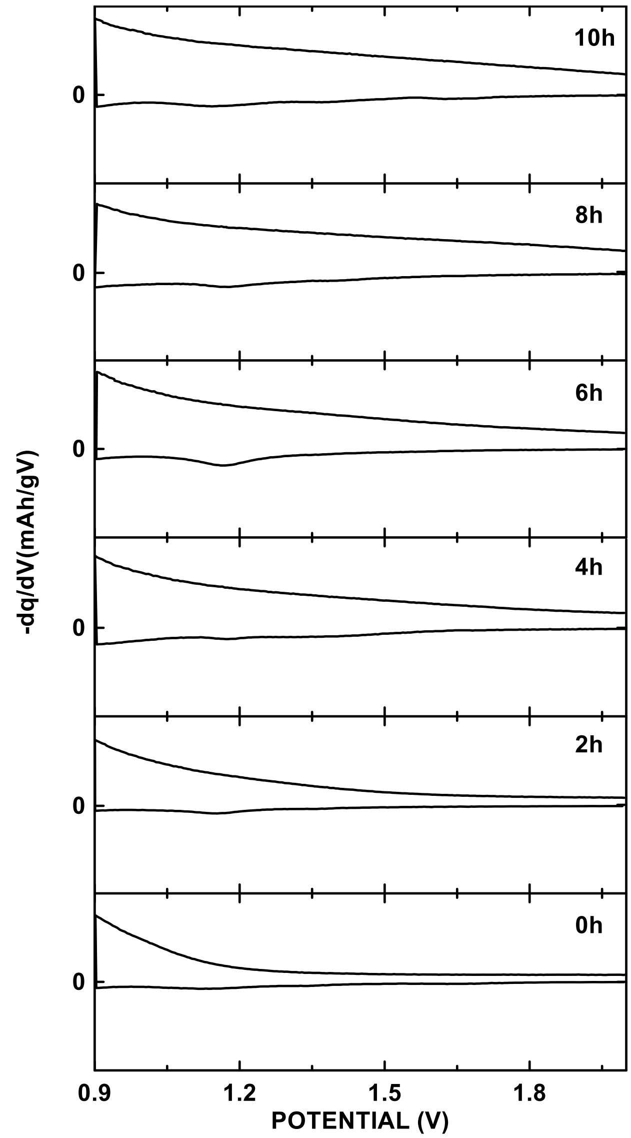

Figure 3.15 Potential profiles of as-milled $Si_{85}Fe_{15}O_x$ alloys between 0.9-2.0 V.

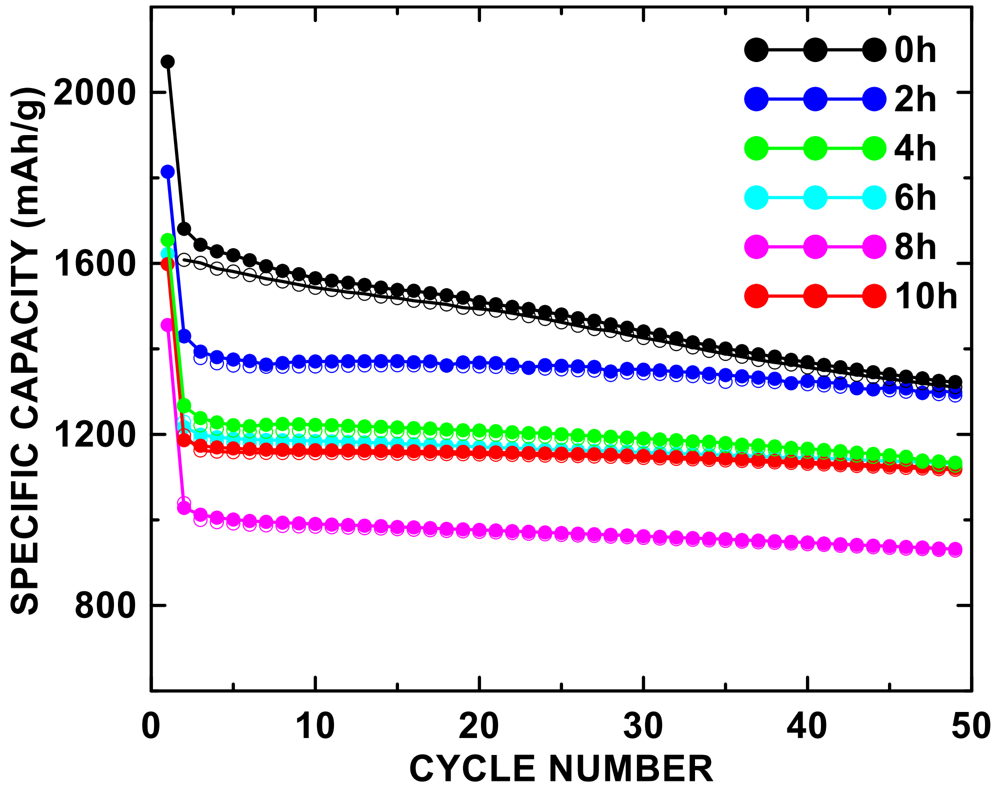

Figure 3.16 Specific capacity versus cycle number of $Si_{85}Fe_{15}O_x$ alloys with different air milling times.

Figure 3.17 shows the CE plots of ball milled $Si_{85}Fe_{15}O_x$ alloys made at different air milling times. The air milled samples generally have better CE performance than the non air-exposed $Si_{85}Fe_{15}$ alloy, indicating less side reaction with electrolyte during cycling. Further improvements to cycling performance can be made by incorporating these alloys in electrodes with graphite, which will be discussed in Chapter 5 and 6.

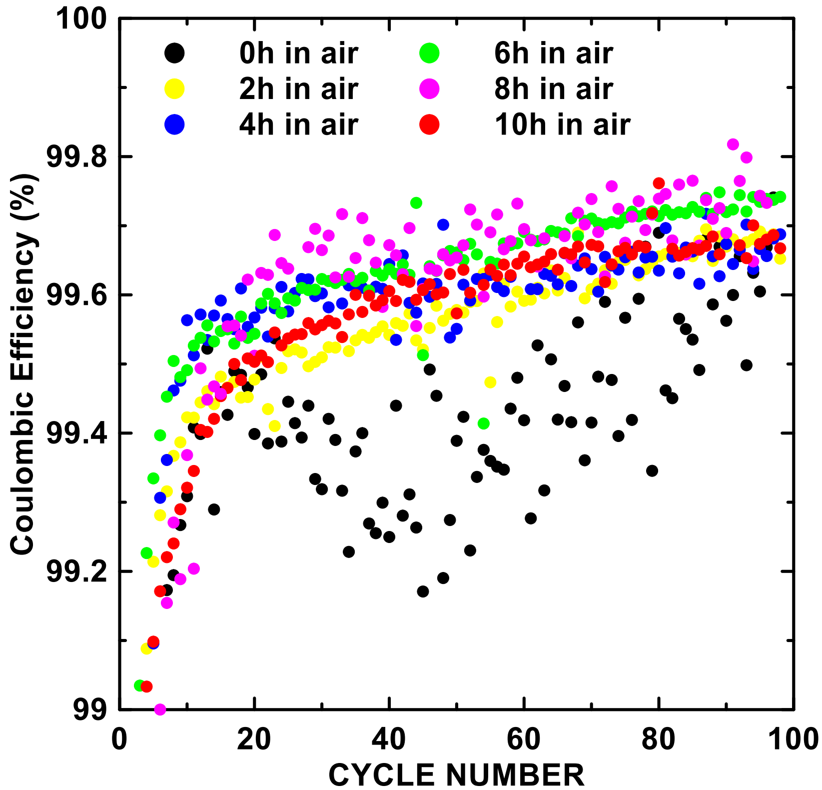

Figure 3.17 CE versus cycle number of $Si_{85}Fe_{15}Ox$ alloy made at different air milling times, air milling hours are indicated in different colors.

Figure 3.10 and 3.11 also show the potential profiles and differential capacity curves of $Si_{85}Fe_{15}O_x$ alloys as milled and after different thermal treatment. The potential profiles of the 600°C annealed alloys are very similar to the as-milled alloys, excepting that the initial lithiation high potential plateaus have become reduced in potential and in capacity. The similarity between the as-milled alloys and the 600°C annealed alloys reflects the similarity also in the XRD patterns and TEM images of these samples. For the 800°C samples and for air milling times less than 6h, the high potential plateaus have completely disappeared. This effect is associated with the healing of oxygen defects during thermal processing [161]. For the $Si_{85}Fe_{15}O_x$ (0h) RT and 600°C alloys, the lithiation differential capacity curve comprises an initial sharp peak at about 0.29 V and 0.18 V, respectively, which likely correspond to a nucleation and growth process as the alloy is initially lithiated. However, this peak is not present for $Si_{85}Fe_{15}O_x$ (2-10h) alloys. Presumably, the initial lithiation process at high voltage due to the high potential oxygen plateau precludes the nucleation and growth process in the oxygen-containing alloys. For the 800°C annealed samples milled less than 6h in air where the high potential plateau is not present, a sharp peak corresponding to the nucleation and growth of lithiated phases during the first lithiation is present at about 0.14 V. For longer milling times, when the high potential plateau precludes nucleation and growth, this sharp peak disappears.

For the 800°C annealed alloys, a flat plateau is observed in the potential curves during delithiation for the $Si_{85}Fe_{15}O_x$ alloys with short air milling time and a corresponding delithiation peak appears near 0.43 V in their differential capacity curves. This peak is associated with the delithiation of $Li_{15}Si_4$ and indicates that this phase has been formed during the previous lithiation half-cycle. The formation of $Li_{15}Si_4$ occurs if the active Si phase in the alloy has aggregated or is poorly connected to the inactive phase and is associated with capacity fade [39,46,50,51,165]. The sharpest 0.43 V peak appears for the 800°C annealed 0 h air milled alloy, where the crystallization of Si can be identified from the XRD pattern (Figure 3.4(b)). Indeed, the presence of the 0.43 V peak in the differential capacity curves is directly correlated with the size of the crystalline Si peak shown in Figure 3.4(b). As demonstrated in Figures 3.4(b) and 3.10, alloys with higher air milling time are more effective at suppressing Si crystallization during annealing and suppressing $Li_{15}Si_4$ formation. The $Si_{85}Fe_{15}O_x$(6-10h) alloys are particularly thermally stable, with both Si crystallization and $Li_{15}Si_4$ formation being nearly completely suppressed in these samples after heating to 800°C.

The cycling performance of the 800°C heated alloys are shown in Figure 3.18. After heating, the alloys have a lower capacity than the unheated alloys. This is likely due to the disproportionation of Si-O species to Si and inactive SiO_2, resulting in the isolation of active Si regions, making them inaccessible towards lithiation, as has been previously observed in heated SiO_x [61]. Severe capacity fade occurs for the heated alloys with short air milling time. As the air milling time is increased (and Si crystallization and $Li_{15}Si_4$ formation is suppressed), capacity fade is reduced. In particular, the 800°C annealed $Si_{85}Fe_{15}O_x$(10h) alloy maintain a capacity about 1000 mAh/g with almost no loss after 50 cycles. This good thermal stability enables these alloys to be amenable towards high-temperature processing.

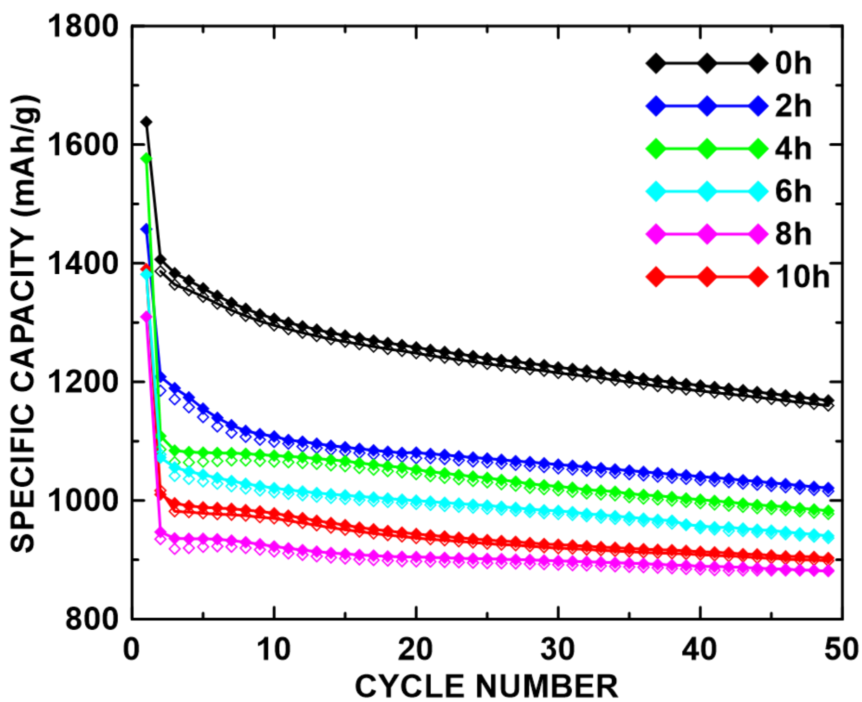

Figure 3.18 Specific capacity versus cycle number of $Si_{85}Fe_{15}Ox$ alloys with different air milling times after annealing to 800°C.

3.4 Conclusion

The microstructure of ball milled $Si_{85}Fe_{15}O_x$ alloys were investigated as a function of air milling time. Oxygen content of the milled alloys was found to increase with the air milling time from 0 h to 6 h, followed by a steady state after 6 h. The electrochemical behavior of ball milled $Si_{85}Fe_{15}O_x$ alloys (with initial composition $Si_{0.85}Fe_{0.15}$) made at different air milling times (0 h, 2 h, 4 h, 6 h, 8 h and 10 h) was examined in Li cells. It was found that increasing air milling time decreases the specific capacity as the introduced oxygen reacts with Si. However, increasing air milling time can help improve the cycling stability and suppress the formation of $Li_{15}Si_4$. The 10 h air milled $Si_{85}Fe_{15}O_x$ alloy shows high volumetric capacity and good cycle life.

The ball milled $Si_{85}Fe_{15}O_x$ alloys were then heated to test their thermal stability. No significant changes (no additional features in the potential profiles, measured capacity within 5 %) can be observed between the potential curves of the unheated and 600°C annealed $Si_{85}Fe_{15}O_x$ alloys, which is consistent with the XRD results. Some of the annealed alloys even show improved capacity retention. Although crystallization occurred in some of the 800°C annealed alloys and a more noticeable plateau at 0.43 V presented in the potential curves, the 800°C annealed alloys still have good cycling stability with some decrease in the specific capacity. It is also found that the potential curves of $Si_{85}Fe_{15}O_x$ alloys with higher oxygen content are less affected by high-temperature treatment, as evident by no sign of $Li_{15}Si_4$ formation at 0.43 V. In general, $Si_{85}Fe_{15}O_x$ alloys have excellent thermal stability, even after being annealed to 800°C. For instance, the 10 h air milled $Si_{85}Fe_{15}O_x$ alloy is an outstanding candidate among the examined alloys for use in commercial cells. It retains a capacity of 1000 mAh/g after 50 cycles with little $Li_{15}Si_4$ formation after high-temperature treatment.

CHAPTER 4 $SiFe_xO_y$ ALLOYS

4.1 Introduction

Chapter 3 discusses ball milled $Si_{85}Fe_{15}O_x$ alloy microstructure and electrochemical performance. All $Si_{85}Fe_{15}O_x$ alloys were prepared with a fixed 85:15 stoichiometric ratio of Si and Fe. Chapter 3 describes the effect of oxygen introduced by air milling on $Si_{85}Fe_{15}O_x$ alloy electrochemical performance. Miyachi et al. found that the Fe doped SiO anode has improved electrical properties compared to SiO. They claimed that the inclusion of Fe can help the diffusion of lithium ions in the electrode [168]. Ruttert et al. prepared Si-Fe alloys at different Si:Fe ratios and different electrochemical performance were obtained [51]. Therefore, it would be very interesting to investigate the effect of iron content on the electrochemical performance of the air milled $SiFe_xO_y$ system. In this chapter, Si and Fe powders were loaded at different atomic ratios (Si, $Si_{95}Fe_5$, $Si_{90}Fe_{10}$, $Si_{85}Fe_{15}$ and $Si_{80}Fe_{20}$) and ball milled for 16 hours with 10 hours of air exposure in order to investigate the effect of iron content on structure and electrochemical performance. In addition, the most promising composition was also prepared by ball milling different starting materials (Si + Fe_2O_3 powders and SiO_2 + Si + Fe powders) under Ar atmosphere. Their corresponding electrochemical performance and thermal stability were compared.

4.2 Results

Table 4.1 lists the chemical compositions of the as-milled alloys determined by EDS chemical analysis. It is noted that the oxygen content is overestimated because of the low atomic number of the oxygen and its different interaction volume compared to Fe or Si. However, the amounts of Si and Fe on a metals basis are consistent with the initial loading compositions and about 0.91 at. % of iron identified in the iron-free sample. This amount of iron is considered to be contamination from the milling media (milling vessel and milling balls). In order to accurately determine the final compositions of the resulting materials, LECO tests were used to determine the oxygen contents. Based on LECO results for oxygen content and SEM-EDS results for metals content, the compositions of the resulting alloys were calculated and are listed in Table 4.2 (normalized to the Si content). These compositions are represented in a ternary composition diagram in Figure 4.1. The influence of the Fe to Si ratio on the oxygen content was also investigated and is discussed below in Section 4.2.2.

Table 4.1 Chemical composition by EDS (at. %) determined for the as-milled alloys. Standard Errors were calculated from at least five replicates.

Loading composition	**Si**	**Fe**	**O**	**Si (metals basis)**	**Fe(metals basis)**
Si	59.59	0.55	39.86	99.09 ± 2.28	0.91 ±0.02
$Si_{95}Fe_5$	50.68	3.68	45.64	93.22 ± 1.88	6.78± 0.16
Si_{90}Fe10	54.23	6.63	39.14	89.11 ± 0.49	10.89 ± 0.05
$Si_{85}Fe_{15}$	45.00	9.00	46.00	83.33± 0.39	16.67 ± 0.13
$Si_{80}Fe_{20}$	44.36	12.44	43.19	78.10 ± 0.76	21.90 ± 0.28

Table 4.2 Compositions and measured densities of the as-milled alloys determined by EDS and LECO. Five replicates were taken for density measurement.

Initial composition	**As-milled alloy composition**	**Measured Densities (g/cm^3)**
Si	$SiO_{0.32}$	2.249±0.007
$Si_{95}Fe_5$	$SiFe_{0.07}O_{0.38}$	2.620±0.004
$Si_{90}Fe_{10}$	$SiFe_{0.12}O_{0.29}$	2.740±0.009
$Si_{85}Fe_{15}$	$SiFe_{0.20}O_{0.39}$	3.242±0.006
$Si_{80}Fe_{20}$	$SiFe_{0.28}O_{0.44}$	3.574±0.007

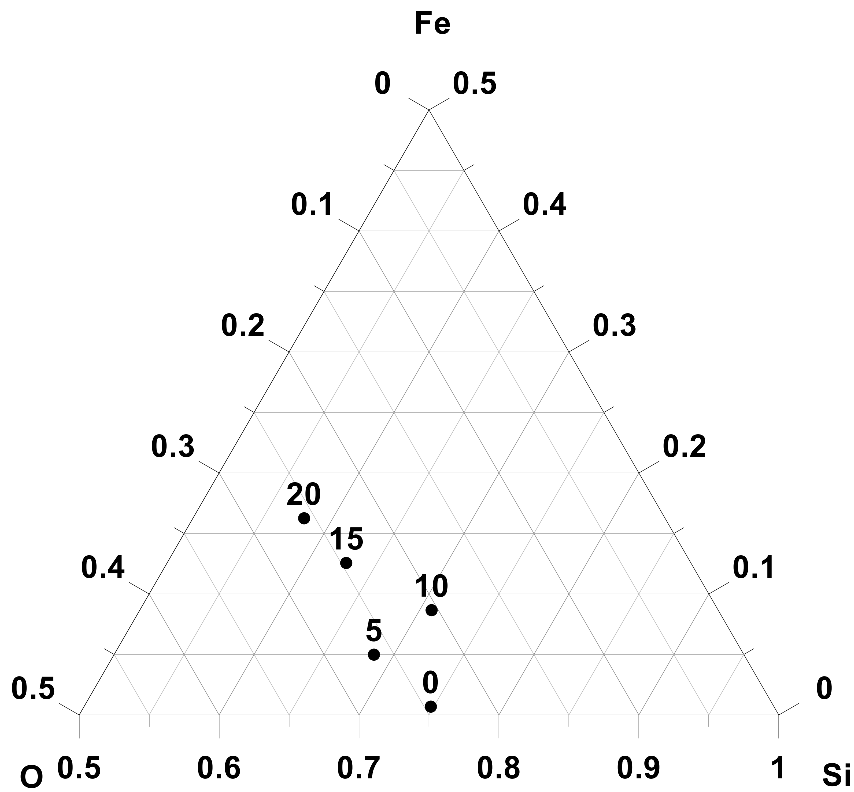

Figure 4.1 Ternary composition diagram of the $SiFe_xO_y$ alloys prepared in this study, with intended iron contents labelled.

4.2.1 Material Characterization

Figure 4.2 shows powder XRD patterns of ball milled $SiFe_xO_y$. Peaks of known phases are indicated. In the XRD pattern of $SiO_{0.32}$, amorphous Si as well as some X-ray intensity from silicon oxide are present [66]. In $SiFe_{0.07}O_{0.38}$, α-$FeSi_2$ (PDF: 00-089-2024) is formed, due to the reaction between Si and Fe during ball milling. In $SiFe_{0.12}O_{0.29}$ and $SiFe_{0.20}O_{0.39}$ alloys, both α-$FeSi_2$ (PDF: 00-089-2024) and β-$FeSi_2$ (PDF: 00-071-0642) are produced during ball milling. Here α-$FeSi_2$ is the high temperature (>937 °C) stable phase of $FeSi_2$ and β-$FeSi_2$ is thermodynamically stable below 937 °C. However, when the iron content is further increased, the β-$FeSi_2$ phase becomes the dominant phase and peaks from α-$FeSi_2$ phase almost disappear in the XRD pattern of $SiFe_{0.28}O_{0.44}$. The predominant formation of β-$FeSi_2$ was also found in ball milled $Si_{85}Fe_{15}$ prepared by Cao et al. [4]. They explained that the ball milling process can introduce a high level of defects, which favours the formation of the disordered β-$FeSi_2$ structure. However, the opposite dominating phase was reported in $Fe_{14}Si_{86}$, $Fe_{20}Si_{80}$, $Fe_{25}Si_{75}$, and $Fe_{33}Si_{67}$ prepared by a planetary ball milling method [2]. It is not very clear what the exact milling conditions are for the preferred formation of the two silicide phases. But different initial compositions, milling parameters, temperatures, and grain sizes can result in very different phase distributions.

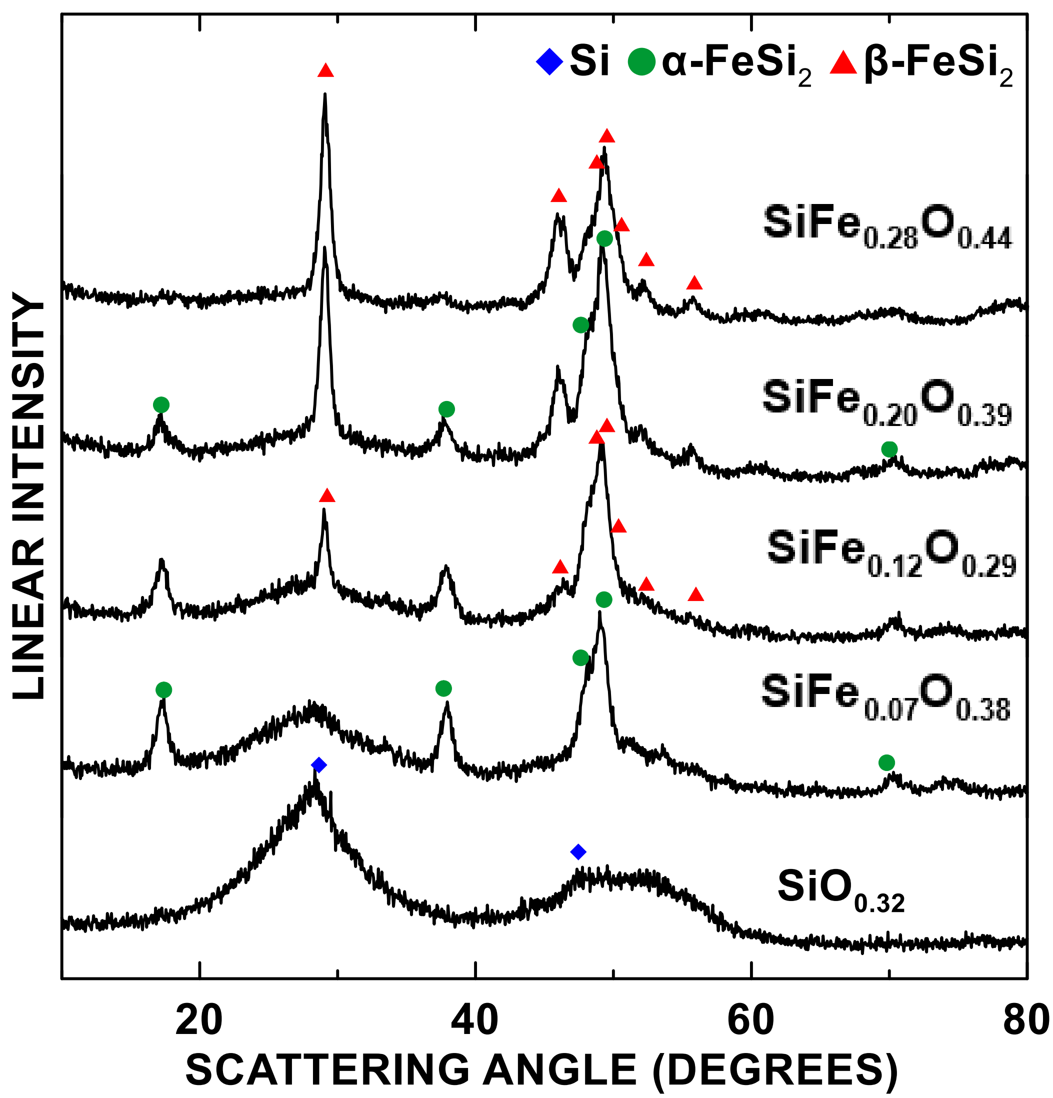

Figure 4.2 XRD patterns of ball milled $SiFe_xO_y$ alloys.

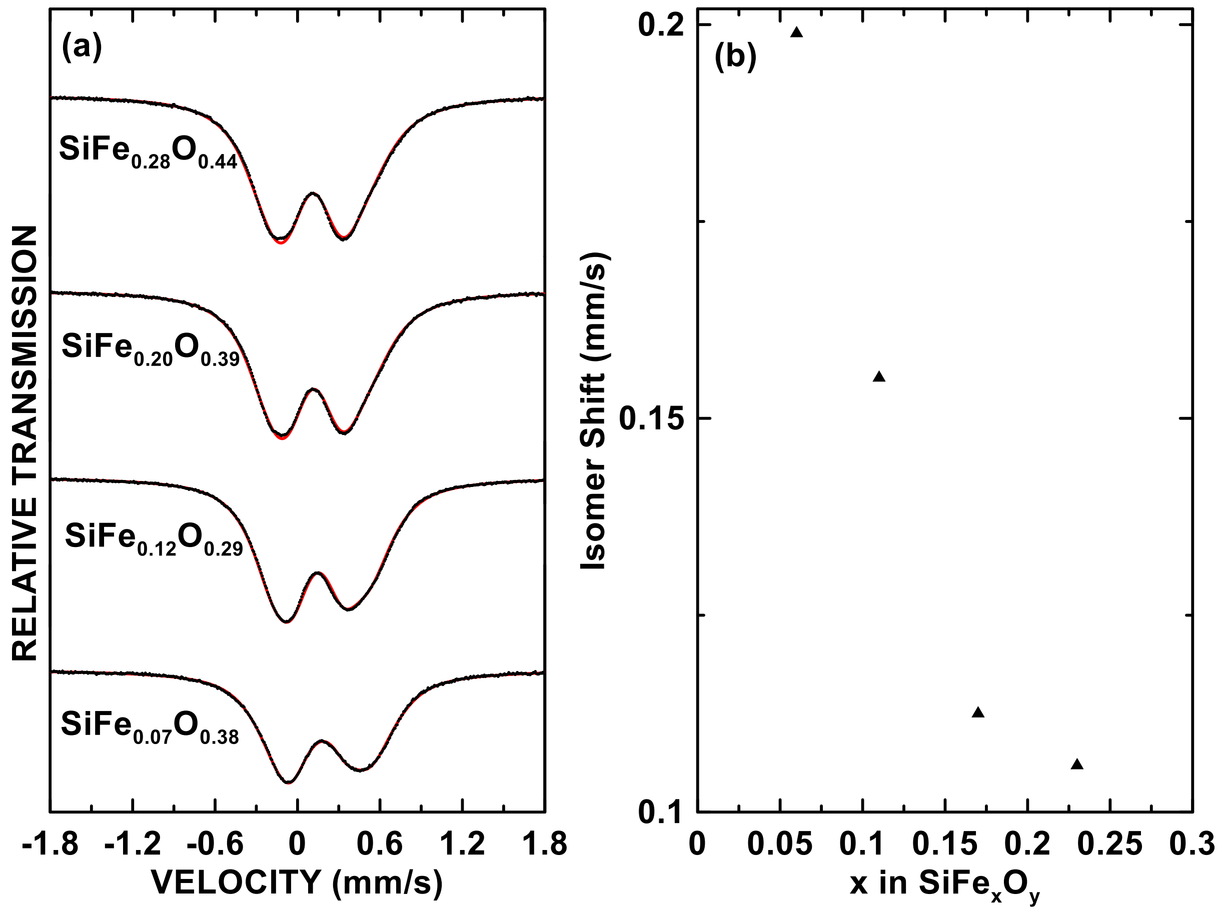

Figure 4.3 (a) Mössbauer spectra of Si-Fe-O alloys. The data are shown in circles and overall fits are shown in solid red lines. (b) Isomer shift relative to room temperature α-Fe for all spectra that were fit to a distribution of doublets as a function of x in $SiFe_xO_y$.

^{57}Fe Mössbauer experiments were conducted to provide more details of $SiFe_xO_y$ alloy phase composition as a function of iron content. The resulting Mössbauer spectra are shown in Figure 4.3 The spectra show a quadrupole split doublet and were fit to one quadrupole site distribution using a Voigt-based function. The quadrupole doublet shifts to lower velocity with increasing Fe content, which indicates an increase in electron density at the Fe nucleus [55]. Figure 4.3(b) plots the isomer shift (δ) as a function of iron content. The value of isomer shift decreases from +0.199 mm/s to +0.106 mm/s with increasing Fe content. A previous study prepared α-$FeSi_2$ and β-$FeSi_2$ by ball milling and arc-melting to study the parameters of each $FeSi_2$ phase [55]. The determined isomer shift for ball milled α-$FeSi_2$ is 0.201 mm/s and 0.139 mm/s for β-$FeSi_2$ [55]. While some references reported the isomer shift of β-$FeSi_2$ is less than +0.100 mm/s and around +0.260 mm/s for α-$FeSi_2$, measured from crystalline or thin films [169–171]. Nevertheless, β-$FeSi_2$ has a lower centre shift than α-$FeSi_2$ and therefore the presence of β-$FeSi_2$ will decrease the observed centre shift. The decreasing trend in Figure 4.3(b) confirms the observations from XRD, as iron content increases, β-$FeSi_2$ becomes the dominating phase. The isomer shift value for the alloy with the highest iron content ($SiFe_{0.28}O_{0.44}$) is only +0.106 mm/s, which is very close to reported value for pure β-$FeSi_2$ phase.

4.2.2 Electrochemical Performance of $SiFe_xO_y$ Alloys

Figure 4.4 shows the potential profiles and the corresponding differential capacity curves (first three cycles) of $SiFe_xO_y$ alloys. The potential profiles demonstrate that the capacity becomes reduced as x in $SiFe_xO_y$ increases from 0 to 0.28. The initial plateau at ~0.6 V during the first lithiation is observed for all the $SiFe_xO_y$ alloys and disappears in the following cycles. A corresponding high potential initial lithiation peak can be seen in the differential capacity curves. As mentioned in Chapter 3, this high potential plateau is believed to be associated with the irreversible formation of Li_4SiO_4 at oxygen defect sites. For SiO_x, the capacity of this plateau has been found to be directly related with the oxygen content (i.e. 1 Li per formula unit of O, according to the formation of Li_4SiO_4), while the potential of the plateau has been associated with the number of defect oxygen sites [66,161]. The higher incidence of defects, e.g. due to ball milling, the higher the potential of this plateau. After annealing to heal defects, the plateau potential becomes lower, such that it merges with features in the potential profile associated with the lithiation of silicon [161]. For simplicity, the plateau associated with the formation of Li_4SiO_4 will be referred to here as the oxygen plateau.

The behavior of the oxygen plateau for the potential profiles of the $SiFe_xO_y$ alloys shown in Figure 4.4 are consistent with the observations in Chapter 3: the oxygen plateau was only observed during the first lithiation and no corresponding peak was found in the subsequent delithiation curves. If compared with the iron-free $SiO_{0.32}$ sample, the oxygen plateau seems to appear at a higher potential when iron is present. The capacity of the oxygen plateau will be discussed quantitatively below. Except for their oxygen plateaus, all $SiFe_xO_y$ alloys show very similar features: two broad peaks during lithiation processes and two corresponding broad peaks during delithiation, which are typical of amorphous Si [22]. In addition, no pronounced peaks were observed at around 0.43 V during the delithiation of all samples, demonstrating good suppression of $Li_{15}Si_4$ formation.

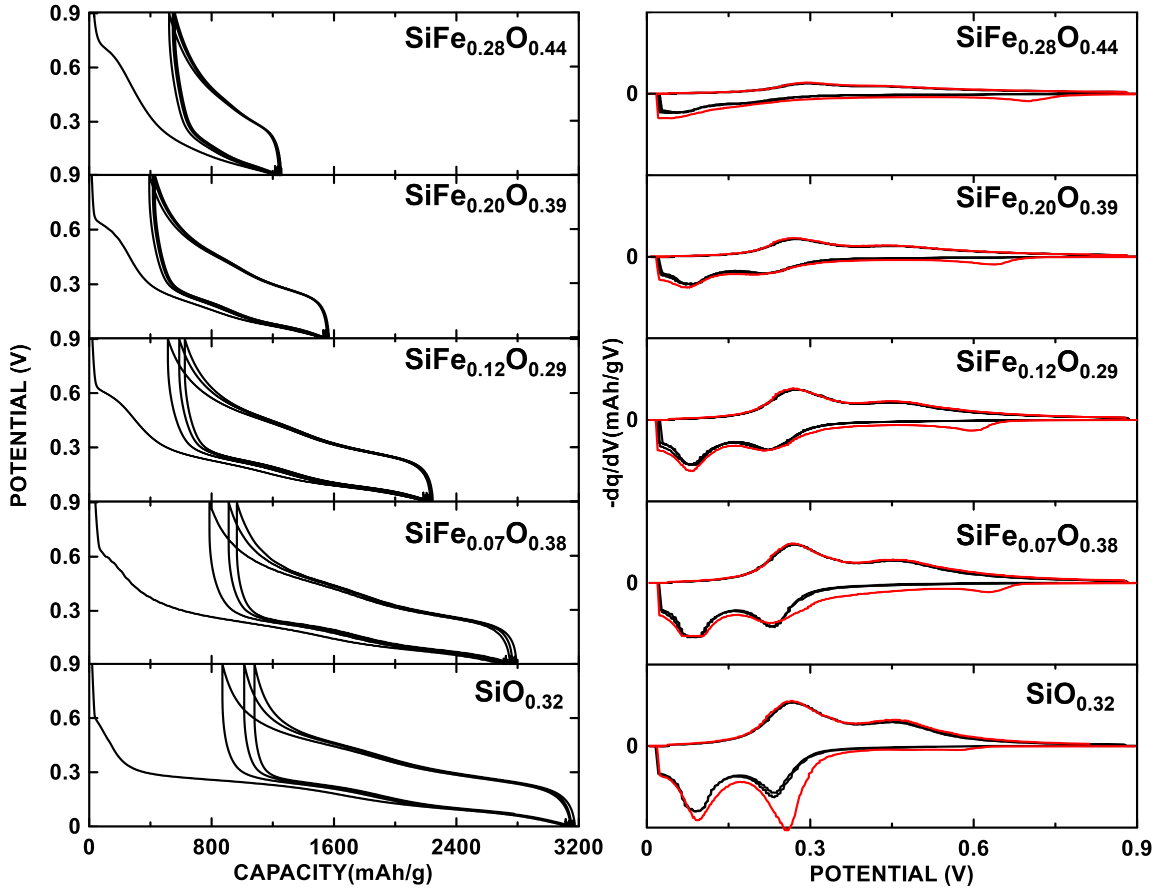

Figure 4.4 Potential and differential capacity curves of ball milled Si-Fe-O alloys at indicated compositions. Red curves indicate the initial cycle differential capacity curves.

Figure 4.5 shows the capacities of the $SiFe_xO_y$ alloys plotted as a function of the iron content. It was found that the observed first lithiation and delithiation capacities decreases as a function of x in $SiFe_xO_y$. As described in Chapter 3, the $SiFe_xO_y$ alloys are composed of inactive $FeSi_2$ phases, amorphous Si, and the silicon suboxide $SiO_{2-\delta}$. During the first lithiation, $SiO_{2-\delta}$ and amorphous Si are the only active phases and the lithiation process is described in Equations 4.1 and 4.2. The products of these reactions are Li_4SiO_4 (corresponding to the reaction that occurs at the oxygen plateau, the formation of this phase is irreversible at potentials below 1 V) and amorphous lithiated silicon, which is assumed here to have the same composition as $Li_{15}Si_4$ (the highest lithiated phase of silicon achievable at room temperature). The calculated capacities assumes that all Fe has reacted with Si to form inactive $FeSi_2$ during ball milling and all oxygen has irreversibly reacted with Li and Si during the first lithiation to form Li_4SiO_4, according to Equations 4.1 and 4.2. During the first delithiation process, the amorphous a-$Li_{15}Si_4$ phase becomes delithiated, to form amorphous Si, which is shown in Equation 4.3.

The theoretical capacities of the $SiFe_xO_y$ alloys were derived from the stoichiometries in Equations 4.1-4.3, with the total lithium stoichiometry in Equations 4.1 and 4.2 (that is, $y + 15(1-2x-y/4)/4$) representing the first lithiation capacity per $SiFe_xO_y$ formula unit and the lithium stoichiometry in Equation 4.3 ($15(1-2x-y/4)/4$), being the reversible capacity per $SiFe_xO_y$ formula unit. In actual measurements, the first lithiation is expected to be larger than the model, because the formation of SEI will consume additional Li beyond the theoretical capacity. On the other hand, the first delithiation is expected to be less than predicted by the model, due to loss of capacity from disconnected particles or particle fracture. In Figure 4.5 the theoretical capacities as a function of x for the $SiFe_xO_y$ alloys are shown in addition to the measured capacities. The theoretical model is a good predictor of the initial lithiation and delithiation capacities. As expected, the first lithiation capacities all exceed the theoretical value because of SEI formation. The first delithiation capacities are all very close to their theoretical values, indicating good reversibility.

First lithiation:

$$SiFe_xO_y + yLi \rightarrow \left(1 - 2x - \frac{y}{4}\right) Si + xFeSi_2 + \frac{y}{4} Li_4SiO_4 \tag{4.1}$$

$$\left(1 - 2x - \frac{y}{4}\right) Si + \frac{15\left(1 - 2x - \frac{y}{4}\right)}{4} Li \rightarrow \left(\frac{1 - 2x - \frac{y}{4}}{4}\right) a\text{-}Li_{15}Si_4 \tag{4.2}$$

First delithiation:

$$\left(\frac{1 - 2x - \frac{y}{4}}{4}\right) a\text{-}Li_{15}Si_4 \rightarrow \left(1 - 2x - \frac{y}{4}\right) a\text{-}Si + \frac{15\left(1 - 2x - \frac{y}{4}\right)}{4} Li \tag{4.3}$$

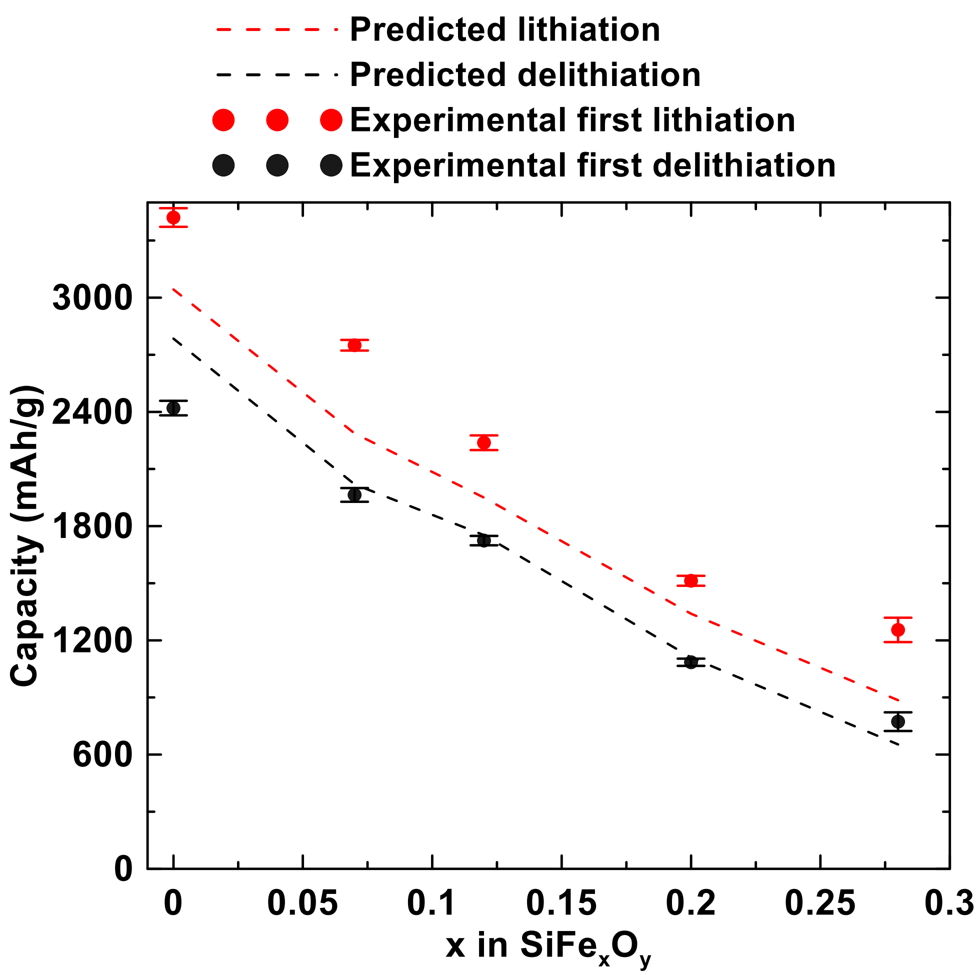

Figure 4.5 The observed and predicted capacities as a function of x of the $SiFe_xO_y$ alloys prepared in this study (error bars based on the standard error of 3-5 replicates).

As mentioned above, the oxygen plateau that occurs during the first lithiation of the as-milled $SiFe_xO_y$ alloys seems appear at higher potential than the iron-free $SiO_{0.32}$ sample, which can be clearly seen in Figure 4.6. This suggests that the presence of Fe makes the formation of Li_4SiO_4 more thermodynamically favourable. The differential capacity peak associated with the oxygen plateau for the $SiFe_xO_y$ ($x > 0$) alloys also have a larger area than the $SiO_{0.32}$ sample. However, when the iron content, x, increases from 0.07 to 0.20, the oxygen plateau appears at the same position and there is no significant difference in the peak areas (all differences within 1 %).

The oxygen plateau peak shifts to a higher potential when x increases from 0.20 to 0.28, but again the peak area is not significantly changed (areas within 1.2 % of each other).

Figure 4.7 shows the amount of oxygen in the $SiFe_xO_y$ alloys according to Equation 4.1 vs. their Fe content, where y was obtained by measuring the area under the oxygen plateau peaks in the differential capacity curves of Figure 4.6. For comparison, the oxygen content as obtained from LECO analysis is also shown in the figure. The y values determined from the oxygen plateau capacities are systematically lower than those determined by LECO analysis. This could indicate that not all oxygen in the $SiFe_xO_y$ alloys has reacted with Li to form Li_4SiO_4 or that the area under the initial lithiation curve does not represent all the capacity associated with the formation of Li_4SiO_4. According to Figure 4.7, there is a slight increase in the oxygen content as measured both by LECO analysis and according to the oxygen plateau capacity. This may suggest that the addition of Fe to Si increases oxygen uptake during the ball milling process.

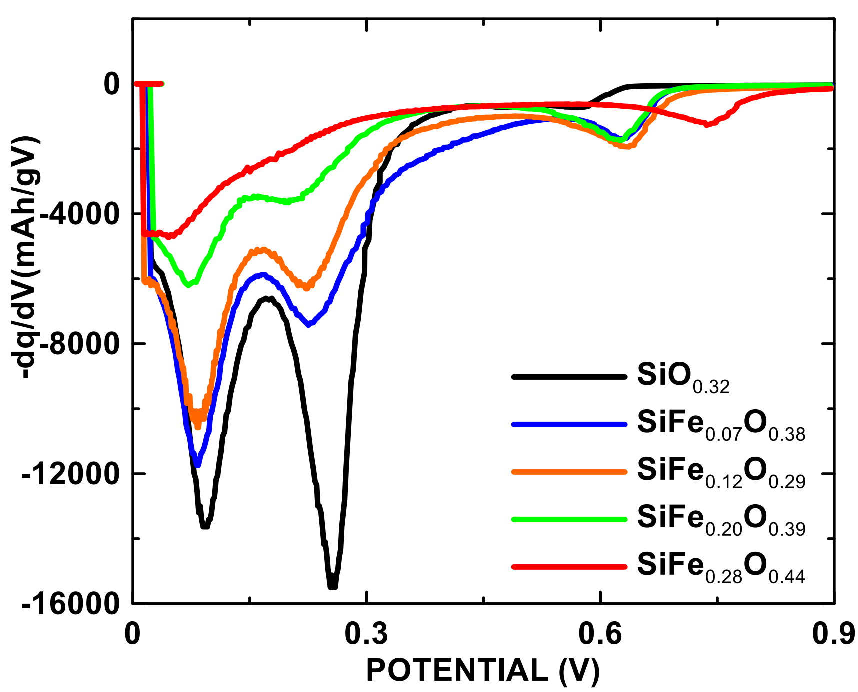

Figure 4.6 Potential and differential capacity curves of ball milled Si-Fe-O alloys at indicated compositions

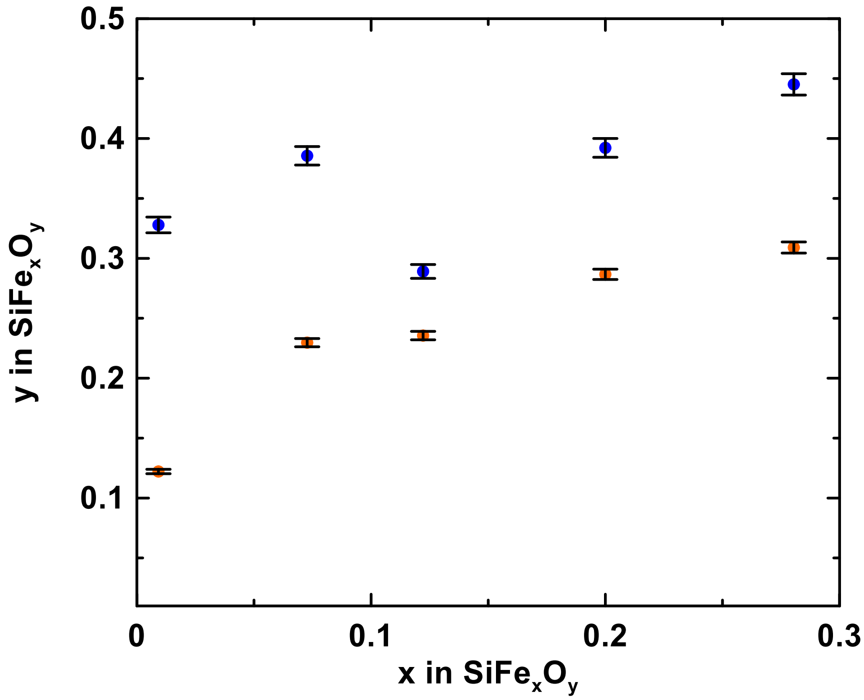

Figure 4.7 The dependence of the oxygen content (y) in $SiFe_xO_y$ alloys as a function of their iron content (x), where y was determined both by LECO analysis (blue circles) and calculated based on the measured oxygen plateau capacities and Equation 4.1(orange circles). Error bars based on the standard error of 3-5 replicates.

Figure 4.8 shows specific and volumetric capacities vs. cycle number of ball-milled $SiFe_xO_y$ alloys. The iron-free $SiO_{0.32}$ sample exhibits severe capacity fade, its reversible capacity decreases from 2200 mAh/g to 1300 mAh/g after 100 cycles. With increasing iron content, the initial reversible capacity decreases as the formation of inactive iron silicide. However, improved cycling performance was obtained for alloys containing more iron. The increasing amount of inactive $FeSi_2$ phases can further buffer the volume expansion of $SiFe_xO_y$ alloys, better performance was therefore expected. The $SiFe_{0.20}O_{0.39}$ alloy has the best combined performance in terms of high capacity and good capacity retention.

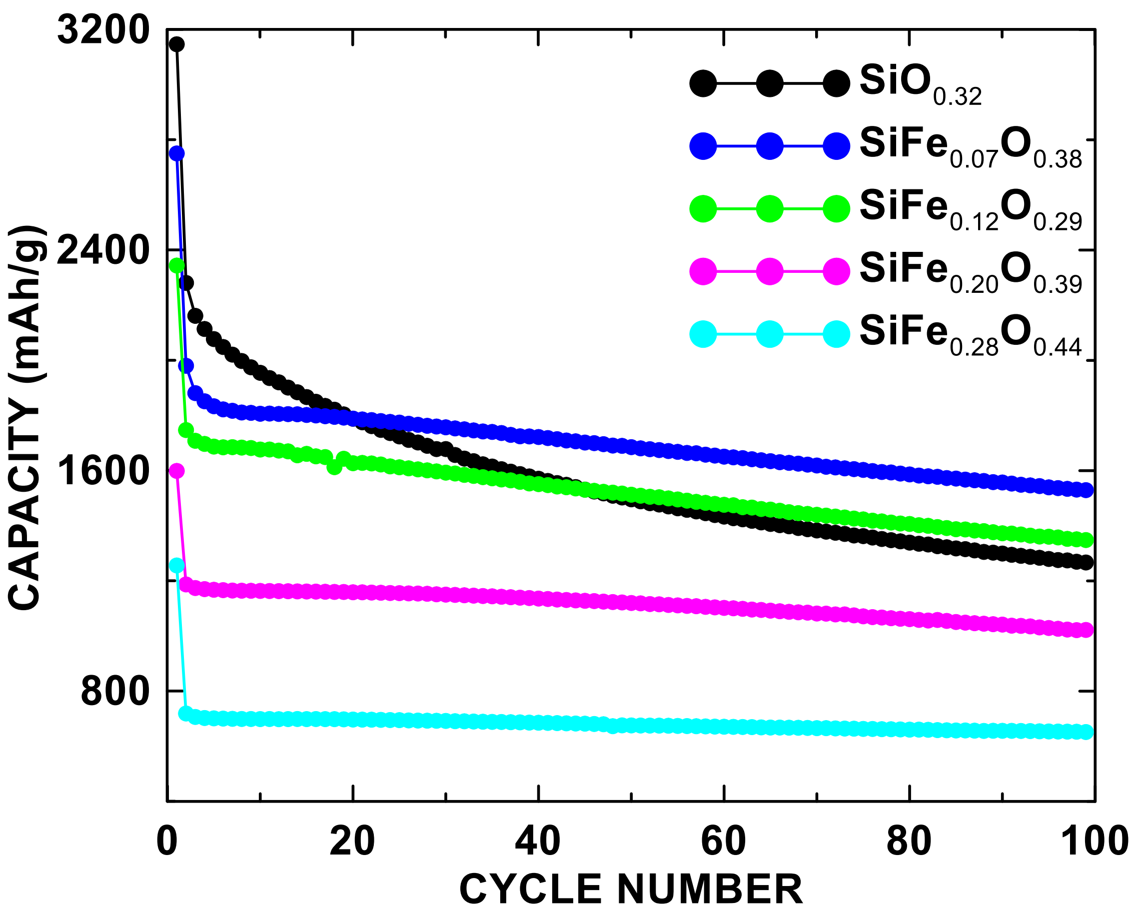

Figure 4.8 Specific capacity versus cycle number of the cells shown in Figure 4.4, different compositions are indicated in different colors.

Table 4.3 lists the volume expansion during the first lithiation, reversible volume expansion, and the theoretical and measured reversible volumetric capacities of $SiFe_xO_y$ alloys. The volume expansion during the first lithiation was calculated based on the stoichiometries in Equations 4.1 and 4.2, using the measured densities listed in Table 4.3 for the alloys prior to lithiation and assuming the density is 4.93 g/cm^3 for $FeSi_2$ [172] and 2.35 g/cm^3 for Li_4SiO_4 [173]. During subsequent cycling, volume expansion/contraction is only due to the lithiation/delithiation of the active Si phase. Therefore, the volume expansion/contraction that occurs during the first delithiation and subsequent cycling is smaller than the first lithiation volume expansion. The smaller volume expansion that occurs during cycling will be referred to here as the "reversible volume expansion." The reversible volume expansion determined from the measured second lithiation capacity is also listed in Table 4.3. Figure 4.9 shows the measured reversible volumetric capacity, the first volume expansion, and the reversible lithiation volume expansion of $SiFe_xO_y$ alloys. Both volumetric capacity and volume expansion are reduced with increasing x, as expected. The $SiFe_{0.20}O_{0.39}$ alloy has a high reversible capacity of 1600 Ah/L with a relatively low volume expansion of 132% for the first lithiation. The volume expansion of this alloy is expected to be even lower after the second lithiation process, according to the calculations in Table 4.3.

Table 4.3 Theoretical first lithiation volume expansion, reversible volumetric capacity, reversible volume expansion, and the reversible volumetric capacity of $SiFe_xO_y$ alloys. Standard errors are calculated from 3-5 replicates.

Alloy Composition	**1st Lithiation Volume Expansion (%)**	**Reversible Lithiation Volume Expansion (%)**	**Theoretical Reversible Volumetric Capacity (mAh/cm^3)**	**Reversible Volumetric Capacity (mAh/cm^3)**
$SiO_{0.32}$	213	168	2000	$(1.87 \pm 0.03) \times 10^3$
$SiFe_{0.07}O_{0.38}$	185	160	1853	$(1.83 \pm 0.03) \times 10^3$
$SiFe_{0.12}O_{0.29}$	163	154	1822	$(1.82 \pm 0.03) \times 10^3$
$SiFe_{0.20}O_{0.39}$	132	111	1552	$(1.60 \pm 0.03) \times 10^3$
$SiFe_{0.28}O_{0.44}$	91	79	1224	$(1.30 \pm 0.09) \times 10^3$

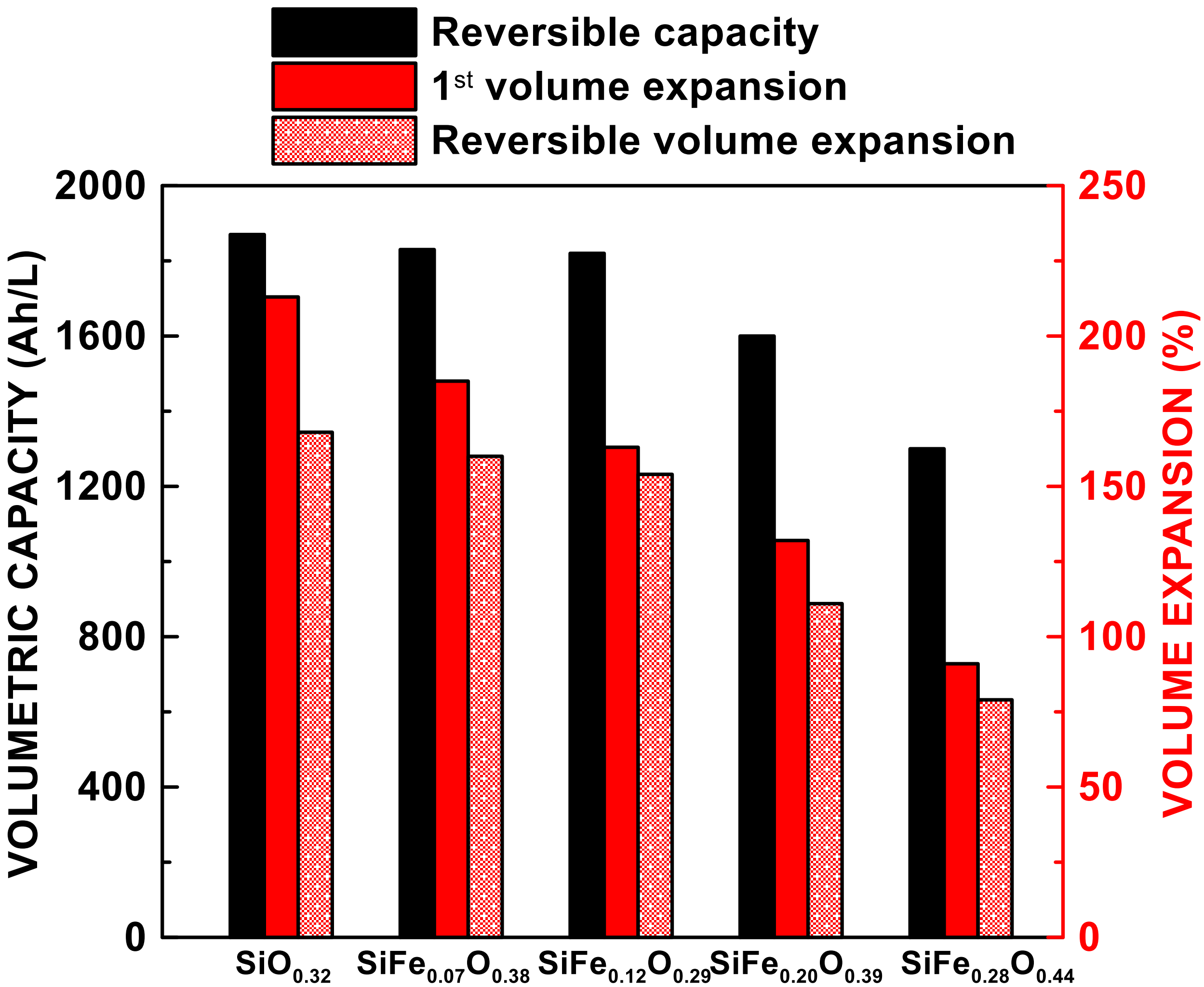

Figure 4.9 Reversible volumetric capacity and first lithiation and reversible volume expansion of $SiFe_xO_y$ alloys.

4.2.3 Cross-sectional SEM Images of Post-cycled Electrodes

Cross-sectional SEM images of cycled electrodes can provide useful information, such as SEI growth, particle fracturing, loss of contact with current collector, and binder failure. SEM image analysis can provide a quantitative measure of electrode porosity, active volume fraction, active surface area, particle size distribution, and tortuosity [174]. Combined with corresponding electrochemical performance, all this information can help interpret cell degradation mechanisms.

Figure 4.10 shows a cross-sectional SEM image of a pristine $SiFe_{0.20}O_{0.39}$ electrode. In this image, the alloy particles appear as bright regions with sharp edges, black regions indicate porosity, and dark grey regions represent conductive carbon and binder. Cross-sectional SEM images of $SiFe_xO_y$ electrodes obtained after 100 cycles are shown in Figure 4.11. There are three main features in the post-cycled electrodes: alloy particles shown as bright regions, grey regions that correspond to a mixture of nano-sized fractured alloy and SEI, and black regions corresponding to porosity. It was found that $SiFe_xO_y$ electrodes have very different morphologies after 100 cycles, depending on their composition. The SEM image of the $SiO_{0.32}$ alloy electrode after 100 cycles, shown in Figure 4.11(a), mostly comprises grey regions corresponding to SEI and fractured alloy. Very little bulk alloy (white regions) remains. This indicates that this alloy has undergone significant surface erosion (i.e. ~40 % of the alloy has been eroded) and particle fracture during cycling. However, when comparing $SiO_{0.32}$ to compositions with increasing x, shown in Figures 4.11(a) to (e), there are more bright regions and less fractured alloy/SEI regions with increasing x in $SiFe_xO_y$. In particular, $SiFe_{0.28}O_{0.44}$ alloy particles in Figure 4.11(e) still show clear margins that are almost like pristine particles, with very little alloy surface erosion and SEI formation. These images suggest that higher iron contents can benefit the structural integrity of the cycled electrodes. This is consistent with the good cycling stability of the $SiFe_{0.28}O_{0.44}$ alloy electrode shown in Figure 4.8. The improved structural integrity with increased Fe content occurs either because the addition of Fe reduces alloy fracture, the addition of Fe reduces electrolyte reactivity at the alloy surface, the addition of Fe reduces alloy volume expansion or some combination of these factors.

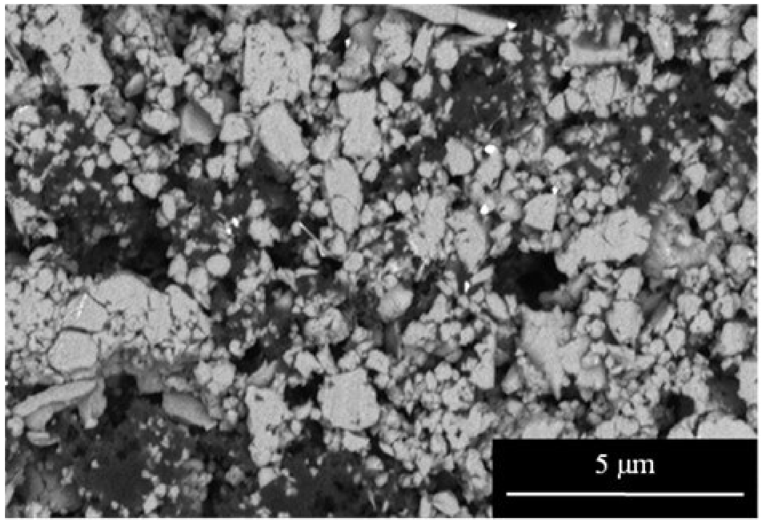

Figure 4.10 Cross-sectional SEM image of pristine electrode of $SiFe_{0.20}O_{0.39}$

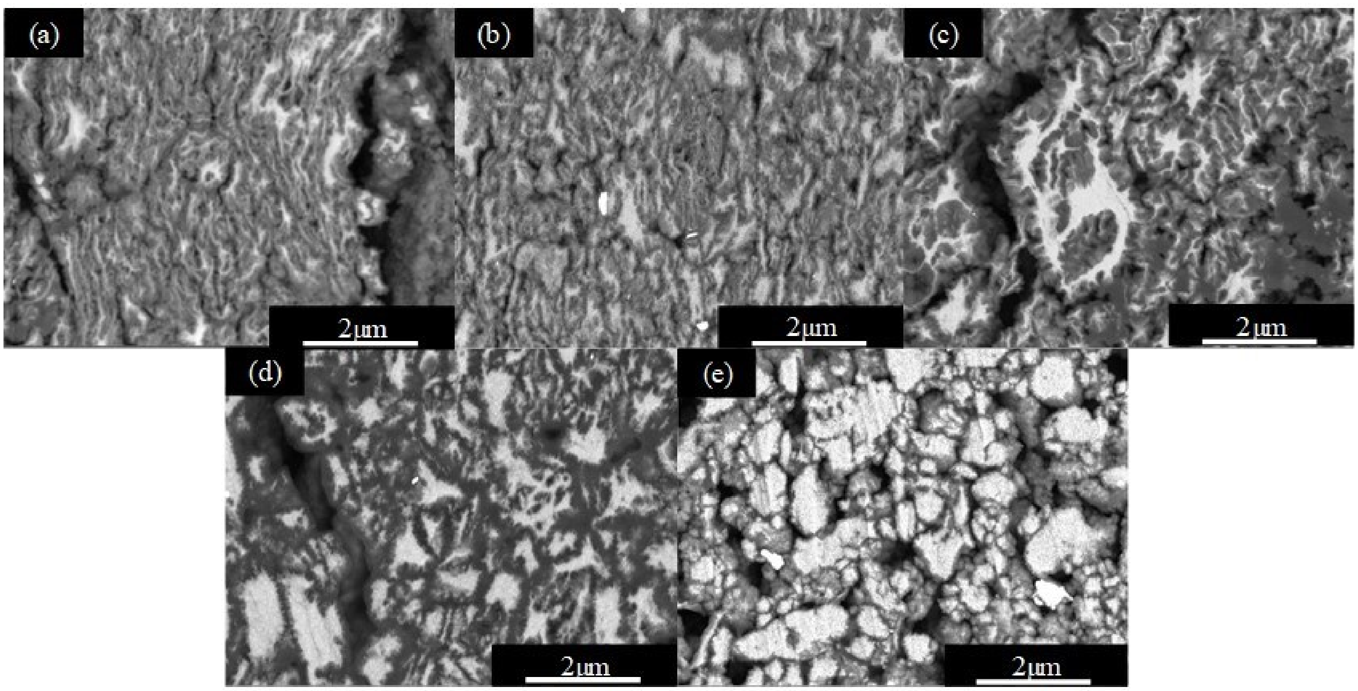

Figure 4.11 Cross-sectional SEM images of post cycled electrodes of (a) $SiO_{0.32}$ (b) $SiFe_{0.07}O_{0.38}$ (c) $SiFe_{0.12}O_{0.29}$ (d) $SiFe_{0.20}O_{0.39}$ (e) $SiFe_{0.28}O_{0.44}$.

In order to quantify differences between the $SiFe_xO_y$ electrodes after 100 cycles, the SEM images in Figure 4.11 were analyzed by ImageJ software [175]. The main goal of this analysis is to determine the area fraction of the bright alloy regions in each SEM image, which should roughly correspond to the amount of unfractured alloy in the electrode. All images were first processed to increase the image contrast, so that the processed images consisted of the white alloy fraction and the black non-alloy (i.e. porosity, fractured alloy or SEI) fraction. Then optimized threshold values were selected for each image to obtain the white alloy fraction. The reported vales are the means of 3-5 selected regions. Figure 4.12 demonstrates the evolution of alloy fractions in each cycled electrode as a function of iron content. As clearly shown in Figure 4.12, the alloy fraction in each cycled electrode increases with x in $SiFe_xO_y$, while the iron-rich composition $SiFe_{0.23}O_{0.43}$ has a significantly higher alloy fraction than other compositions. The increase in alloy fraction from $SiO_{0.32}$ to $SiFe_{0.20}O_{0.39}$ is greater than a factor of 2.5. This indicates the possibility of huge improvements in cycling stability for Fe additions to SiO compositions, which has implications for commercial battery materials. Because the $SiFe_{0.20}O_{0.39}$ alloy has a higher volumetric capacity than the $SiFe_{0.28}O_{0.44}$ alloy after 100 cycles, while the cycling performance and capacity retention are almost as good as the $SiFe_{0.28}O_{0.44}$ alloy, $SiFe_{0.20}O_{0.39}$ was selected as the standard composition for the rest of the studies in this thesis.

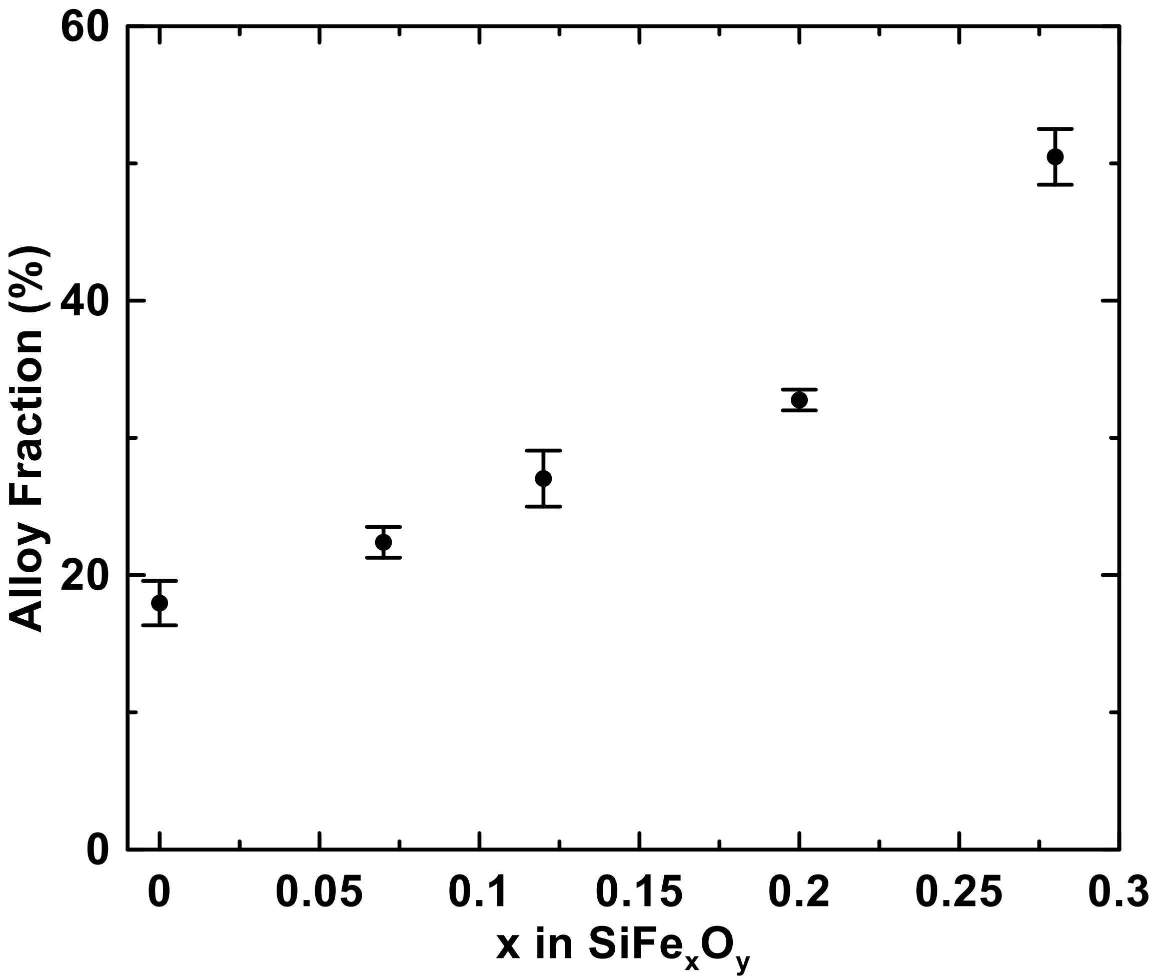

Figure 4.12 Alloy fractions of the electrodes shown in Figure 4.11 versus x in $SiFe_xO_y$ (error bars based on the standard error of five replicates).

4.2.4 $SiFe_{0.20}O_{0.39}$ thermal stability and Comparisons with alloys prepared with different starting materials

The most promising composition from the abovementioned studies, $SiFe_{0.20}O_{0.39}$, were also prepared by ball milling Si and Fe_2O_3 powders under argon atmosphere and ball milling Si, SiO_2 and Fe under argon atmosphere. Figure 4.13 shows the resulting XRD patterns of the resulting alloys. Also shown is an XRD of $SiFe_{0.20}O_{0.39}$ prepared by ball milling Si and Fe in air for comparison. The XRD patterns of the as-milled alloys prepared via different methods are almost identical, amorphous Si, some X-ray intensity from silicon oxide, α-$FeSi_2$ phase and the dominant β-$FeSi_2$ phase are present. These results are different than that obtained by Zhao et al., who prepared $Si_xFe_yO_{1-x-y}$ alloy by roller milling Si and Fe_2O_3 powders. In that case, the resulting XRD patterns were very different and the β-$FeSi_2$ phase was not present [56]. This difference may result from differences in milling impact energy between jar milling (low energy) and SPEX milling (high energy). All $SiFe_{0.20}O_{0.39}$ alloys were heated to high temperatures to investigate their thermal behavior. Corresponding XRD patterns are also shown in Figure 4.13. For the 600ºC annealed samples, no significant differences in the XRD patterns can be observed between the 600ºC annealed alloys and the unheated alloys (all differences within 2 % of noise level). In the case of the 800ºC annealed samples, slight peak sharpening was observed for the β-$FeSi_2$ phase in all alloys.

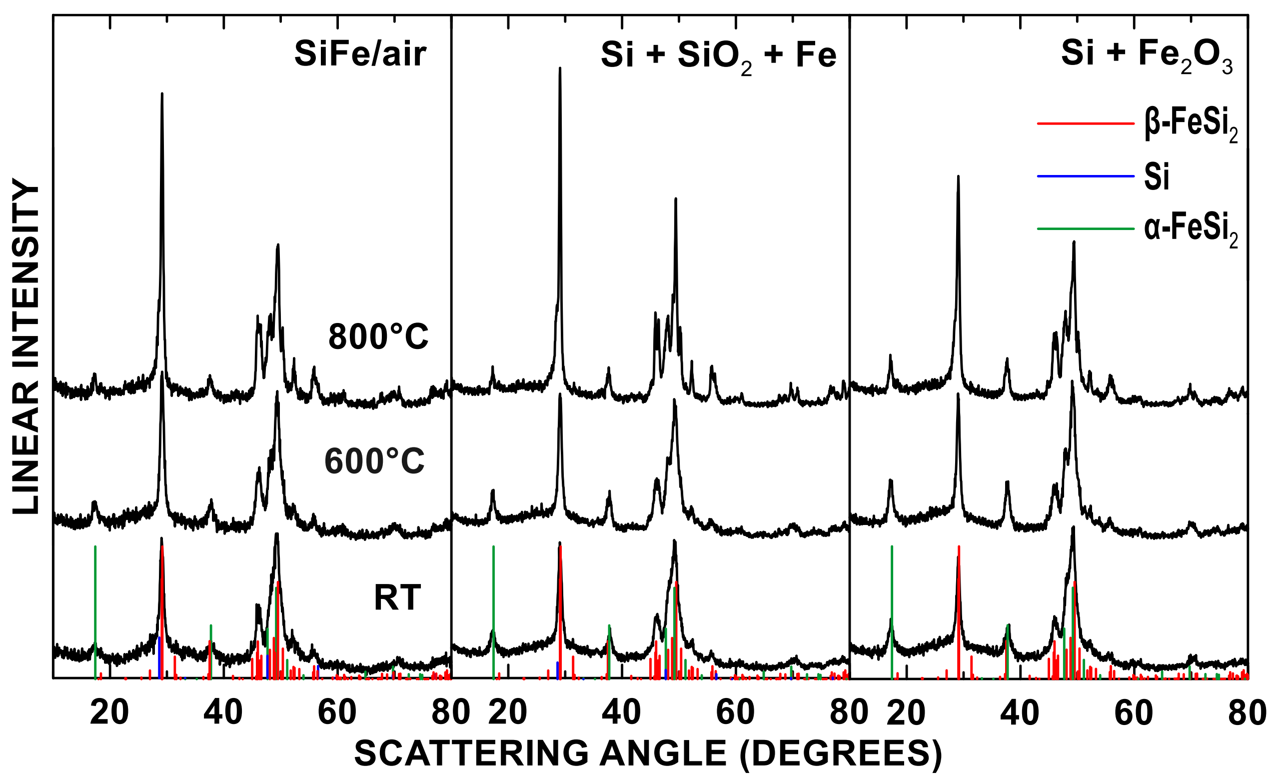

Figure 4.13 XRD patterns of $SiFe_{0.20}O_{0.39}$ alloys prepared using three different starting materials.

In Figure 4.14, XRD patterns from 25 to 35º for the 800ºC annealed alloys are compared to capture any minor differences. It can be seen from these XRD patterns that the crystallization of β-$FeSi_2$ is more pronounced at 800ºC for the alloy that was prepared by ball milling Si, SiO_2 and Fe powders. Except for this, no other significant changes can be observed in the XRD patterns (any differences within 2 % of noise level) for all alloys at all heat treatment temperatures.

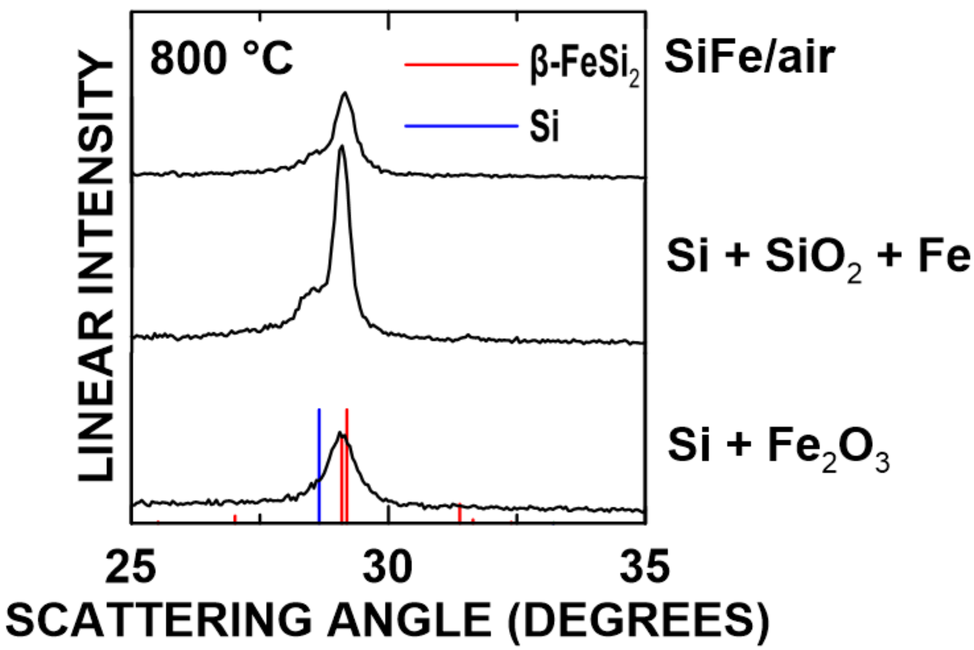

Figure 4.14 XRD patterns of 800ºC annealed $SiFe_{0.20}O_{0.39}$ alloys prepared by different starting materials in the range of 25-30º.

Alloys shown in Figure 4.13 were incorporated into Li cells to evaluate their electrochemical performance. Figure 4.15 shows their potential profiles and corresponding differential performance. All alloys prepared with the three different starting materials show very similar features: a Li-O related high potential plateau during first lithiation and this plateau shifts to a lower potential after the heat treatments; after the initial cycle, amorphous Si is the only active phase and the potential profiles are typical of a-Si electrodes; all alloys showing good $Li_{15}Si_4$ suppression, even after high temperature processing.

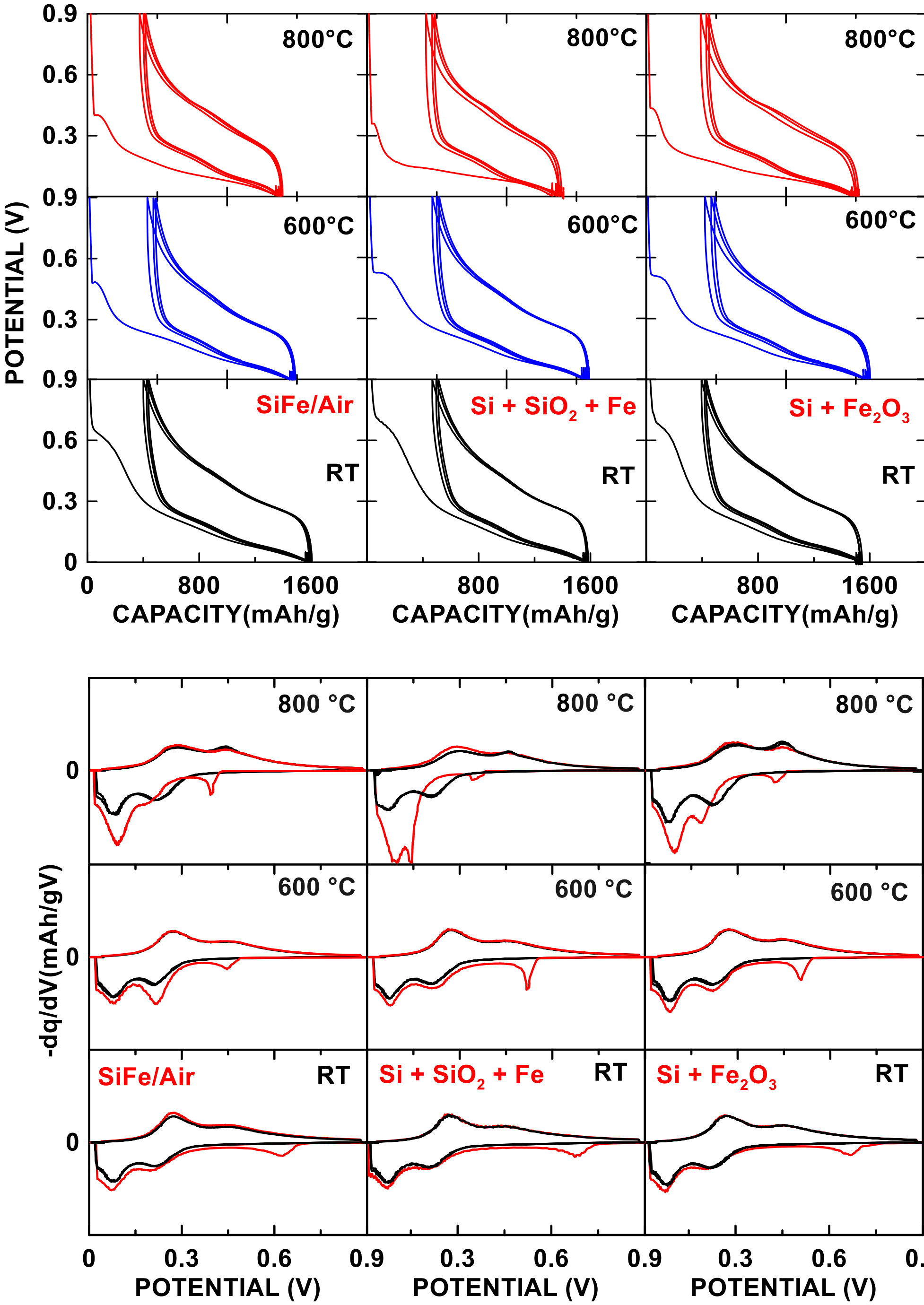

Figure 4.15 Potential and corresponding differential capacity curves (first 3 cycles) of $SiFe_{0.20}O_{0.39}$ alloys shown in Figure 4.13.

Cycling performance of the $SiFe_{0.20}O_{0.39}$ alloys prepared with different starting materials as milled and after heating is shown in Figure 4.16. The as-milled $SiFe_{0.20}O_{0.39}$ alloys prepared by the SiFe/air and $Si+Fe_2O_3$/Ar methods show very good cycling performance, with the reversible capacity almost unchanged after 50 cycles. However, the as-milled alloy prepared by the $Si+SiO_2+Fe$ method shows some capacity fade, the capacity retention after 50 cycles being about 10% lower than the other two methods Figure 4.17 shows the coulombic efficiencies of the $SiFe_{0.20}O_{0.39}$ alloys that prepared by different starting materials. The $Si+SiO_2+Fe$ method represented by red dots also show unstable CE performance, variations exist in its CE values, indicating either poor maintenance of particle electrical contact or unstable parasitic electrolyte decomposition reactions. The coulombic efficiencies for the other two methods are much more stable. Although the $Si+Fe_2O_3$ method shows good cycling and CE performance for the as-milled sample, the thermal stability is not as good as the SiFe/air method, more capacity fade was observed for both the 600ºC and 800ºC annealed samples. Severe capacity fade was also observed for the sample made with $Si+SiO_2+Fe$ precursors. In summary, the $SiFe_{0.20}O_{0.39}$ alloy prepared by the SiFe/air method has the best cycling performance and thermal stability. This makes it the best candidate to be incorporated in composite alloy particles whose synthesis requires high temperature processing.

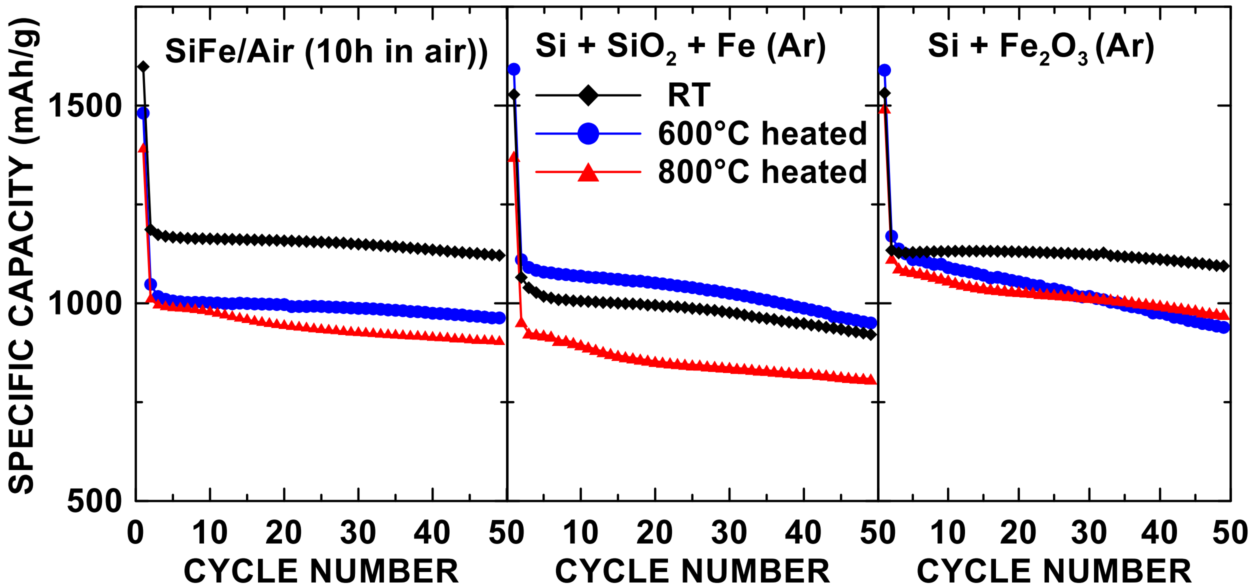

Figure 4.16 Specific capacity versus cycle number of the cells shown in Figure 4.15. Different alloy heat treatment temperatures are indicated in different colors.

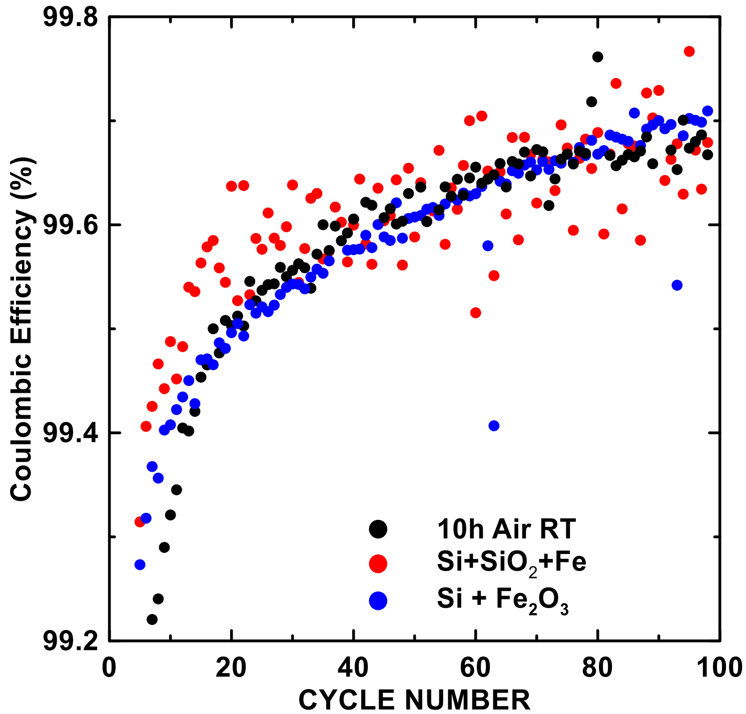

Figure 4.17 Coulombic efficiency of $SiFe_{0.20}O_{0.39}$ alloys prepared by different methods.

4.3 Conclusion

The electrochemistry of ball milled $SiFe_xO_y$ alloys was investigated as a function of iron content. It was found that increasing iron content decreases the specific capacity because of the formation of inactive iron silicide phases. However, increasing iron content helps improve cycling stability. In addition, the increased iron content helps protect electrode structural integrity during cycling. The most promising composition was then prepared by different starting materials. It was found that the air milling method has the best combination of microstructure, thermally stability, and cycling performance. This chapter provides more details about the promising composition from the Si-Fe-O alloy series and further confirms the results discussed on Chapter 3. The studies on Chapter 3 and Chapter 4 provide the most promising Si-Fe-O alloy candidate for further optimization such as carbon coating and making composite materials. The following two chapters will focus on the optimization methods to prepare Si-Fe-O alloy-based composite materials.

CHAPTER 5 PRELIMINARY INVESTIGATION OF $SiFe_{0.20}O_{0.39}/C$ COMPOSITES FOR USE IN PRACTICAL Li-ION BATTERY ANODES

5.1 Introduction

This chapter will describe a study whose goal is to take advantage of the high thermal stability of Si-Fe-O alloys in making practical carbon-coated Si-alloys. Carbon coating, as a surface modification strategy, helping stabilize the SEI layer of Si-based alloys. The introduction of C can further buffer the volume expansion and improve the electrical conductivity of Si-based alloy materials [123]. Many studies have reported that nanostructured Si/C and SiO_x/C materials demonstrate excellent electrochemical performance [16][40][176][177][178]. Carbon coating is commonly realized by methods such as CVD [84], pyrolysis [179], hydrothermal [180], and dry coating [53] [133]. It is noted that most of these methods require high-temperature processing (> 600°C). This is incompatible with most nanocrystalline Si-transition metal alloy negative electrode materials, since such alloys typically crystallize at 600°C. In contrast, as discussed in Chapter 3, ball milled Si-Fe-O alloys exhibit excellent thermal stability even after annealing to 800°C, which makes them compatible with carbon coating processing temperatures.

In addition to carbon coating, as described in Chapter 1, blending Si-based alloys with graphite to make a composite material is a very promising solution to alleviate the volume expansion issue as well as to achieve improved cycling performance. Indeed, SiO_x/graphite composites are commercially available from BTR China with capacity of 500-600 mAh/g and high capacity retention over hundreds of cycles [68]. It is also revealed that SiO_x/graphite materials are already utilized in batteries for Tesla electric vehicles [69]. Although anode capacities could be improved to 600–800 mAh g^{-1} with excellent cycling performance by making Si-based/graphite composites, the amount of active Si-based materials is normally low in order to minimize modifications to the electrolyte or other cell components in practical applications [71][180].

Another goal of this study was to evaluate the performance of Si-Fe-O alloy/graphite composite materials and explore an appropriate alloy/graphite ratio for increased energy density while maintaining good cycle life.

5.2 $SiFe_{0.20}O_{0.39}$/C(PVC) Composites

Carbon coating of $SiFe_{0.20}O_{0.39}$ alloys was attempted by blending them with PVC and heating under inert gas to produce $SiFe_{0.20}O_{0.39}$ alloy-carbon composite materials, which will be referred to here as $SiFe_{0.20}O_{0.39}$/C(PVC,T) composites, where T is the heating temperaure. The $SiFe_{0.20}O_{0.39}$ composition was chosen because of its high thermal stability, stable cycling performance and moderate volumetric capacity. Polyvinylchloride (PVC) can be carbonized in its liquid phase during heat treatment. The pyrolysis of PVC normally takes place in two steps: (1) the pyrolysis of polyvinylchloride to polyene with elimination of HCl at 200-350°C and (2) carbonization with evolution of hydrocarbons when heating at 350-550°C [181]. The pyrolysis of PVC has successfully been used for the carbon-coating of ceramic particles such as Al_2O_3, TiO_2 and MgO by mixing ceramic powders with polyvinylchloride powders and heating at 1000°C in an inert atmosphere. It was reported that the PVC pitch formed at 400–450°C can coat the target particles and that this layer will undergo further carbonization at higher temperatures (>500°C) to form carbon-coated particles. A coating with uniform and adhesive carbonaceous layers was achieved in oxide particles by this method [182].

In the present study, 0.5g of the as-milled $SiFe_{0.20}O_{0.39}$ alloy was mixed with 0.7 g PVC in a planetary mill for one hour. The powder mixture was firstly heated to 280°C in an Ar flow for 0.5 h to eliminate the HCl, the temperature was then further raised to 450°C and maintained for 0.5 hour and finally heated to a higher temperature (700, 800 and 900°C) and kept at this temperature for 3 hours to complete the carbonization process. The reaction products were identified by XRD and observed using SEM.

Figure 5.1 shows the XRD patterns of the resulting $SiFe_{0.20}O_{0.39}$/C(PVC) materials, with the XRD pattern of the as-milled $SiFe_{0.20}O_{0.39}$ alloy and $SiFe_{0.20}O_{0.39}$ alloy heated at 800°C in argon shown for comparison. In the region of 20-30º, some intensity from amorphous carbon can be observed for all $SiFe_{0.20}O_{0.39}$/C(PVC) samples. The $SiFe_{0.20}O_{0.39}$/C(PVC,700ºC) and $SiFe_{0.20}O_{0.39}$/C(PVC,800ºC) composites have very similar XRD patterns as the 800ºC heated neat $SiFe_{0.20}O_{0.39}$ alloy, which only presents slight crystallization of β-$FeSi_2$ and no crystallization of a-Si occurred as compared to the unheated $SiFe_{0.20}O_{0.39}$ alloy. In addition, some increased intensity was observed for the β-$FeSi_2$ phase while the intensity of the α- $FeSi_2$ phase decreases as the heating temperature increases. This was very obvious for $SiFe_{0.20}O_{0.39}$/C(PVC,900°C), as almost no intensity from α-$FeSi_2$ can be observed in its XRD pattern. This indicates that the high temperature α-$FeSi_2$ phase transformed into the thermally stable phase β-$FeSi_2$ phase (< 937ºC) during heating. The crystallization of a-Si occurred at this high temperature (900ºC), as is evident by a shoulder at around 28º in the XRD pattern. Because the crystallization of a-Si is normally accompanied with capacity fade, the corresponding electrochemical performance for this sample is not expected to be as good as the $SiFe_{0.20}O_{0.39}$/C(PVC,700ºC) and/or the $SiFe_{0.20}O_{0.39}$/C(PVC,800ºC) samples.

Figure 5.2 shows SEM images of $SiFe_{0.20}O_{0.39}$/C(PVC) composites. The expected morphology with a thin and uniform carbon coating on the alloy surface was not obtained by heating the alloy/PVC mixture. In Figure 5.2(a), the overall morphology of the resulting material was very similar to that of the neat $SiFe_{0.20}O_{0.39}$ alloy particles shown in Figure 3.6, while in some regions shown in Figure 5.2(b), the micron sized $SiFe_{0.20}O_{0.39}$ alloy particles appeared to be coated onto larger carbon particles (as identified by point element analysis by EDS). Therefore, instead of being uniformly coated, the prepared $SiFe_{0.20}O_{0.39}$/C(PVC) materials appear to be a composite of $SiFe_{0.20}O_{0.39}$ alloy and carbon particles, where there appears to be good mechanical contact between the two. Nevertheless, the SEM images in Figure 5.2 do not establish whether the small $SiFe_{0.20}O_{0.39}$ alloy particles are carbon coated or not. Further studies (e.g. by TEM) would be needed to confirm this.

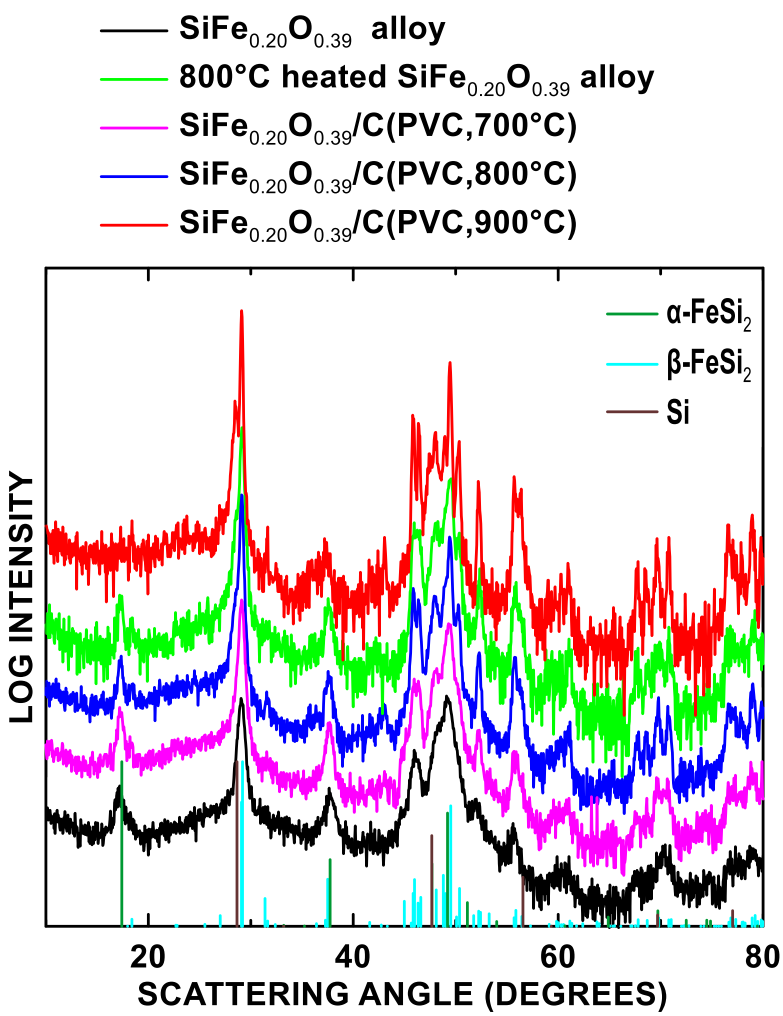

Figure 5.1 XRD patterns of the as-milled $SiFe_{0.20}O_{0.39}$ alloy, 800ºC heated $SiFe_{0.20}O_{0.39}$ alloy and $SiFe_{0.20}O_{0.39}$/C(PVC) composites.

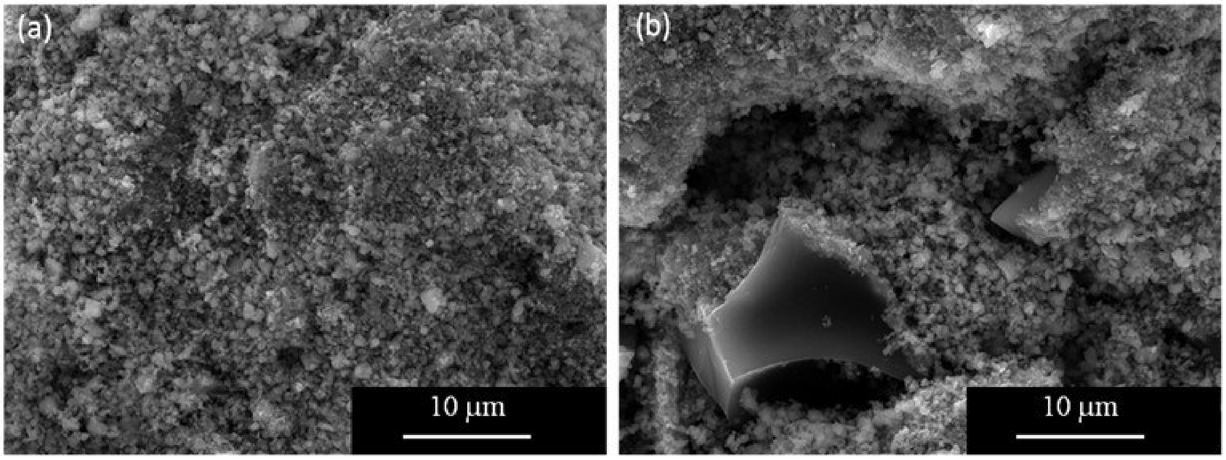

Figure 5.2 SEM images of $SiFe_{0.20}O_{0.39}$/C(PVC,800°C).

Figure 5.3 shows the differential capacity curves of $SiFe_{0.20}O_{0.39}$/C(PVC) composites, as well as those of the as-milled and 800°C heated $SiFe_{0.20}O_{0.39}$ alloys shown for comparison. It was found that the $SiFe_{0.20}O_{0.39}$ alloy is remarkably thermally stable during the $SiFe_{0.20}O_{0.39}$/C(PVC) synthesis process. There is no pronounced peak at 0.45 V in the differential capacity curve of $SiFe_{0.20}O_{0.39}$/C(PVC,700°C), even after 50 cycles, suggesting only small cr-$Li_{15}Si_4$ formation occurring. It is noted that in the differential capacity curves of the 800°C heated $SiFe_{0.20}O_{0.39}$ alloy and $SiFe_{0.20}O_{0.39}$/C(PVC,800°C), the two broad lithiation peaks shift toward higher potential after 50 cycles. The $Li_{15}Si_4$ phase is suppressed due to compressive stress from the inactive phases in the early stage of cycling. As the lithiation peaks shift to higher potential as cycling proceeds, this compressive stress towards active Si phase decreases and a peak at 0.45 V starts to form, indicating cr-$Li_{15}Si_4$ formation. This phenomenon was previously discussed in Reference [127].When the heating temperature of the $SiFe_{0.20}O_{0.39}$ alloy/PVC mixture was increased to 900°C, the resulting $SiFe_{0.20}O_{0.39}$/C(PVC,900°C) composite shows a peak at 0.45 V in its differential capacity curve even at the initial cycle, which is consistent with the observation of Si crystallization in the XRD pattern. It is likely that 700°C is a moderate treatment temperature to enable longer term cycling among the $SiFe_{0.20}O_{0.39}$ alloy/C composites, as evident by good $Li_{15}Si_4$ suppression of $SiFe_{0.20}O_{0.39}$/C(PVC,700°C) and little changes in its differential capacity curve after 50 cycles.

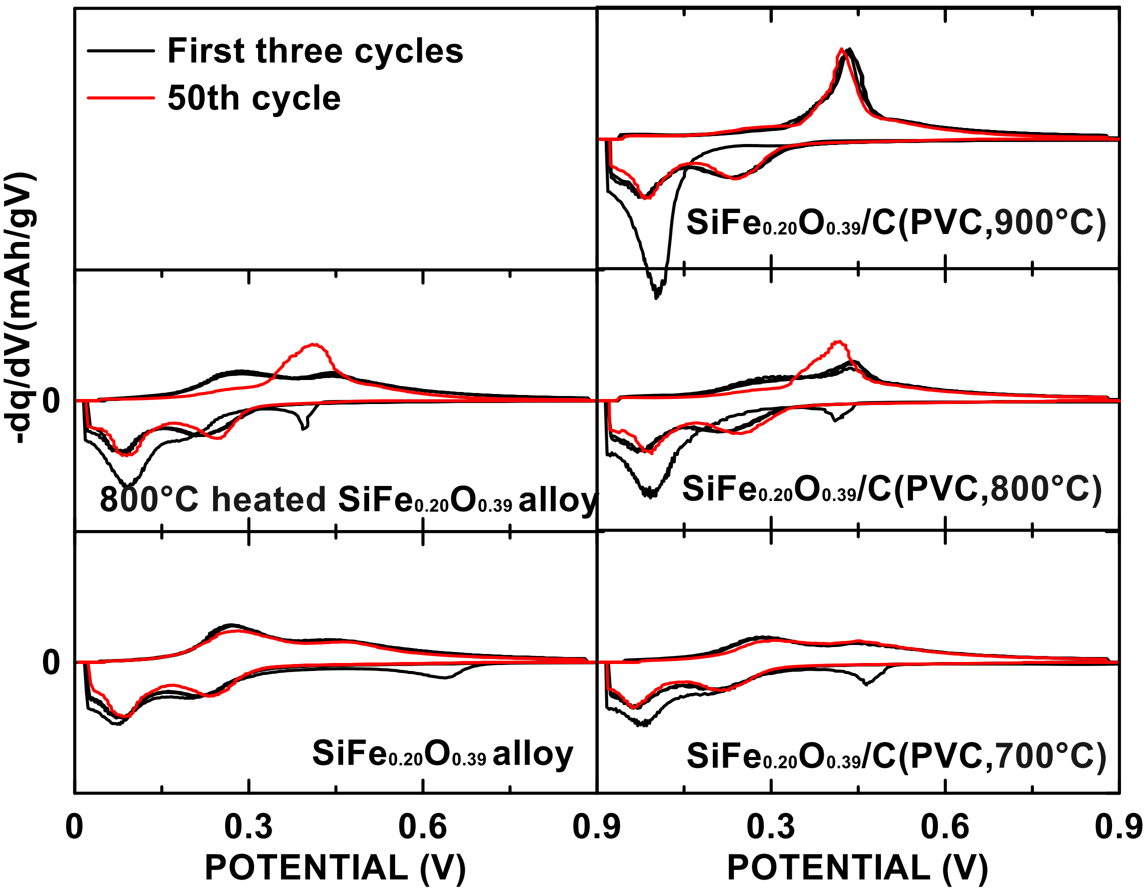

Figure 5.3 Differential curves of as-milled $SiFe_{0.20}O_{0.39}$ alloy, 800ºC heated $SiFe_{0.20}O_{0.39}$ alloy, and $SiFe_{0.20}O_{0.39}$/C(PVC) composites prepared at the indicated temperatures.

Figure 5.4(a) and (b) show the cycling performance of the as-milled $SiFe_{0.20}O_{0.39}$ alloy, the 800°C heated $SiFe_{0.20}O_{0.39}$ alloy and $SiFe_{0.20}O_{0.39}$/C(PVC) composites prepared at different temperatures. The as-milled $SiFe_{0.20}O_{0.39}$ alloy has the highest reversible capacity in Figure 5.4(a), while the 800°C heated $SiFe_{0.20}O_{0.39}$ alloy has a lower capacity. This is likely due to the disproportionation of Si-O species to Si and inactive SiO_2, isolating some of the active Si towards lithiation, as discussed in Chapter 3. While the capacity reduction in $SiFe_{0.20}O_{0.39}$/C(PVC) composites are due to the introduction of C. However, $SiFe_{0.20}O_{0.39}$/C(PVC,700°C) and

$SiFe_{0.20}O_{0.39}$/C(PVC,800°C) show improved capacity retention as compared to the 800°C heated $SiFe_{0.20}O_{0.39}$ alloy. The $SiFe_{0.20}O_{0.39}$/C(PVC,900°C) has a larger capacity fade when compared with $SiFe_{0.20}O_{0.39}$/C(PVC,700°C) and $SiFe_{0.20}O_{0.39}$/C(PVC,800°C). However, it still has higher capacity retention than the 800°C heated $SiFe_{0.20}O_{0.39}$ alloy in the assessed 50 cycles (Figure 5.4(b). In Figure 5.4(c), both $SiFe_{0.20}O_{0.39}$/C(PVC,700°C) and $SiFe_{0.20}O_{0.39}$/C(PVC,800°C) show higher CE values than the as-milled and 800°C heated $SiFe_{0.20}O_{0.39}$ alloys. Although improved cycling performance was obtained for the $SiFe_{0.20}O_{0.39}$/C(PVC,700°C) and $SiFe_{0.20}O_{0.39}$/C(PVC,800°C) materials, alternative carbon coating methods are still required to achieve the desirable thin and uniform carbon coatings.

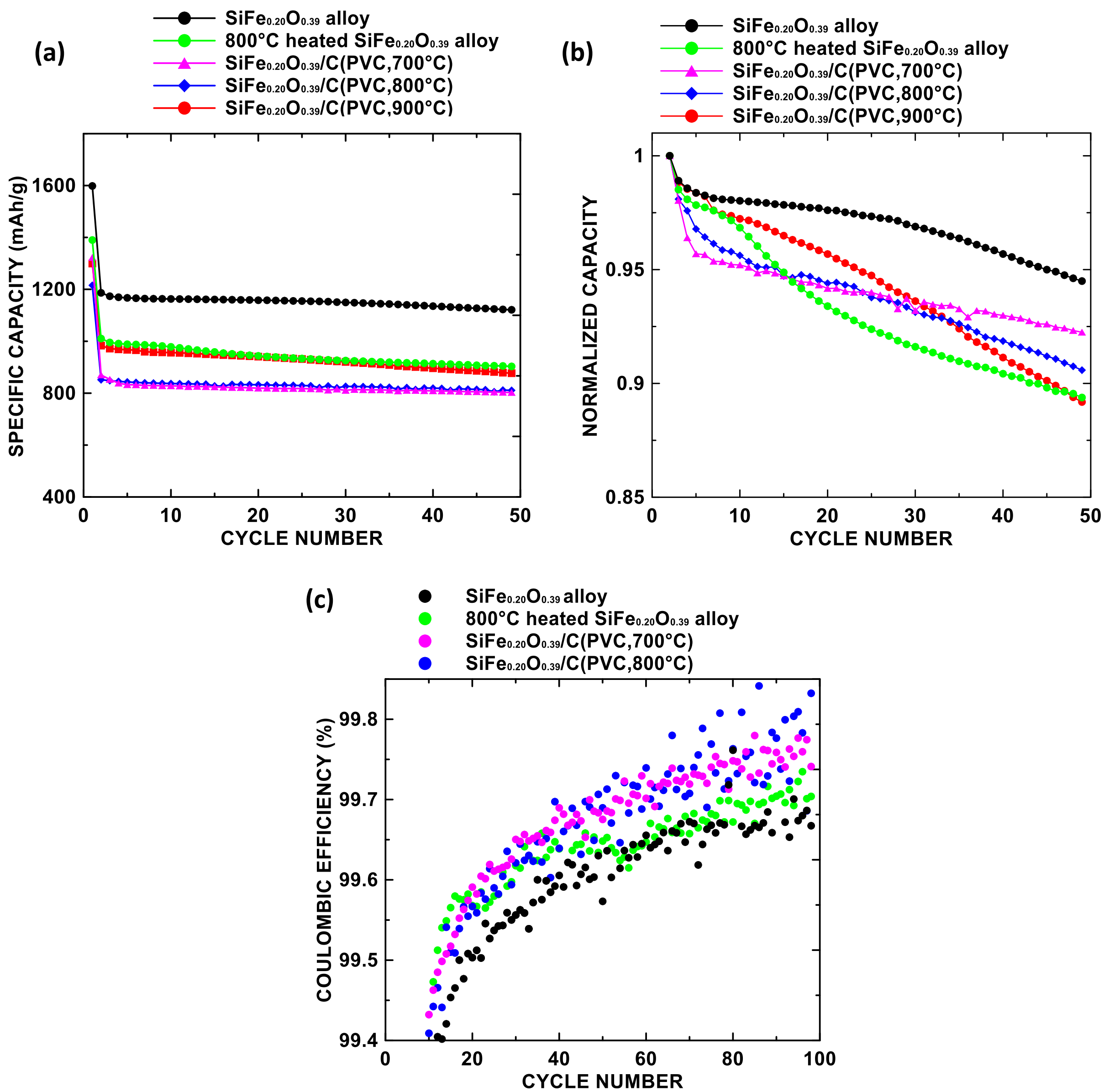

Figure 5.4 (a-b) Cycling performance and (c) coulombic efficiencies of the as-milled $SiFe_{0.20}O_{0.39}$ alloy, 800ºC heated $SiFe_{0.20}O_{0.39}$ alloy and the $SiFe_{0.20}O_{0.39}$/C(PVC) composites prepared at the indicated temperatures.

5.3 $SiFe_{0.20}O_{0.39}$/graphite Composite Particles

As a preliminary study of making $SiFe_{0.20}O_{0.39}$/graphite composite particles, as-milled $SiFe_{0.20}O_{0.39}$ alloys were mixed with graphite (SFG6L, Timcal) and phenolic resin (PR, resole phenol-formaldehyde resin, having phenol to formaldehyde ratio of 1.5–2.1/1, catalyzed with 2.5 percent potassium hydroxide, ~75% solution in water, 3M Co.) with excess N-methyl pyrrolidinone (NMP, Sigma Aldrich, anhydrous 99.5%) in planetary mill and air dried. The phenolic resin was diluted with NMP to make a 20% by weight solution before mixing with the $SiFe_{0.20}O_{0.39}$ alloys and graphite. Three composite formulations were used, which are listed in Table 5.1. Volumetric quantities were calculated based on the densities of the unheated precursors, $SiFe_{0.20}O_{0.39}$ (3.24 g/cm^3), graphite (2.26 g/cm^3) and PR (1.1 g/cm^3). The dried mixture was heated under Ar at 300°C for 3h. The 300°C annealed mixture was ground and sieved (<53 µm), annealed at 600°C for another 3 hours, and then ground and sieved (<53 µm) again. In these particles, carbonized PR acted as a binder to hold the $SiFe_{0.20}O_{0.39}$/graphite composite particles together. These $SiFe_{0.20}O_{0.39}$/graphite composites will be referred to here by their alloy/graphite/PR weight ratios prior to the heating step: e.g. as (30/59/19). In this notation (100/0/0) refers to neat $SiFe_{0.20}O_{0.39}$ alloy heated under the same conditions as the $SiFe_{0.20}O_{0.39}$/graphite composites and (0/62/23) refers to a 62/23 by weight mixture of graphite and PR also heated under the same conditions as the $SiFe_{0.20}O_{0.39}$/graphite composites.

Table 5.1 Initial compositions in weight percent of the $SiFe_{0.20}O_{0.39}$/graphite composites discussed in Section 5.4. Compositions in volume percent are given in brackets.

Composition	$SiFe_{0.20}O_{0.39}$	Graphite	PR
1	15 (9)	62 (51)	23 (40)
2	30 (19)	51 (46)	19 (35)
3	50 (36)	38 (39)	12 (25)

Figure 5.5 shows the XRD patterns of the $SiFe_{0.20}O_{0.39}$/graphite composite materials, as well as the XRD patterns of (100/0/0) and (0/62/23) for comparison. Compared to (100/0/0), some new peaks are present after making the $SiFe_{0.20}O_{0.39}$/graphite composites, which can be assigned as peaks from graphite and other unidentified impurities, presumably from the phenolic resin, since such peaks are also present in the XRD pattern of (0/62/23). No significant crystallization (any peak intensity increase greater than 10%) of both phases of $FeSi_2$ can be observed in the XRD patterns of all composite materials

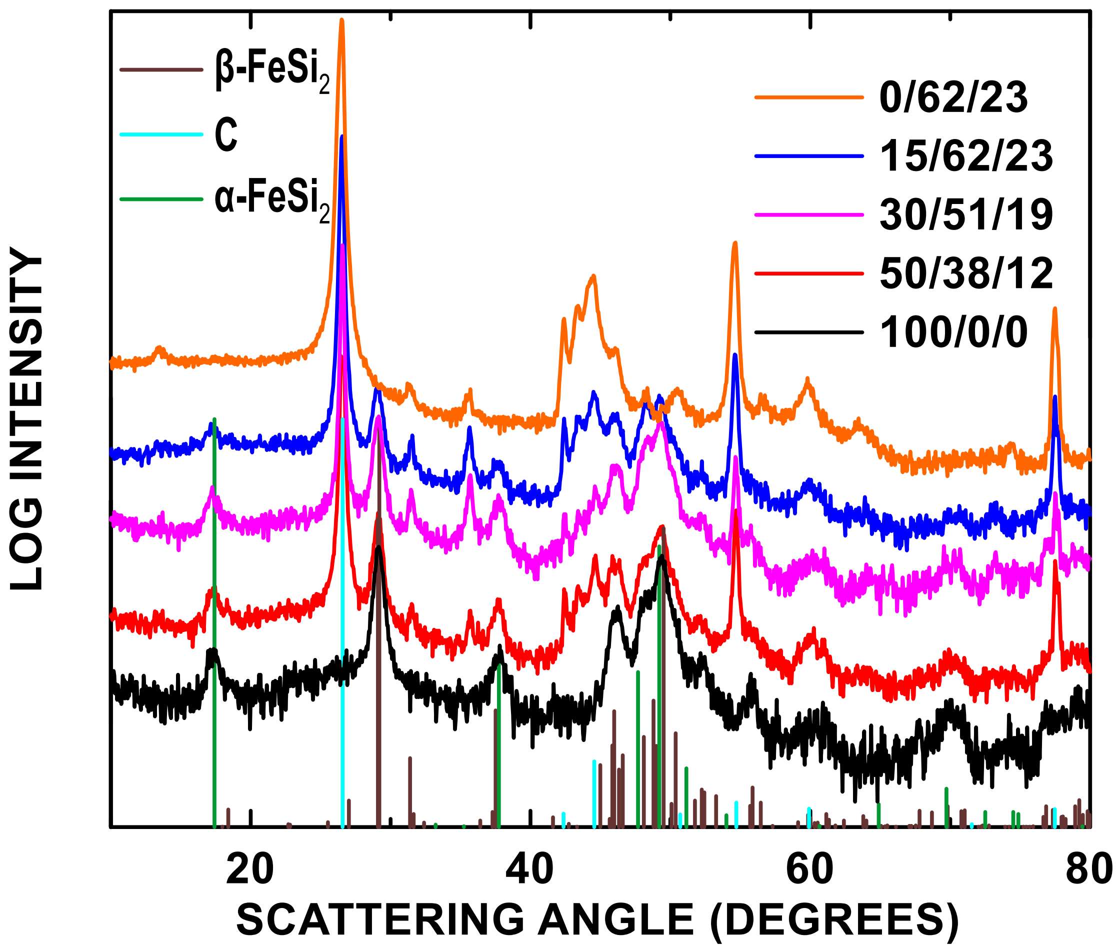

Figure 5.5 XRD patterns of $SiFe_{0.20}O_{0.39}$/graphite composite electrodes with $SiFe_{0.20}O_{0.39}$/graphite/PR weight ratios as indicated.

Figure 5.6 shows SEM images of the (15/62/23) composite. Figure 5.6(a) shows the overall morphology of the resulting composite, which consists of small aggregates of the flake graphite and alloy, where carbonized PR may act as a glue to bind the individual alloy and graphite particles. Figure 5.6 (b) and (c) show secondary electron and back-scattered electron SEM images of the same region at a higher magnification. In Figure 5.6 (b), very little $SiFe_{0.20}O_{0.39}$ alloy particles can be observed from the surface of composite particle. This could indicate that the $SiFe_{0.20}O_{0.39}$ alloy particles have been successfully embedded inside the composite aggregates. The corresponding BSE image also supports this observation, the bright alloy particles seem to have different shades in Figure 5.6 (c), indicating that they are embedded below the particle surface. For example, the isolated alloy particles are white and bright, while many of the alloy particles associated with the alloy/graphite aggregates are grey in color, due to their being embedded within the particle. Figure 5.6 (d) shows the cross-section of an (15/62/23) electrode coating. After the process of making electrode coatings, the presence of such aggregates is not obvious. Therefore, it is not known if the small aggregates shown in Figure 5.6 (a) and (b) have broken apart during electrode slurry preparation in the planetary mill. This should be determined in the future by, for example, dissolving the electrode binder in water and examining the solids by SEM.

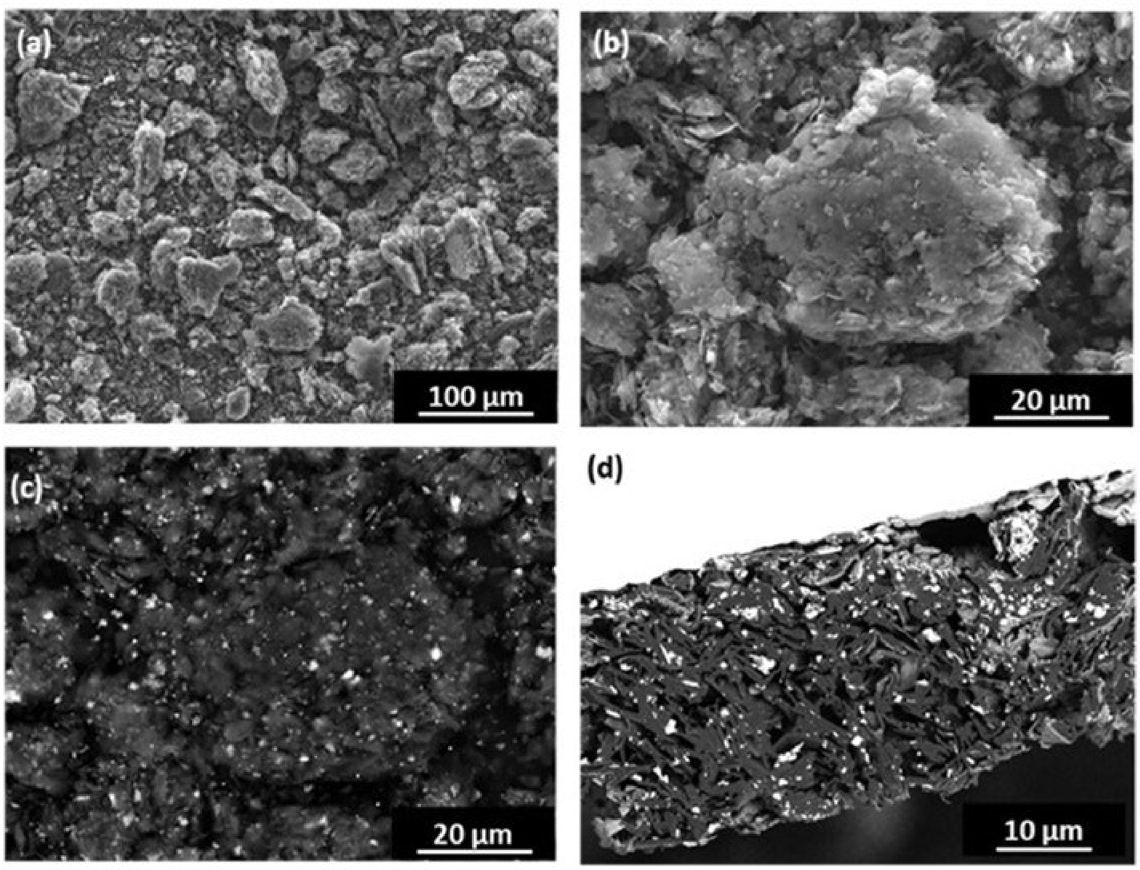

Figure 5.6 (a,b) Secondary SEM images and (c) back-scattered SEM image of the (15/62/23) composite. (d) Cross-sectional SEM image of a (15/62/23) composite electrode.

Figure 5.7 shows SEM images of (30/51/19) composite powder and a (31/51/19) electrode cross section. The overall morphology of the (31/51/19) composite is shown in Figure 5.7 (a). A wide size range of aggregates was observed for this formulation, but much of this sample comprised smaller aggregates than the (15/62/23) composite. Figure 5.7 (c)-(d) and (e)-(f) show SEM images of selected aggregates in the (31/51/19) sample. For large aggregates shown in Figure 5.7 (c)-(d), the graphite flakes were well-mixed with the $SiFe_{0.20}O_{0.39}$ alloy particles and some alloy particles were covered by the graphite flakes on the surface of the aggregates. In contrast, more alloy particles are exposed on the surface in Figure 5.7 (e)-(f). Figure 5.7 (b) shows the cross-sectional SEM image of a (30/51/19) electrode. This electrode was made by mixing the 30/51/19 $SiFe_{0.20}O_{0.39}$/graphite PR composite with carbon black and LiPAA in a volumetric ratio of 70/5/25 for 10 min using a 1" diameter Cowles blade at 5000 rpm, and then spread onto copper foil with a 0.004" coating bar. This high sheer mixing method may not disturb the aggregates during the slurry-making process. As a result, some of the $SiFe_{0.20}O_{0.39}$ alloy particles in Figure 5.7 (b) seem to be well-surrounded by the graphite under the function of PR binder. However, it is hard to tell differences between the two electrodes that are prepared with planetary mill (Figure 5.6 (d)) and high sheer mixer (Figure 5.7 (b)) in terms of the preservation of aggregates.

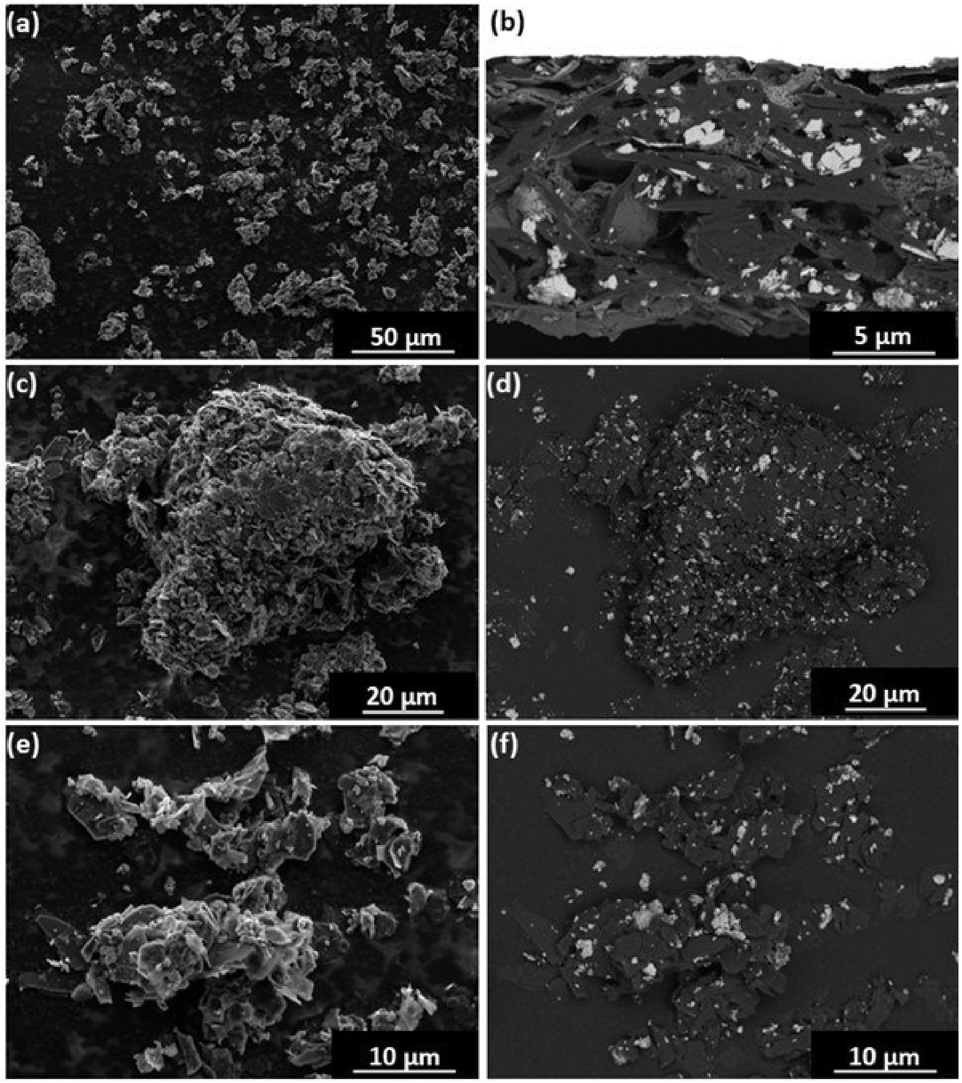

Figure 5.7 (a) SEM image of (30/51/19) composite powder. (b) Cross-sectional SEM image of a (30/51/19) composite electrode. (c)-(d) and (e)-(f) Secondary and back-scattered SEM images, respectively, of selected regions of a (30/51/19) powder sample.

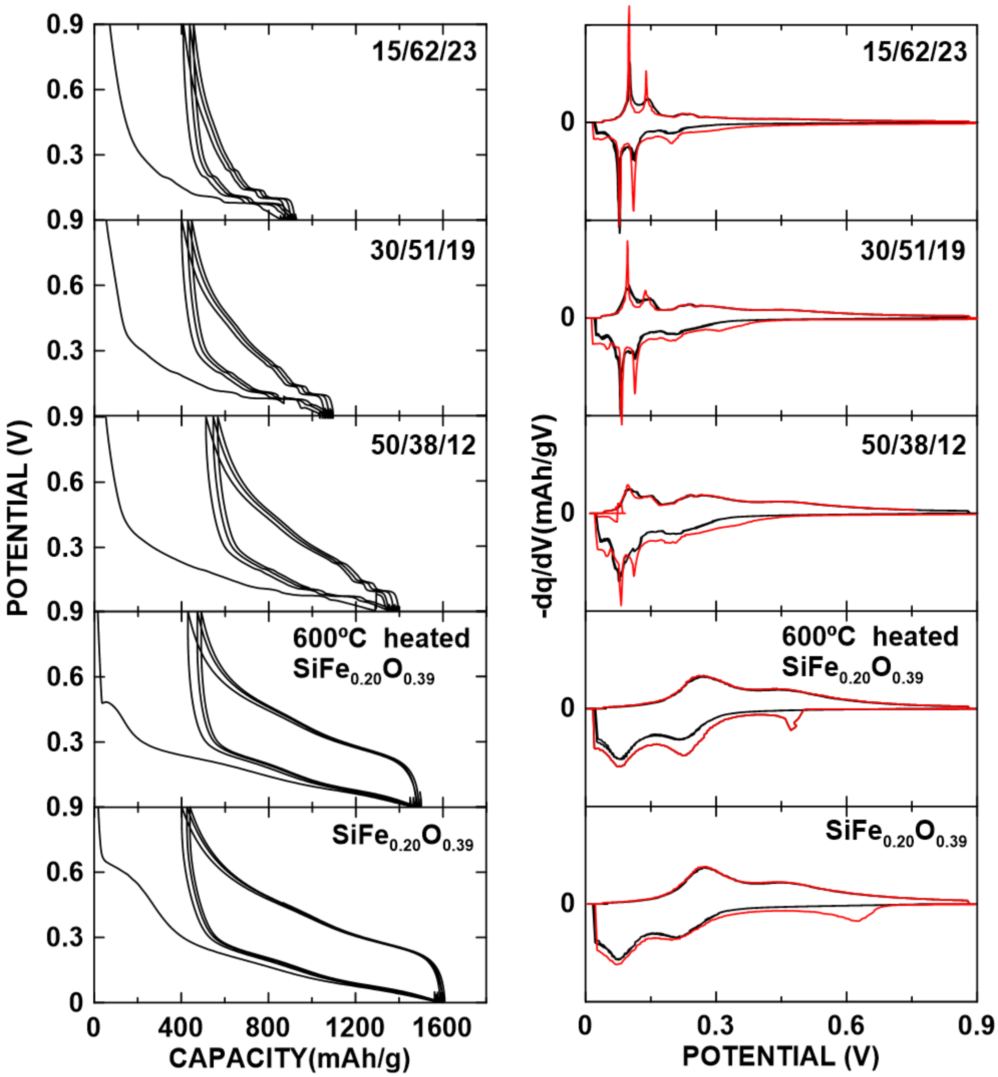

Figure 5.8 Potential profiles and corresponding differential capacity curves of $SiFe_{0.20}O_{0.39}$/graphite composite electrodes, initial cycles are shown in red in the differential capacity curves.

Figure 5.8 shows the potential profiles and the corresponding differential capacity curves of $SiFe_{20}O_{39}$ alloy/graphite/PR composites, with the electrochemical performance of the neat as-milled and 600ºC heated $SiFe_{20}O_{39}$ alloys shown for comparison. As the alloy content increases from (15/65/23) to (50/38/12), the reversible capacity increases and the potential profiles more resemble that of a pure alloy. In addition, all alloy/graphite composite materials show good $Li_{15}Si_4$ suppression even after the high temperature treatment at 600 ºC.

Figure 5.9 and 5.10 show the cycling performance in FEC containing and FEC-free electrolyte, respectively, of the three composite materials with different alloy contents, as well as the neat $SiFe_{0.20}O_{0.39}$ alloy for reference. In panel (a) of these figures the capacity vs. cycle number is shown. In panel (b) the capacity retention as a percentage of the second lithiation capacity is shown. All three composite materials show very stable cycling, with a capacity retention greater than 95% even after 100 cycles when FEC-containing electrolyte was used. In contrast, the capacity retention of the neat $SiFe_{0.20}O_{0.39}$ alloy is about 85% of its initial reversible capacity after 100 cycles. When FEC-free electrolyte is used, the neat $SiFe_{0.20}O_{0.39}$ electrode suffers from severe capacity fade after 20 cycles. In contrast, the composite materials still show very stable cycling for 100 cycles. The capacity retention of the composite electrodes only decreases from ~95% to ~85% when FEC is not used, which is impressive.

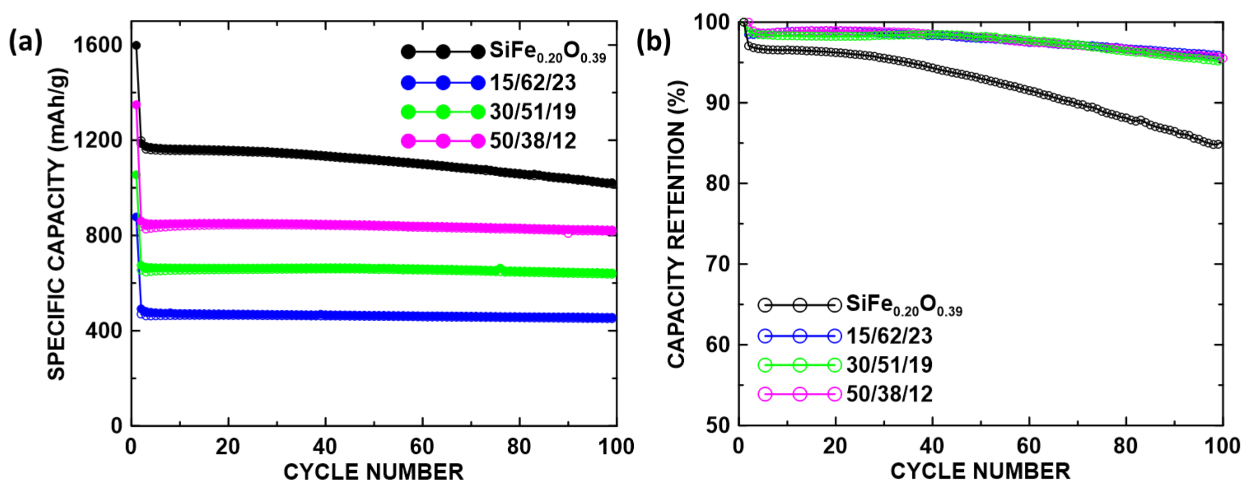

Figure 5.9 (a) Specific capacity and (b) capacity retention versus cycle number of $SiFe_{0.20}O_{0.39}$ /graphite composite electrodes cycling in 1 M $LiPF_6$ in FEC: EC: DEC=1:3:6 electrolyte.

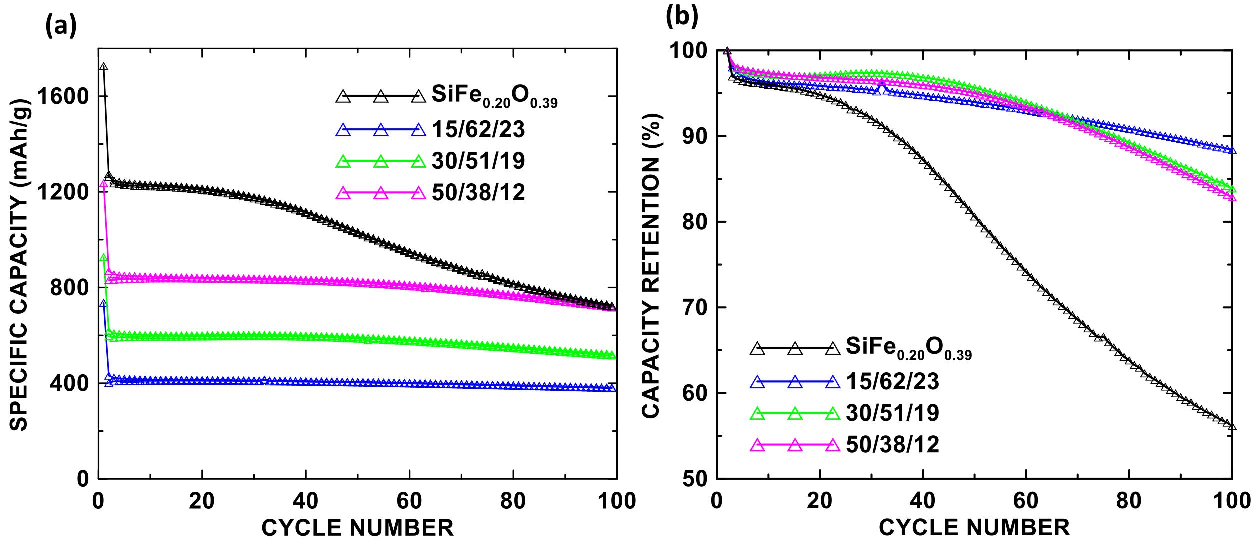

Figure 5.10 (a) Specific capacity and (b) capacity retention versus cycle number of $SiFe_{0.20}O_{0.39}$/graphite/PR composites, prepared in three alloy/graphite/PR weight ratios, as indicated in figures, with the cycling performance of neat $SiFe_{0.20}O_{0.39}$ for comparison. All electrodes were cycled in 1 M $LiPF_6$ in EC: DEC=1:2 electrolyte.

According to Figure 5.8, the delithiation of the $SiFe_{0.20}O_{0.39}$ alloy and graphite components of the $SiFe_{0.20}O_{0.39}$/graphite/PR composites occurs over different potential ranges. Above 0.18 V, graphite has no delithiation capacity, while the alloy still has considerable capacity. The amount of $SiFe_{0.20}O_{0.39}$ alloy capacity above 0.18 V was determined to be 96 % of its total capacity. Therefore, from the delithiation capacity of the $SiFe_{0.20}O_{0.39}$/graphite composites above 0.18 V, the total alloy capacity could be determined. The graphite contribution to the capacity could then be found by subtracting the alloy capacity from the total capacity. The alloy capacity as a function of cycle number was then calculated by subtracting the graphite capacity from the capacity of each cycle (i.e. it was assumed that the graphite portion of the electrode has zero fade). This allows quantitative comparison of the alloy cycling performance in the environments of being incorporated into different composites and in the environment of a conventional electrode coating.

Figure 5.11 shows the calculated capacity of $SiFe_{0.20}O_{0.39}$ alloy in different $SiFe_{0.20}O_{0.39}$ /graphite composites as a function of cycle number cycled in FEC-containing (Figure 5.11 (a)) and FEC-free (Figure 5.11 (b)) electrolytes, with the neat $SiFe_{0.20}O_{0.39}$ alloy electrode for comparison. When cycled in FEC-containing electrolyte, the $SiFe_{0.20}O_{0.39}$ alloy in all $SiFe_{0.20}O_{0.39}$ /graphite composite electrodes have very good capacity retention, with little capacity loss even after 100 cycles. This capacity retention is better than the neat $SiFe_{0.20}O_{0.39}$ alloy, which loses about 30% of its capacity in 100 cycles. When FEC-free electrolyte is used, the $SiFe_{0.20}O_{0.39}$ alloy suffers from capacity fade in all electrodes. However, the $SiFe_{0.20}O_{0.39}$ alloy in all alloy/graphite electrodes have a significantly lower fade rate than that of the neat $SiFe_{0.20}O_{0.39}$ electrode cycled in FEC-free electrolyte (i.e. all electrodes show about 20% higher capacity retention after 50 cycles than the neat $SiFe_{0.20}O_{0.39}$ electrode). Therefore, the cycling performance of the $SiFe_{0.20}O_{0.39}$ alloy is significantly improved in an alloy/graphite composite, even without the use of FEC in the electrolyte. The composite structure of the $SiFe_{0.20}O_{0.39}$ /graphite materials likely either protects the alloy from contact with electrolyte, better maintains electrical contact with the alloy, or both. However, it is noted in Figure 5.11(b) that the calculated capacity of $SiFe_{0.20}O_{0.39}$ alloy decreases as the alloy content decreases in the composite when composite electrodes were cycled in FEC-free electrolyte. This may result from the impedance growth during cycling. Although the cycling protocol was C/10 for all electrodes, alloys in in the composite such as 15/62/23 were cycled at about C/2 for this composition above 0.4 V, this may cause the reduced capacity.

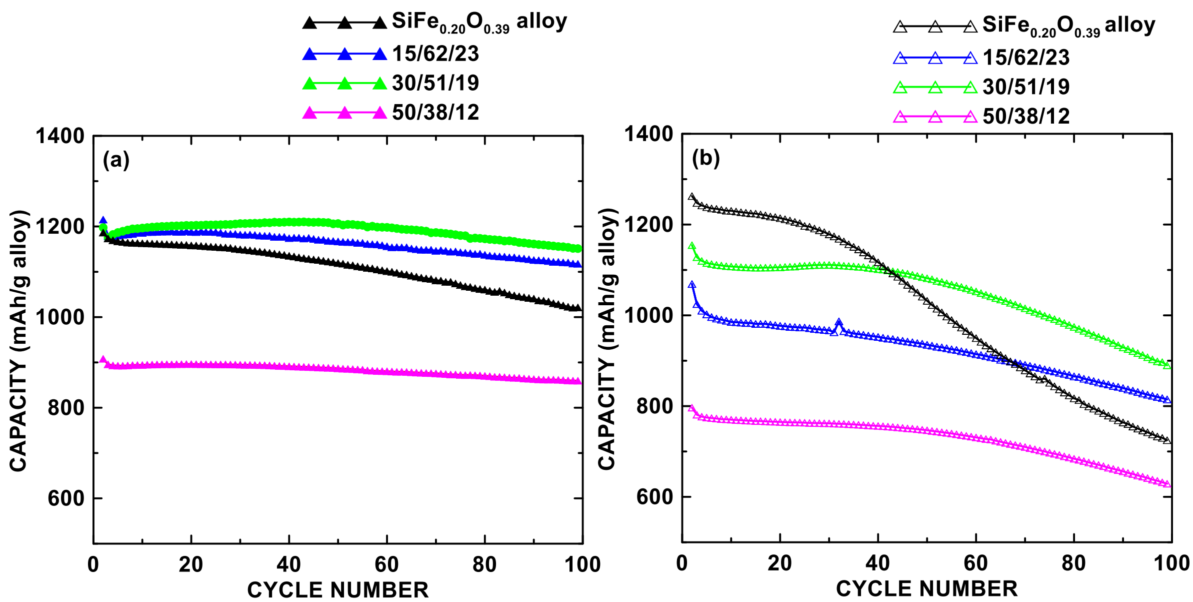

Figure 5.11 Capacity of $SiFe_{0.20}O_{0.39}$ alloy in $SiFe_{0.20}O_{0.39}$/graphite composite electrodes cycled in different electrolytes: (a) 1 M $LiPF_6$ in FEC: EC: DEC=1:3:6 electrolyte (b) 1 M $LiPF_6$ in EC: DEC=1:2 electrolyte.

Figure 5.12 shows the cross-sectional SEM images of the post-cycled electrodes of the (100/0/0) (30/51/19), and (50/38/12) electrodes after 100 cycles. The morphologies of the $SiFe_{0.20}O_{0.39}$ alloy particles are very similar in all of the electrodes, where the erosion of alloy particle surface is all about the same extent. The alloy particle in Figure 5.12 is fracturing at the surface and are surrounded by some grey areas which possibly due to electrolyte decomposition products. This may indicate that even though improved cycling stability was achieved for this method of making a composite material, this method of making composite material still cannot efficiently suppress the reaction between alloy particles and electrolyte and/or reduce alloy fracture upon repeated lithiation/delithiation. The improvement in cycling performance of the alloy in the alloy/graphite composites is likely mainly due to improved electrical contact by the graphite matrix. However, the reaction with electrolyte needs to be confirmed by compositional analysis (e.g. EDS) that can detect if any electrolyte components (e.g. P or F) are present within the cycled particles.

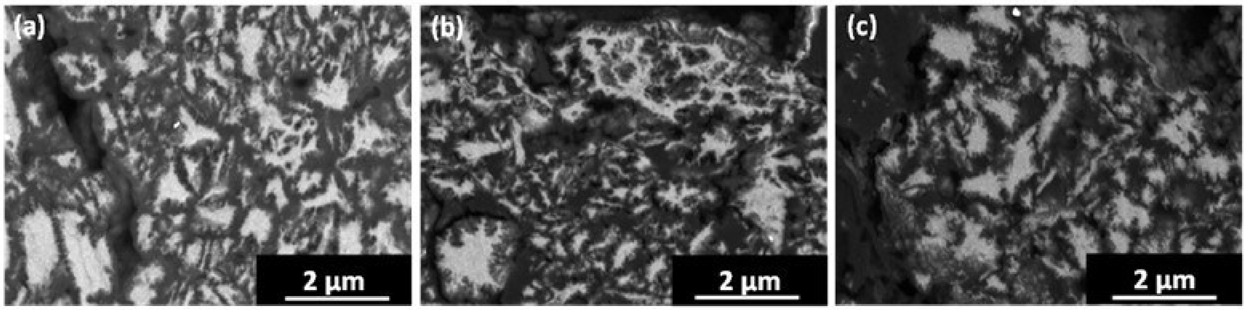

Figure 5.12 Cross sectional SEM images of (a) (100/0/0), (b) (30/51/19), and (c) (50/38/12) electrodes after 100 cycles in 1 M $LiPF_6$ in FEC: EC: DEC=1:3:6 electrolyte.

In addition, it was found that the good cycling performance of the composite materials is also associated with the choice of alloy. Figure 5.13 shows the cycling performance of alloy/graphite composite materials that were prepared using the same method and alloy/graphite/PR ratio (30/51/19 by weight), but with different alloys: the $SiFe_{0.20}O_{0.39}$ alloy, ball milled $Si_{85}Fe_{15}$ alloy and V7 alloy (a previously commercially available Si-based alloy from 3M Company). The $Si_{85}Fe_{15}$/graphite composite shows the highest reversible capacity due to the high content of active Si. However, it has a higher rate of capacity fade than the $SiFe_{0.20}O_{0.39}$/graphite composite. The V7 alloy composite has a relative low capacity, and the capacity retention is lower than the rest two composite materials in the assessed 100 cycles. Among the three composite materials, the $SiFe_{0.20}O_{0.39}$/graphite composite has the best performance in terms of capacity retention and cycling stability.

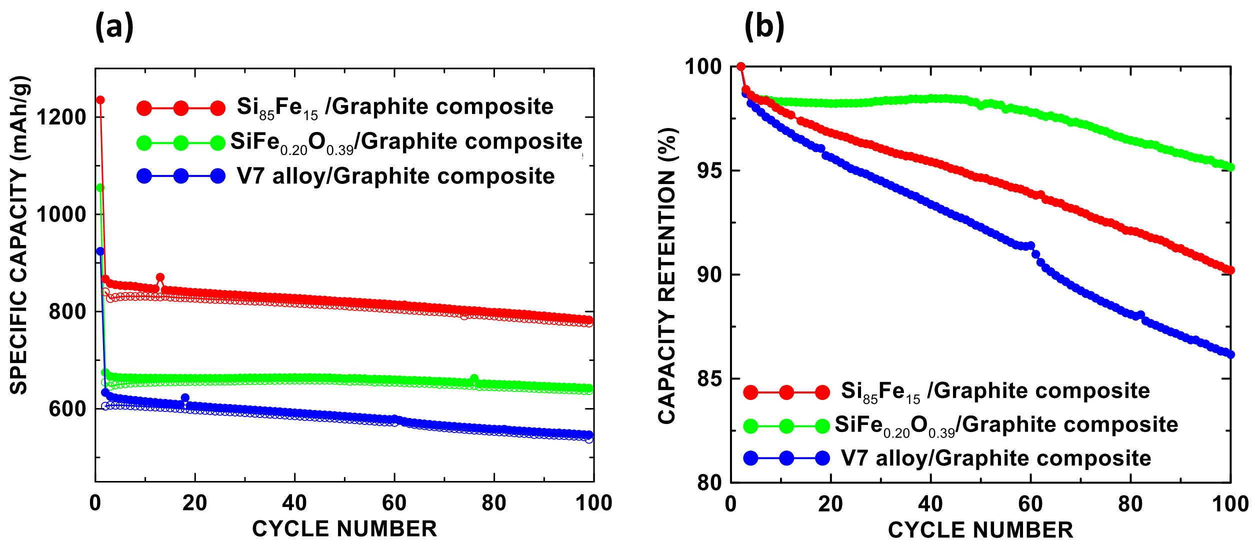

Figure 5.13 (a) Specific capacity and (b) capacity retention of initial delithiation capacity versus cycle number of different Si alloy/graphite composite electrodes cycled in FEC-containing electrolyte. Here, all alloy/graphite composites were prepared in the same formulation (30/51/19), but with different alloys ($Si_{85}Fe_{15}$ alloy, V7 alloy and $SiFe_{0.20}O_{0.39}$ alloy), as indicated.

The good performance of the $SiFe_{0.20}O_{0.39}$/graphite composite is even more significant when the composite materials were tested in FEC-free electrolyte, as shown in Figure 5.14. The $Si_{85}Fe_{15}$/graphite composite shows the highest initial reversible capacity due to its higher content of active Si. However, after 100 cycles, its capacity retention is only 67%, with a capacity lower than the $SiFe_{0.20}O_{0.39}$/graphite composite electrode. The V7 alloy/graphite composite electrode has a very close capacity to the $SiFe_{0.20}O_{0.39}$/graphite composite electrode for the first 20 cycles, but after 20 cycles, it shows an increased capacity fade. In comparison, the $SiFe_{0.20}O_{0.39}$/graphite composite electrode has good capacity retention even when no-FEC additive is present in the electrolyte.

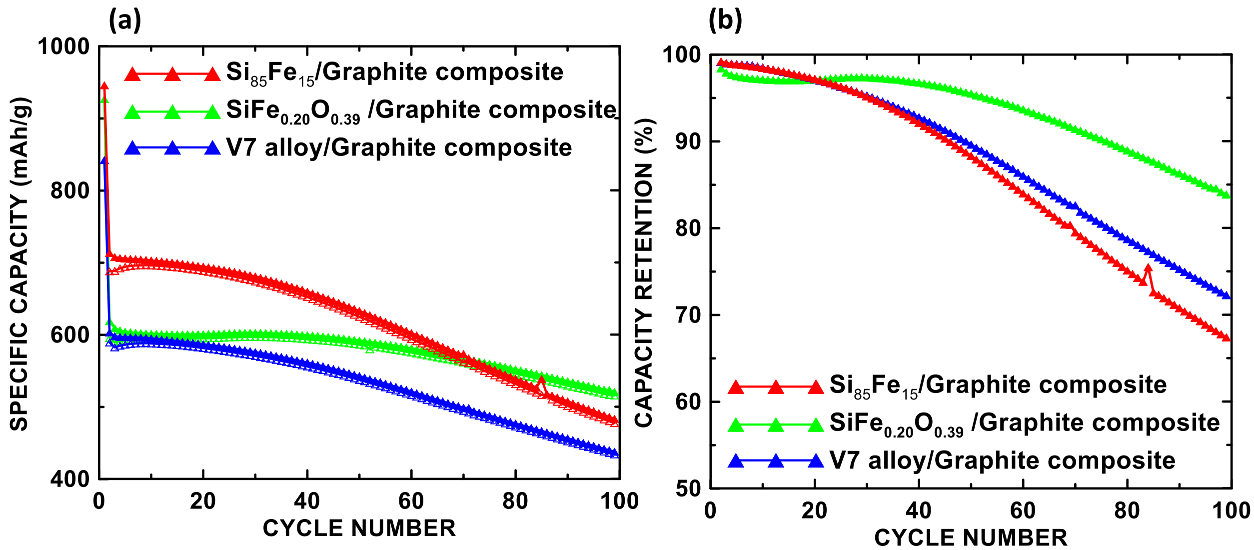

Figure 5.14 (a) Specific capacity and (b) capacity retention of initial delithiation capacity versus cycle number of different Si alloy/graphite composite electrodes cycled in FEC-free electrolyte. Here, all alloy/graphite composites were prepared in the same formulation (30/51/19), but with different alloys ($Si_{85}Fe_{15}$ alloy, V7 alloy and $SiFe_{0.20}O_{0.39}$ alloy), as indicated.

Cross-sectional SEM images of the post-cycled alloy/graphite electrodes made with different Si alloy types with the same 30/51/19 initial alloy/graphite/PR weight ratio are shown in Figure 5.15 (a-c). Severe alloy fracture is observed in the $Si_{85}Fe_{15}$/graphite composite electrode (Figure 5.15 (b)) after cycling, the total bright area associated with the alloy in this SEM image is less than the $SiFe_{0.20}O_{0.39}$/graphite composite in Figure 5.15 (a). The alloy fracture in $Si_{85}Fe_{15}$/graphite composite (Figure 5.15 (b)) can be a result of the heating process when making this composite material, as the 600ºC heating temperature will cause the crystallization of a-Si in the $Si_{85}Fe_{15}$ alloy. It is noted that $SiFe_{0.20}O_{0.39}$ alloy particles that are well-surrounded by graphite flakes tend to have better structural integrity after 100 cycles than the other $SiFe_{0.20}O_{0.39}$ alloy particles in the $SiFe_{0.20}O_{0.39}$/graphite composite electrode. The electrode morphology in the post-cycled V7 alloy/graphite composite electrode (Figure 5.15 (c)) is quite different from the $SiFe_{0.20}O_{0.39}$/graphite and $Si_{85}Fe_{15}$/graphite composite electrodes. Some large V7 alloy particles were present in the V7 alloy/graphite/PR composite electrode (Figure 5.15 (c)), the presence of larger alloy particles could reduce the capability of the PR to bind the alloy/graphite composite. Therefore, the $SiFe_{0.20}O_{0.39}$ alloy with its good thermal stability and appropriate particle size has advantages over the other two alloys in alloy/graphite composite performance.

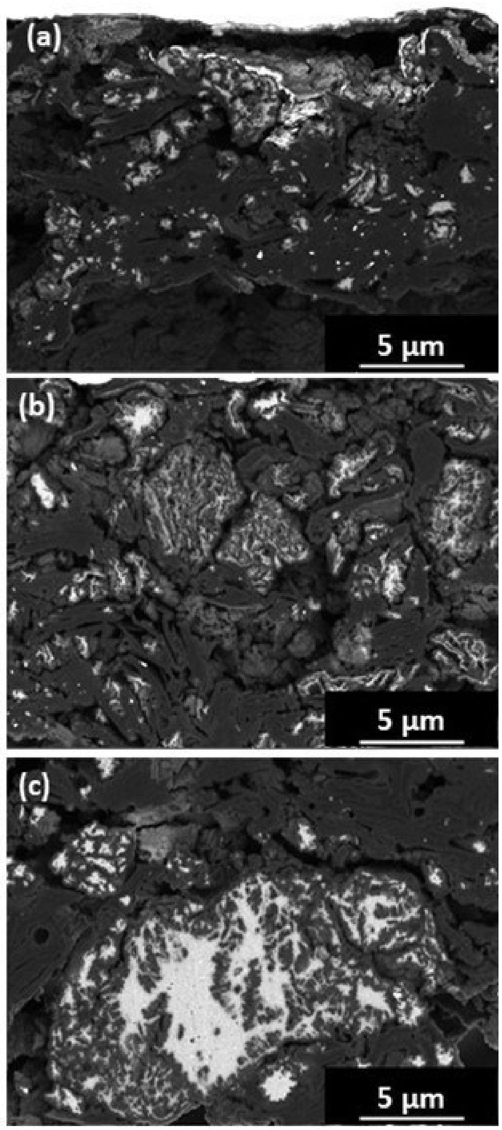

Figure 5.15 Cross-sectional SEM images of post-cycled electrodes of (a) $SiFe_{0.20}O_{0.39}$/graphite, (b) $Si_{85}Fe_{15}$/graphite, and (c) V7 alloy/graphite all having the same initial (30/51/19) formulation and cycled in FEC-containing electrolyte for 100 cycles.

A comparison study was conducted to learn if this method of making composite particles resulted in better electrode performance than just blending the alloy with a pyrolyzed graphite/PR composite. The composite materials just discussed were prepared by annealing the alloy, graphite, and phenolic resin together under Ar flow. A $SiFe_{0.20}O_{0.39}$ alloy mixture with pyrolyzed graphite/PR composite was prepared by heating separately. The resulting powders were simply mixed by hand as a final step and this final mixture will be referred to here as (50//38/12). Figure 5.16 shows SEM images of (50/38/12) and (50//38/12) electrode cross sections. No significant difference can be observed in terms of the electrode morphology. The bright alloy particles are evenly distributed in a flake graphite matrix in both electrodes.

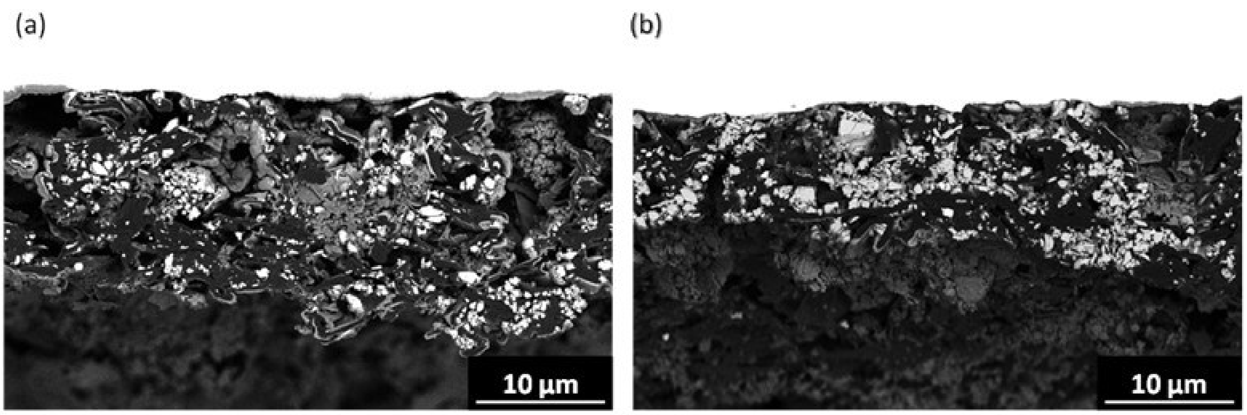

Figure 5.16 Cross-sectional SEM images of (a) (50/38/12) electrode and (b) (50//38/12) electrodes.

The (50/38/12) and (50//38/12) electrodes were incorporated in coin cells and cells were prepared with two different formulations of electrolyte (FEC-containing and FEC-free). During the first three cycles, the (50/38/12) and (50//38/12) electrodes show very similar potential profiles in both electrolyte formulations. Differences were observed between the (50/38/12) and (50//38/12) electrodes in terms of cycling performance. Figure 5.17(a) shows the specific capacity versus cycling number of the (50/38/12) and (50//38/12) electrodes, both cycled in FEC-containing and

FEC-free electrolytes. Figure 5.17(b) shows the capacity retention versus cycling number for electrodes in Figure 5.17(a). Both the (50/38/12) and (50//38/12) electrodes have a very close reversible capacity to the theoretical capacity (calculated based on the measured capacity of neat $SiFe_{0.20}O_{0.39}$ alloy and theoretical capacity of graphite). In terms of cycling stability, the composite electrode has significant advantages over the mixture electrode, both in FEC-containing and FEC-free electrolytes. For example, after 100 cycles, the mixture electrode cycled in FEC-free electrolyte can only retain ~61% of its initial reversible capacity while this value is ~83% for the composite electrode.

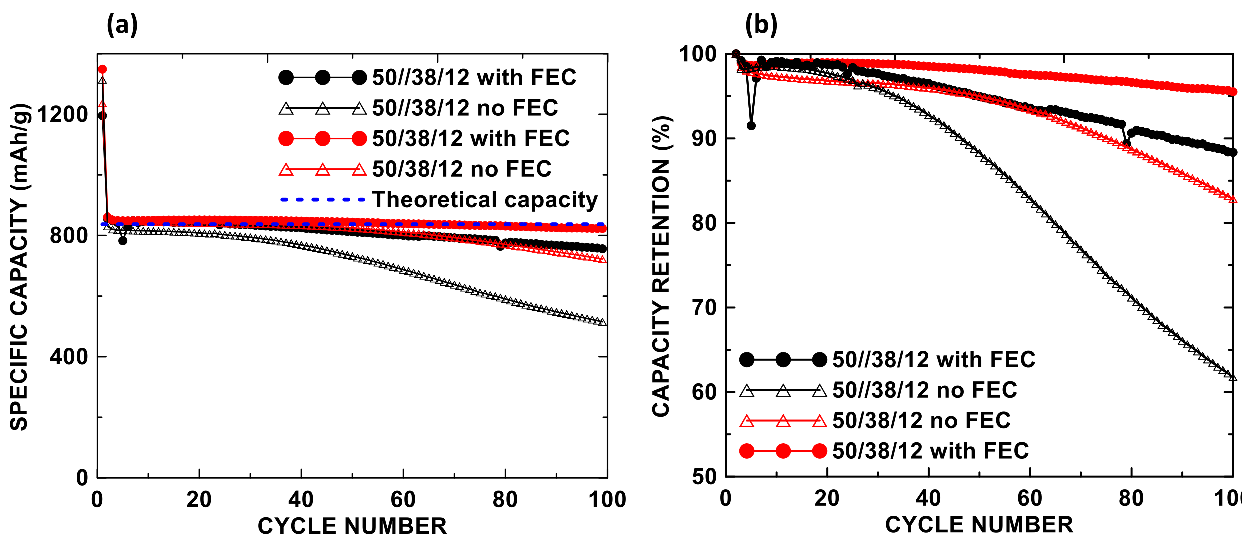

Figure 5.17 (a) Specific capacity and (b) capacity retention versus cycle number of the (50/38/12) and (50//38/12) electrodes, cycled in FEC-containing and FEC-free electrolytes.

Differences between the two electrodes can be clearly identified from the cross-sectional SEM images of the post-cycled electrodes. When FEC-containing electrolyte is used, there are no obvious differences between the two electrodes. The alloy fracturing pattern in the (50/38/12) and (50//38/12) electrodes are both very similar to that of cycled neat $SiFe_{0.20}O_{0.39}$ alloy (Figure

4.10(d)). However, when FEC is not used, most of the bulk alloy regions are still present for the (50/38/12) composite electrode, corresponding to the bright white regions in the image. In contrast, the (50//38/12) mixture electrode (Figure 5.18 (d)) only contains very small regions where bulk alloy particles still exist. The vast majority of the electrode being made up of graphite and a mixture of SEI and fractured alloy, which indicates excessive SEI formation and severe alloy fracture. This is also consistent with the severe capacity fade observed in the (50//38/12) electrode in Figure 5.17 (b). These findings show that the composite 50/38/12 material structure can inhibit alloy reactivity with the electrolyte, resulting in improved cycling performance.

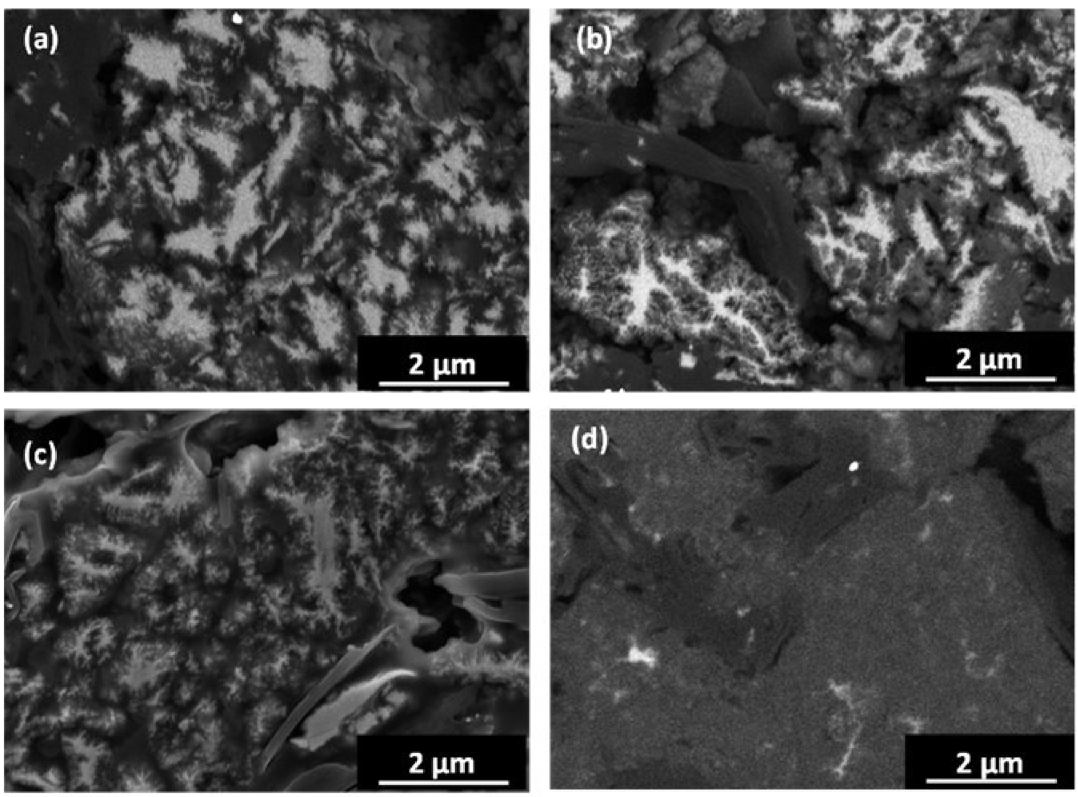

Figure 5.18 Cross-sectional SEM images of post-cycled (a) (50/38/12) and(b) (50//38/12) electrodes cycled in FEC-containing electrolyte, and (c) (50/38/12) and (d) (50//38/12) electrodes cycled in FEC-free electrolyte.

5.4 Conclusion

Taking advantage of the high thermal stability and good cycling properties of $SiFe_{0.20}O_{0.39}$ alloy, some preliminary investigations were made of $SiFe_{0.20}O_{0.39}$/C composite materials were undertaken. It was shown that the $SiFe_{0.20}O_{0.39}$ alloy can withstand high temperature processing when annealed with PVC at temperatures as high as 800ºC. The resulting $SiFe_{0.20}O_{0.39}$/C materials have improved cycling stability and this good cycling performance are maintained even in FEC-free electrolyte.

$SiFe_{0.20}O_{0.39}$/graphite composites were prepared by annealing a mixture of $SiFe_{0.20}O_{0.39}$ alloy, graphite, and phenolic resin at 600ºC. The $SiFe_{0.20}O_{0.39}$/graphite composites show excellent cycling stability, with a capacity retention above 95% over 100 cycles. The $SiFe_{0.20}O_{0.39}$/graphite composites made here also show excellent cycling performance when the electrolyte additive FEC is not used. This chapter provides some fundamental understanding in making alloy composite materials, the effect of the alloy to graphite ratio, the thermal stability of the alloy and size compatibility between the alloy and graphite on electrode performance. In addition, it was shown that the use of FEC-free electrolyte can help further differentiate the performance of electrode materials. The work in this chapter will help further optimizations of the $SiFe_{0.20}O_{0.39}$/graphite composite material towards a practical battery material, which will be discussed in Chapter 6.

CHAPTER 6 ENGINEERED $SiFe_{0.20}O_{0.39}$/GRAPHITE/C COMPOSITE MATERIALS

6.1 Introduction

Mechanofusion (MF) is a processing method in which small particles can be embedded into larger particles. Past work from the Obrovac group has shown that submicron Si can be embedded into ~10 μm spherical natural graphite particles by MF [90]. The resulting particles are then carbon coated to stop electrolyte infiltration. This results in improved alloy cycling, since the alloy is protected from exposure to the electrolyte. $SiFe_{0.20}O_{0.39}$ particles synthesized in this study are ideal for this purpose, since they have primary particle sizes of ~0.5 μm, which can be embedded into ~10 μm graphite particles without changing their morphology. In addition, as demonstrated in Chapter 5, the $SiFe_{0.20}O_{0.39}$ alloy can retain its nanostructured Si phase and good cycling characteristics even when heated to CVD processing temperatures (~800 °C). The goal of this chapter is to create $SiFe_{0.20}O_{0.39}$/graphite composite particles by mechanofusion, in which $SiFe_{0.20}O_{0.39}$ particles are embedded within graphite particles, and subsequently carbon-coating the composite particles to eliminate electrolyte/alloy interactions. The use of simple and economical methods to produce such engineered particles open doors to low-cost synthesis of Si alloy/graphite composite materials with high energy density for Li-ion batteries.

6.2 Material Preparation

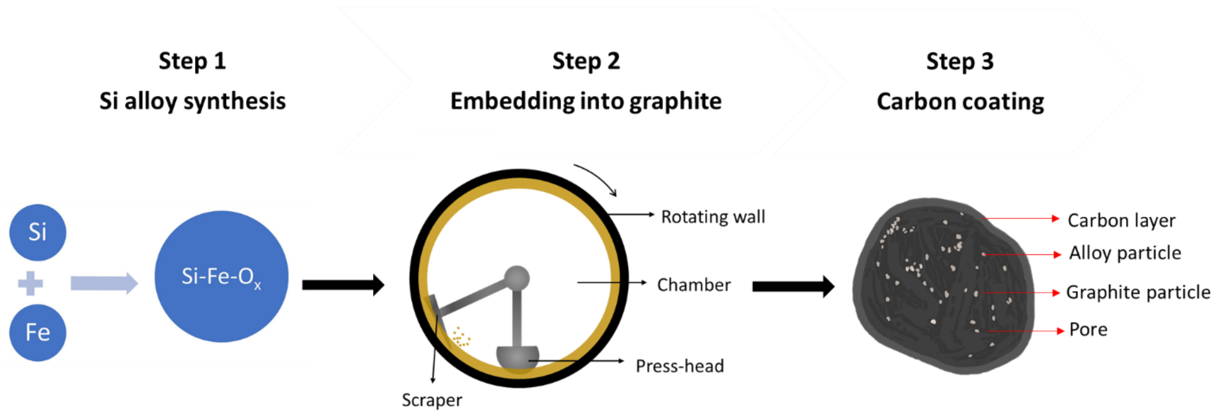

Figure 6.1 Schematic of the preparation of the $SiFe_{0.20}O_{0.39}$/graphite/C composite. The three-step involves ball milling, mechanofusion and carbon coating.

The procedure for fabrication of $SiFe_{0.20}O_{0.39}$/graphite/C composites is schematically illustrated in Figure 6.1. In the first-step, the $SiFe_{0.20}O_{0.39}$ alloy samples were prepared by the reactive gas milling method, as described in Chapter 3. The $SiFe_{0.20}O_{0.39}$ alloy was selected as the alloy material to be incorporated with spherical graphite due to its excellent thermal stability and good electrochemical performance. In the second step, the as-prepared $SiFe_{0.20}O_{0.39}$ alloy was processed in the mechanofusion machine with spherical natural graphite (A3901, Asbury Carbons). 33 g of a 1:6 by mass mixture of $SiFe_{0.20}O_{0.39}$ alloy and graphite was dry processed using a 10 cm diameter mechanofusion machine (Dry Particle Fusion Machine, DPM Solutions, Hebville NS Canada). Mechanofusion was conducted at 2500 rpm with a 1 mm press-head/wall gap to embed the alloy into the graphite particles. In the last step, CVD carbon coating was applied to the MF-processed $SiFe_{0.20}O_{0.39}$/graphite composite using ethylene as the carbon source at 800°C in a rotating fluidized bed for 1 or 2 hours, followed by 1 hour of argon flow. The resulting $SiFe_{0.20}O_{0.39}$/graphite/C composites will be referred to here by their mechanofusion processing and CVD processing times. For example, MF(1h)-$SiFe_{0.20}O_{0.39}$/SG refers to 1h mechanofusion processed $SiFe_{0.20}O_{0.39}$/spherical graphite (SG) composite and MF(1h)-$SiFe_{0.20}O_{0.39}$/SG/C(CVD,1h) means the 1h MF-processed composite particles have been subsequently CVD carbon coated for 1h.

In this chapter, electrode slurries of MF(3h)-$SiFe_{0.20}O_{0.39}$/SG and MF(1h)-$SiFe_{0.20}O_{0.39}$/SG/C(CVD,2h) were made by mixing the composite particles with carbon black (Super C65, Imery's Graphite and Carbon) and LiPAA (70/5/25 by volume) in distilled water using a 1" diameter Cowles blade at 5000 rpm for 10 min. A thin layer of slurry was coated on Cu foil (Furukawa Electric, Japan) using a 0.004" coating bar. The coating was then dried in air at 120°C for 1 hour. All other electrodes consisted of the MF-processed $SiFe_{0.20}O_{0.39}$/SG/C composites, carbon black (Super C65, Imery's Graphite and Carbon) and PVDF binder (polyvinylidene fluoride, Kynar HSV 900) (90/5/5 by weight) were made by mixing in N-methyl2-pyrrolidone (Sigma Aldrich, anhydrous 99.5%) using a 1" diameter Cowles blade at 5000 rpm for 10 min and spread onto copper foil with a 0.004" coating bar. The coatings were then dried in air for 1 hour at 120 °C. Electrodes were incorporated into 2325 type coin cells with a Li metal counter electrode. 1M $LiPF_6$ in FEC:EC:DEC (1:3:6 by volume) electrolyte was used for cells with electrodes made with LiPAA binder and 1M $LiPF_6$ in EC:DEC (3:6 by volume) electrolyte was used for cells with electrodes made with PVDF binder. Cells were cycled at 30°C, between 5 mV and 0.9 V at a rate of C/20 and signature discharged (explained in Section 2.2.7.2) to C/40 for the first cycle; and at a C/10 and signature discharged to C/20 for following cycles.

6.3 Characterization and Cycling Performance of MF-$SiFe_{0.20}O_{0.39}$/SG/C Composites

Figure 6.2 shows SEM images of MF(1h)-$SiFe_{0.20}O_{0.39}$/SG and MF(3h)-$SiFe_{0.20}O_{0.39}$/SG composite powders and their electrode cross sections. Figure 6.2 (a) shows the overall morphology of the MF(1h)-$SiFe_{0.20}O_{0.39}$/SG composite powder. This sample appears to be a simple mixture of alloy (bright particles) and graphite (dark particles). Not many alloy particles are embedded inside of the graphite particles, as shown in its cross-sectional SEM image (Figure 6.2 (b)). After 3 hours of mechanofusion, less alloy particles are observed (Figure 6.2 (c)) and most of the observed alloy particles are adhered on or embedded in the graphite particle surfaces. In addition, when the MF processing time is increased to 3 hours, more alloy is embedded inside of the graphite particles and more alloy particles are found embedded within graphite particles in the cross section of MF(3h)-$SiFe_{0.20}O_{0.39}$/SG electrode (Figure 6.2(d)) than that of the MF(1h)-$SiFe_{0.20}O_{0.39}$/SG electrode (Figure 6.2(b)).

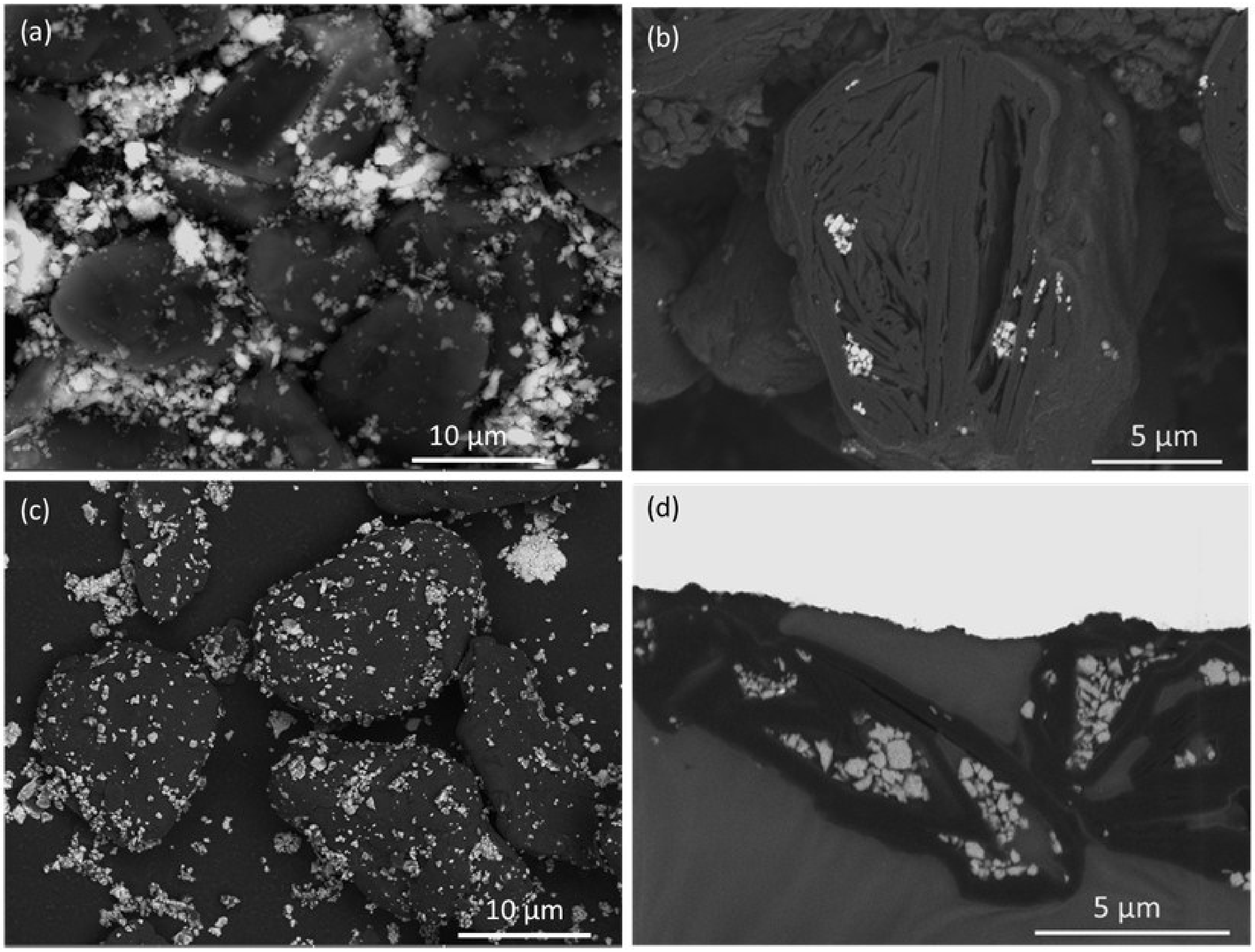

Figure 6.2 (a) SEM image of MF(1h)-$SiFe_{0.20}O_{0.39}$/SG composite powder;(b) cross-sectional SEM image of MF(1h)-$SiFe_{0.20}O_{0.39}$/SG composite electrode (c) SEM image of MF(3h)-$SiFe_{0.20}O_{0.39}$/SG composite powder (d) cross-sectional SEM image of MF(3h)-$SiFe_{0.20}O_{0.39}$/SG composite electrode.

Different CVD processing hours (1 and 2 hours) were used to apply a carbon coating layer to the MF(3h)-$SiFe_{0.20}O_{0.39}$/SG composites to investigate the effect of carbon coating on the performance of MF-$SiFe_{0.20}O_{0.39}$/SG composites. Figure 6.3(a) and (b) show an overview image and a cross-sectional image of the MF(3h)-$SiFe_{0.20}O_{0.39}$/SG composite before carbon coating. The graphite surface is smooth, with the exception of some $SiFe_{0.20}O_{0.39}$ alloy particles that are not embedded into the graphite particles. After 1h carbon coating of these composite particles, many carbon fibers appear on the graphite surface (Figure 6.3 (c)). Carbon fibers are also present in the inner voids of the graphite according to the electrode cross sectional SEM image shown in Figure 6.3 (d). The formation of carbon fibers is not desirable because it will increase the surface area of the composite particle, causing excessive electrolyte reaction. In addition, the fibers likely wouldn't efficiently protect the embedded alloy particles from electrolyte penetration. It is suspected that the $SiFe_{0.20}O_{0.39}$ alloy particles may catalyze the formation of carbon fibers during CVD. However, when the carbon coating time is increased to 2 hours, much fewer carbon fibers were formed both on the inner voids and outside graphite surface, as shown in Figure 6.3(e). Figure 6.3(f) shows a cross-sectional SEM image of the MF(3h)-$SiFe_{0.20}O_{0.39}$/SG(CVD,2h) composite electrode. Almost no carbon fibers were formed inside of the graphite particles. Also in this figure, a thin layer of grey color was found on some of the graphite particles, this could be considered as the CVD-deposited carbon layer, because the amorphous carbon layer obtained here has less electron density than graphite. However, it is also possible that this grey layer was caused by the redeposition of material itself when preparing the electrode cross section. More investigations of the optimal CVD carbon coating conditions are required to obtain a more homogeneous and dense carbon coating layer on the MF-$SiFe_{0.20}O_{0.39}$/SG composite particles that efficiently isolates the embedded alloy particles from electrolyte and binder.

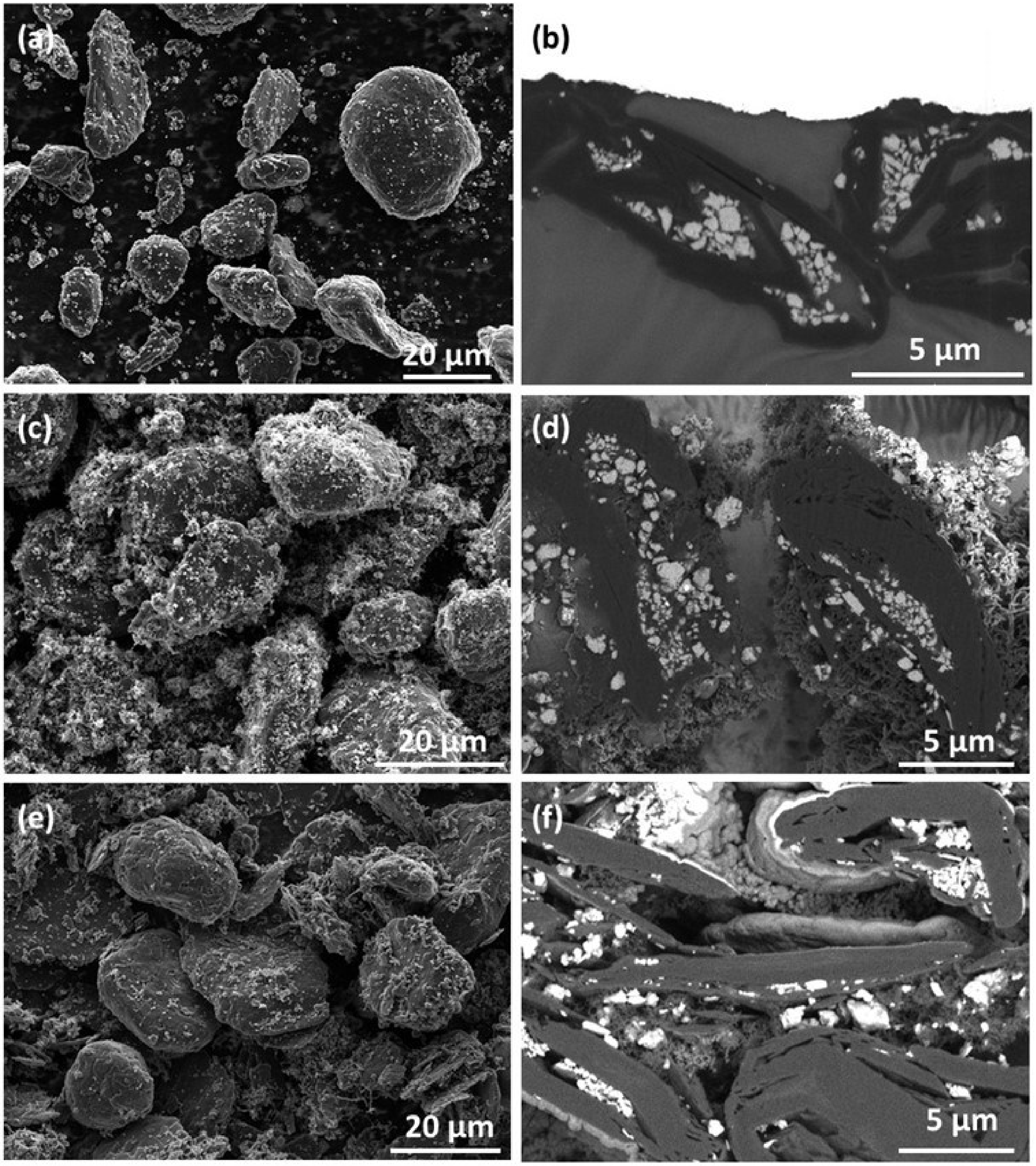

Figure 6.3(a) SEM image of MF(3h)-$SiFe_{0.20}O_{0.39}$/SG composite (b) cross-sectional SEM image of MF(3h)-$SiFe_{0.20}O_{0.39}$/SG electrode. (c) and (d) SEM image and cross-sectional SEM image of MF(3h)-$SiFe_{0.20}O_{0.39}$/SG /C(CVD,1h) composite electrode, (e) and (f) SEM image and cross section SEM image of MF(3h)-$SiFe_{0.20}O_{0.39}$/SG(CVD,2h) composite electrode.

Figure 6.4 compares the cycling performance of the uncoated and CVD carbon coated MF(3h)-$SiFe_{0.20}O_{0.39}$/SG composites in electrodes with PVDF binder and cycled in FEC-free electrolyte. The cycling performance of uncoated MF(3h)-$SiFe_{0.20}O_{0.39}$/SG in an electrode with LiPAA binder and cycled in FEC-containing electrolyte is shown for comparison. Before CVD carbon coating, the electrode of MF(3h)-$SiFe_{0.20}O_{0.39}$/SG composite cycles well with LiPAA binder in a FEC-containing electrolyte, its reversible capacity is nearly unchanged in the assessed 100 cycles. However, when conventional PVDF binder is used, the uncoated MF(3h)-$SiFe_{0.20}O_{0.39}$/SG composite shows a capacity fade. It has a fast capacity fade during the first 10 cycles and continues to fade at a slower fade rate up to the 100th cycle. This is not surprising, since Si-based alloys are known to have extremely poor cycling performance with PVDF binder and FEC-free electrolyte. In addition, the first lithiation capacity of the PVDF electrode is about 100 mAh/g higher than the LiPAA electrode. This extra capacity is likely due to the formation of excessive SEI on exposed alloy surfaces. In contrast, the MF(3h)-$SiFe_{0.20}O_{0.39}$/SG/C(CVD,1h) composite electrode does not show a severe initial capacity fade during the first 20 cycles when cycled with the same binder (PVDF) and electrolyte (FEC-free), however, after 40 cycles, it fades at a similar rate as the uncoated MF(3h)-$SiFe_{0.20}O_{0.39}$/SG electrode. The MF(3h)-$SiFe_{0.20}O_{0.39}$/SG/C(CVD,2h) composite electrode shows remarkably good cycling in PVDF binder and FEC-free electrolyte. The cycling performance is almost identical to the MF(3h)-$SiFe_{0.20}O_{0.39}$/SG electrode cycled with advanced LiPAA binder and FEC electrolyte additive. This implies that this carbon coating layer deposited via CVD can sufficiently improve the cycling performance of the $SiFe_{0.20}O_{0.39}$/graphite composite and enable the use of the common binder and electrolyte system of graphite. Such a drop-in solution to increase battery energy density without requiring any changes to binder or electrolyte formulation is highly desirable for battery manufacturers.

In order to observe the fracturing pattern of $SiFe_{0.20}O_{0.39}$ alloy in the MF-$SiFe_{0.20}O_{0.39}$/SG and MF-$SiFe_{0.20}O_{0.39}$/SG/C(CVD) composite particles, cross-sectional SEM images of post-cycled MF(3h)-$SiFe_{0.20}O_{0.39}$/SG and MF(3h)-$SiFe_{0.20}O_{0.39}$/SG/C(CVD) electrodes were obtained and are shown in Figure 6.5. Figure 6.5(a) and (b) show cross sectional images of the MF(3h)-$SiFe_{0.20}O_{0.39}$/SG electrode made with LiPAA and cycled in FEC-containing electrolyte. All alloy surfaces show signs of fracture/reaction with electrolyte. This fracturing pattern is very similar to that of cycled neat $SiFe_{0.20}O_{0.39}$ alloy (Figure 4.10(d)). However, when this electrode is cycled with PVDF binder and FEC-free electrolyte (Figure 6.5 (c) and (d)), some alloy surfaces are eroded, while many alloy particles appear to be pristine. This is likely due to alloy particles becoming electrically disconnected in early cycles. This helps explain this electrode's cycling performance, shown in Figure 6.4, where the early capacity fade is likely due to electrical disconnection of alloy particles (the ones which appear pristine in Figure 6.5(c) and (d)), while other alloy particles maintain connected, but react with electrolyte, resulting in subsequent linear fade (these alloy particles appear to have eroded surfaces in Figure 6.5(c) and (d)).

Figure 6.5(g) and (h) show cross-sectional SEM images of MF(3h)-$SiFe_{0.20}O_{0.39}$/SG/C(CVD,1h) cycled with PVDF and FEC-free electrolyte. In these images, the embedded $SiFe_{0.20}O_{0.39}$ alloy particles also show severe fracture, where alloy particles in Figure 6.5(f) have been eroded into many small pieces. A similar alloy fracturing pattern was also observed in the MF(3h)-$SiFe_{0.20}O_{0.39}$/SG/C(CVD,2h) electrode (Figure 6.5 (g) and (h)). It is difficult to discern from these images if the existence of the CVD carbon coating helps avoid electrolyte infiltration, as intended. This needs to be confirmed by some experimental technique such as EDS, which can detect if any electrolyte components (e.g. P or F) are present within the cycled particles.

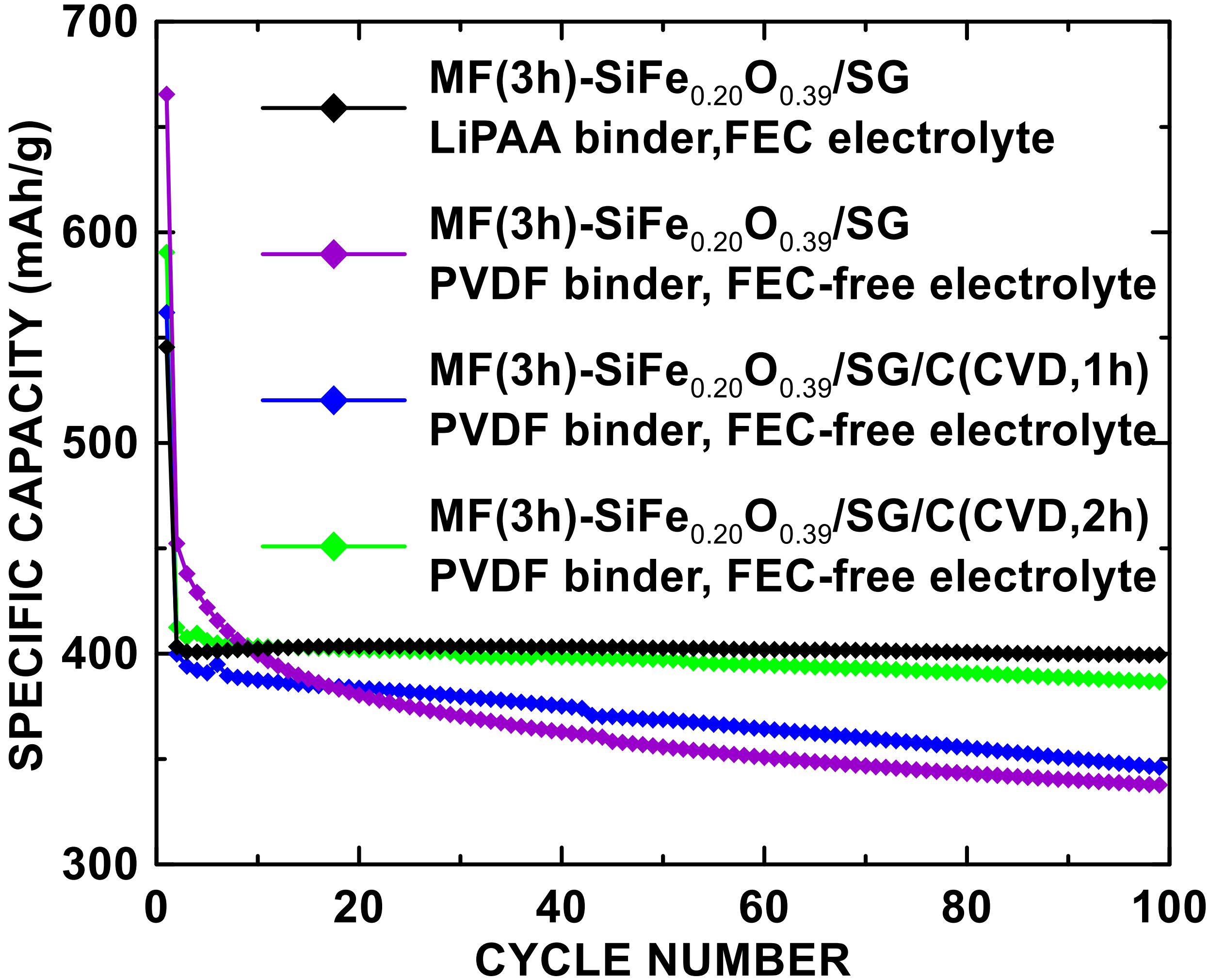

Figure 6.4 Specific capacity versus cycle number of MF(3h)-$SiFe_{0.20}O_{0.39}$/graphite composite electrode made with LiPAA binder, MF(3h)-$SiFe_{0.20}O_{0.39}$/graphite composite electrode made with PVDF binder, MF(3h)-$SiFe_{0.20}O_{0.39}$/graphite/C(CVD,1h) composite electrode made with PVDF binder and MF(3h)-$SiFe_{0.20}O_{0.39}$/graphite/C(CVD,2h) composite electrode made with PVDF binder. FEC and FEC-free electrolyte was used as indicated.

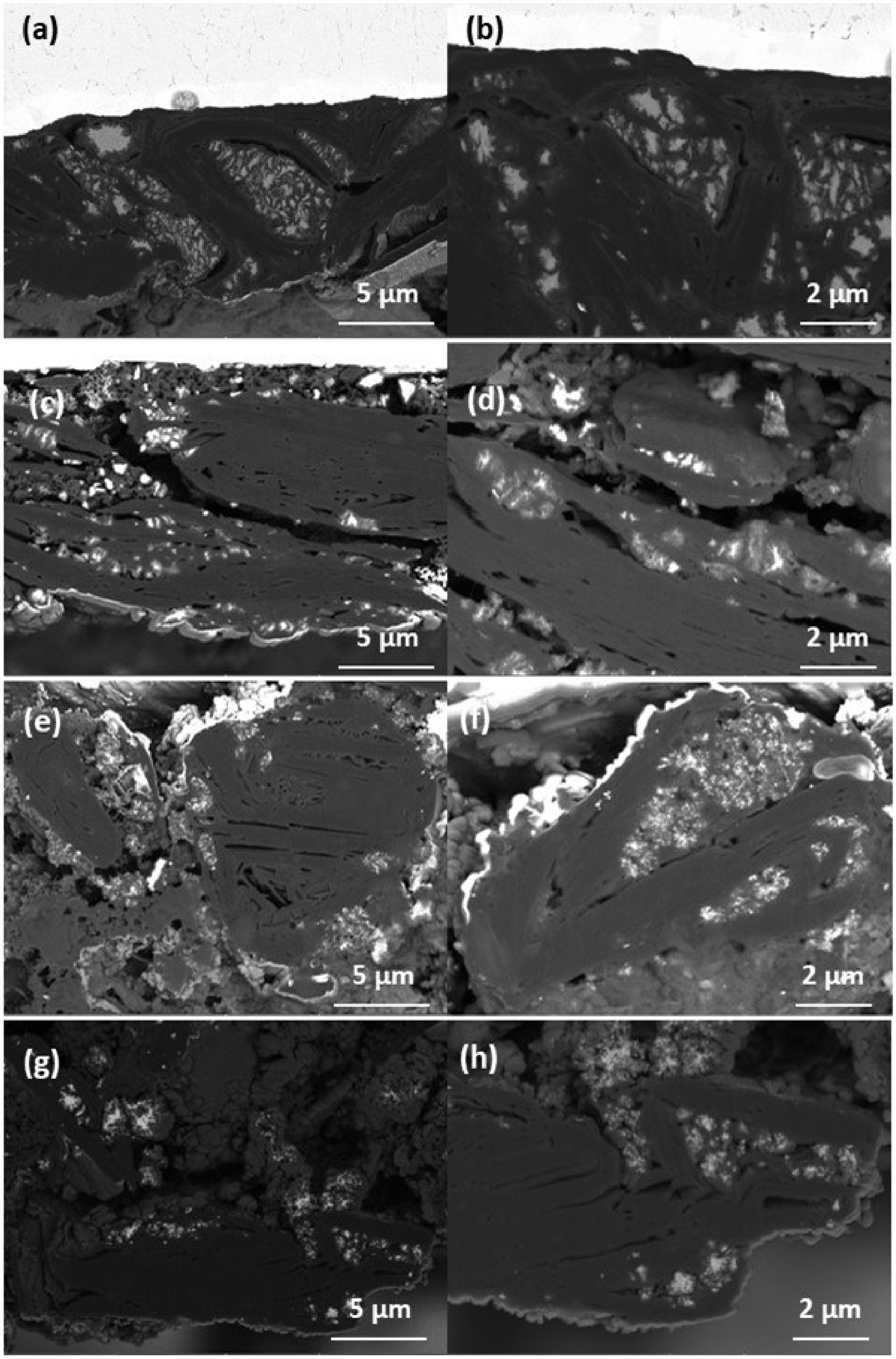

Figure 6.5 Cross-sectional SEM images of post-cycled electrodes of (a)-(b): MF(3h)-$SiFe_{0.20}O_{0.39}$/SG made with LiPAA binder and cycled in FEC-containing electrolyte, (c)-(d) MF(3h)-$SiFe_{0.20}O_{0.39}$/SG made with PVDF binder and cycled in FEC-free electrolyte, (e)-(f) MF(3h)-$SiFe_{0.20}O_{0.39}$/SG/C(CVD,1h) made with PVDF binder and cycled in FEC-free electrolyte, (g)-(h) MF(3h)-$SiFe_{0.20}O_{0.39}$/SG/(CVD,2h) made with PVDF binder and cycled in FEC-free electrolyte.

Figure 6.6 compares the cycling performance of MF(1h)-$SiFe_{0.20}O_{0.39}$/SG/C(CVD,2h) composite and MF(3h)-$SiFe_{0.20}O_{0.39}$/SG/C(CVD,2h) composite electrodes. The two electrodes have about the same first reversible capacity. However, the MF(3h)-$SiFe_{0.20}O_{0.39}$/SG/C(CVD,2h) composite electrode shows higher cycling stability than the MF(1h)-$SiFe_{0.20}O_{0.39}$/SG/C(CVD,2h) composite electrode during the assessed 100 cycles, with almost no capacity loss of its first reversible capacity. It is noted that the 1h MF composite was cycled with advanced LiPAA binder and FEC-containing electrolyte while the 3h MF composite was cycled in an extreme condition (PVDF binder, FEC-free electrolyte). This result indicates that longer MF processing time helps the embedding process of $SiFe_{0.20}O_{0.39}$ particles into the graphite particle as well as benefiting cycling performance.

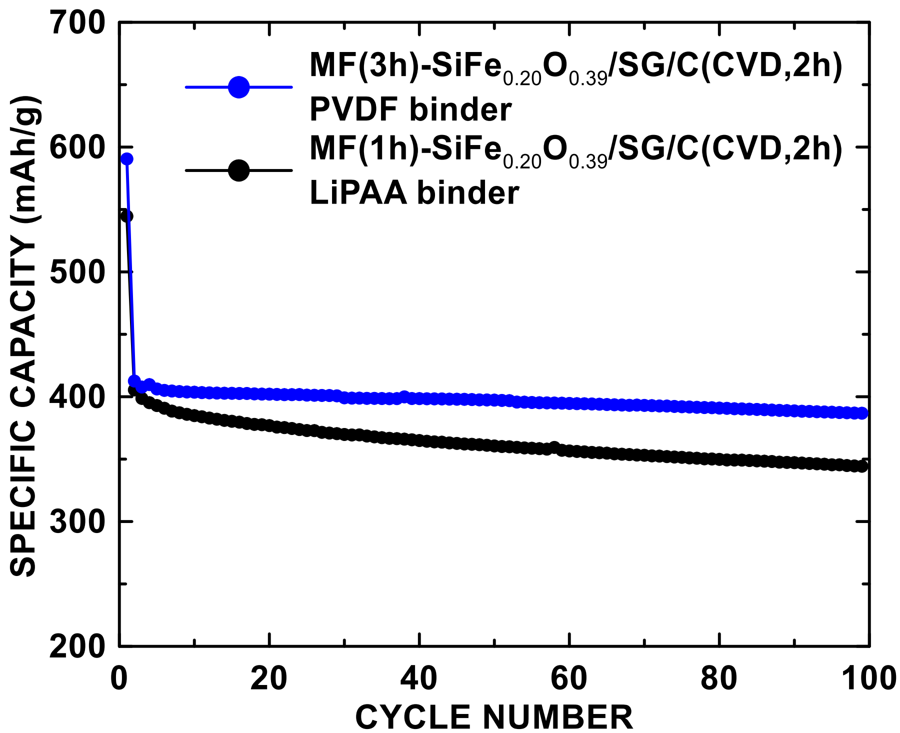

Figure 6.6 Specific capacity versus cycle number of MF(1h)-$SiFe_{0.20}O_{0.39}$/SG(CVD,2h) and MF(3h)-$SiFe_{0.20}O_{0.39}$/SG(CVD,2h) composite electrodes. MF(1h)-$SiFe_{0.20}O_{0.39}$/SG(CVD,2h) electrode was prepared with LiPAA binder and cycled in FEC-containing electrolyte. MF(3h)-$SiFe_{0.20}O_{0.39}$/SG(CVD,2h) electrode was prepared with PVDF binder and cycled in FEC-free electrolyte.

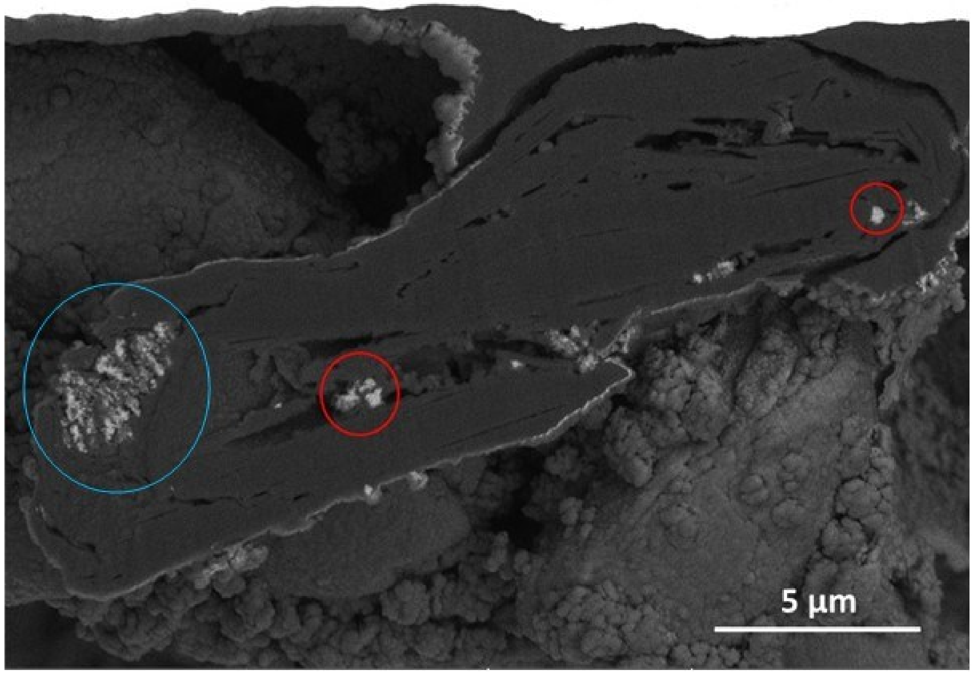

Figure 6.7 Cross-sectional SEM image of post-cycled MF(1h)-SiFeO/SG(CVD,2h) electrode with LiPAA binder and cycled in FEC-containing electrolyte.

A cross-sectional SEM image of MF(1h)-$SiFe_{0.20}O_{0.39}$/SG/C(CVD,2h) composite electrode with LiPAA binder obtained after 100 cycles in FEC-containing electrolyte is shown in Figure 6.7. The alloy particles seem to have different morphologies in different regions of the composite particle. Alloy particles close to the graphite surface (indicated by a blue circle in Figure 6.7) show a more fractured and/or SEI-surrounded region. However, for alloy particles that are embedded deeply inside of the graphite structure (indicated by red circles in Figure 6.7), they still show clear margins that are almost like pristine particles, with very little alloy surface erosion and SEI formation. This may indicate that those deeply embedded alloys are protected by the “sealed” structure from electrolyte penetration. Again, this needs to be confirmed by element mapping of the post-cycled electrode to observe the electrolyte infiltration. The result in this section encourages further optimization on the MF-$SiFe_{0.20}O_{0.39}$/SG/C composite synthesis process to achieve a composite particle that having well embedded alloy particles inside of the graphite voids and uniform carbon coating on the graphite surface to completely protect alloys from electrolyte penetration.

6.4 Optimizations on Synthesis Method

6.4.1. Use of Flake Graphite to Further Optimize Composite Particles

The undesired carbon fibers observed in Figure 6.3 (c) and (d) are suspected to be associated with alloy particles on the graphite surface. Therefore, it would be ideal if alloy particles can be fully embedded inside the graphite particle. Here, a small amount of flake graphite was added to MF(3h)-$SiFe_{0.20}O_{0.39}$/SG composite particles with the hope to reduce the amount of alloy particles on the graphite surface. The flake graphite may work by coating the MF(3h)-$SiFe_{0.20}O_{0.39}$/SG composite particles, helping the embedding process of MF by lubricating the regions between the composite particles, separating alloy aggregates on the graphite surface, or any combination of these.

0.57g of flake graphite (KS6L, Imerys Graphite and Carbon) was added to 20g of MF(3h)-$SiFe_{0.20}O_{0.39}$/SG composite (denoted as SiFeOSG1 in this section) and dry processed using mechanofusion for 1h, the resulting $SiFe_{0.20}O_{0.39}$/SG/FG composite was referred as SiFeOSGFG1. 6 g of the SiFeOSGFG1 was mixed with additional 10.68 g of spherical natural graphite and processed by MF for another 3 hours to lower the $SiFe_{0.20}O_{0.39}$ content to 5 wt. %, the resulting alloy/graphite composite was called SiFeOSGFG2. For comparison, a $SiFe_{0.20}O_{0.39}$/SG composite (denoted as SiFeOSG2) consisting of 5 wt.% of $SiFe_{0.20}O_{0.39}$ was prepared by diluting the SiFeOSG1 with additional spherical graphite in the mechanofusion for another 4 hours, so that the total MF time is the same as SiFeOSGFG2. Table 6.1 lists compositions of all $SiFe_{0.20}O_{0.39}$/SG and $SiFe_{0.20}O_{0.39}$/SG/FG composites mentioned in this section.

Table 6.1 Compositions of MF processed $SiFe_{0.20}O_{0.39}$/graphite composites

sample	$SiFe_{0.20}O_{0.39}$ (wt.%)	Spherical Graphite (wt.%)	Flake Graphite(wt.%)	MF Time (hours)
SiFeOSG1	14.3	85.7	/	3
SiFeOSG2	5	95	/	7
SiFeOSGFG1	13.9	83.4	2.7	4
SiFeOSGFG2	5	94.08	0.98	7

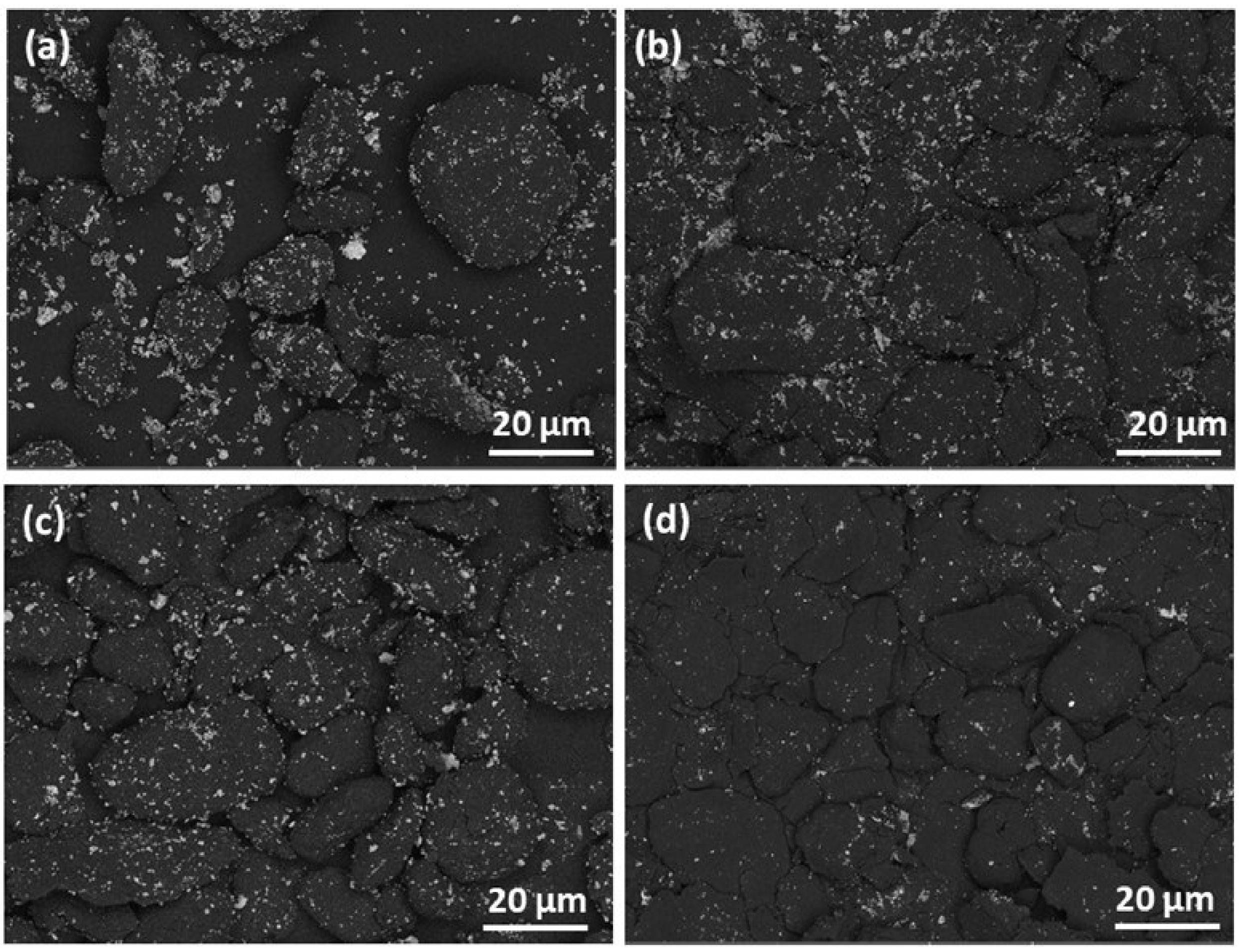

Figure 6.8 SEM image (a) SiFeOSG1(b) SiFeOSGFG1 (c)SiFeOSG2, and (d) SiFeOSGFG2.

Figure 6.8 shows SEM images of the composites listed in Table 6.1. Figure 6.8(a) shows the overall morphology of the SiFeOSG1 composite. This SiFeOSG1 composite contains 14.3 wt. % of $SiFe_{0.20}O_{0.39}$ alloy particles and has been MF-processed for 3 hours. Significant amounts of alloy particles are observed both on the graphite surface and distributed separately. Alloy particles in this image have different particle sizes, and some secondary aggregates of alloy particles are present. Small primary alloy particles are mostly present on the surface of the graphite particles, while larger aggregates tended to be adhered to the underlying carbon tape by themselves. The SiFeOSGFG1 composite was prepared by adding 2.7 wt.% of flake graphite to SiFeOSG1 and MF processing for another hour. The overall morphology of the SiFeOSGFG1 composite shown in Figure 6.8(b) is similar to SiFeOSG1. However, $SiFe_{0.20}O_{0.39}$ particles in Figure 6.8(b) seem to have smaller particle sizes and are distributed more evenly. The small amount of flake graphite in SiFeOSGFG1 composite particle may help separate the large alloy aggregates observed in SiFeOSG1. Nevertheless, many alloy particles are present on the graphite surface. In Figure 6.8 (c) and (d), alloy content was decreased to 5 wt. %. The composite powder shown in Figure 6.8(c) was prepared by diluting SiFeOSG1 with additional graphite and MF processing for four more hours. It was expected that longer mechanofusion processing time may help embed more of the $SiFe_{0.20}O_{0.39}$ particles from the graphite surface into the inner voids. This effect was very obvious when the MF hours is increased from 1h to 3h as discussed in Figure 6.2. However, in Figure 6.8(c), even thougth this SiFeOSG2 sample was dry processed in MF for 7h and the alloy content is only 5%, many $SiFe_{0.20}O_{0.39}$ particles remain on the graphite surface. In contrast, the SiFeOSGFG2 sample in Figure 6.8(d), with the same MF processing time (7h) and same $SiFe_{0.20}O_{0.39}$ alloy content (5 wt. %), shows less alloy particles in its SEM images, this indicates that more alloys have been successfully embedded inside of the graphite voids or that the flake graphite was able to coat the $SiFe_{0.20}O_{0.39}$/SG composite particles.

Figure 6.9 show SEM images of the SiFeOSGFG2 and SiFeOSG2 composite particles at a higher magnification, as well as their electrode cross sections. Very few $SiFe_{0.20}O_{0.39}$ particles are present on the graphite surface in SiFeOSGFG2, shown in Figure 6.9 (a). In contrast, more $SiFe_{0.20}O_{0.39}$ particles are observed in SiFeOSG2 (Figure 6.9 (c)). In addition, $SiFe_{0.20}O_{0.39}$ alloy particles that remain on the graphite surface also show larger particle sizes in Figure 6.9(c). Composite particles in Figure 6.9 (a) and (c) contain the same amount (5 wt. %) of $SiFe_{0.20}O_{0.39}$ particles and were both processed in MF for 7 hours. The only difference is that the SiFeOSGFG2 contains about 1 wt.% of flake graphite. This amount of flake graphite may act as an embedding aid to break down the large particles of $SiFe_{0.20}O_{0.39}$ on the graphite surface to small particles, which facilitates the embedding of $SiFe_{0.20}O_{0.39}$ particles inside of the graphite voids. Figure 6.9(b) shows the cross-sectional SEM image of the SiFeOSGFG2 particle. It seems that more alloy particles are embedded into the top graphite particle shown in Figure 6.9(b). However, almost no alloy particles can be found inside of the bottom graphite particle in the same image. This could also relate to the different morphology of natural spherical graphite particles, for example, some graphite particles may have less available entrances on the surface for the alloy particle to be embedded in. Figure 6.9 (d) shows the cross section of SiFeOSG2 composite particles, some alloy particles were embedded inside of the graphite particles, but on average less than that in Figure 6.9 (b). This comparison would be more convincing if multiple cross-section images were taken for each electrode to show the distribution of alloy particles in the graphite voids. As another possible reason for the fewer alloy particles on the graphite surface observed in Figure 6.9(a), the flake graphite added in the SiFeOSGFG2 composite may coat the SiFeOSG particles during MF process. However, it is hard to determine the existence of such coating layer from present SEM images. It is also possible that the flake graphite has acted in both ways to reduce the surface alloy particles.

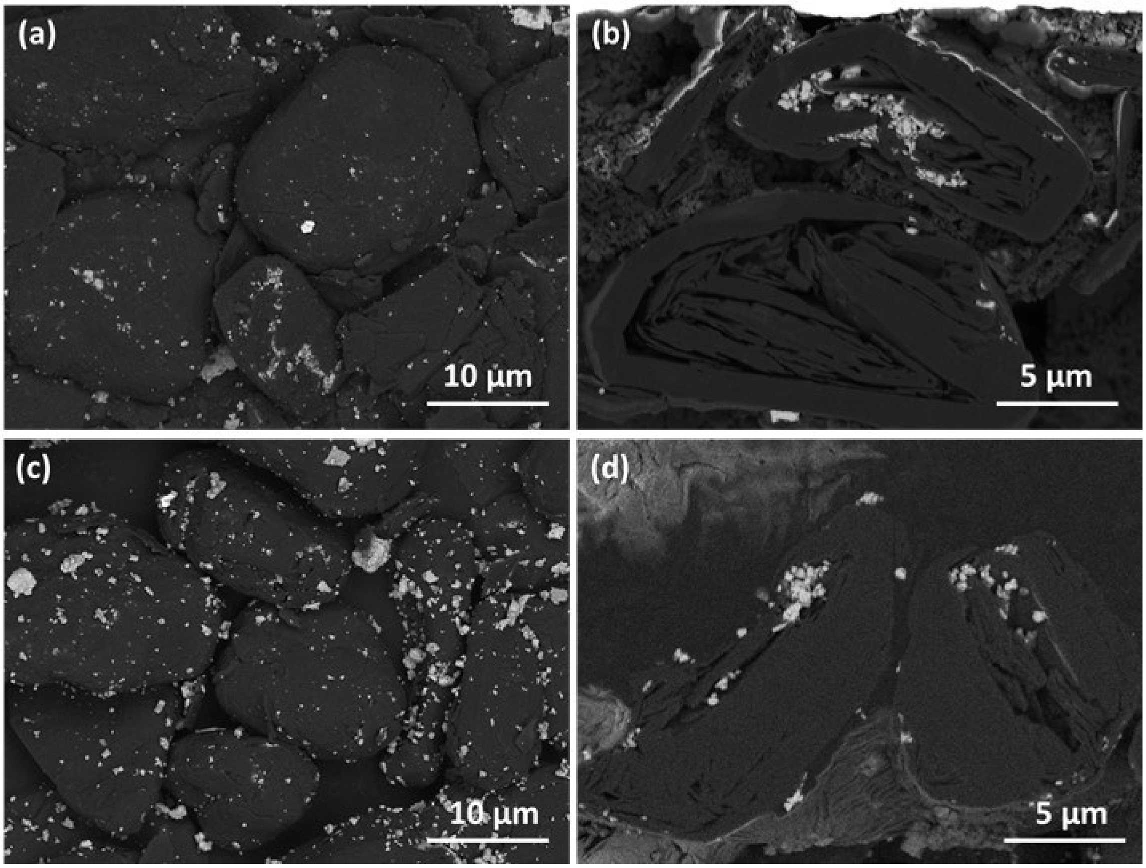

Figure 6.9 (a) and (b) SEM image and cross-sectional SEM image of SiFeOSGFG2 electrode. (c) and (d) SEM image and cross-sectional SEM image of SiFeOSG2 electrode.

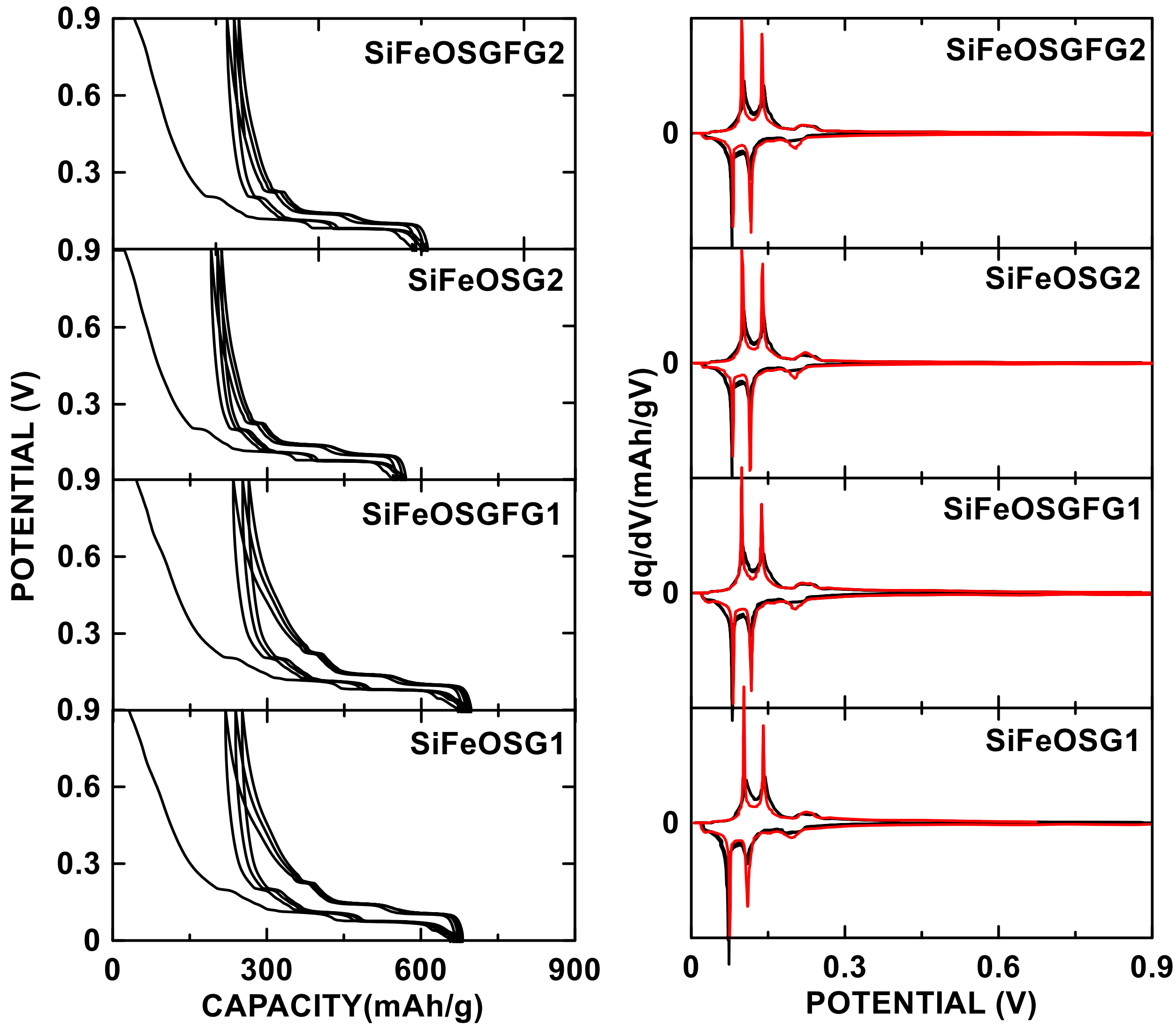

Figure 6.10 Potential profiles and corresponding differential capacity curves of SiFeOSG and SiFeOSGFG composites listed in Table 6.1, initial cycles are shown in red in the differential capacity curves.

Figure 6.10 shows the potential profiles and the corresponding differential capacity curves of the four MF processed composite materials with different alloy and graphite contents, as listed in Table 6.1. As the alloy content decreases from 14.3% and 13.9% (SiFeOSG1 and SiFeOSGFG1) to 5 % (SiFeOSG2 and SiFeOSGFG2), the reversible capacity decreases and the potential profiles more resemble that of a graphite anode. Figure 6.11 (a) shows the cycling performance of the four MF processed composite materials with different alloy and graphite contents. All electrodes were prepared with PVDF binder and cycled in FEC-free electrolyte. In Figure 6.11 (a), SiFeOSG1 and SiFeOSGFG1 show higher first lithiation capacity due to their higher alloy content (14.3 wt.% and 13.9 wt. % alloy, respectively) than SiFeOSG2 and SiFeOSGFG2 (5 wt. % alloy). However, no significant differences can be identified (all difference within 5 %) between the SiFeOSG1 and SiFeOSGFG1 electrodes in terms of cycling performance. They both show some degree of capacity fade, due to the extreme cycling conditions (PVDF binder and FEC-free electrolyte).

From Figure 6.11 (a) it is tempting to infer that the SiFeOSGFG2 electrode has the best cycling performance, possibly because of the success in embedding most of the alloy particles, as shown in Figure 6.8(d). However, the presence of different amounts of graphite in these composites can make such conjectures misleading. To better compare the capacity retention of the $SiFe_{0.20}O_{0.39}$ alloy itself in these composites, the $SiFe_{0.20}O_{0.39}$ alloy contribution to the capacity of these composites were calculated from the fraction of the electrode capacity above 0.18 V during delithiation, as described in Chapter 4, and are plotted in Figure 6.11 (b). Unexpectedly, the calculated capacity of the $SiFe_{0.20}O_{0.39}$ alloy in the SiFeOSG2 and SiFeOSGFG2 electrodes is higher than the measured capacity of the neat $SiFe_{0.20}O_{0.39}$ alloy electrode (~1200 mAh/g). This is likely caused by the loss of graphite during the long mechanofusion processing (7h), since severe powder leakage was observed during machine operation and graphite tends to leak preferentially during mechanofusion because of its low density. Further investigation is required to confirm the powder composition after the mechanofusion processing. All $SiFe_{0.20}O_{0.39}$ alloys show severe capacity fade when cycled in these composite materials. None of the $SiFe_{0.20}O_{0.39}$ alloys in these composites show significantly improved cycling (improvement in capacity retention after 100 cycles greater than 10%)over the $SiFe_{0.20}O_{0.39}$ alloy in the SiFeOSG1 composite. Indeed, the capacity retention of $SiFe_{0.20}O_{0.39}$ alloy in the SiFeOSGFG2 composite is much worse. More work is needed to optimize these composite materials. Figure 6.11 represents a good demonstration that improved capacity retention by the addition of graphite to an alloy may be misleading. The alloy itself may have worse capacity retention, even though the capacity of the composite as a whole is improved by the addition of graphite.

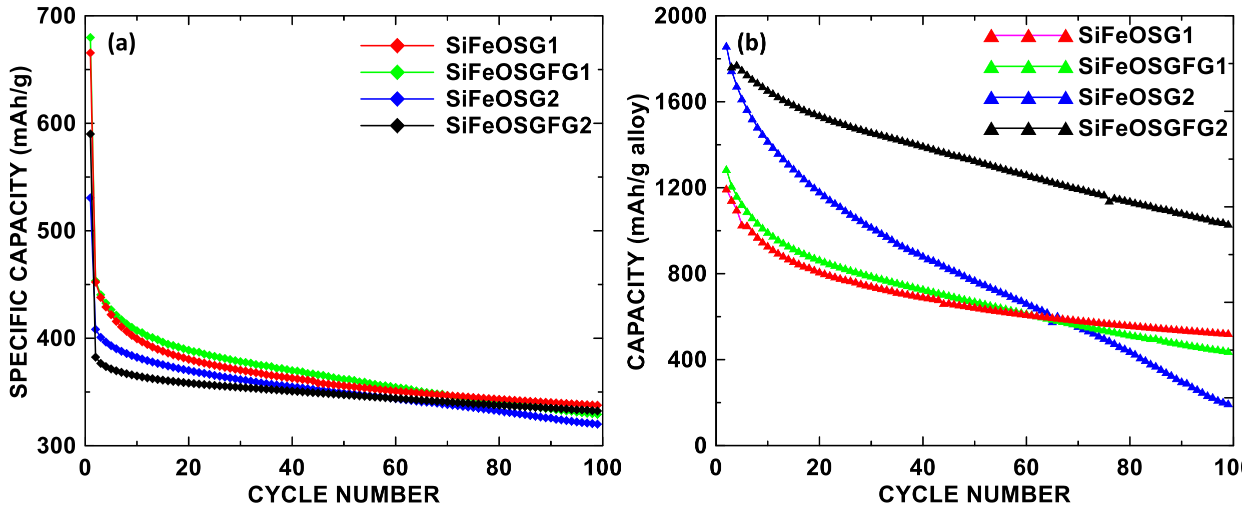

Figure 6.11 (a) Specific capacity versus cycle number of SiFeOSG and SiFeOSGFG composites listed in Table 6.1 (b) capacity of $SiFe_{0.20}O_{0.39}$ alloy in SiFeOSG and SiFeOSGFG composites electrode. All electrodes were made with PVDF binder and cycled in FEC-free electrolyte.

6.4.2. Search Other Carbon Coating Methods and Study of Electrolyte Penetration

In order to cycle $SiFe_{0.20}O_{0.39}$/SG composite electrodes well without the use of advanced binders or electrolyte additives, alloy particles should be completely isolated from the electrolyte and binder. To obtain this goal, good carbon coating methods as well as ways to examine the electrolyte and binder penetration are of great importance. This section will show a preliminary work to coat the spherical graphite using citric acid as a precursor and investigate its effect on preventing electrolyte penetration using EDS mapping.

0.5 g spherical graphite and 1.25g citric acid were dispersed in 5ml of ethanol and mixed in a high sheer mixer for 10 mins. The dried powder mixture was heated under Ar flow for 2 hours.

In order to investigate whether electrolyte will penetrate within the graphite particles, electrodes of carbon-coated graphite and uncoated graphite were soaked in the standard electrolyte (1 M LiPF6 in EC:DEC:FEC(3:6:1)) overnight, separately. Electrode coatings were made by mixing graphite, carbon black and PVDF binder in a mass ratio of 90:5:5. The soaked electrodes were cross sectioned and EDS mapping was used to detect traces of electrolyte.

Figure 6.12 (a) shows the cross-section of the soaked uncoated graphite electrode, some bright spots were observed both within graphite particle and on the graphite particle surface. Such bright spots are also shown in higher intensity in the F-mapping (Figure 6.12 (b)) and P-mapping (Figure 6.12 (c)) of the image. According to Figure 6.12(b-c), fluorine and phosphorus exist everywhere outside the graphite particle and everywhere within the voids of the graphite particle. The fluorine can come from the PVDF binder and the electrolyte solution, while the phosphorus can come from the $LiPF_6$ salt in the electrolyte. As a comparison, Figure 6.12 (d-f) show cross-section SEM and EDS mapping images of the carbon-coated graphite electrode. In this electrode, much less P and F were identified within the graphite particle. However, significant amounts of P and F (as shown in bright-coloured regions) were observed in the graphite voids that are close to the outside surface, as shown in Figure 6.12(e) and (f). For those voids that are deep inside of the graphite particle, both F and P were not detected. This indicates the carbon-coated graphite made here may only slow down the penetration rate of the electrolyte, but it cannot well seal the graphite from electrolyte infiltration.

The carbon coating achieved here has a very limited effect in terms of preventing the penetration of electrolyte and/or binder into graphite particles. However, this preliminary work shows an effective experimental method to study electrolyte penetration. This method can be applied to the post-cycled electrode of $SiFe_{0.20}O_{0.39}$/graphite/C composite, which seems to be protected from electrolyte penetration by the carbon coating obtained by CVD. Nevertheless, more controllable carbon coating methods are still required to produce an amorphous carbon layer with appropriate thickness to enhance the electrode conductivity and prevent electrolyte penetration.

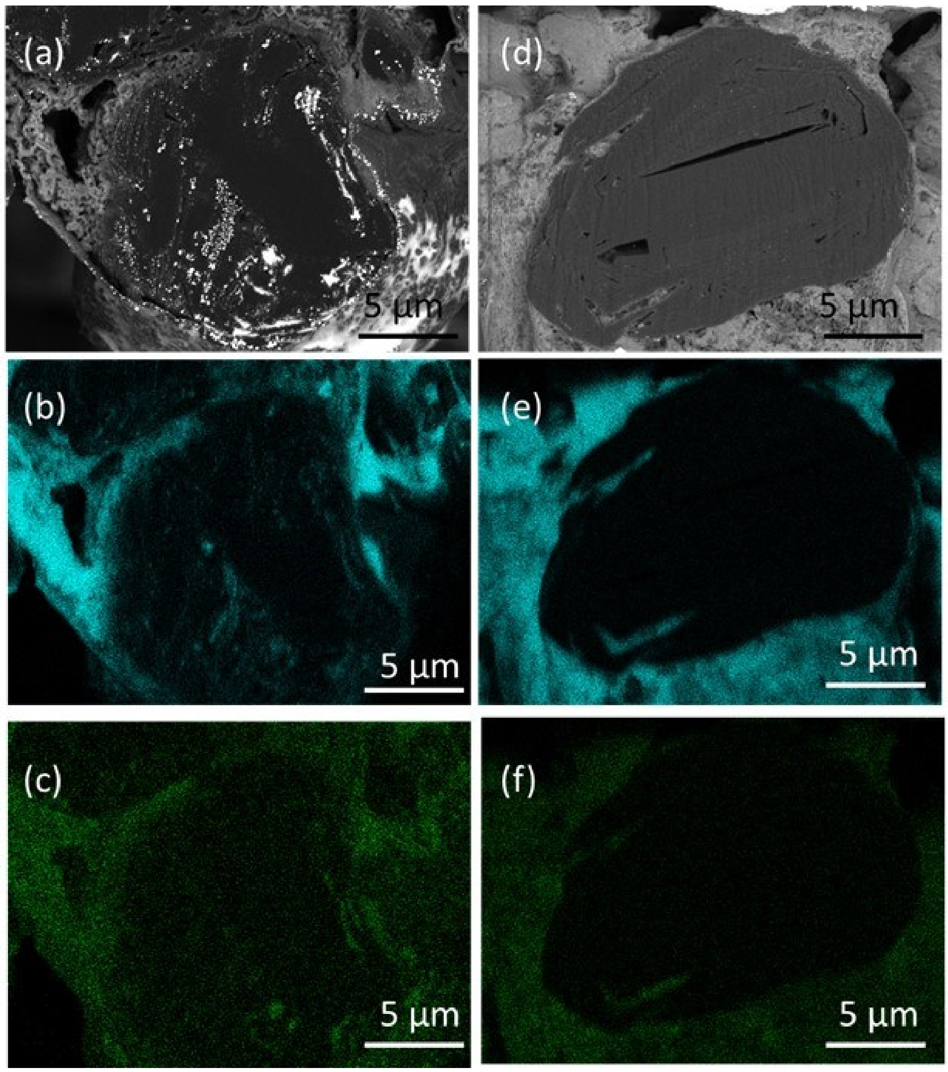

Figure 6.12 (a-c) Cross-sectional SEM image and corresponding EDS mapping results of spherical graphite electrode soaked in electrolyte (1M $LiPF_6$ in EC:DEC:FEC(3:6:1) overnight. (a) graphite (b) F mapping image, (c) P mapping image; (e-f) Cross-sectional SEM image and corresponding EDS mapping results of carbon-coated spherical graphite electrode soaked in electrolyte (1M $LiPF_6$ in EC:DEC:FEC(3:6:1) overnight. (a) carbon-coated graphite, (e) F mapping image, (f) P mapping image.

6.5 Conclusion

$SiFe_{0.20}O_{0.39}$/SG/C composites were prepared by a dry powder processing method, mechanofusion and subsequently CVD carbon coated. In the resulting engineered composite particle, $SiFe_{0.20}O_{0.39}$ alloy particles are well embedded inside spherical graphite particles. The carbon coating prepared by CVD on the spherical $SiFe_{0.20}O_{0.39}$ alloy/graphite composites can further protect the embedded alloy particles from reaction with the electrolyte. Therefore, $SiFe_{0.20}O_{0.39}$/graphite/C composite electrodes show good cycling performance without using advanced binders and electrolyte additives. Such composite materials are promising for a drop-in method to increase the energy density of Li-ion batteries without the need for special electrolyte additives or binders. They also present an interesting research vehicle to study alloy materials without interference from electrolyte interactions or electrode structural issues.

CHAPTER 7 CONCLUSIONS AND FUTURE WORK

7.1 Conclusions

In this thesis, systematic investigations of Si-based nanostructured composites were conducted with the goal of improving electrochemical performance. Composites of Si-Fe-O alloys and carbonaceous materials were selected as effective materials to realize this main objective. $Si_{85}Fe_{15}O_x$ alloys were prepared by a simple reactive gas milling method with tunable oxygen content, as described in Chapter 3. The oxygen content of the milled alloys was found to increase with air milling time from 0 h to 6 h and then reached a steady state. It was found that increasing air milling time decreases the specific capacity as the introduced oxygen reacts with Si. However, increasing air milling time can help improve the cycling stability and suppress the formation of $Li_{15}Si_4$. The 10 h air milled $Si_{85}Fe_{15}O_x$ alloy shows high volumetric capacity and good cycle life. $Si_{85}Fe_{15}O_x$ alloys also have excellent thermal stability, even after being annealed to 800°C. For instance, the 10 h air milled $Si_{85}Fe_{15}O_x$ alloy is an outstanding candidate among the examined alloys for the further development of increased capacity anode materials for commercial cells (e.g. by incorporating the alloy into graphite composites).

The electrochemistry of ball milled $SiFe_xO_y$ alloys was investigated as a function of iron content in Chapter 4. It was found that increasing iron content decreases the specific capacity because of the formation of inactive iron silicide phases. However, increasing iron content helps improve cycling stability. In addition, the increased iron content helps protect electrode structural integrity during cycling. The studies on Chapter 3 and Chapter 4 provide the most promising Si-Fe-O alloy candidate ($SiFe_{0.20}O_{0.39}$) for further optimization to increase cycle life, such as by carbon coating and making composite materials with graphite.

Chapter 5 introduces some preliminary investigations of $SiFe_{0.20}O_{0.39}$/C composite materials by taking advantage of the high thermal stability and good cycling properties of $SiFe_{0.20}O_{0.39}$ alloy. It was shown that the $SiFe_{0.20}O_{0.39}$ alloy can withstand high temperature processing when annealed with PVC at temperatures as high as 800ºC. The resulting $SiFe_{0.20}O_{0.39}$/C materials have improved cycling stability and this good cycling performance is maintained even in FEC-free electrolyte. $SiFe_{0.20}O_{0.39}$/graphite composites were prepared by annealing a mixture of $SiFe_{0.20}O_{0.39}$ alloy, graphite, and phenolic resin at 600ºC. The $SiFe_{0.20}O_{0.39}$/graphite composites show improved cycling stability, with a capacity retention above 95% over 100 cycles. This cycling performance is maintained even when the electrolyte additive FEC is not used.

Further optimizations of the $SiFe_{0.20}O_{0.39}$/graphite composite material towards a practical battery material are discussed in Chapter 6. $SiFe_{0.20}O_{0.39}$/SG/C composites were prepared by a dry powder processing method, mechanofusion and subsequently CVD carbon coated. In the resulting engineered composite particle, $SiFe_{0.20}O_{0.39}$ alloy particles are well embedded inside spherical graphite layers. The carbon coating prepared by CVD on the spherical $SiFe_{0.20}O_{0.39}$ alloy/graphite composites was added to further protect the embedded alloy particles from reaction with the electrolyte. The resulting $SiFe_{0.20}O_{0.39}$/graphite/C composite electrodes show good cycling performance without using advanced binders and electrolyte additives.

The combination of synthetic methods of ball milling, mechanofusion and CVD techniques, was adopted to obtain a high-capacity Si-based composite anode for LIBs. Therefore, this present study suggests an optimized and practical nanostructured Si-based composite anode for superior LIBs.

7.2 Future Work

7.2.1 Investigations on Carbon Coating Methods

Some attempts were made to prepare carbon coatings on either neat $SiFe_{0.20}O_{0.39}$ alloy and $SiFe_{0.20}O_{0.39}$/graphite composites in this thesis. Instead of the desired carbon-coated $SiFe_{0.20}O_{0.39}$ particle, heating $SiFe_{0.20}O_{0.39}$ and PVC mixture resulted in a $SiFe_{0.20}O_{0.39}$/C composites. However, this $SiFe_{0.20}O_{0.39}$/C composite still shows improved cycling performance, further studies on its microstructure via experimental techniques such as TEM would be helpful to understand its corresponding electrochemical performance. At the same time, it would be valuable to explore other precursors to prepare carbon coatings via the pyrolysis method. In addition, the $SiFe_{0.20}O_{0.39}$ alloy particles in the $SiFe_{0.20}O_{0.39}$/graphite/C(CVD) composites prepared in this thesis seem to show reduced electrolyte erosion from its morphology in the post-cycled electrode. This needs to be confirmed by some compositional analysis to show that less F and P (elements in the electrolyte) were identified with the carbon coating layers.

7.2.2 Compatibility and Interactions between Si Alloys and Graphite

Unlike Si, graphite has low volume expansion upon lithiation (~10%) [183]. The big difference in the volume changes of graphite and Si alloy during lithiation/delithiation may result in electrical contact loss for graphite [184]. A previous study of a Si/graphite composite found that the graphite component loses its intrinsic capacity after cycling due to the repeated expansion and contraction of the Si particle during lithiation/delithiation, which causes excessive SEI formation at the interface and degradation of electrodes [185]. This resulted in the graphite particles becoming electrically isolated. It was also found that the graphite particles in the Si/graphite composite are partially displaced and become randomly oriented as the expansion of the Si/graphite electrodes proceeds [186]. It is important to study the interaction between graphite and

Si during the lithiation/delithiation process in the Si alloy/graphite composite electrodes, such as the (de)lithiation kinetics, the potential behavior, and electrochemical performance of calendered electrodes [187].

In addition, the incompatibility between the irregular particle sizes of Si alloy and graphite should be carefully considered. Modifications on the morphology, size, and surface area of graphite may increase the compatibility of graphite with Si by adjusting the distribution of Si and graphite in the composite [184]. In the development of Si alloy/graphite anodes for high energy density LIBs, properties of both graphite and Si alloy should be carefully considered. Comprehensive studies on compatibility and interactions between Si-based alloy and graphite are necessary.

7.2.3 Alloy Morphology Changes

It is important to study the alloy fading mechanism within a structure such as the $SiFe_{0.20}O_{0.39}$ /C(CVD) composite particle in Chapter 5. If the alloy is indeed isolated from the electrolyte, the behavior of the $SiFe_{0.20}O_{0.39}$ alloy particles during lithiation/delithiation processes without the interaction of electrolyte can be monitored. It will help understand alloy morphology changes during cycling. According to the current study on the $SiFe_{0.20}O_{0.39}$ /C(CVD) composite, the alloy surface is still fractured compared to the pristine electrode. This may indicate that alloy surface erosion is not solely due to electrolyte reaction, but also because of repeated expansion/contraction. More comprehensive understanding of the morphology changes of embedded alloys in graphite will guide future design of optimal microstructures.

7.2.4 Further Optimizations towards Practical Application

The syntheses described in this thesis are on a lab bench scale. It is necessary to explore low-cost and large-scale production methods to prepare $SiFe_{0.20}O_{0.39}$ alloy with the same quality of the reactive gas milled $SiFe_{0.20}O_{0.39}$ alloy (e.g. microstructure and thermal stability) to achieve both high capacity and stable cycling. In addition, the preparation of $SiFe_{0.20}O_{0.39}$ /graphite materials should consider scalable manufacturing processes to realize its practical application. The mechanofusion and CVD synthesis steps utilized in present study is advantageous in this perspective. In addition, further improvements on the particle structural design are important. For example, an appropriate amount of the flake graphite needs to be determined to help the embedding process of $SiFe_{0.20}O_{0.39}$ alloy particles inside the void spaces of graphite particles.

7.2.5 Pre-lithiation Methods and Full Cell Evaluation

Although the as prepared $SiFe_{0.20}O_{0.39}$ alloys show improved ICE than SiO_x materials, due to the reduced formation of inactive Li silicates, the ICE is still not very high (about 70%). In half cells, this is often not a problem as there is excessive lithium available. However, anode materials with lower ICE will cause the consumption of active lithium to compensate for the first cycle, leading to a low overall energy density in full cells. In practical applications, a first cycle capacity loss of < 10% is normally required for the anode [180]. Many methods have been developed to improve the ICE of SiO_x materials by preloading anodes with excess Li to compensate for the low ICE (e.g. prelithiation). For example, stabilized lithium metal powder (SLMP) was used to pretreat Si-based anodes before cell assembly [71,180,188–190]. The electrodes prelithiated with 8.3% SLMP can improve the ICE from 80.4% (without prelithiation) to 93.1%, while still maintaining similar cycling performance of the untreated electrode [180]. Prelithition can also be achieved by electrochemical lithiation using a temporary cell and pre-charging process [191]. Prelithiation is very useful method to increase the ICE of $SiFe_{0.20}O_{0.39}$ electrodes, which is worth investigation in full cell configurations.

It is valuable to investigate full cell performance when $SiFe_{0.20}O_{0.39}$/graphite composite materials are used as the negative electrode and matched with commercial positive electrodes. Fundamental studies of the interaction between positive electrodes and $SiFe_{0.20}O_{0.39}$/graphite composite negative electrodes need to be explored. Optimal cycling conditions of $SiFe_{0.20}O_{0.39}$/graphite composite in full cells are important to evaluate its full potentials as high energy density electrode materials. Thoughtful research in full cells will help the understandings of cell failure mechanisms and contribute practical applications of Si-based anodes for future LIBS.

7.2.6 Binder and Electrolyte System

The development of a compatible binder and electrolyte system that works well for both Si-based alloy and graphite is of great importance. For example, conventional PVDF binder works well with graphite electrode, but it results in severe capacity fades when used in Si-based materials. It was found that some binders will have different interactions with different components in a Si/graphite composite [94]. This is because of the different nature of graphite (hydrophobic) and Si (hydrophilic) [192]. In addition, it was claimed that the use of water-based binders, such as carboxymethyl cellulose (CMC), styrene butadiene rubber (SBR), and poly(acrylic acid) (PAA) will cause cell failure of the Si/graphite anode [193]. The nonremovable residual water will cause the hydrolysis of $LiPF_6$ to produce HF, and the harmful HF will penetrate through the SEI layer and etch the Si surface, so that the electrode degradation is accelerated [194,195]. Therefore, the binder design for a composite must consider the different properties of each component carefully.

Electrolyte studies are also essential to enhance the overall electrochemical performance. The development of electrolyte systems should consider the whole system, instead of the Si-based materials or graphite alone. For example, vinylene carbonate (VC) is a useful electrolyte additive for graphite, but it doesn't work well for Si-based alloys [196,197]. In addition, for a full cell with nickel-rich cathode and silicon-based anode, a good electrolyte system should be able to stabilize the high-voltage cathode electrolyte interface and the SEI layer at the same time [97]. The use of multiple additives is one useful strategy. For example, the co-use of lithium fluoromalonato-(difluoro)borate (LiFMDFB) and FEC were found to stabilize both Li-rich cathode and Si/graphite anode in a full cell. The Si/graphite particles are covered by the uniform SEI even after 200 cycles in this electrolyte system. This dual-function electrolyte system demonstrates a very useful method to design electrolytes for high-performance batteries [173].

7.3 Personal Reflection

This section aims at sharing personal thoughts concerning the whole process of the thesis. It was overall an enjoyable journey. I liked conducting research that is practical and holding the promise to solve real-world issues.

This thesis mainly introduces the synthesis of two series of Si-Fe-O alloys and some preliminary work of making $SiFe_{0.20}O_{0.39}$/graphite composites. However, as stated in the future work part, more work needs to be done to optimize the composite material, such as improvements on embedding process, carbon coating process, determination of carbon content, and optimal alloy content in the composites.

Some of the interpretations need to be supported by more strong experimental evidence. Experimental techniques such as XPS, TEM, EDS mapping, in-situ XRD, and electrochemical impedance spectroscopy(EIS) can be utilized to provide complementary information. For example, the interpretations of SEM images of the post-cycled electrodes need to be confirmed by the EDS elemental mapping to confirm the existence of P and/or F that are associated with the electrolyte.

In addition, some of the experimental procedures could have been more carefully designed. In Chapter 6, when using flake graphite to further optimize composite particles, it is worth blending alloy particles with flake graphite before adding the spherical graphite particles.

By overcoming the abovementioned limitations, more understandings of the Si-based alloy /graphite composite material could be revealed.

BIBLIOGRAPHY

[1] Lithium-Ion Battery Market by Type (Li-NMC, LFP, LCO, LTO), Power Capacity (0-3,000 mAh, 3,000 mAh-10,000 mAh, 10,000 mAh-60,000 mAh, above 60,000 mAh), Industry (Consumer Electronics, Automotive, Industrial), Voltage, Region – Global Forecast to 2025, 2020. https://www.researchandmarkets.com/research/x6cdsn/lithium_ion?w=12 (accessed March 1, 2021).

[2] D. Lopez-Behar, M. Tran, J.R. Mayaud, T. Froese, O.E. Herrera, W. Merida, Putting electric vehicles on the map: A policy agenda for residential charging infrastructure in Canada, Energy Res. Soc. Sci. 50 (2019) 29–37. https://doi.org/10.1016/j.erss.2018.11.009.

[3] Canada not on track to hit 1st electric vehicle target by 2025 - National | Globalnews.ca, (2019). https://globalnews.ca/news/7448683/canada-electric-car-target/ (accessed March 1, 2021).

[4] J.M. Tarascon, M. Armand, Issues and challenges facing rechargeable lithium batteries., Nature. 414 (2001) 359–67. https://doi.org/10.1038/35104644.

[5] B. Scrosati, J. Hassoun, Y.-K. Sun, Lithium-ion batteries. A look into the future, Energy Environ. Sci. 4 (2011) 3287. https://doi.org/10.1039/c1ee01388b.

[6] M. Yoshio, R.J. Brodd, A. Kozawa, eds., Lithium-Ion Batteries, Springer, New York, 2009. https://doi.org/10.1016/B978-0-444-59513-3.00002-9.

[7] B. Scrosati, J. Garche, Lithium batteries: Status, prospects and future, J. Power Sources. 195 (2010) 2419–2430. https://doi.org/10.1016/j.jpowsour.2009.11.048.

[8] T. Linden, Linden's Handbook of Batteries, 4th ed., McGraw-Hill, New York, 2011. https://doi.org/10.1016/b978-0-444-41345-1.50007-1.

[9] M.S. Whittingham, Lithium batteries and cathode materials, Chem. Rev. 104 (2004) 4271–4301. https://doi.org/10.1021/cr020731c.

[10] A. Manthiram, J.C. Knight, S.T. Myung, S.M. Oh, Y.K. Sun, Nickel-Rich and Lithium-Rich Layered Oxide Cathodes: Progress and Perspectives, Adv. Energy Mater. 6 (2016). https://doi.org/10.1002/aenm.201501010.

[11] K. Xu, Nonaqueous liquid electrolytes for lithium-based rechargeable batteries, Chem. Rev. 104 (2004) 4303–4418.

[12] M.N. Obrovac, V.L. Chevrier, Alloy negative electrodes for Li-ion batteries, Chem. Rev. 114 (2014) 11444–11502. https://doi.org/10.1021/cr500207g.

[13] R. Schmuch, R. Wagner, G. Hörpel, T. Placke, M. Winter, Performance and cost of materials for lithium-based rechargeable automotive batteries, Nat. Energy. 3 (2018) 267–278. https://doi.org/10.1038/s41560-018-0107-2.

[14] C.J. Wen, Thermodynamic and Mass Transport Properties of "LiAl," J. Electrochem. Soc. 126 (2006) 2258. https://doi.org/10.1149/1.2128939.

[15] Statista, Germanium price U.S. 2014-2019, (2019). https://www.statista.com/statistics/1061511/us-germanium-price/ (accessed March 1, 2021).

[16] D. Larcher, S. Beattie, M. Morcrette, K. Edström, J.-C. Jumas, J.-M. Tarascon, Recent findings and prospects in the field of pure metals as negative electrodes for Li-ion batteries, J. Mater. Chem. 17 (2007) 3759. https://doi.org/10.1039/b705421c.

[17] Graphite 101 | Focus Graphite, (2019). http://www.focusgraphite.com/technology/ (accessed September 6, 2019).

[18] InvestmentMine, Tin Prices and Tin Price Charts, (2019). http://www.infomine.com/investment/metal-prices/tin/ (accessed September 6, 2019).

[19] S. Ranjan, S. Balaji, R.A. Panella, B.E. Ydstie, Silicon solar cell production, Comput. Chem. Eng. 35 (2011) 1439–1453. https://doi.org/10.1016/j.compchemeng.2011.04.017.

[20] M.N. Obrovac, L. Christensen, D.B. Le, J.R. Dahn, Alloy Design for Lithium-Ion Battery Anodes, J. Electrochem. Soc. 154 (2007) A849. https://doi.org/10.1149/1.2752985.

[21] M.T. McDowell, S.W. Lee, W.D. Nix, Y. Cui, 25th anniversary article: Understanding the lithiation of silicon and other alloying anodes for lithium-ion batteries, Adv. Mater. 25 (2013) 4966–4985. https://doi.org/10.1002/adma.201301795.

[22] M.N. Obrovac, L.J. Krause, Reversible Cycling of Crystalline Silicon Powder, J. Electrochem. Soc. 154 (2007) A103. https://doi.org/10.1149/1.2402112.

[23] M.N. Obrovac, L. Christensen, Structural Changes in Silicon Anodes during Lithium Insertion/Extraction, Electrochem. Solid-State Lett. 7 (2004) A93–A96. https://doi.org/10.1149/1.1652421.

[24] J. Li, J.R. Dahn, An in situ X-ray diffraction study of the reaction of Li with crystalline Si, J. Electrochem. Soc. 154 (2007) A156–A161. https://doi.org/Doi 10.1149/1.2409862.

[25] J. Li, A. Smith, R.J. Sanderson, T.D. Hatchard, R.A. Dunlap, J.R. Dahn, In Situ [sup 119]Sn Mössbauer Effect Study of the Reaction of Lithium with Si Using a Sn Probe, J. Electrochem. Soc. 156 (2009) A283. https://doi.org/10.1149/1.3073879.

[26] J.W. Choi, D. Aurbach, Promise and reality of post-lithium-ion batteries with high energy densities, Nat. Rev. Mater. 1 (2016) 16013. https://doi.org/10.1038/natrevmats.2016.13.

[27] A.M. Wilson, Lithium Insertion in Carbons Containing Nanodispersed Silicon, J. Electrochem. Soc. 142 (1995) 326. https://doi.org/10.1149/1.2043994.

[28] I. Ryu, J.W. Choi, Y. Cui, W.D. Nix, Size-dependent fracture of Si nanowire battery anodes, J. Mech. Phys. Solids. 59 (2011) 1717–1730. https://doi.org/10.1016/j.jmps.2011.06.003.

[29] J.-Y. Li, Q. Xu, G. Li, Y.-X. Yin, L.-J. Wan, Y.-G. Guo, Research progress regarding Si-based anode materials towards practical application in high energy density Li-ion batteries, Mater. Chem. Front. 44 (2017) 6749–6773. https://doi.org/10.1039/C6QM00302H.

[30] S.P. Kim, A.C.T.V. Duin, V.B. Shenoy, Effect of electrolytes on the structure and evolution of the solid electrolyte interphase (SEI) in Li-ion batteries: A molecular dynamics study, J. Power Sources. 196 (2011) 8590–8597. https://doi.org/10.1016/j.jpowsour.2011.05.061.

[31] I.A. Courtney, J.R. Dahn, Electrochemical and in situ X-ray diffraction studies of the reaction of lithium with tin oxide composites, J. Electrochem. Soc. 144 (1997) 2045–2052.

[32] T.D. Hatchard, J.M. Topple, M.D. Fleischauer, J.R. Dahn, Electrochemical Performance of SiAlSn Films Prepared by Combinatorial Sputtering, Electrochem. Solid-State Lett. 6 (2003) A129. https://doi.org/10.1149/1.1574231.

[33] O. Mao, R.L. Turner, I.A. Courtney, B.D. Fredericksen, M.I. Buckett, L.J. Krause, J.R. Dahn, Active/Inactive Nanocomposites as Anodes for Li-Ion Batteries, Electrochem. Solid-State Lett. 2 (1999) 3–5. https://doi.org/10.1149/1.1390715.

[34] L.F. Cui, R. Ruffo, C.K. Chan, H. Peng, Y. Cui, Crystalline-amorphous core-shell silicon nanowires for high capacity and high current battery electrodes, Nano Lett. 9 (2009) 491–495. https://doi.org/10.1021/nl8036323.

[35] J. Wan, A.F. Kaplan, J. Zheng, X. Han, Y. Chen, N.J. Weadock, N. Faenza, S. Lacey, T. Li, J. Guo, L. Hu, Two dimensional silicon nanowalls for lithium ion batteries, J. Mater. Chem. A. 2 (2014) 6051–6057. https://doi.org/10.1039/C3TA13546B.

[36] W.S. Kim, Y. Hwa, J.H. Shin, M. Yang, H.J. Sohn, S.H. Hong, Scalable synthesis of silicon nanosheets from sand as an anode for Li-ion batteries, Nanoscale. 6 (2014) 4297–4302. https://doi.org/10.1039/c3nr05354g.

[37] X.H. Liu, L. Zhong, S. Huang, S.X. Mao, T. Zhu, J.Y. Huang, Size-dependent fracture of silicon nanoparticles during lithiation, ACS Nano. 6 (2012) 1522–1531. https://doi.org/10.1021/nn204476h.

[38] H. Gao, L. Xiao, I. Plümel, G.L. Xu, Y. Ren, X. Zuo, Y. Liu, C. Schulz, H. Wiggers, K. Amine, Z. Chen, Parasitic Reactions in Nanosized Silicon Anodes for Lithium-Ion Batteries, Nano Lett. 17 (2017) 1512–1519. https://doi.org/10.1021/acs.nanolett.6b04551.

[39] D.S.M. Iaboni, M.N. Obrovac, Li 15 Si 4 Formation in Silicon Thin Film Negative Electrodes, J. Electrochem. Soc. 163 (2016) A255–A261. https://doi.org/10.1149/2.0551602jes.

[40] M.L. Terranova, S. Orlanducci, E. Tamburri, V. Guglielmotti, M. Rossi, Si/C hybrid nanostructures for Li-ion anodes: An overview, J. Power Sources. 246 (2014) 167–177. https://doi.org/10.1016/j.jpowsour.2013.07.065.

[41] N.-S. Choi, K.H. Yew, H. Kim, S.-S. Kim, W.-U. Choi, Surface layer formed on silicon thin-film electrode in lithium bis(oxalato) borate-based electrolyte, J. Power Sources. 172 (2007) 404–409. https://doi.org/10.1016/J.JPOWSOUR.2007.07.058.

[42] V.L. Chevrier, L. Liu, D.B. Le, J. Lund, B. Molla, K. Reimer, L.J. Krause, L.D. Jensen, E. Figgemeier, K.W. Eberman, Evaluating Si-Based Materials for Li-Ion Batteries in Commercially Relevant Negative Electrodes, J. Electrochem. Soc. 161 (2014) A783–A791. https://doi.org/10.1149/2.066405jes.

[43] Z. Du, R.A. Dunlap, M.N. Obrovac, High Energy Density Calendered Si Alloy/Graphite Anodes, J. Electrochem. Soc. 161 (2014) A1698–A1705. https://doi.org/10.1149/2.0941410jes.

[44] S.J. Lee, H.K. Baik, S.M. Lee, An all-solid-state thin film battery using LISIPON electrolyte and Si-V negative electrode films, Electrochem. Commun. 5 (2003) 32–35. https://doi.org/10.1016/S1388-2481(02)00528-3.

[45] M.D. Fleischauer, J.M. Topple, J.R. Dahn, Combinatorial Investigations of Si-M (M = Cr + Ni, Fe, Mn) Thin Film Negative Electrode Materials, Electrochem. Solid-State Lett. 8 (2005) A137. https://doi.org/10.1149/1.1850395.

[46] Z. Du, R.A. Dunlap, M.N. Obrovac, Structural and Electrochemical Investigation of Fe x Si 1-x Thin Films in Li Cells, J. Electrochem. Soc. 163 (2016) A2011–A2016. https://doi.org/10.1149/2.0961609jes.

[47] Y.L. Kim, H.Y. Lee, S.W. Jang, S.H. Lim, S.J. Lee, H.K. Baik, Y.S. Yoon, S.M. Lee, Electrochemical characteristics of Co-Si alloy and multilayer films as anodes for lithium ion microbatteries, Electrochim. Acta. 48 (2003) 2593–2597. https://doi.org/10.1016/S0013-4686(03)00302-5.

[48] Z. Du, S.N. Ellis, R.A. Dunlap, M.N. Obrovac, Ni x Si 1-x Alloys Prepared by Mechanical Milling as Negative Electrode Materials for Lithium Ion Batteries, J. Electrochem. Soc. 163 (2016) A13–A18. https://doi.org/10.1149/2.0011602jes.

[49] Y. Wang, S. Cao, M. Kalinina, L. Zheng, L. Li, M. Zhu, M.N. Obrovac, Lithium Insertion in Nanostructured Si 1-x Ti x Alloys, J. Electrochem. Soc. 164 (2017) A3006–A3010. https://doi.org/10.1149/2.0491713jes.

[50] Z. Du, T.D. Hatchard, R.A. Dunlap, M.N. Obrovac, Combinatorial Investigations of Ni-Si Negative Electrode Materials for Li-Ion Batteries, J. Electrochem. Soc. 162 (2015) A1858–A1863. https://doi.org/10.1149/2.0731509jes.

[51] M. Ruttert, V. Siozios, M. Winter, T. Placke, Mechanochemical Synthesis of Fe-Si-Based Anode Materials for High-Energy Lithium Ion Full-Cells, ACS Appl. Energy Mater. 3 (2020) 743–758. https://doi.org/10.1021/acsaem.9b01926.

[52] L. MacEachern, R.A. Dunlap, M.N. Obrovac, A Combinatorial Investigation of Fe-Si-Zn Thin Film Negative Electrodes for Li-Ion Batteries, J. Electrochem. Soc. 162 (2015) A229–A234. https://doi.org/10.1149/2.1051501jes.

[53] Y. Chen, J. Qian, Y. Cao, H. Yang, X. Ai, Green synthesis and stable Li-storage performance of FeSi 2/Si@C nanocomposite for lithium-ion batteries, ACS Appl. Mater. Interfaces. 4 (2012) 3753–3758. https://doi.org/10.1021/am300952b.

[54] H.-T. Kwon, A.-R. Park, S.-S. Lee, H. Cho, H. Jung, C.-M. Park, Nanostructured Si-FeSi 2 -Graphite-C Composite: An Optimized and Practical Solution for Si-Based Anodes for Superior Li-Ion Batteries, J. Electrochem. Soc. 166 (2019) A2221–A2229. https://doi.org/10.1149/2.1401910jes.

[55] Y. Cao, B. Scott, R.A. Dunlap, J. Wang, M.N. Obrovac, An Investigation of the Fe-Mn-Si System for Li-Ion Battery Negative Electrodes, J. Electrochem. Soc. 165 (2018) 1–6. https://doi.org/10.1149/2.1111816jes.

[56] X. Zhao, R.J. Sanderson, M.A. Al-Maghrabi, R.A. Dunlap, M.N. Obrovac, Electrochemistry of Sputtered and Ball Milled Si-Fe-O Alloys in Li Cells, J. Electrochem. Soc. 164 (2017) A1165–A1172. https://doi.org/10.1149/2.1031706jes.

[57] H.-Y. Lee, S.-M. Lee, Graphite–FeSi alloy composites as anode materials for rechargeable lithium batteries, J. Power Sources. 112 (2002) 649–654. https://doi.org/10.1016/S0378-7753(02)00461-5.

[58] J. Kaiser, V. Chevrier, E. Figgemeier, K. Eberman, Commercialization of Silicon Anodes for Electric Vehicle Applications, 2017. http://cii-resource.com/cet/AABE-03-17/Presentations/BTMT/Kaiser_Joerg.pdf (accessed February 26, 2021).

[59] A. Hohl, T. Wieder, P.A. Van Aken, T.E. Weirich, G. Denninger, M. Vidal, S. Oswald, C. Deneke, J. Mayer, H. Fuess, An interface clusters mixture model for the structure of amorphous silicon monoxide (SiO), J. Non. Cryst. Solids. 320 (2003) 255–280. https://doi.org/10.1016/S0022-3093(03)00031-0.

[60] M.A. Al-Maghrabi, J. Suzuki, R.J. Sanderson, V.L. Chevrier, R.A. Dunlap, J.R. Dahn, Combinatorial Studies of Si 1−x O x as a Potential Negative Electrode Material for Li-Ion Battery Applications, J. Electrochem. Soc. 160160 (2013) 1587–1593. https://doi.org/10.1149/2.115309jes.

[61] C.M. Park, W. Choi, Y. Hwa, J.H. Kim, G. Jeong, H.J. Sohn, Characterizations and electrochemical behaviors of disproportionated SiO and its composite for rechargeable Li-ion batteries, J. Mater. Chem. 20 (2010) 4854–4860. https://doi.org/10.1039/b923926j.

[62] Y. Hwa, C.M. Park, H.J. Sohn, Modified SiO as a high performance anode for Li-ion batteries, J. Power Sources. 222 (2013) 129–134. https://doi.org/10.1016/j.jpowsour.2012.08.060.

[63] M. Mamiya, M. Kikuchi, H. Takei, Crystallization of fine silicon particles from silicon monoxide, J. Cryst. Growth. 237–239 (2002) 1909–1914. https://doi.org/10.1016/S0022-0248(01)02244-8.

[64] K. Yasuda, Y. Kashitani, S. Kizaki, K. Takeshita, T. Fujita, S. Shimosaki, Thermodynamic analysis and effect of crystallinity for silicon monoxide negative electrode for lithium ion batteries, J. Power Sources. 329 (2016) 462–472. https://doi.org/10.1016/j.jpowsour.2016.08.110.

[65] C.C. Nguyen, H. Choi, S.-W. Song, Roles of Oxygen and Interfacial Stabilization in Enhancing the Cycling Ability of Silicon Oxide Anodes for Rechargeable Lithium Batteries, J. Electrochem. Soc. 160 (2013) A906–A914. https://doi.org/10.1149/2.118306jes.

[66] Y. Cao, J.C. Bennett, R.A. Dunlap, M.N. Obrovac, A Simple Synthesis Route for High-Capacity SiO x Anode Materials with Tunable Oxygen Content for Lithium-Ion Batteries, Chem. Mater. 30 (2018) 7418–7422. https://doi.org/10.1021/acs.chemmater.8b02977.

[67] S.S. Suh, W.Y. Yoon, D.H. Kim, S.U. Kwon, J.H. Kim, Y.U. Kim, C.U. Jeong, Y.Y. Chan, S.H. Kang, J.K. Lee, Electrochemical behavior of SiOx anodes with variation of oxygen ratio for Li-ion batteries, Electrochim. Acta. 148 (2014) 111–117. https://doi.org/10.1016/j.electacta.2014.08.104.

[68] http://www.btrchina.com/product/84.html, (2019). http://www.btrchina.com/product/84.html (accessed September 12, 2019).

[69] Elon Musk: Our lithium ion batteries should be called Nickel-Graphite..., Benchmark Miner. Intell. (2019). https://www.benchmarkminerals.com/elon-musk-our-lithium-ion-batteries-should-be-called-nickel-graphite/ (accessed September 12, 2019).

[70] Y.N. Jo, Y. Kim, J.S. Kim, J.H. Song, K.J. Kim, C.Y. Kwag, D.J. Lee, C.W. Park, Y.J. Kim, Si-graphite composites as anode materials for lithium secondary batteries, J. Power Sources. 195 (2010) 6031–6036. https://doi.org/10.1016/j.jpowsour.2010.03.008.

[71] T. Chen, J. Wu, Q. Zhang, X. Su, Recent advancement of SiOxbased anodes for lithium-ion batteries, J. Power Sources. 363 (2017) 126–144. https://doi.org/10.1016/j.jpowsour.2017.07.073.

[72] A.M. Escamilla-Pérez, A. Roland, S. Giraud, C. Guiraud, H. Virieux, K. Demoulin, Y. Oudart, N. Louvain, L. Monconduit, Pitch-based carbon/nano-silicon composite, an efficient anode for Li-ion batteries, RSC Adv. 9 (2019) 10546–10553. https://doi.org/10.1039/c9ra00437h.

[73] Z.S. Wen, J. Yang, B.F. Wang, K. Wang, Y. Liu, High capacity silicon/carbon composite anode materials for lithium ion batteries, Electrochem. Commun. 5 (2003) 165–168. https://doi.org/10.1016/S1388-2481(03)00009-2.

[74] Y. Xu, G. Yin, Y. Ma, P. Zuo, X. Cheng, Nanosized core/shell silicon@carbon anode material for lithium ion batteries with polyvinylidene fluoride as carbon source, J. Mater. Chem. 20 (2010) 3216–3220. https://doi.org/10.1039/b921979j.

[75] W. Li, Y. Tang, W. Kang, Z. Zhang, X. Yang, Y. Zhu, W. Zhang, C.S. Lee, Core-Shell Si/C Nanospheres Embedded in Bubble Sheet-like Carbon Film with Enhanced Performance as Lithium Ion Battery Anodes, Small. 11 (2015) 1345–1351. https://doi.org/10.1002/smll.201402072.

[76] J. Yu, J. Yang, X. Feng, H. Jia, J. Wang, W. Lu, Uniform carbon coating on silicon nanoparticles by dynamic CVD process for electrochemical lithium storage, Ind. Eng. Chem. Res. 53 (2014) 12697–12704. https://doi.org/10.1021/ie5010465.

[77] T. Kasukabe, H. Nishihara, S. Iwamura, T. Kyotani, Remarkable performance improvement of inexpensive ball-milled Si nanoparticles by carbon-coating for Li-ion batteries, J. Power Sources. 319 (2016) 99–103. https://doi.org/10.1016/j.jpowsour.2016.04.050.

[78] T. Hirose, M. Morishita, H. Yoshitake, T. Sakai, Study of structural changes that occurred during charge/discharge of carbon-coated SiO anode by nuclear magnetic resonance, Solid State Ionics. 303 (2017) 154–160. https://doi.org/10.1016/j.ssi.2017.03.004.

[79] C. Wang, F. Luo, H. Lu, X. Rong, B. Liu, G. Chu, Y. Sun, B. Quan, J. Zheng, J. Li, C. Gu, X. Qiu, H. Li, L. Chen, A well-defined silicon nanocone-carbon structure for demonstrating exclusive influences of carbon coating on silicon anode of lithium-ion batteries, ACS Appl. Mater. Interfaces. 9 (2017) 2806–2814. https://doi.org/10.1021/acsami.6b13028.

[80] W. Luo, X. Chen, Y. Xia, M. Chen, L. Wang, Q. Wang, W. Li, J. Yang, Surface and Interface Engineering of Silicon-Based Anode Materials for Lithium-Ion Batteries, Adv. Energy Mater. 7 (2017) 1701083. https://doi.org/10.1002/aenm.201701083.

[81] N. Dimov, S. Kugino, M. Yoshio, Carbon-coated silicon as anode material for lithium ion batteries: Advantages and limitations, Electrochim. Acta. 48 (2003) 1579–1587. https://doi.org/10.1016/S0013-4686(03)00030-6.

[82] M. Alias, O. Crosnier, I. Sandu, G. Jestin, A. Papadimopoulos, F. Le Cras, D.M. Schleich, T. Brousse, Silicon/graphite nanocomposite electrodes prepared by low pressure chemical vapor deposition, J. Power Sources. 174 (2007) 900–904. https://doi.org/10.1016/j.jpowsour.2007.06.088.

[83] P. Li, G. Zhao, X. Zheng, X. Xu, C. Yao, W. Sun, S.X. Dou, Recent progress on silicon-based anode materials for practical lithium-ion battery applications, Energy Storage Mater. 15 (2018) 422–446. https://doi.org/10.1016/j.ensm.2018.07.014.

[84] M. Ko, S. Chae, J. Ma, N. Kim, H.W. Lee, Y. Cui, J. Cho, Scalable synthesis of silicon-nanolayer-embedded graphite for high-energy lithium-ion batteries, Nat. Energy. 1 (2016). https://doi.org/10.1038/nenergy.2016.113.

[85] Z. Lu, N. Liu, H.W. Lee, J. Zhao, W. Li, Y. Li, Y. Cui, Nonfilling carbon coating of porous silicon micrometer-sized particles for high-performance lithium battery anodes, ACS Nano. 9 (2015) 2540–2547. https://doi.org/10.1021/nn505410q.

[86] N. Liu, Z. Lu, J. Zhao, M.T. McDowell, H.-W. Lee, W. Zhao, Y. Cui, A pomegranate-inspired nanoscale design for large-volume-change lithium battery anodes, Nat. Nanotechnol. 9 (2014) 187–192. https://doi.org/10.1038/nnano.2014.6.

[87] N. Liu, H. Wu, M.T. McDowell, Y. Yao, C. Wang, Y. Cui, A yolk-shell design for stabilized and scalable Li-ion battery alloy anodes, Nano Lett. 12 (2012) 3315–3321. https://doi.org/10.1021/nl3014814.

[88] Y. Li, K. Yan, H.-W. Lee, Z. Lu, N. Liu, Y. Cui, Growth of conformal graphene cages on micrometre-sized silicon particles as stable battery anodes, Nat. Energy. 1 (2016) 15029. https://doi.org/10.1038/nenergy.2015.29.

[89] J. Luo, X. Zhao, J. Wu, H.D. Jang, H.H. Kung, J. Huang, Crumpled Graphene-Encapsulated Si Nanoparticles for Lithium Ion Battery Anodes, J. Phys. Chem. Lett. 3 (2012) 20. https://doi.org/10.1021/jz3006892.

[90] Y. Cao, T.D. Hatchard, R.A. Dunlap, M.N. Obrovac, Mechanofusion-derived Si-alloy/graphite composite electrode materials for Li-ion batteries, J. Mater. Chem. A. 7 (2019) 8335–8343. https://doi.org/10.1039/c9ta00132h.

[91] M. Wu, X. Xiao, N. Vukmirovic, S. Xun, P.K. Das, X. Song, P. Olalde-Velasco, D. Wang, A.Z. Weber, L.W. Wang, V.S. Battaglia, W. Yang, G. Liu, Toward an ideal polymer binder design for high-capacity battery anodes, J. Am. Chem. Soc. 135 (2013) 12048–12056. https://doi.org/10.1021/ja4054465.

[92] S. Komaba, K. Shimomura, N. Yabuuchi, T. Ozeki, H. Yui, K. Konno, Study on polymer binders for high-capacity SiO negative electrode of Li-Ion batteries, J. Phys. Chem. C. 115 (2011) 13487–13495. https://doi.org/10.1021/jp201691g.

[93] C.C. Nguyen, T. Yoon, D.M. Seo, P. Guduru, B.L. Lucht, Systematic Investigation of Binders for Silicon Anodes: Interactions of Binder with Silicon Particles and Electrolytes and Effects of Binders on Solid Electrolyte Interphase Formation, ACS Appl. Mater. Interfaces. 8 (2016) 12211–12220. https://doi.org/10.1021/acsami.6b03357.

[94] T.W. Kwon, J.W. Choi, A. Coskun, The emerging era of supramolecular polymeric binders in silicon anodes, Chem. Soc. Rev. 47 (2018) 2145–2164. https://doi.org/10.1039/c7cs00858a.

[95] K. Xu, Electrolytes and interphases in Li-ion batteries and beyond, Chem. Rev. 114 (2014) 11503–11618. https://doi.org/10.1021/cr500003w.

[96] Y.M. Lee, J.Y. Lee, H.-T. Shim, J.K. Lee, J.-K. Park, SEI Layer Formation on Amorphous Si Thin Electrode during Precycling, J. Electrochem. Soc. 154 (2007) A515. https://doi.org/10.1149/1.2719644.

[97] X. Zhao, V.P. Lehto, Challenges and prospects of nanosized silicon anodes in lithium-ion batteries, Nanotechnology. 32 (2021) 42002. https://doi.org/10.1088/1361-6528/abb850.

[98] M. Nie, D.P. Abraham, Y. Chen, A. Bose, B.L. Lucht, Silicon solid electrolyte interphase (SEI) of lithium ion battery characterized by microscopy and spectroscopy, J. Phys. Chem. C. 117 (2013) 13403–13412. https://doi.org/10.1021/jp404155y.

[99] I. Abe, T. Horiba, Y. Abe, K. Hida, T. Matsuyama, S. Yasuno, S. Komaba, Investigation and Improvement of Metallic Aluminum as Alloying Electrode in Non-Aqueous Li Cells, J. Electrochem. Soc. 167 (2020) 110513. https://doi.org/10.1149/1945-7111/aba078.

[100] G.G. Eshetu, E. Figgemeier, Confronting the Challenges of Next-Generation Silicon Anode-Based Lithium-Ion Batteries: Role of Designer Electrolyte Additives and Polymeric Binders, ChemSusChem. 12 (2019) 2515–2539. https://doi.org/10.1002/cssc.201900209.

[101] N.S. Choi, K.H. Yew, K.Y. Lee, M. Sung, H. Kim, S.S. Kim, Effect of fluoroethylene carbonate additive on interfacial properties of silicon thin-film electrode, J. Power Sources. 161 (2006) 1254–1259. https://doi.org/10.1016/j.jpowsour.2006.05.049.

[102] C.C. Nguyen, B.L. Lucht, Comparative Study of Fluoroethylene Carbonate and Vinylene Carbonate for Silicon Anodes in Lithium Ion Batteries, J. Electrochem. Soc. 161 (2014) A1933–A1938. https://doi.org/10.1149/2.0731412jes.

[103] V. Etacheri, O. Haik, Y. Goffer, G.A. Roberts, I.C. Stefan, R. Fasching, D. Aurbach, Effect of fluoroethylene carbonate (FEC) on the performance and surface chemistry of Si-nanowire li-ion battery anodes, Langmuir. 28 (2012) 965–976. https://doi.org/10.1021/la203712s.

[104] K. Schroder, J. Alvarado, T.A. Yersak, J. Li, N. Dudney, L.J. Webb, Y.S. Meng, K.J. Stevenson, The Effect of Fluoroethylene Carbonate as an Additive on the Solid Electrolyte Interphase on Silicon Lithium-Ion Electrodes, Chem. Mater. 27 (2015) 5531–5542. https://doi.org/10.1021/acs.chemmater.5b01627.

[105] H. Nakai, T. Kubota, A. Kita, A. Kawashima, Investigation of the Solid Electrolyte Interphase Formed by Fluoroethylene Carbonate on Si Electrodes, J. Electrochem. Soc. 158 (2011) A798. https://doi.org/10.1149/1.3589300.

[106] R. Petibon, V.L. Chevrier, C.P. Aiken, D.S. Hall, S.R. Hyatt, R. Shunmugasundaram, J.R. Dahn, Studies of the Capacity Fade Mechanisms of LiCoO 2 /Si-Alloy: Graphite Cells, J. Electrochem. Soc. 163 (2016) A1146–A1156. https://doi.org/10.1149/2.0191607jes.

[107] D.Y. Wang, N.N. Sinha, J.C. Burns, C.P. Aiken, R. Petibon, J.R. Dahn, A Comparative Study of Vinylene Carbonate and Fluoroethylene Carbonate Additives for LiCoO 2 /Graphite Pouch Cells, J. Electrochem. Soc. 161 (2014) A467–A472. https://doi.org/10.1149/2.001404jes.

[108] K. Kim, I. Park, S.Y. Ha, Y. Kim, M.H. Woo, M.H. Jeong, W.C. Shin, M. Ue, S.Y. Hong, N.S. Choi, Understanding the thermal instability of fluoroethylene carbonate in LiPF6-based electrolytes for lithium ion batteries, Electrochim. Acta. 225 (2017) 358–368. https://doi.org/10.1016/j.electacta.2016.12.126.

[109] C. Suryanarayana, Mechanical Alloying and Milling Mechanical Engineering, Prog. Mater. Sci. 1 (2001).

[110] C.C. Koch, J.D. Whittenberge, Mechanical milling / alloying of intermetallics, Intermetallics. 4 (1996) 339–355. https://doi.org/10.1016/0966-9795(96)00001-5.

[111] C.C. Koch, O.B. Cavin, C.G. McKamey, J.O. Scarbrough, Preparation of amorphous Ni60Nb40 by mechanical alloying, Appl. Phys. Lett. 43 (1983) 1017–1019. https://doi.org/10.1063/1.94213.

[112] J.S. Benjamin, Mechanical Alloying, Sci. Am. 234 (1976) 40–49. https://www.jstor.org/stable/24950349?seq=3#metadata_info_tab_contents (accessed March 3, 2021).

[113] G. Cocco, F. Delogu, L. Schiffini, Toward a quantitative understanding of the mechanical alloying process, J. Mater. Synth. Process. 8 (2000) 167–180. https://doi.org/10.1023/A:1011308025376.

[114] T.D. Hatchard, A. Genkin, M.N. Obrovac, Rapid mechanochemical synthesis of amorphous alloys, AIP Adv. 7 (2017) 045201. https://doi.org/10.1063/1.4979890.

[115] P.Y. Lee, C.C. Koch, Formation of amorphous Ni-Zr alloy powder by mechanical alloying of intermetallic powder mixtures and mixtures of nickel or zirconium with intermetallics, J. Mater. Sci. 23 (1988) 2837–2845. https://doi.org/10.1007/BF00547458.

[116] B.S. Murty, S. Ranganathan, Novel materials synthesis by mechanical alloying/milling, Int. Mater. Rev. 43 (1998) 101–141. https://doi.org/10.1179/095066098790105654.

[117] Y. Liu, B. Scott, M.N. Obrovac, Ball Milled Si-W Alloys: Part I. Microstructural and Phase Evolution during Ball Milling, J. Electrochem. Soc. 166 (2019) A1170–A1175. https://doi.org/10.1149/2.0851906jes.

[118] M. Gauthier, D. Mazouzi, D. Reyter, B. Lestriez, P. Moreau, D. Guyomard, L. Roué, A low-cost and high performance ball-milled Si-based negative electrode for high-energy Li-ion batteries, Energy Environ. Sci. 6 (2013) 2145. https://doi.org/10.1039/c3ee41318g.

[119] P. Gu, R. Cai, Y. Zhou, Z. Shao, Si/C composite lithium-ion battery anodes synthesized from coarse silicon and citric acid through combined ball milling and thermal pyrolysis, Electrochim. Acta. 55 (2010) 3876–3883. https://doi.org/10.1016/j.electacta.2010.02.006.

[120] S. Cao, J.C. Bennett, Y. Wang, S. Gracious, M. Zhu, M.N. Obrovac, Si–TiN alloy Li-ion battery anode materials prepared by reactive N2 gas milling, J. Power Sources. 438 (2019) 227003. https://doi.org/10.1016/j.jpowsour.2019.227003.

[121] Q. Si, K. Hanai, T. Ichikawa, M.B. Phillipps, A. Hirano, N. Imanishi, O. Yamamoto, Y. Takeda, Improvement of cyclic behavior of a ball-milled SiO and carbon nanofiber composite anode for lithium-ion batteries, J. Power Sources. 196 (2011) 9774–9779. https://doi.org/10.1016/J.JPOWSOUR.2011.08.005.

[122] K.M. Lee, Y.S. Lee, Y.W. Kim, Y.K. Sun, S.M. Lee, Electrochemical characterization of Ti-Si and Ti-Si-Al alloy anodes for Li-ion batteries produced by mechanical ball milling, J. Alloys Compd. 472 (2009) 461–465. https://doi.org/10.1016/j.jallcom.2008.04.102.

[123] T. Kasukabe, H. Nishihara, S. Iwamura, T. Kyotani, Remarkable performance improvement of inexpensive ball-milled Si nanoparticles by carbon-coating for Li-ion batteries, J. Power Sources. 319 (2016) 99–103. https://doi.org/10.1016/j.jpowsour.2016.04.050.

[124] Y.S. Yoon, S.H. Jee, S.H. Lee, S.C. Nam, Nano Si-coated graphite composite anode synthesized by semi-mass production ball milling for lithium secondary batteries, Surf. Coatings Technol. 206 (2011) 553–558. https://doi.org/10.1016/j.surfcoat.2011.07.076.

[125] Y. Wang, J.M. Lee, X. Wang, An investigation of the origin of the electrochemical hydrogen storage capacities of the ball-milled Co-Si composites, Int. J. Hydrogen Energy. 35 (2010) 1669–1673. https://doi.org/10.1016/j.ijhydene.2009.12.026.

[126] L. MacEachern, R.A. Dunlap, M.N. Obrovac, Mechanically Milled Fe-Si-Zn Alloys as Negative Electrodes for Li-Ion Batteries, J. Electrochem. Soc. 162 (2015) A2319–A2324. https://doi.org/10.1149/2.0601512jes.

[127] Y. Cao, J.C. Bennett, R.A. Dunlap, M.N. Obrovac, Li Insertion in Ball Milled Si-Mn Alloys, J. Electrochem. Soc. 165 (2018) A1734–A1740. https://doi.org/10.1149/2.0381809jes.

[128] M. Gauthier, D. Mazouzi, D. Reyter, B. Lestriez, P. Moreau, D. Guyomard, L. Roué, A low-cost and high performance ball-milled Si-based negative electrode for high-energy Li-ion batteries, Energy Environ. Sci. 6 (2013) 2145–2155. https://doi.org/10.1039/c3ee41318g.

[129] G.. Wang, L. Sun, D.. Bradhurst, S. Zhong, S.. Dou, H.. Liu, Innovative nanosize lithium storage alloys with silica as active centre, J. Power Sources. 88 (2000) 278–281. https://doi.org/10.1016/S0378-7753(00)00385-2.

[130] P.P. Ferguson, A.D.W. Todd, J.R. Dahn, Comparison of mechanically alloyed and sputtered tin-cobalt-carbon as an anode material for lithium-ion batteries, Electrochem. Commun. 10 (2008) 25–31. https://doi.org/10.1016/j.elecom.2007.10.025.

[131] Z. Du, H. Liu, S.N. Ellis, R.A. Dunlap, M. Zhu, M.N. Obrovac, Electrochemistry of Cu x Si 1−x Alloys in Li Cells, J. Electrochem. Soc. 163 (2016) A1275–A1279. https://doi.org/10.1149/2.0811607jes.

[132] P. Wang, Y. NuLi, J. Yang, Y. Zheng, Carbon-coated Si-Cu/graphite composite as anode material for lithium-ion batteries, Int. J. Electrochem. Sci. 1 (2006) 122–129.

[133] X. Chen, X. Li, F. Ding, W. Xu, J. Xiao, Y. Cao, P. Meduri, J. Liu, G.L. Graff, J.G. Zhang, Conductive rigid skeleton supported silicon as high-performance Li-Ion battery anodes, Nano Lett. 12 (2012) 4124–4130. https://doi.org/10.1021/nl301657y.

[134] T.D. Hatchard, A. Genkin, M.N. Obrovac, Rapid mechanochemical synthesis of amorphous alloys, AIP Adv. 7 (2017). https://doi.org/10.1063/1.4979890.

[135] T. Yokoyania, K. Urayama, T. Yokoyama, Ultra-Fine Grinding and Consequent Changes of Powder Characteristics, KONA Powder Part. J. 1 (1983) 53–63. https://doi.org/10.14356/kona.1983010.

[136] M. Naito, A. Kondo, T. Yokoyama, Applications of Comminution Techniques for the Surface Modification of Powder Materials, ISIJ Int. 33 (1993) 915–924. https://doi.org/10.2355/isijinternational.33.915.

[137] C.S. and T.T. Y. Wakizaka, Carbon material for negative electrode for lithium ion secondary battery, manufacturing process therefor and use thereof, US20180226649A1, 2018. https://patents.google.com/patent/US20180226649A1/en?oq=US20180226649A1 (accessed March 13, 2021).

[138] T.H. and A.S. T. Suzuki, N. Ishimaru, T. Oyama, T. Tano, T. Oda, I. Fujinaga, T. Urai, S. Okazaki, K. Kurata, Graphite material for negative electrodes of lithium ion secondary battery, manufacturing method for said material, and lithium ion secondary battery using same, US9142832B2, 2015. https://patents.google.com/patent/US9142832B2/en?oq=US+9%2C142%2C832+B2 (accessed March 13, 2021).

[139] R.C. Roop, Solid State Chemistry, 2003.

[140] J. Camardese, Core-Shell Materials as Positive Electrodes in Lithium-Ion Batteries, Dalhousie University, 2015. https://dalspace.library.dal.ca/handle/10222/56358 (accessed February 23, 2018).

[141] JCPDS International Centre for Diffraction Data, International Centre for Diffraction Data, PDF-2. (2002).

[142] W. Zhou, Z.L. Wang, Scanning microscopy for nanotechnology: Techniques and applications, Springer Science & Business Media, 2007. https://doi.org/10.1007/978-0-387-39620-0.

[143] P. Echlin, Handbook of Sample Preparation for Scanning Electron Microscopy and X-Ray microanalysis, Springer Science & Business Media, 2009. https://books.google.ca/books?hl=en&lr=&id=TDDM3VN_I4wC&oi=fnd&pg=PP2&dq=Echlin,+P.+Handbook+of+Sample+Preparation+for+Scanning+Electron+Microscopy+and+X-Ray+Microanalysis%3B+Springer+Science+%2B+Business+Media,+New+York,+2009.+(227)&ots=6kvPvTwvK1&sig=TE.

[144] R.F. Egerton, Physical Principles of Electron Microscopy, Springer Science & Business Media, New York, 2005. ftp://nozdr.ru/biblio/kolxo3/P/PQm/Egerton R.F. Physical Principles of Electron Microscopy (Springer, 2005)(ISBN 0387258000)(211s)_PQm_.pdf.

[145] C.A. Evans, S. Wilson, Materials characterization, 1992. https://doi.org/10.1002/9783527670772.

[146] G. Stingeder, S. Gara, S. Pahlke, H. Schwenk, E. Guerrero, M. Grasserbauer, Quantitative determination of oxygen in silicon by combination of FTIR-spectroscopy, inert gas fusion analysis and secondary ion mass spectroscopy, Fresenius' Zeitschrift Für Anal. Chemie. 333 (1989) 576–582. https://doi.org/10.1007/BF00572379.

[147] LECO analyzer 836 Series, (2021). https://www.leco.com/product/836-series (accessed March 15, 2021).

[148] R.A. Anani, A., & Huggins, Multinary alloy electrodes for solid state batteries I. A phase diagram approach for the selection and storage properties determination of candidate electrode materials., J. Power Sources. 38 (1992) 351–362.

[149] W. Zhang, Lithium insertion/extraction mechanism in alloy anodes for lithium-ion batteries, J. Power Sources. 196 (2011) 877–885. https://doi.org/10.1016/j.jpowsour.2010.08.114.

[150] T.D. Hatchard, J.R. Dahn, In Situ XRD and Electrochemical Study of the Reaction of Lithium with Amorphous Silicon, J. Electrochem. Soc. 151 (2004) A838. https://doi.org/10.1149/1.1739217.

[151] P. Zuo, G. Yin, Si-Mn composite anodes for lithium ion batteries, J. Alloys Compd. 414 (2006) 265–268. https://doi.org/10.1016/j.jallcom.2005.07.026.

[152] W. He, H. Tian, F. Xin, W. Han, Scalable fabrication of micro-sized bulk porous Si from Fe-Si alloy as a high performance anode for lithium-ion batteries, J. Mater. Chem. A. 3 (2015) 17956–17962. https://doi.org/10.1039/c5ta04857e.

[153] X. Li, Y. Zheng, Z. Li, Y. Liu, H. Huang, Q. Wang, C. Dong, Effect of dual local structures of amorphous Fe–Si films on the performance of anode of lithium-ion batteries, Mater. Chem. Phys. 243 (2020) 122666. https://doi.org/10.1016/j.matchemphys.2020.122666.

[154] M. Ruttert, V. Siozios, M. Winter, T. Placke, Mechanochemical Synthesis of Fe-Si-Based Anode Materials for High-Energy Lithium Ion Full-Cells, ACS Appl. Energy Mater. 3 (2020) 743–758. https://doi.org/10.1021/acsaem.9b01926.

[155] H. Wang, S. Fan, Y. Cao, H. Yang, X. Ai, F. Zhong, Building a Cycle-Stable Fe-Si Alloy/Carbon Nanocomposite Anode for Li-Ion Batteries through a Covalent-Bonding Method, ACS Appl. Mater. Interfaces. 12 (2020) 30503–30509. https://doi.org/10.1021/acsami.0c08456.

[156] M. Oh, I. Kim, H.J. Lee, S. Hyun, C. Kang, The role of thermal annealing on the microstructures of (Ti, Fe)-alloyed Si thin-film anodes for high-performance Li-ion batteries, RSC Adv. 8 (2018) 9168–9174. https://doi.org/10.1039/c7ra13172k.

[157] Y. Du, Z. Yang, L. Bai, F. Ding, H. Jin, Y. Yang, T.D. Lam, G. Hou, F. Yuan, Si/FeSi2 Nanoparticles Prepared by Thermal Plasma with Stress-releasing Effect for Li-ion Storage, ChemNanoMat. 7 (2021) 467–475. https://doi.org/10.1002/cnma.202100039.

[158] J. Jang, I. Kang, M.S. Kim, J.H. Kim, Y.S. Lee, K.W. Yi, Y.W. Cho, Si/iron silicide nanocomposite anodes with furfuryl-alcohol-derived carbon coating for Li-ion batteries, J. Mater. Sci. 52 (2017) 5027–5037. https://doi.org/10.1007/s10853-016-0740-8.

[159] M. Ruttert, V. Siozios, M. Winter, T. Placke, Synthesis and Comparative Investigation of Silicon Transition Metal Silicide Composite Anodes for Lithium Ion Batteries, Zeitschrift Fur Anorg. Und Allg. Chemie. 645 (2019) 248–256. https://doi.org/10.1002/zaac.201800436.

[160] L.J. Krause, T. Brandt, V.L. Chevrier, L.D. Jensen, Surface Area Increase of Silicon Alloys in Li-Ion Full Cells Measured by Isothermal Heat Flow Calorimetry, J. Electrochem. Soc. 164 (2017) A2277–A2282. https://doi.org/10.1149/2.0501712jes.

[161] Y. Cao, R.A. Dunlap, M.N. Obrovac, Electrochemistry and Thermal Behavior of SiO x Made by Reactive Gas Milling , J. Electrochem. Soc. 167 (2020) 110501. https://doi.org/10.1149/1945-7111/ab9e83.

[162] E. Gaffet, N. Malhouroux, M. Abdellaoui, Far from equilibrium phase transition induced by solid-state reaction in the FeSi system, J. Alloys Compd. 194 (1993) 339–360. https://doi.org/10.1016/0925-8388(93)90020-N.

[163] O. Kubaschewski, H. Okamoto, Phase diagrams of binary iron alloys, ASM Int. (1993) 364–366.

[164] B. Scott, C.A.M. Brown, R.A. Dunlap, M.N. Obrovac, Quantitative composition determination by Mössbauer spectroscopy, MRS Commun. 10 (2020) 123–128. https://doi.org/10.1557/mrc.2019.158.

[165] H. Liu, M. Zhu, Z. Du, M.N. Obrovac, The Electrochemistry of Amorphous Si-B Thin Film Electrodes in Li Cells, J. Electrochem. Soc. 163 (2016) A192–A196. https://doi.org/10.1149/2.0451602jes.

[166] J.Y. Kim, A.Y. Kim, G. Liu, J.Y. Woo, H. Kim, J.K. Lee, Li4SiO4-Based Artificial Passivation Thin Film for Improving Interfacial Stability of Li Metal Anodes, ACS Appl. Mater. Interfaces. 10 (2018) 8692–8701. https://doi.org/10.1021/acsami.7b18997.

[167] W. Wu, J. Shi, Y. Liang, F. Liu, Y. Peng, H. Yang, A low-cost and advanced SiOx-C composite with hierarchical structure as an anode material for lithium-ion batteries, Phys. Chem. Chem. Phys. 17 (2015) 13451–13456. https://doi.org/10.1039/c5cp01212k.

[168] M. Miyachi, H. Yamamoto, H. Kawai, Electrochemical Properties and Chemical Structures of Metal-Doped SiO Anodes for Li-Ion Rechargeable Batteries, J. Electrochem. Soc. 154 (2007) A376. https://doi.org/10.1149/1.2455963.

[169] J. Desimoni, F.H. Sánchez, Overview of the Mössbauer results obtained on silicon-rich iron silicide epitaxial phases on Si, Hyperfine Interact. 122 (1999) 277–307. https://doi.org/10.1023/A:1012686815556.

[170] G.K. Wertheim, J.H. Wernick, D.N.E. Buchanan, Mössbauer effect in Co1-xfexSi, J. Appl. Phys. 37 (1966) 3333–3337. https://doi.org/10.1063/1.1708858.

[171] I. Dézsi, C. Fetzer, L. Bujdosó, J. Brötz, A.G. Balogh, Mechanical alloying of Fe-Si and milling of α- And β-FeSi 2 bulk phases, J. Alloys Compd. 508 (2010) 51–54. https://doi.org/10.1016/j.jallcom.2010.07.178.

[172] K.F. Cai, E. Mueller, C. Drasar, C. Stiewe, The effect of titanium diboride addition on the thermoelectric properties of β-FeSi2 semiconductors, Solid State Commun. 131 (2004) 325–329. https://doi.org/10.1016/j.ssc.2004.04.028.

[173] N. Zaccari, D. Aquaro, Mechanical characterization of Li2TiO3 and Li4SiO4 pebble beds: Experimental determination of the material properties and of the pebble bed effective values, Fusion Eng. Des. 82 (2007) 2375–2382. https://doi.org/10.1016/j.fusengdes.2007.05.008.

[174] B. Song, T. Sui, S. Ying, L. Li, L. Lu, A.M. Korsunsky, Nano-structural changes in Li-ion battery cathodes during cycling revealed by FIB-SEM serial sectioning tomography, J. Mater. Chem. A. 3 (2015) 18171–18179. https://doi.org/10.1039/c5ta04151a.

[175] W.S. Rasband, Imagej, us national institutes of health, bethesda, maryland, usa, Http//Imagej. Nih. Gov/Ij/. (2011).

[176] A. Timmons, A.D.W. Todd, S.D. Mead, G.H. Carey, R.J. Sanderson, R.E. Mar, J.R. Dahn, Studies of Si[sub 1−x]C[sub x] Electrode Materials Prepared by High-Energy Mechanical Milling and Combinatorial Sputter Deposition, J. Electrochem. Soc. 154 (2007) A865. https://doi.org/10.1149/1.2755782.

[177] C.-H. Doh, C.-W. Park, H.-M. Shin, D.-H. Kim, Y.-D. Chung, S.-I. Moon, B.-S. Jin, H.-S. Kim, A. Veluchamy, A new SiO/C anode composition for lithium-ion battery, J. Power Sources. 179 (2008) 367–370. https://doi.org/10.1016/j.jpowsour.2007.12.074.

[178] D.L. Zhang, Processing of advanced materials using high-energy mechanical milling, in: Prog. Mater. Sci., 2004: pp. 537–560. https://doi.org/10.1016/S0079-6425(03)00034-3.

[179] B. Zhu, Y. Jin, Y. Tan, L. Zong, Y. Hu, L. Chen, Y. Chen, Q. Zhang, J. Zhu, Scalable Production of Si Nanoparticles Directly from Low Grade Sources for Lithium-Ion Battery Anode, Nano Lett. 15 (2015) 5750–5754. https://doi.org/10.1021/acs.nanolett.5b01698.

[180] S. Jeong, X. Li, J. Zheng, P. Yan, R. Cao, H.J. Jung, C. Wang, J. Liu, J.G. Zhang, Hard carbon coated nano-Si/graphite composite as a high performance anode for Li-ion batteries, J. Power Sources. 329 (2016) 323–329. https://doi.org/10.1016/j.jpowsour.2016.08.089.

[181] D. Dollimore, G.R. Heal, The degradation of selected polymers to carbons in an inert atmosphere, Carbon N. Y. 5 (1967) 65–72. https://doi.org/10.1016/0008-6223(67)90108-X.

[182] M. Inagaki, Y. Okada, H. Miura, H. Konno, Preparation of carbon-coated transition metal particles from mixtures of metal oxide and Polyvinylchloride, Carbon N. Y. 37 (1999) 329–334. https://doi.org/10.1016/S0008-6223(98)00200-0.

[183] J. Kohanoff, G. Galli, M. Parrinello, Theoretical Study of LiC6 My Citations, Le J. Phys. IV. (1991) 1. https://doi.org/10.1051/jp4:1991541ï.

[184] J. Wu, Y. Cao, H. Zhao, J. Mao, Z. Guo, The critical role of carbon in marrying silicon and graphite anodes for high-energy lithium-ion batteries, Carbon Energy. 1 (2019) 57–76. https://doi.org/10.1002/cey2.2.

[185] S.B. Son, L. Cao, T. Yoon, A. Cresce, S.E. Hafner, J. Liu, M. Groner, K. Xu, C. Ban, Interfacially Induced Cascading Failure in Graphite-Silicon Composite Anodes, Adv. Sci. 6 (2019). https://doi.org/10.1002/advs.201801007.

[186] M. Wetjen, M. Trunk, L. Werner, R. Gernhäuser, B. Märkisch, Z. Révay, R. Gilles, H.A. Gasteiger, Quantifying the Distribution of Electrolyte Decomposition Products in Silicon-Graphite Electrodes by Neutron Depth Profiling, J. Electrochem. Soc. 165 (2018) A2340–A2348. https://doi.org/10.1149/2.1341810jes.

[187] S. Chae, S.H. Choi, N. Kim, J. Sung, J. Cho, Integration of Graphite and Silicon Anodes for the Commercialization of High-Energy Lithium-Ion Batteries, Angew. Chemie - Int. Ed. 59 (2020) 110–135. https://doi.org/10.1002/anie.201902085.

[188] G. Ai, Z. Wang, H. Zhao, W. Mao, Y. Fu, R. Yi, Y. Gao, V. Battaglia, D. Wang, S. Lopatin, G. Liu, Scalable process for application of stabilized lithium metal powder in Li-ion batteries, J. Power Sources. 309 (2016) 33–41. https://doi.org/10.1016/j.jpowsour.2016.01.061.

[189] M.W. Forney, M.J. Ganter, J.W. Staub, R.D. Ridgley, B.J. Landi, Prelithiation of silicon-carbon nanotube anodes for lithium ion batteries by stabilized lithium metal powder (SLMP), Nano Lett. 13 (2013) 4158–4163. https://doi.org/10.1021/nl401776d.

[190] Z. Wang, Y. Fu, Z. Zhang, S. Yuan, K. Amine, V. Battaglia, G. Liu, Application of Stabilized Lithium Metal Powder (SLMP®) in graphite anode - A high efficient prelithiation method for lithium-ion batteries, J. Power Sources. 260 (2014) 57–61. https://doi.org/10.1016/j.jpowsour.2014.02.112.

[191] H.J. Kim, S. Choi, S.J. Lee, M.W. Seo, J.G. Lee, E. Deniz, Y.J. Lee, E.K. Kim, J.W. Choi, Controlled Prelithiation of Silicon Monoxide for High Performance Lithium-Ion Rechargeable Full Cells, Nano Lett. 16 (2016) 282–288. https://doi.org/10.1021/acs.nanolett.5b03776.

[192] T.W. Kwon, J.W. Choi, A. Coskun, The emerging era of supramolecular polymeric binders in silicon anodes, Chem. Soc. Rev. 47 (2018) 2145–2164. https://doi.org/10.1039/c7cs00858a.

[193] H. Zhao, W. Yuan, G. Liu, Hierarchical electrode design of high-capacity alloy nanomaterials for lithium-ion batteries, Nano Today. 10 (2015) 193–212. https://doi.org/10.1016/j.nantod.2015.02.009.

[194] J. Bareño, I.A. Shkrob, J.A. Gilbert, M. Klett, D.P. Abraham, Capacity Fade and Its Mitigation in Li-Ion Cells with Silicon-Graphite Electrodes, J. Phys. Chem. C. 121 (2017) 20640–20649. https://doi.org/10.1021/acs.jpcc.7b06118.

[195] M. Wetjen, M. Trunk, L. Werner, R. Gernhäuser, B. Märkisch, Z. Révay, R. Gilles, H.A. Gasteiger, Quantifying the Distribution of Electrolyte Decomposition Products in Silicon-Graphite Electrodes by Neutron Depth Profiling, J. Electrochem. Soc. 165 (2018) A2340–A2348. https://doi.org/10.1149/2.1341810jes.

[196] C.C. Nguyen, B.L. Lucht, Comparative Study of Fluoroethylene Carbonate and Vinylene Carbonate for Silicon Anodes in Lithium Ion Batteries, J. Electrochem. Soc. 161 (2014) A1933–A1938. https://doi.org/10.1149/2.0731412jes.

[197] Y. Jin, N.J.H. Kneusels, L.E. Marbella, E. Castillo-Martínez, P.C.M.M. Magusin, R.S. Weatherup, E. Jónsson, T. Liu, S. Paul, C.P. Grey, Understanding Fluoroethylene Carbonate and Vinylene Carbonate Based Electrolytes for Si Anodes in Lithium Ion Batteries with NMR Spectroscopy, J. Am. Chem. Soc. 140 (2018) 9854–9867. https://doi.org/10.1021/jacs.8b03408.

APPENDIX I

CCC Marketplace™

McGraw Hill LLC - License Terms and Conditions

This is a License Agreement between Yijia Liu ("You") and McGraw Hill LLC ("Publisher") provided by Copyright Clearance Center ("CCC"). The license consists of your order details, the terms and conditions provided by McGraw Hill LLC, and the CCC terms and conditions.

All payments must be made in full to CCC.

Order Date	05-Jun-2021	**Type of Use**	Republish in a thesis/dissertation
Order License ID	1123843-1	**Publisher**	McGraw-Hill
ISBN-13	9780071624213	**Portion**	Chart/graph/table/figure

LICENSED CONTENT

Publication Title	Linden's handbook of batteries	**Country**	United States of America
Author/Editor	Reddy, Thomas B., Linden, David.	**Rightsholder**	McGraw Hill LLC
Date	01/01/2010	**Publication Type**	Book
Language	English		

REQUEST DETAILS

Portion Type	Chart/graph/table/figure	**Distribution**	Worldwide
Number of charts / graphs / tables / figures requested	1	**Translation**	Original language of publication
Format (select all that apply)	Electronic	**Copies for the disabled?**	No
Who will republish the content?	Not-for-profit entity	**Minor editing privileges?**	No
Duration of Use	Current edition and up to 5 years	**Incidental promotional use?**	No
Lifetime Unit Quantity	Up to 499	**Currency**	CAD
Rights Requested	Main product		

NEW WORK DETAILS

Title	Si-Fe-O-based Anodes for Lithium-ion Batteries	**Institution name**	Dalhousie University
Instructor name	Mark Obrovac	**Expected presentation date**	2022-07-22

CCC Marketplace™

IOP Publishing, Ltd - License Terms and Conditions

This is a License Agreement between Yijia Liu ("You") and IOP Publishing, Ltd ("Publisher") provided by Copyright Clearance Center ("CCC"). The license consists of your order details, the terms and conditions provided by IOP Publishing, Ltd, and the CCC terms and conditions.

All payments must be made in full to CCC.

Order Date	05-Jun-2021	**Type of Use**	Republish in a thesis/dissertation
Order License ID	1123841-1	**Publisher**	IOP Publishing
ISSN	1945-7111	**Portion**	Chart/graph/table/figure

LICENSED CONTENT

Publication Title	Journal of the Electrochemical Society	**Country**	United States of America
Author/Editor	Electrochemical Society.	**Rightsholder**	IOP Publishing, Ltd
Date	01/01/1948	**Publication Type**	e-Journal
Language	English	**URL**	http://www.scitation.org/JES

REQUEST DETAILS

Portion Type	Chart/graph/table/figure	**Distribution**	Worldwide
Number of charts / graphs / tables / figures requested	1	**Translation**	Original language of publication
Format (select all that apply)	Electronic	**Copies for the disabled?**	No
Who will republish the content?	Not-for-profit entity	**Minor editing privileges?**	No
Duration of Use	Current edition and up to 5 years	**Incidental promotional use?**	No
Lifetime Unit Quantity	Up to 499	**Currency**	CAD
Rights Requested	Main product		

NEW WORK DETAILS

Title	Si-Fe-O-based Anodes for Lithium-ion Batteries	**Institution name**	Dalhousie University
Instructor name	Mark Obrovac	**Expected presentation date**	2021-07-22

CCC Marketplace™

IOP Publishing, Ltd - License Terms and Conditions

Order Date	05-Jun-2021	**Type of Use**	Republish in a thesis/dissertation
Order License ID	1123844-1	**Publisher**	IOP Publishing
ISSN	0013-4651	**Portion**	Chart/graph/table/figure

LICENSED CONTENT

Publication Title	Journal of the Electrochemical Society	**Rightsholder**	IOP Publishing, Ltd
Article Title	Reversible Cycling of Crystalline Silicon Powder	**Publication Type**	Journal
Author/Editor	ELECTROCHEMICAL SOCIETY.	**Start Page**	A103
Date	01/01/1948	**Issue**	2
Language	English	**Volume**	154
Country	United States of America		

REQUEST DETAILS

Portion Type	Chart/graph/table/figure	**Distribution**	Worldwide
Number of charts / graphs / tables / figures requested	1	**Translation**	Original language of publication
Format (select all that apply)	Electronic	**Copies for the disabled?**	No
Who will republish the content?	Not-for-profit entity	**Minor editing privileges?**	No
Duration of Use	Current edition and up to 5 years	**Incidental promotional use?**	No
Lifetime Unit Quantity	Up to 499	**Currency**	CAD
Rights Requested	Main product		

NEW WORK DETAILS

Title	Si-Fe-O-based Anodes for Lithium-ion Batteries	**Institution name**	Dalhousie University
Instructor name	Mark Obrovac	**Expected presentation date**	2021-07-22

CCC Marketplace™

Springer Nature BV - License Terms and Conditions

This is a License Agreement between Yijia Liu ("You") and Springer Nature BV ("Publisher") provided by Copyright Clearance Center ("CCC"). The license consists of your order details, the terms and conditions provided by Springer Nature BV, and the CCC terms and conditions.

All payments must be made in full to CCC.

Order Date	05-Jun-2021	**Type of Use**	Republish in a thesis/dissertation
Order License ID	1123845-1	**Publisher**	Nature Research
ISSN	2058-8437	**Portion**	Chart/graph/table/figure

LICENSED CONTENT

Publication Title	Nature Reviews Materials	**Rightsholder**	Springer Nature BV
Article Title	Promise and reality of post-lithium-ion batteries with high energy densities	**Publication Type**	e-Journal
		Start Page	16013
		Issue	4
Date	01/01/2016	**Volume**	1
Language	English		
Country	United Kingdom of Great Britain and Northern Ireland		

REQUEST DETAILS

Portion Type	Chart/graph/table/figure	**Distribution**	Worldwide
Number of charts / graphs / tables / figures requested	1	**Translation**	Original language of publication
		Copies for the disabled?	No
Format (select all that apply)	Electronic	**Minor editing privileges?**	No
Who will republish the content?	Not-for-profit entity	**Incidental promotional use?**	No
Duration of Use	Life of current edition	**Currency**	CAD
Lifetime Unit Quantity	Up to 499		
Rights Requested	Main product		

NEW WORK DETAILS

Title	Si-Fe-O-based Anodes for Lithium-ion Batteries	**Institution name**	Dalhousie University
Instructor name	Mark Obrovac	**Expected presentation date**	2021-07-22

CCC Marketplace™

IOP Publishing, Ltd - License Terms and Conditions

Order Date	05-Jun-2021	**Type of Use**	Republish in a thesis/dissertation
Order License ID	1123846-1	**Publisher**	IOP Publishing
ISSN	1945-7111	**Portion**	Chart/graph/table/figure

LICENSED CONTENT

Publication Title	Journal of the Electrochemical Society	**Publication Type**	e-Journal
Article Title	Evaluating Si-Based Materials for Li-Ion Batteries in Commercially Relevant Negative Electrodes	**Start Page**	A783
		End Page	A791
		Issue	5
		Volume	161
		URL	http://www.scitation.org/JES
Author/Editor	Electrochemical Society.		
Date	01/01/1948		
Language	English		
Country	United States of America		
Rightsholder	IOP Publishing, Ltd		

REQUEST DETAILS

Portion Type	Chart/graph/table/figure	**Distribution**	Worldwide
Number of charts / graphs / tables / figures requested	1	**Translation**	Original language of publication
		Copies for the disabled?	No
Format (select all that apply)	Electronic	**Minor editing privileges?**	No
Who will republish the content?	Not-for-profit entity	**Incidental promotional use?**	No
Duration of Use	Current edition and up to 5 years	**Currency**	CAD
Lifetime Unit Quantity	Up to 499		
Rights Requested	Main product		

NEW WORK DETAILS

Title	Si-Fe-O-based Anodes for Lithium-ion Batteries	**Institution name**	Dalhousie University
Instructor name	Mark obrovac	**Expected presentation date**	2021-07-22

CCC Marketplace™

Springer Nature BV - License Terms and Conditions

This is a License Agreement between Yijia Liu ("You") and Springer Nature BV ("Publisher") provided by Copyright Clearance Center ("CCC"). The license consists of your order details, the terms and conditions provided by Springer Nature BV, and the CCC terms and conditions.

All payments must be made in full to CCC.

Order Date	05-Jun-2021	**Type of Use**	Republish in a thesis/dissertation
Order License ID	1123847-1	**Publisher**	Nature Research
ISSN	2058-7546	**Portion**	Chart/graph/table/figure

LICENSED CONTENT

Publication Title	Nature Energy	**Rightsholder**	Springer Nature BV
Article Title	Scalable synthesis of silicon-nanolayer-embedded graphite for high-energy lithium-ion batteries	**Publication Type**	e-Journal
		Start Page	16113
		Issue	9
		Volume	1
Date	01/01/2016		
Language	English		
Country	United Kingdom of Great Britain and Northern Ireland		

REQUEST DETAILS

Portion Type	Chart/graph/table/figure	**Distribution**	Worldwide
Number of charts / graphs / tables / figures requested	1	**Translation**	Original language of publication
		Copies for the disabled?	No
Format (select all that apply)	Electronic	**Minor editing privileges?**	No
Who will republish the content?	Not-for-profit entity	**Incidental promotional use?**	No
Duration of Use	Life of current edition	**Currency**	CAD
Lifetime Unit Quantity	Up to 499		
Rights Requested	Main product		

NEW WORK DETAILS

Title	Si-Fe-O-based Anodes for Lithium-ion Batteries	**Institution name**	Dalhousie University
Instructor name	Mark Obrovac	**Expected presentation date**	2021-07-22

CCC Marketplace™

IOP Publishing, Ltd - License Terms and Conditions

This is a License Agreement between Yijia Liu ("You") and IOP Publishing, Ltd ("Publisher") provided by Copyright Clearance Center ("CCC"). The license consists of your order details, the terms and conditions provided by IOP Publishing, Ltd, and the CCC terms and conditions.

All payments must be made in full to CCC.

Order Date	05-Jun-2021	**Type of Use**	Republish in a thesis/dissertation
Order License ID	1123849-2	**Publisher**	IOP Publishing
ISSN	2151-2043	**Portion**	Chart/graph/table/figure

LICENSED CONTENT

Publication Title	Electrochemical Society. Meeting Abstracts	**Language**	English
Article Title	Mechanofusion-Derived Si Alloy-Graphite Composite Electrode Material for Li-Ion Battery	**Country**	United States of America
Author/Editor	Electrochemical Society, Electrochemical Society.Meeting, International Society of Electrochemistry.	**Rightsholder**	IOP Publishing, Ltd
Date	01/01/1960	**Publication Type**	Journal

REQUEST DETAILS

Portion Type	Chart/graph/table/figure	**Distribution**	Worldwide
Number of charts / graphs / tables / figures requested	1	**Translation**	Original language of publication
Format (select all that apply)	Electronic	**Copies for the disabled?**	No
Who will republish the content?	Not-for-profit entity	**Minor editing privileges?**	No
Duration of Use	Current edition and up to 5 years	**Incidental promotional use?**	No
Lifetime Unit Quantity	Up to 499	**Currency**	CAD
Rights Requested	Main product		

NEW WORK DETAILS

Title	Si-Fe-O-based Anodes for Lithium-ion Batteries	**Institution name**	Dalhousie University
Instructor name	Mark Obrovac	**Expected presentation date**	2021-07-22

RightsLink®

Home | Help | Email Support | Yijia Liu

ACS Publications
Most Trusted. Most Cited. Most Read.

Systematic Investigation of Binders for Silicon Anodes: Interactions of Binder with Silicon Particles and Electrolytes and Effects of Binders on Solid Electrolyte Interphase Formation

Author: Cao Cuong Nguyen, Taeho Yoon, Daniel M. Seo, et al

Publication: Applied Materials

Publisher: American Chemical Society

Date: May 1, 2016

PERMISSION/LICENSE IS GRANTED FOR YOUR ORDER AT NO CHARGE

This type of permission/license, instead of the standard Terms & Conditions, is sent to you because no fee is being charged for your order. Please note the following:

- Permission is granted for your request in both print and electronic formats, and translations.
- If figures and/or tables were requested, they may be adapted or used in part.
- Please print this page for your records and send a copy of it to your publisher/graduate school.
- Appropriate credit for the requested material should be given as follows: "Reprinted (adapted) with permission from (COMPLETE REFERENCE CITATION). Copyright (YEAR) American Chemical Society." Insert appropriate information in place of the capitalized words.
- One-time permission is granted only for the use specified in your request. No additional uses are granted (such as derivative works or other editions). For any other uses, please submit a new request.

If credit is given to another source for the material you requested, permission must be obtained from that source.

BACK CLOSE WINDOW

ACS Publications
Most Trusted. Most Cited. Most Read.

Study on Polymer Binders for High-Capacity SiO Negative Electrode of Li-Ion Batteries

Author: Shinichi Komaba, Keiji Shimomura, Naoaki Yabuuchi, et al

Publication: The Journal of Physical Chemistry C

Publisher: American Chemical Society

Date: Jul 1, 2011

PERMISSION/LICENSE IS GRANTED FOR YOUR ORDER AT NO CHARGE

This type of permission/license, instead of the standard Terms & Conditions, is sent to you because no fee is being charged for your order. Please note the following:

- Permission is granted for your request in both print and electronic formats, and translations.
- If figures and/or tables were requested, they may be adapted or used in part.
- Please print this page for your records and send a copy of it to your publisher/graduate school.
- Appropriate credit for the requested material should be given as follows: "Reprinted (adapted) with permission from (COMPLETE REFERENCE CITATION). Copyright (YEAR) American Chemical Society." Insert appropriate information in place of the capitalized words.
- One-time permission is granted only for the use specified in your request. No additional uses are granted (such as derivative works or other editions). For any other uses, please submit a new request.

If credit is given to another source for the material you requested, permission must be obtained from that source.

BACK CLOSE WINDOW

Home | Help | Email Support | Yijia Liu

The Effect of Fluoroethylene Carbonate as an Additive on the Solid Electrolyte Interphase on Silicon Lithium-Ion Electrodes

Author: Kjell Schroder, Judith Alvarado, Thomas A. Yersak, et al
Publication: Chemistry of Materials
Publisher: American Chemical Society
Date: Aug 1, 2015

PERMISSION/LICENSE IS GRANTED FOR YOUR ORDER AT NO CHARGE

This type of permission/license, instead of the standard Terms & Conditions, is sent to you because no fee is being charged for your order. Please note the following:

- Permission is granted for your request in both print and electronic formats, and translations.
- If figures and/or tables were requested, they may be adapted or used in part.
- Please print this page for your records and send a copy of it to your publisher/graduate school.
- Appropriate credit for the requested material should be given as follows: "Reprinted (adapted) with permission from (COMPLETE REFERENCE CITATION). Copyright (YEAR) American Chemical Society." Insert appropriate information in place of the capitalized words.
- One-time permission is granted only for the use specified in your request. No additional uses are granted (such as derivative works or other editions). For any other uses, please submit a new request.

If credit is given to another source for the material you requested, permission must be obtained from that source.

BACK CLOSE WINDOW

CCC Marketplace™

ASM International - License Terms and Conditions

This is a License Agreement between Yijia Liu ("You") and ASM International ("Publisher") provided by Copyright Clearance Center ("CCC"). The license consists of your order details, the terms and conditions provided by ASM International, and the CCC terms and conditions.

All payments must be made in full to CCC.

Order Date	03-Jun-2021
Order License ID	1123425-1
ISBN-13	978-1-62708-163-4
Type of Use	Republish in a thesis/dissertation
Publisher	ASM International
Portion	Chart/graph/table/figure

LICENSED CONTENT

Publication Title	ASM Handbook, Volume 3 : Alloy Phase Diagrams
Date	01/01/2016
Language	English
Country	United States of America
Rightsholder	ASM International
Publication Type	e-Book

REQUEST DETAILS

Portion Type	Chart/graph/table/figure
Number of charts / graphs / tables / figures requested	1
Format (select all that apply)	Electronic
Who will republish the content?	Academic institution
Duration of Use	Current edition and up to 5 years
Lifetime Unit Quantity	Up to 499
Rights Requested	Main product
Distribution	Worldwide
Translation	Original language of publication
Copies for the disabled?	No
Minor editing privileges?	No
Incidental promotional use?	No
Currency	CAD